Magnetic Fields in the Interstellar Medium

Susan E. Clark

Submitted in partial fulfillment of the
requirements for the degree
of Doctor of Philosophy
in the Graduate School of Arts and Sciences

COLUMBIA UNIVERSITY

2017

ABSTRACT

Magnetic Fields in the Interstellar Medium

Susan E. Clark

The interstellar medium – the space between the stars in our Galaxy – is multiphase, turbulent, and magnetic. Magnetism in the interstellar medium is difficult to observe and to simulate, and the study of interstellar magnetic fields is riddled with open questions. In this Thesis we make progress in several important areas. We use analytic theory, simulations, and observations to advance our understanding of an important plasma instability, of the diffuse neutral medium, and of prospects for uncovering cosmic inflation.

We take an unusual approach to the study of the magnetorotational instability, the mechanism thought to be the primary driver of turbulence and angular momentum transport in astrophysical accretion disks. We conduct a weakly nonlinear analysis of the instability in several important geometries, and derive an envelope equation that governs the evolution of the system on long length- and timescales. We show that the saturated state of the magnetorotational instability may itself be unstable on these large spatial and temporal scales, and we demonstrate that the character of these instabilities will depend on the geometry of the background magnetic field. We posit a possible new saturation mechanism for the magnetorotational instability in a local geometry, when a particular nonideal effect is considered.

We derive new insights into the diffuse interstellar medium, where we present the discovery that thin, linear neutral hydrogen structures are ubiquitous in the cold neutral medium. We demonstrate that these linear features are extremely well aligned with the interstellar magnetic field, as traced by both starlight polarization and polarized dust emission. We discuss the implications of this discovery for cosmological studies. A major goal of modern cosmology is the detection of a particular signature in the polarized cosmic microwave background that would be direct evidence for inflation. This goal has thus far been thwarted by the polarized foreground emission from magnetically aligned interstellar dust grains. We demonstrate that the alignment of neutral hydrogen with the interstellar magnetic field can be used to produce higher-fidelity maps of the foreground polarization field, and we present and test a new Bayesian method for constructing improved foreground maps.

Contents

List of Figures

List of Tables

(This page left intentionally blank.)

ACKNOWLEDGMENTS

First and foremost, thank you to my advisors, Mary Putman and Josh Peek. I feel incredibly privileged to have had not one, but two such wonderful mentors. Thank you for being so supportive of my career and my life, and for giving me enormous latitude to chase my scientific interests in many directions. Thank you to Mary for hikes in Colorado and views in Hawaii, and for being a grounding and inspiring mentor back in New York. Thank you to Josh for giving me a second scientific home in Baltimore, for group beach retreats, and for always being willing to drop everything and hack on a new idea. I have learned an amazing amount from you both.

I have had the benefit of working with many wonderful collaborators in the course of this work. Thank you to the other members of my thesis committee: Greg, Mordecai, and Amber. Special thank you to Jeff Oishi, my collaborator on two of the chapters in this Thesis. I am grateful for many engaging discussions in all of the best lunch spots around the American Museum of Natural History. Thank you to Colin Hill, also a two-chapter collaborator, for being the only person that emails me back immediately when I figure something out at three in the morning. Thank you for always being equally willing to keep staring at a problem, or to take a break and get a beer, as circumstances and sanity dictate.

There are many reasons I went into physics, but there is only one reason I did not abandon it long ago: Laura Havener. I really can't put into words how thankful I am that we managed to tackle physics together at both UNC and Columbia. Every aspect of this journey was improved by your friendship, from lab report all-nighters at Carolina to late nights drinking wine and eating Taco Hut in our New York apartment. Thank you for always saying "yes you can" when I insisted that I could not. This Thesis would not exist without your patient, hilarious, amazingly supportive presence in my life.

Thank you to my sisters, Helen and Karen, for your wit and perspective through the good, the bad, and the silly. You are the people and the scientists that I aspire to be. Thank you to my parents, Bob and Rose, for your unwavering support and love.

My eternal gratitude to the Morehead-Cain Foundation.

I have had so many great advisors in my scientific career so far. Thank you to Fabian Heitsch and Bob Goldstein at UNC, and to Kevin Douglas at Arecibo. Thank you to Debbie Hinton for being an early and formative role model.

I am deeply grateful to everyone in the department at Columbia. Thanks to Millie and Ayoune for all your help and support. Thank you to Summer for all your support and work on outreach. Thank you to all of the faculty, especially Jacqueline, Kathryn, Lam, Jules, Marcel, David, and Zoltan. Thank you to all of the other graduate students, especially Sarah and Andrew, for all of the nights we ordered too much sushi and worked on problem sets together; to Yong, my academic sister and partner in crime on trips to Baltimore; to my wonderful officemates David, Steven, and Alex; to Aleksey, Alejandro, Steph, Maria, Dan, Adrian, Jia, and so many others.

Thank you to so many incredible friends. Thank you especially to Ami, Gillian, Jackie, Kate, Kristin, and Meliha, for being quick to mollify my sorrows and amplify my joys. Thank you to my transient New York crew, which has variously included Joel, Joe, Karl, Sonia, Ivan, and Ethan. Thank you to everyone at TJ beachweek, this year and every year.

Finally, thank you to James. For reading every word of every paper; for cross-timezone video calls so I could practice every talk. For installing a whiteboard in our apartment so I could work out the MRI equations in my pajamas. For being there for every success and every setback, in Thesis life and real life. Thank you for being so dependably wonderful.

2017, New York City

Chapter 1

Introduction

> *The argument in the past has frequently been a process of elimination: one observed certain phenomena, and one investigated what part of the phenomena could be explained; then the unexplained part was taken to show the effects of the magnetic field. It is clear in this case that, the larger one's ignorance, the stronger the magnetic field.*
>
> – Lo Woltjer, 1967

Space is magnetic. Interstellar magnetism is one of the newer mysteries of the cosmos: early stargazers, beguiled by our sky's chatoyant arc of Milky Way, had little cause to suspect that space is permeated by invisible magnetic fields. It was not until the mid-twentieth century, when light from distant stars was observed to be polarized, that an interstellar field was inferred (Hiltner 1949; Davis & Greenstein 1951). Since then, advances in instrumentation and computing have opened new windows into the magnetized universe. Still, magnetism has retained a reputation as an occult field of study. Magnetic fields remain relatively difficult to observe and difficult to simulate. If this is true among astrophysicists it is perhaps even more so in popular culture, where our terrestrial experience – with wireless charging, magnetic levitation, auroras – qualifies magnetism as an abstruse, borderline magical, phenomenon.

This Thesis explores magnetism in the interstellar medium (ISM). The ISM is the stuff between the stars, but is far from the featureless void that that description connotes. The ISM is a churning, turbulent broth, tenuous but intricate, filled with gas, dust, cosmic rays, and magnetic fields. Indeed, calling this rich Galactic ecosystem the "interstellar medium" seems dismissive of its role in the cosmos, akin to calling the ocean the stuff between the whales. Even this analogy belies the true interdependence of the stars and the medium they reside in, since the ISM begets the stars, and the stars become the ISM.

In this Thesis we derive new insights into interstellar magnetic fields, exploring their role in accretion disks, in the diffuse interstellar medium, and as a foreground for cosmology experiments.

1.1 Observing the magnetized interstellar medium

Interstellar space is wondrously complicated. The ISM is influenced by physical processes over an enormous range of scales, including sweeping Galactic spiral arms, supernova explosions, exchange of material with the Galactic halo, and turbulent energy transfer from Galactic length scales down to small-scale density fluctuations. The magnetic field contributes an important energy density component of the ISM, both on its own and through its influence on cosmic rays. The energy densities of magnetic fields, cosmic rays, and turbulence are in approximate equipartition in the ISM, and their combined pressure support keeps the disk gas aloft (Boulares & Cox 1990; Heiles & Crutcher 2005).

The ordinary matter in the ISM is distributed into several phases. The picture of a multiphase ISM has evolved over time, but remains a powerful paradigm for understanding the organization of interstellar material, from dense molecular clouds to hot ionized regions (McKee & Ostriker 1977; Ferrière 2001; Cox 2005). Approximately half of the mass of the

ISM is concentrated into cold molecular clouds, the birthplaces of stars. These clouds remain cold ($T \sim 10 - 20$ K) because they are dense enough ($n \sim 10^2 - 10^6$ cm^{-3}) to block the ambient starlight radiation. Another significant mass fraction of the ISM is in cold atomic gas ($T \sim 50 - 100$ K), or the cold neutral medium, which is mostly organized into diffuse clouds. There is also a warm neutral component of the ISM ($T \sim 10^4$ K), and an ionized component that can reach temperatures of $T \sim 10^6$ K (Ferrière 2001).

Since its unexpected discovery, the interstellar magnetic field has been measured with a number of techniques. Each probes only particular components of the three-dimensional magnetic field vector $\mathbf{B}$, so our picture of the overall field structure is a bricolage of partial information. The polarization of background starlight, polarized dust emission, spectral line polarimetry, synchrotron emission, and Faraday rotation each contribute to our picture of the magnetized ISM.

1.1.1 Polarization by interstellar dust

Starlight polarization traces the plane-of-sky magnetic field orientation along the line of sight to a star. The starlight is polarized by the preferential absorption of charged, spinning dust grains that are aligned with the interstellar magnetic field. The detailed physics of dust grain alignment is an area of active research, and depends on the size and composition of the grains, and the properties of the ambient radiation (Draine 2003; Andersson et al. 2015). Despite these complications, the starlight polarization is strikingly aligned with large-scale features of the Galaxy, and provided the first observational evidence that the large-scale magnetic field is aligned with the Galactic plane (Fosalba et al. 2002; Heiles & Crutcher 2005). The dispersion of starlight polarization angles is often used to estimate the mean field strength in a region (Davis 1951; Chandrasekhar & Fermi 1953; Heitsch et al. 2001), but the polarization data does not directly measure the magnitude of $\mathbf{B}$. The polarization of optical starlight generally traces magnetic fields in the diffuse interstellar dust. Polarimetry in other wavelength ranges, most notably the infrared, traces the field in denser environments (Goodman 1996; Clemens et al. 2012).

Interstellar dust grains communicate their magnetic alignment via a converse process: polarized thermal dust emission. Polarized dust emission likewise traces the plane-of-sky magnetic field orientation and since its first detection was also found to be aligned with the Galactic plane (Benoît et al. 2004). When dust grains align their long axes with the ambient magnetic field, the dust emission polarization angle is typically orthogonal to the plane-of-sky magnetic field orientation, while the starlight polarization angle is parallel. Another key difference between these tracers is that whereas the starlight polarization traces the line of sight between observer and star, the dust polarization necessarily traces the entire line of sight out to infinity. Changes in the field along the line of sight will tend to depolarize the emission, so that the measured polarization is biased toward nearby regions, but inferring the distance to the polarizing regions is not as straightforward in principle as measuring the distance to a star.

1.1.2 Spectral line polarization

The polarization of spectral lines is a window into the denser regions of the magnetic ISM. An atom sitting in a magnetic field will feel a torque on its magnetic dipole, which perturbs the Hamiltonian of the molecule by an amount proportional to the field strength. The hyperfine energy levels split, from a single energy level that depends only on the principal quantum number to a multiplet that also depends on the magnetic quantum number. The energy level change is

$$\Delta E = \mu_B g_J B m_j, \tag{1.1}$$

where μ_B is the Bohr magneton, g_J is the Landé g factor, B is the strength of the external magnetic field, and m_j is the relevant quantum number, provided that the external magnetic field is much smaller than the internal field (e.g. Griffiths 2005). In principle the frequency shift $\Delta\nu$ associated with Equation 1.1 is directly measurable, and can be used to measure all components of the magnetic field vector. Indeed, Zeeman splitting measurements provided the first detection of a celestial magnetic field, observed in sunspots by Hale in 1908. In the interstellar medium, however, the $\Delta\nu$ is typically much smaller than the observed line width ($\Delta\nu/\delta\nu \ll 1$), and the Stokes Q and U are negligible. Zeeman measurements must instead be measured in the difference between components of the circular polarization, i.e. Stokes V. The usual approach is to fit the derivative of the Stokes I spectrum to the observed Stokes V spectrum,

$$V(\nu) \propto \frac{\mathrm{d}I(\nu)}{\mathrm{d}\nu} B_{\parallel}, \tag{1.2}$$

to obtain $B_{\parallel}$ (Heiles et al. 1993). Thus observational constraints reduce the Zeeman effect to a probe of the line-of-sight field strength in the ISM, from which only a lower limit to the total field strength can be surmised. The exceptions to this limitation are masers, for which linear polarization can often also be detected (Crutcher 2012). The first measurement of the Zeeman effect in the ISM was in HI line absorption toward the Casseopia A supernova remnant (Verschuur 1968). The effect was later measured in OH (Crutcher & Kazes 1983) and CN (Crutcher et al. 1999) spectral lines. The sixty year delay between the first solar Zeeman measurement and the first detection in the diffuse ISM is a testament to the challenging nature of this technique.

The Goldreich-Kylafis effect is another form of molecular line polarization (Goldreich & Kylafis 1981; Kylafis 1983; Deguchi & Watson 1984). Because magnetic fields split the energy states of a molecule into different magnetic sublevels, the molecule will only absorb or emit certain polarizations of light. If the magnetic sublevels are populated by anisotropic radiation, and this radiative excitation is at least comparable to collisional excitation, the molecule will radiate with a net linear polarization. A velocity gradient in the region will anisotropically populate the magnetic sublevels because the line optical depth will appear anisotropic. Goldreich-Kylafis line polarization may be parallel or perpendicular to the local magnetic field, depending on the relative orientations of the magnetic field, anisotropic radiation field, and the line of sight (Heiles et al. 1993; Crutcher 2012). As with Zeeman splitting, the articulation of the Goldreich-Kylafis effect preceded its detection: after its prediction in 1981, it took until 1997 (Glenn et al.) for this line polarization to be detected, and until 1999 (Greaves et al.) for it to be detected in the ISM. Our knowledge of ISM polarization mechanisms surely remains incomplete, as a recently proposed new source of non-Zeeman circular polarization demonstrates (Houde et al. 2013).

Compilations of Zeeman measurements have so far yielded the clearest picture of the strength of the magnetic field in the cold neutral medium component of the ISM. The field strength is remarkably constant over nearly three orders of magnitude in density where $n(H) \lesssim 300$ cm^{-3} (Crutcher et al. 2010). This may indicate that density structures in the more diffuse HI primarily accumulate along field lines, if flux is not otherwise removed from the gas. Motion parallel to field lines allows gas to become more dense without dragging field lines closer together, thereby increasing the field strength. At higher densities ($n(H) > 300$ cm^{-3}), the field strength scales with density as approximately $\rho^{2/3}$ (Crutcher 2012). This is one probe of the magnetic field's controversial role in star formation. The $\rho^{2/3}$ scaling, and observed mass-to-flux ratios, suggest that gravity dominates over magnetic pressure in molecular clouds. This contradicts an earlier paradigm in which molecular clouds are long lived and magnetically supported, and form stars only after ambipolar diffusion allows sufficient neutral gas to condense that the core of a cloud can collapse. Static magnetic pressure support apparently cannot be relied upon to mediate star formation in galaxies, but the role of magnetism in star formation continues to inspire debate (see Mouschovias 1991; Mac Low & Klessen 2004; McKee & Ostriker 2007; Federrath & Klessen 2012, among many others).

1.1.3 Radio-wavelength polarization

Charged particles radiate when accelerated in a magnetic field. The magnetic field is thus also traced by emission from cosmic rays – electrons and nuclei moving at relativistic speeds. Some of these high-energy particles are thought to be produced in supernova remnants, but their origins are not entirely understood, particularly at the highest energies (e.g. Ahlers & Mertsch 2017). The synchrotron emissivity is proportional to the density of cosmic rays, the component of the magnetic field perpendicular to the line of sight, and the spectral index of the cosmic ray radiation. This emission is highly polarized, with an intrinsic polarization fraction that can theoretically reach $\sim 75\%$ in a perfectly regular magnetic field, though the measured synchrotron polarization fraction is lower because of various depolarizing effects. The total and polarized synchrotron intensities can be used to trace the total magnetic field strength, as well as to infer properties of its geometry. The total field strength from synchrotron emission, derived by assuming equipartition between the magnetic energy density and the energy density in cosmic ray electrons, is found to be $\sim 6\ \mu$G in the local ISM, with field strengths rising to $\sim 10\ \mu$G close to the Galactic center (Beck 2001).

As linearly polarized light passes through a magnetized medium, its plane of polarization is rotated by an angle proportional to the rotation measure,

$$\mathrm{RM} = C \int_0^L n_e B_\parallel \mathrm{d}l, \tag{1.3}$$

where $C = 0.81$ rad m^{-2}, n_e is the free electron density in cm^{-3}, $B_\parallel$ is the line-of-sight component of the magnetic field vector in μG, and L is the distance to the source in pc (Gardner & Whiteoak 1966). The rotation measure thus probes the magneto-ionic medium between an observer and some polarized background source, such as a quasar or pulsar. Pulsars are particularly advantageous, because their dispersion measure,

$$\mathrm{DM} = \int_0^L n_e \mathrm{d}l, \tag{1.4}$$

is a direct measurement of the free electron column between the observer and the pulsar. Dividing Equation 1.3 by Equation 1.4 gives the electron-density-weighted average $B_\parallel$ along the line of sight. Surveys of the interstellar magnetic field toward pulsars find a local magnetic field strength of $\sim 1.4 - 2$ μG in the uniform component, and an increasing field strength toward the center of the Galaxy (Rand & Kulkarni 1989; Rand & Lyne 1994; Han et al. 2006).

1.2 The Galactic magnetic field

Faraday rotation measures have been used extensively to infer the three-dimensional structure of the Galactic magnetic field (e.g. Vallée 2005; Brown et al. 2007; Van Eck et al. 2011). There are many challenges to this technique: pulsars lie within the Galaxy and so can probe the intervening field at a number of distances, but are relatively sparsely sampled. Extragalactic radio sources probe the entire line of sight through the Galaxy, plus whatever magneto-ionic material might lie within their host galaxy or the intergalactic medium, and the electron column along these lengthy sightlines is poorly constrained. Local structures such as superbubbles and HII regions significantly impact the magnetic field structure, complicating the interpretation of structure in the RM map (Mitra et al. 2003; Stil et al.

2011).

In part to mitigate these difficulties, a number of modelers have combined Faraday rotation data with other tracers. Polarized synchrotron emission is widely used, and complements RMs because it probes $B_\perp$, the component of the magnetic field perpendicular to the line of sight (e.g. Sun et al. 2008; Jansson & Farrar 2012). As the quality of available data improves, models are beginning to incorporate polarized dust emission as well (Jaffe et al. 2013; Adam et al. 2016). Models often decompose the overall magnetic field into a large-scale, or regular, component, and a small-scale, or random, component. The random component is sometimes modeled as both an "ordered random" component, containing small-scale variations in direction but not in orientation, and an "isotropic random" component, which varies three-dimensionally in both strength and direction. These distinctions are motivated theoretically: the large-scale component probes galaxy-scale dynamics, the isotropic random component probes ISM turbulence, and the ordered random component may arise via shearing or compression of the isotropic random field. These components also produce different Faraday and synchrotron signatures (Jaffe et al. 2010).

These models vary widely in their input data, fixed and variable fit parameters, assumed field components, and so forth, and broadly disagree on the overall shape or even basic symmetries of the Galactic magnetic field. Nevertheless, a few points of consensus have emerged, which are nicely summarized in Haverkorn (2015). The large-scale magnetic field is roughly oriented along the spiral arms in the Galactic disk. The Milky Way is apparently typical in this regard: nearly all radio polarimetric observations of other spiral galaxies show ordered fields following the spiral arms (Beck 2015). Observations also mostly concur on the existence of one large-scale field reversal between the Sun and the Galactic Center (e.g. Simard-Normandin & Kronberg 1980). The total number of field reversals and their locations is still debated. Given the spiral structure of the Galactic magnetic field, one parameter that is often estimated is its pitch angle,

$$\alpha_p = \arctan \frac{B_r}{B_\phi}, \tag{1.5}$$

where B_r and B_ϕ are the radial and azimuthal components of the field. Current estimates of the local pitch angle range from $-5°$ to $-30°$ based on tracer, and may vary with location because of the interaction between spiral density waves and the magnetic field (Gomez & Cox 2004). The total field strength in the Solar neighborhood is $B_{total} \sim 6\ \mu$G, with a large-scale component $B_{regular} \sim 2\mu$G and a random component $B_{random} \sim 3 - 4\mu$G (Haverkorn 2015).

The origin of the Galactic magnetic field remains an open question. Theories of Galactic field generation typically advocate a field origin that either predates the formation of the Galaxy or is created and continually sustained by a Galactic dynamo. Neither picture is currently strongly preferred nor ruled out by observations (Zweibel 2005). Indeed, magnetogenesis in the Universe at large is an unanswered question of fundamental importance (Durrer & Neronov 2013).

1.3 The magnetohydrodynamic interstellar medium

Terrestrially, we think of magnetism as arising from the influence of currents – generated at the flip of a switch and decaying just as quickly. Astrophysically, however, decay times are long, and the magnetic field is in some ways more fundamental to a system's evolution than its corresponding current. The diffuse ISM is well-ionized enough that the role of the induction equation in a magnetohydrodynamic description of the ISM is primarily advective rather than diffusive. Idealizing the ISM as a perfectly conducting medium with perfect coupling between ions and neutrals, the induction equation reduces to

$$\partial_t \mathbf{B} = \nabla \times (\mathbf{v} \times \mathbf{B})\,, \tag{1.6}$$

which implies that

$$\frac{\mathrm{d}}{\mathrm{d}t} \int_S \mathbf{B} \cdot \mathrm{d}S = 0, \tag{1.7}$$

in other words the magnetic flux through a Lagrangian surface S is constant in time. This condition is known as “flux-freezing”, or Alfvén’s theorem. Flux freezing is often oversimplified: its colloquial description that “gas and magnetic fields move together” is misread to imply that gas and magnetic fields must be correlated. This is incorrect. In the flux freezing approximation only fluid motions perpendicular to the magnetic field will drag the field lines along, while gas motions parallel to the field remain uninhibited (e.g. Vazquez-Semadeni 2012). We are therefore invited to visualize the magnetized ISM as a structured substrate, imbued with directionality. Cox (2005) uses the analogy of a woven polymer, or a piece of felt. Whatever your analogy, it is clear that fluids are qualitatively altered in the presence of magnetism. Our intuition may be better served by appreciating this at the outset rather than imposing magnetic fields onto our conceptualizations of hydrodynamic behavior. The magnetorotational instability, which we will encounter in the next section, is a quintessential example of the surprising character of magnetohydrodynamic flows.

1.4 Magnetic fields in astrophysical disks

The ISM fills the space between the stars in our Galaxy, and so is bordered on the largest scales by the circumgalactic medium, and on the smallest scales by the outer boundaries of stars. The circumstellar material around forming stars is thus the edge of the ISM: the frontier of its ever-changing topology. Here, magnetic fields play a crucial role in ushering material between its interstellar and stellar incarnations.

Stars form from the gravitational collapse of giant molecular clouds in the ISM. As a molecular cloud contracts, conservation of angular momentum will tend to flatten the cloud into a disk. This led to a longstanding problem in accretion physics: how is matter collapsing onto a central object able to coalesce despite the conservation of specific angular momentum? The Galaxy is host to a panoply of accretion disks: disks around protostars, black holes, and binary stars comprise a portrait of the centrifugal barrier faced by infalling material. And yet, stars form and black holes grow, so clearly efficient accretion is taking place. Some viscous mechanism must redistribute angular momentum in the disk. Molecular viscosity is woefully insufficient, and Keplerian disks are hydrodynamically stable by the Rayleigh criterion. Thus, magnetohydrodynamic turbulence was implicated even before a plausible catalyst was identified (Shakura & Sunyaev 1973; Pringle 1981).

1.4.1 The magnetorotational instability

One such catalyst of magnetohydrodynamic turbulence is the magnetorotational instability (MRI). The MRI was actually discovered by Chandrasekhar (1960) and Velikhov (1959), but since its rediscovery and application to accretion disks by Balbus & Hawley (1991), the MRI remains the leading explanation for rapid angular momentum transport in astrophysical disks.

The MRI in its simplest geometry requires only two ingredients: outwardly decreasing differential rotation and a weak vertical magnetic field. The essence of the MRI can be appreciated by considering the journeys of two fluid elements which are initially rotating at the same radial point in the disk. Our two elements experience some small radial displacement, such that one finds itself slightly interior to its starting point, and one slightly exterior. In a hydrodynamic disk, this might be the end of our story: the fluid elements retain their original angular momentum, and so settle back to their original orbit after their brief epicyclic detour (Balbus 2001). Conservation of specific angular momentum means that rotating hydrodynamic fluids remain stable to axisymmetric radial perturbations provided that

$$\frac{\mathrm{d}}{\mathrm{d}r}\left[(r^2\Omega)^2\right] > 0. \tag{1.8}$$

This is the Rayleigh stability criterion (Rayleigh 1917), long thought to be the last word on the local stability of differentially rotating fluids.

In the presence of a vertical magnetic field, however, we have hardly reached the denouement. Our fluid elements, once displaced, find themselves tethered by a magnetic field line, which acts to resist the displacement. We need observe nothing about the properties of magnetic fields except their tendency to enforce isorotation, and therefore to resist the difference in shear at the two points in the disk. We thus take the angular *velocity* to be conserved. Now the displaced fluid parcel will only return to its starting point if

$$\frac{\mathrm{d}}{\mathrm{d}r}\Omega^2 > 0, \tag{1.9}$$

which is never the case in a Keplerian disk, where the rotation velocity decreases with radius. Instead, our outwardly displaced fluid element arrives in its new orbit with too much angular momentum to remain there. Differential rotation increases its displacement from its original position, while magnetic tension acts, proportionally to the displacement, to increase its velocity. The inwardly displaced fluid drifts ever inward, and the outwardly displaced, ever outward (Balbus & Hawley 1998).

Several qualities should be appreciated which are central to the MRI's success in solving the efficient accretion problem. First, angular momentum transfer is no secondary consequence of the MRI: the essence of the linear instability is the exchange of angular momentum along radial field line components. Second, a weakly magnetized fluid is generically unstable to this process: the fluid-tethering property of weak magnetic fields unlocks the free energy of the shear. The mere quality of being magnetized radically changes the dynamical evolution of a disk. Indeed, the MRI growth rate is independent of the field strength, and the instability remains robust even in the limit $\mathbf{B} \rightarrow 0$ (Balbus & Hawley 1991; Hawley et al. 1996; Balbus 2003).

1.5 Interstellar magnetism as a cosmological foreground

For all its beauty and complexity, the ISM is but a nuisance to cosmological studies. The discovery of the cosmic microwave background (CMB) was dramatic evidence for the Big Bang theory: that the Universe began in a hot dense state and has spent its ensuing lifetime expanding and cooling (Penzias & Wilson 1965; Dicke et al. 1965). Since its initial detection the CMB has provided a wealth of information on the state of the Universe when it first became transparent to radiation, at a redshift $z \sim 1100$. Mapping the CMB in increasingly exquisite detail has enabled precise measurements of the parameters of the standard model of cosmology.

The original Hot Big Bang cosmology posed a number of difficulties, often summarized as the flatness, horizon, and monopole problems. Simply put, the Universe is too flat, too isotropic and homogenous: it seems an untenably extraordinary coincidence that the Universe possesses its observed curvature and uniformity. The Universe is also puzzlingly devoid of magnetic monopoles, particles predicted to exist by Grand Unified Theories of particle physics. The theory of inflation solves these problems by positing that the early Universe underwent a period of extremely rapid inflation, such that regions which were initially in causal contact were rapidly spread to great distances (Guth 1981). Quantum fluctuations in the primordial Universe were flung to distances farther than the cosmic horizon. Inflation simultaneously diluted the number density of magnetic monopoles to below detectable levels.

The inflationary paradigm is a satisfactory explanation for current CMB observations (Ade et al. 2013). However a direct detection of a signal predicted by inflation remains elusive. In principle such a confirmation is possible: If inflation occurred we should see lingering traces of the violent expansion of spacetime in the polarization of the CMB. The CMB is linearly polarized by Thompson scattering of an anisotropic distribution of electrons at the surface of last scattering. This polarization is dominated by an E-mode (curl-free) polarization pattern first detected by DASI (Kovac et al. 2002). E-mode polarization is primarily produced by scalar density perturbations. Gravitational waves produced during the epoch of inflation are predicted to cause tensor perturbations that would imprint a B-mode (gradient-free) polarization signature: a particular combination of Stokes Q and U that cannot be produced by scalar modes (Seljak 1997). B-mode polarization is also produced from E-mode polarization by the gravitational lensing of the large scale structure of the Universe. Lensing B-modes were detected for the first time by the South Pole Telescope (Hanson et al. 2013). Fortunately this lensing B-mode peaks at much smaller angular scales than the inflationary gravitational wave B-mode signal, so they are not easily confused.

The first detection of primordial B-mode polarization was claimed by the BICEP2 collaboration (Ade et al. 2014b). However, the authors did not properly account for the polarized dust emission produced by the ISM, and it was quickly shown that the measured B-mode signal was not in excess of the polarized dust signal discussed in Section 1.1 (Flauger et al. 2014; Ade et al. 2015a). Hence, the ISM's role as nuisance: one of the most important cosmological questions of our era is impeded by the emission of dust grains aligned with the interstellar magnetic field. Prospects for measuring the inflationary signal now hinge on our ability to characterize this polarized dust foreground. The study of the history of the Universe is inextricably linked to our understanding of the magnetized ISM.

1.6 Structure of Dissertation

This Thesis examines the magnetorotational instability, the magnetic nature of the cold neutral medium of the ISM, and the use of the magnetized ISM for measuring the polarized CMB foreground. We begin at the edges of newborn stars, and end at the edge of the Universe.

Chapters 2 and 3 examine the MRI from the perspective of pattern formation theory. We present a multiple scales analysis of the non-ideal MRI in the weakly nonlinear regime – that is, when the most unstable MRI mode has a growth rate asymptotically approaching zero from above. In Chapter 2 we develop our theory in a local, Cartesian channel. Our results confirm the finding by Umurhan et al. (2007) that the perturbation amplitude follows a Ginzburg-Landau equation. We further find that the Ginzburg-Landau equation will arise for the local MRI system with shear-periodic boundary conditions when the effects of ambipolar diffusion are considered. A detailed force balance for the saturated azimuthal velocity and vertical magnetic field demonstrates that even when diffusive effects are important, the bulk flow saturates via the combined processes of reducing the background shear and rearranging and strengthening the background vertical magnetic field. We directly simulate the Ginzburg-Landau amplitude evolution for our system and demonstrate the pattern formation our model predicts on long length and time scales. We compare the weakly nonlinear theory results to a direct numerical simulation of the MRI in a thin-gap Taylor Couette flow. Chapter 2 is published as Clark & Oishi (2017b).

In Chapter 3 we conduct a global, multiscale perturbation analysis of the MRI in a

Taylor-Couette flow. We analyze both the standard MRI, initialized by a constant vertical background magnetic field, and the helical MRI, with an azimuthal background field component. This is the first weakly nonlinear analysis of the MRI in a global Taylor-Couette geometry, as well as the first weakly nonlinear analysis of the helical MRI. We find that the evolution of the amplitude of the standard MRI is described by a real Ginzburg-Landau equation, while the amplitude of the helical MRI takes the form of a complex Ginzburg-Landau equation. This suggests that the saturated state of the helical MRI may itself be unstable on long spatial and temporal scales. Chapter 3 is published as Clark & Oishi (2017a).

Chapter 4 presents the discovery that the texture of the diffuse neutral ISM is deeply linked to the structure of the interstellar magnetic field. We present observations of slender, linear HI features we dub "fibers" that extend for many degrees at high Galactic latitude. To characterize and measure the extent and strength of these fibers, we present the Rolling Hough Transform (RHT), a new machine vision method for parameterizing the coherent linearity of structures in the image plane. With this powerful new tool we show the fibers are oriented along the interstellar magnetic field as probed by starlight polarization. We find that these low column density ($N_{HI} \simeq 5 \times 10^{18}$ cm^{-2}) fiber features are most likely a component of the local cavity wall, about 100 pc away. The HI data we use to demonstrate this alignment at high latitude are from the Galactic Arecibo L-Band Feed Array HI (GALFA-HI) Survey and the Parkes Galactic All Sky Survey (GASS). We find better alignment in the higher resolution GALFA-HI data, where the fibers are more visually evident. This trend continues in our investigation of magnetically aligned linear features in the Riegel-Crutcher HI cold cloud, detected in the Southern Galactic Plane Survey (SGPS). We propose an application of the RHT for estimating the field strength in such a cloud, based on the Chandrasekhar-Fermi method. Chapter 4 is published as Clark et al. (2014).

In Chapter 5 we use GALFA-HI data to show that linear structure in diffuse HI correlates with the magnetic field orientation implied by *Planck* 353 GHz polarized dust emission. At high Galactic latitudes, where the *Planck* data are noise-dominated, the HI data provide an independent constraint on the Galactic magnetic field orientation, and hence the local dust polarization angle. We detect strong cross-correlations between template maps constructed from estimates of dust intensity combined with either HI-derived angles, starlight polarization angles, or *Planck* 353 GHz angles. The HI data thus provide a new tool in the search for inflationary gravitational wave B-mode polarization in the cosmic microwave background, which is currently limited by dust foreground contamination. Chapter 5 is published as Clark et al. (2015).

In Chapter 6 we apply the findings in Chapters 4 and 5 that HI features are well aligned with the local magnetic field to the pressing need for high-fidelity maps of the polarized CMB foreground. We develop a Bayesian procedure that uses *Planck* 353 GHz observations as the likelihood of the data, and the RHT of GALFA-HI maps as a prior on the plane-of-sky dust polarization angle. We construct HI-based priors in a number of ways from the RHT data. We sample the resulting Bayesian posteriors to obtain new maps of the dust polarization. We test the performance of these maps by cross-correlating them with *Planck* 217 GHz data. We find that HI-based priors are a promising method for improving maps of the polarized dust foreground. This Chapter describes ongoing work and is not yet published.

Finally, in Chapter 7, we summarize the results of this Thesis, and propose several directions for future research inspired by the work presented here.

Chapter 2

The weakly nonlinear magnetorotational instability in a local geometry

2.1 Introduction

For matter to accrete from a disk onto a central object, angular momentum must be transported radially outward in the disk. The transport mechanism is likely turbulent, as molecular viscosity alone cannot account for the needed angular momentum transfer, and likely magnetic, as this turbulence is excited even in hydrodynamically stable disks (Shakura & Sunyaev 1973). Discovered by Chandrasekhar (1960) and Velikhov (1959) in a global geometry, the magnetorotational instability (MRI) was subsequently rediscovered and applied to accretion disks by Balbus & Hawley (1991). Since then, the MRI remains the leading explanation for rapid angular momentum transport in astrophysical disks. The instability

---

This section contains text from an article published in the Astrophysical Journal (Clark & Oishi 2017b).

in its simplest geometry arises when a differentially rotating disk is threaded by a vertical magnetic field. The presence of the magnetic field linearly destabilizes the disk gas, driving turbulence and angular momentum transport (e.g. Hawley et al. 2011; Parkin & Bicknell 2013; Parkin 2014). The MRI likely plays a role in a diverse host of astrophysical systems, including protoplanetary disks (e.g. Bai 2015) and black hole accretion disks (e.g. Schnittman et al. 2013), as well as stellar interiors (e.g. Wheeler et al. 2015). Despite its importance, many aspects of the MRI remain poorly understood. In particular, the nonlinear saturation mechanism for the MRI is an open question, and a formidable challenge. MRI saturation has been tackled almost exclusively with simulation, with a few notable exceptions detailed below. In this work we analytically investigate the weakly nonlinear saturation of the MRI.

Weakly nonlinear analysis is a perturbative method used to examine the asymptotic behavior of a system near threshold – that is, when the system is just barely unstable to its most unstable mode. The analytical technique follows the multiscale evolution of fluid variables in a perturbation expansion, allowing the controlled interaction of modes between orders in a perturbation series (Bender & Orszag 1978). Weakly nonlinear analysis can be a powerful technique for analytically examining systems which in their full generality exhibit such complicated nonlinear behavior that their study is relegated primarily to the simulation domain. The MRI is one such phenomenon: while there is a rich literature analytically examining the linear MRI, analytical treatments of the *nonlinear* system are relatively few. The weakly nonlinear treatment of the MRI was pioneered by Knobloch & Julien (2005) and Umurhan et al. (2007b, hereafter URM07; see also 2007a). The latter authors undertook the first weakly nonlinear analysis of the MRI in a thin-gap Taylor-Couette (TC) flow with strong dissipation (as is appropriate to liquid metal experiments), and found that the marginal MRI system approaches saturation in a manner analogous to that of Rayleigh-Bénard convection. Weakly nonlinear analysis was instrumental in our understanding of Rayleigh-Bénard convection saturation (Newell & Whitehead 1969), and the similarities between convection and the local MRI are the result of important shared symmetries between the systems. The success of URM07 in modeling the MRI system near threshold merits further consideration, but we are unaware of any other attempts to expand upon their theoretical framework. In this work we rederive the theory of URM07, and expand upon their findings. Our focus here is on fully characterizing the local MRI system, both for independent theoretical interest and to have a robust comparison point for extensions of this theory into more complicated geometries. In a companion paper we derive for the first time the weakly nonlinear theory of the standard and helical MRI in a global, cylindrical TC flow (Clark & Oishi 2017a, hereafter Chapter 3). The thin- and wide-gap treatments complement one another theoretically, and both are important regimes for comparison with simulation.

This work examines TC flow in the thin-gap regime, an idealization in which the radial extent of the channel is very small compared to its distance from the center of rotation, i.e. $(r_2 - r_1) \ll \frac{1}{2}(r_1 + r_2)$ where r_1 and r_2 are the radii of the inner and outer flow boundaries, respectively. The thin-gap approximation eliminates curvature terms, so the domain geometry is Cartesian rather than cylindrical. The excluded curvature terms have an explicit dependence on r, so they make the problem more challenging both analytically and numerically. In particular, in the wide-gap geometry (i.e. true Taylor-Couette flow) the base angular velocity is a function of r, where in the thin-gap approximation the shear flow reduces to a linear profile. The equations of motion in thin-gap TC flow are thus identical to the MRI in a local shearing box, which differs from our fiducial setup only in the application of periodic boundary conditions.

We note several other important analytical studies of MRI saturation. Knobloch & Julien (2005) analyze the MRI in the strongly nonlinear regime, by following the already-developed

MRI modes into asymptotic saturation. They consider a thin-gap regime as well, and so their theory may be considered the strongly nonlinear analogue to the one developed here. Vasil (2015) examines the weakly nonlinear MRI in a thin-gap regime in a minimal model, finding deep mathematical similarities between the MRI system and the elastodynamic instability of a buckling beam. We discuss these results and their relation to ours in Section 2.6. Several authors have investigated the behavior of the MRI when the boundary conditions are shear periodic, and so the MRI has no mechanism by which to modify the background shear flow profile. In this approximation linear MRI growth is dominated by channel modes, a type of MRI mode that, for periodic boundary conditions, are exact solutions of both the linear and nonlinear MRI equations (Goodman & Xu 1994). In this regime the MRI saturates via parasitic instabilities, which feed off and destroy the primary MRI modes. Analytical investigation of this case reveals that MRI saturation can be caused by parasitic Kelvin-Helmholtz and tearing mode instabilities, depending on parameter regime (Pessah 2010). The theory of MRI channel mode parasites is robust (see also Pessah & Goodman 2009; Latter et al. 2010; Rembiasz et al. 2016), but their importance may be overestimated by the local approximation (Latter et al. 2015), and not germane to global analyses like the one presented here. Latter et al. (2015) gives a detailed analysis of the relation between local and global linear MRI modes. In this work we describe the applicability of our weakly nonlinear theory to shear-periodic boxes. We find that under certain conditions the weakly nonlinear mode interaction described here may provide an alternative MRI saturation mechanism in the shearing box that does not rely on parasitic instabilities.

We begin with an overview of our basic model equations for the local MRI in Section 2.2 and then describe our weakly nonlinear analysis and give results for the thin-gap TC flow in Section 2.3. In Section 2.4 we detail the conditions under which our theory applies to the case where the boundary conditions are shear periodic, namely the consideration of ambipolar diffusion. We compare our results to a direct numerical simulation in Section 2.5. We then place our results in the context of previous results from both analytic and computational studies in Section 2.6 and draw conclusions in Section 2.7.

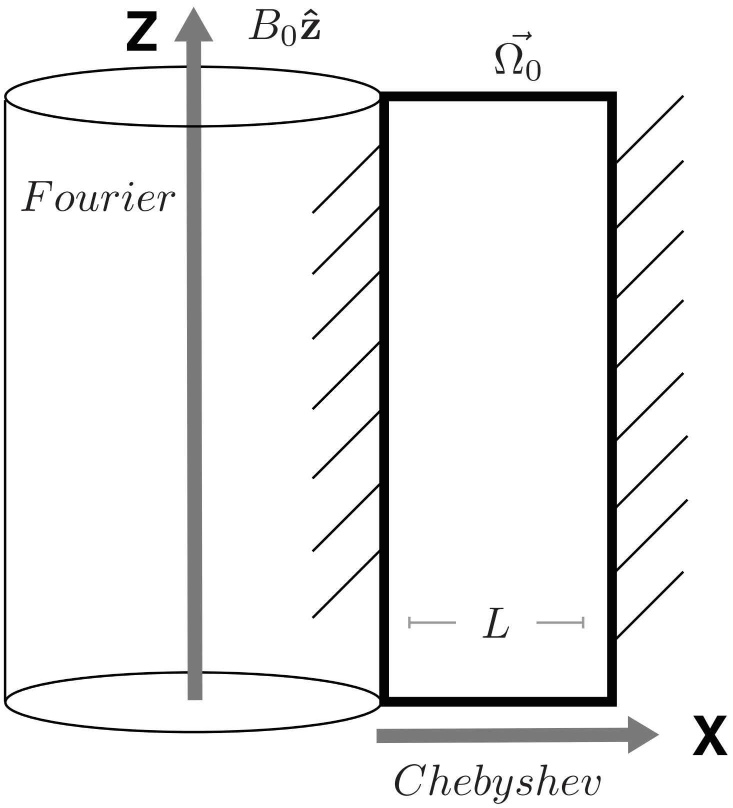

Figure 2.1: Schematic diagram of our set-up, an axisymmetric thin-gap Taylor-Couette flow. We investigate a 2D slice of the X-Z (radial-vertical) plane. Our domain is represented by the bolded black box, of width L. The radial dimension is solved with a basis of Chebyshev polynomials, and the vertical dimension is solved on a Fourier basis.

2.2 Equations

The evolution of a conducting fluid is governed by the momentum and induction equations,

$$\partial_t \mathbf{u} + \mathbf{u} \cdot \nabla \mathbf{u} = -\frac{1}{\rho} \nabla P - \nabla \Phi + \frac{1}{\rho} (\mathbf{J} \times \mathbf{B}) + \nu \nabla^2 \mathbf{u} - 2 \boldsymbol{\Omega} \times \mathbf{u} - \boldsymbol{\Omega} \times (\boldsymbol{\Omega} \times \mathbf{r}) , \quad (2.1)$$

$$\partial_t \mathbf{B} = \nabla \times (\mathbf{u} \times \mathbf{B}) + \eta \nabla^2 \mathbf{B}, \quad (2.2)$$

where P is the gas pressure, ν is the kinematic viscosity, η is the microscopic diffusivity, $\nabla\Phi$ is the gravitational force per unit mass, and the current density is $\mathbf{J} = \nabla \times \mathbf{B}$. Equations 2.1 and 2.2 are subject to the incompressibility and magnetic solenoid constraints,

$$\nabla \cdot \mathbf{u} = 0 \quad (2.3)$$

$$\nabla \cdot \mathbf{B} = 0. \quad (2.4)$$

We axisymmetrically perturb all three vector components of each of the fluid quantities. We nondimensionalize the equations, with lengths nondimensionalized by L, time by Ω_0, velocities by $\Omega_0 L$, magnetic fields by B_0, and pressure by $\Omega_0^2 L^2 \rho_0$, where L is the channel width, Ω_0 is the rotation rate at the center of the channel, and ρ_0 is the constant pressure in the base state (see Figure 2.1). We define the Reynolds number, $\mathrm{Re} \equiv \Omega_0 L^2/\nu$, magnetic Reynolds number, $\mathrm{Rm} \equiv \Omega_0 L^2/\eta$, and Cowling number, $\mathrm{Co} \equiv 2v_A^2/\Omega_0^2 r_0^2$, where the Alfvén speed v_A is $v_A^2 = B_0^2/\rho_0$. The magnetic Prandtl number, $\mathrm{Pm} \equiv \mathrm{Rm}/\mathrm{Re}$, encodes the ratio of microscopic viscosity to magnetic diffusivity. The fluid symbols $\mathbf{u}$, $\mathbf{B}$, etc. will henceforth be used to refer to the nondimensional, perturbed quantities.

We define the streamfunction Ψ and flux function A, where A is the familiar two-dimensional vector potential. Ψ and A are scalar fields. The curl of Ψ and the curl of A are defined as the velocity and magnetic field perturbation, respectively, and so Ψ and A automatically satisfy our constraints (Equations 2.3 and 2.4).

Ψ and A are thus related to the velocity and magnetic field perturbations, respectively, as

$$\mathbf{u} = \begin{bmatrix} \partial_z \Psi \\ u_y \\ -\partial_x \Psi \end{bmatrix}, \tag{2.5}$$

$$\mathbf{B} = \begin{bmatrix} \partial_z A \\ B_y \\ -\partial_x A \end{bmatrix}. \tag{2.6}$$

Our final equation set is

$$\partial_t \nabla^2 \Psi - 2\partial_z u_y - \mathrm{Co} B_0 \partial_z \nabla^2 A - \frac{1}{\mathrm{Re}} \nabla^4 \Psi = \mathrm{Co} J\left(A, \nabla^2 A\right) - J\left(\Psi, \nabla^2 \Psi\right) \tag{2.7}$$

$$\partial_t u_y + (2-q)\,\partial_z \Psi - \mathrm{Co} B_0 \partial_z B_y - \frac{1}{\mathrm{Re}} \nabla^2 u_y = \mathrm{Co} J\left(A, B_y\right) - J\left(\Psi, u_y\right) \tag{2.8}$$

$$\partial_t A - B_0 \partial_z \Psi - \frac{1}{\mathrm{Rm}} \nabla^2 A = J\left(A, \Psi\right) \tag{2.9}$$

$$\partial_t B_y + q\partial_z A - B_0 \partial_z u_y - \frac{1}{\mathrm{Rm}} \nabla^2 B_y = J\left(A, u_y\right) - J\left(\Psi, B_y\right), \tag{2.10}$$

where J is the Jacobian operator,

$$J\left(f, g\right) \equiv \partial_z f \partial_x g - \partial_x f \partial_z g, \tag{2.11}$$

and $q \equiv -d \ln \Omega / \ln R = 3/2$ is the dimensionless shear parameter defining a rotation profile $\Omega(r) = \Omega_0 (r/r_0)^{-q}$, such that the background velocity profile is $u_0 = -q\Omega_0 x$.

The weakly nonlinear regime is where the MRI system is nonlinearly unstable to only the most unstable mode of the linear solution. We find the marginal state, where the most

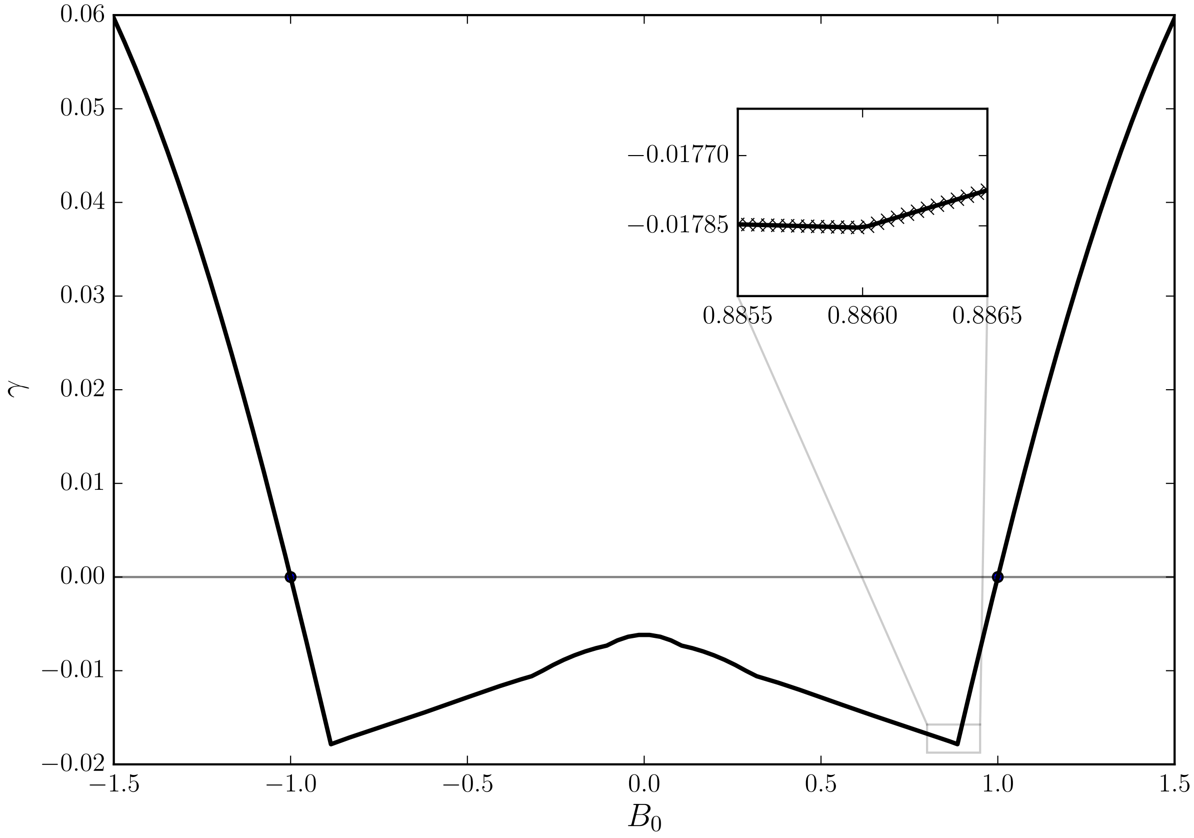

Figure 2.2: Growth rate γ as a function of background magnetic field strength B_0 at $\mathrm{Rm} = \mathrm{Rm}_c$, $k_z = k_c$, $\mathrm{Pm} = 10^{-3}$. Around the critical value $B_0 = 1.$, *strengthening* B_0 tunes the system into instability, while *decreasing* it leads to stability. The inset highlights the fact that γ is determined by the maximum real eigenvalue of the system, which switches from one mode family to another as discussed in the text.

unstable linear MRI mode neither grows nor decays, for a set of dimensionless parameters, and then destabilize the system. We examine the system for fiducial parameters comparable to URM07, namely $\mathrm{Pm} = 1.0 \times 10^{-3}$, $\mathrm{Co} = 0.08$, $q = 1.5$. The system is marginal for a critical wavenumber $k_c = 0.75$ and a critical magnetic Reynolds number $\mathrm{Rm}_c = 4.9$.

Because we nondimensionalize B by the magnitude of the background field strength, $B_0 \equiv 1$ in Equations 2.7 - 2.10. To excite the weakly nonlinear MRI, we tune the background

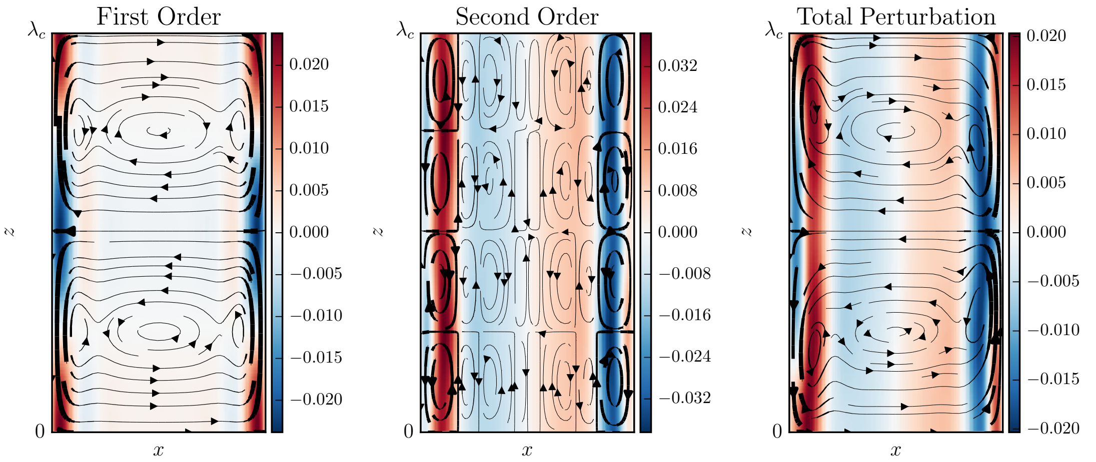

Figure 2.3: First order (left), second order (center), and total (right) velocity perturbations. Streamlines represent velocity in the vertical-radial plane, where thicker streamlines correspond to faster speeds. Colorbar represents azimuthal velocity. We use a constant amplitude $\alpha = \alpha_{saturation}$ and a small parameter $\epsilon = 0.5$.

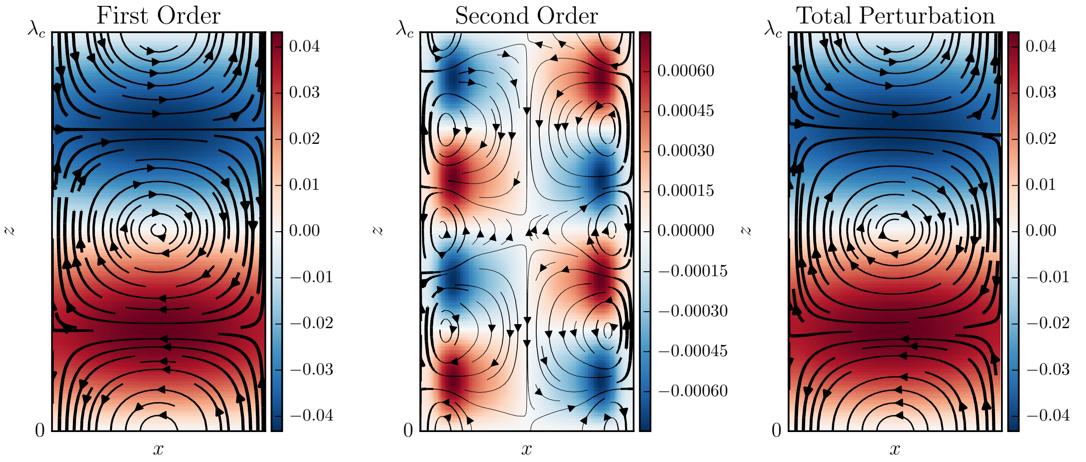

Figure 2.4: As in Figure 2.3 but for the magnetic field. Streamlines represent magnetic field structure in the vertical-radial plane, where thicker streamlines correspond to higher magnetic field strengths. Colorbar represents azimuthal magnetic field strength.

magnetic field away from stability. We do so by substituting $B = B_0 \left(1 + \epsilon^2\right)$. The degree of departure from the marginal state is measured by the small parameter ϵ. An $\mathcal{O}\left(\epsilon^2\right)$ strengthening of the background magnetic field destabilizes a finite band of wave modes with a width of $\mathcal{O}\left(\epsilon\right)$, which interact nonlinearly. We note that this definition of ϵ is opposite in sign to nearly all previous works (e.g. Umurhan et al. 2007a,b). Because in the ideal limit, the MRI can be tuned into instability by setting B_0 to its critical value and then *decreasing* its value, it is natural to consider ϵ^2 as a weakening of the background field (as is done correctly in Vasil 2015, for example). However, as we show in figure 2.2, for the *dissipative* case with $\eta, \nu \neq 0$, when all other parameters are critical, decreasing B_0 leads to stability, while increasing it pushes the system into instability. Figure 2.2 is symmetric about $B_0 = 0$, as it must be, since the MRI is insensitive to the sign of the background field. There are several places at which the derivative of γ appears discontinuous; this is not physical but rather reflects the fact that we define γ as the growth rate of the most unstable mode. That is, it is the maximum real part of the eigenvalues of the linearized system (e.g. equation 2.13 with $\mathbf{N} = 0$). Because there are four wave families in rotating incompressible MHD, each modified differently by changing B_0, when the growth rates of the individual modes cross, there appear piecewise continuous solutions. We highlight one such point in the inset in Figure 2.2, where the MRI mode becomes more stable than another mode which is always stable. Since all of these piecewise discontinuities are below $\gamma = 0$, they do not affect the analysis here.

The destabilizing substitution is made, and Equations 2.7 - 2.10 are rewritten such that the fluid variables are contained in a state vector

$$\mathbf{V} = \left[\Psi, u_y, A, B_y\right]^{\mathrm{T}}. \tag{2.12}$$

This yields the system of equations

$$\mathcal{D}\partial_t \mathbf{V} + \mathcal{L}\mathbf{V} + \epsilon^2 \widetilde{\mathcal{G}} = \mathbf{N}, \tag{2.13}$$

where we leave the definition of the matrices $\mathcal{D}$, $\mathcal{L}$, and $\widetilde{\mathcal{G}}$ to Appendix 2.A, and the detailed form of the nonlinear vector $\mathbf{N}$ to Appendix 2.B. We solve this system subject to no-slip, perfectly conducting radial boundary conditions, defined as

$$\Psi = \partial_x \Psi = u_y = A = \partial_x B_y = 0. \tag{2.14}$$

2.3 Weakly nonlinear analysis

We conduct a formal multiple scales analysis of this system. Our perturbations are characterized in terms of fast- and slow-moving variables, that we treat as independent in order to simultaneously track the evolution of the system on two scales. The relative scalings of the fast and slow variables are chosen such that each of the temporal and spatial eigenvalues appear at the same lowest order in the linear dispersion relation (Appendix 2.C). The scalings are

$$X \equiv \epsilon x, \; Y \equiv \epsilon y, \; Z \equiv \epsilon z, \; T \equiv \epsilon^2 t. \tag{2.15}$$

Note that these are the same scalings as apply to Rayleigh-Bénard convection and hydrodynamic TC flow. Our x dimension, the direction of angular momentum transport, is analogous to the direction of temperature transport in the convection problem. In analogy to these problems, we posit slow variation in both Z and T. Each operator in Equations 2.7 - 2.10 is expanded to reflect these scalings – for instance, ∂_z becomes $\partial_z + \epsilon\partial_Z$.

The multiple scale dependencies of our solution are encoded into an ansatz for the linear

MRI solution at marginality,

$$\mathbf{V_1} = \alpha(T, Z)\mathbb{V}_{11}(x)e^{ik_c z} + c.c. + \beta(T, Z)\mathbb{U}_{11}(x) \tag{2.16}$$

where $\alpha(T, Z)$ is a slowly-varying amplitude and *c.c.* denotes the complex conjugate. The x dependence is contained in $\mathbb{V}_{11} = (\Psi_{11}, u_{11}, A_{11}, B_{11})^{\mathbf{T}}$, and must be solved subject to the radial boundary conditions. The periodic vertical boundary conditions allow us to posit the z dependence, where k_c is the value of the vertical wavenumber at marginality. As noted by URM07, there exists a spatially constant neutral mode solution to the B_y equation, with $\mathbb{U}_{11} = (0, 0, 0, 1)^{\mathbf{T}}$. The amplitude $\beta(T, Z)$ encodes the slow evolution of this mode. This spatially constant mode cannot contribute to the nonlinear saturation of the MRI because all of the nonlinearities involve derivatives. The long-term evolution of $\beta(T, Z)$ is described by a simple diffusion equation that decouples from $\alpha(T, Z)$, and so we neglect it in what follows.

The state vector is expanded in a perturbation series in orders of ϵ,

$$\mathbf{V} = \epsilon\mathbf{V_1} + \epsilon^2\mathbf{V_2} + \epsilon^3\mathbf{V_3} + h.o.t. \tag{2.17}$$

Our perturbed system is then expressed order by order as

$$\mathcal{O}(\epsilon) \qquad : \boldsymbol{\mathcal{L}}\mathbf{V_1} + \mathcal{D}\partial_t\mathbf{V_1} = 0. \tag{2.18}$$

$$\mathcal{O}(\epsilon^2) \qquad : \boldsymbol{\mathcal{L}}\mathbf{V_2} + \widetilde{\mathcal{L}}_1\partial_Z\mathbf{V_1} = \mathbf{N_2} \tag{2.19}$$

$$\mathcal{O}(\epsilon^3) \quad : \boldsymbol{\mathcal{L}}\mathbf{V_3} + \mathcal{D}\partial_T\mathbf{V_1} + \widetilde{\mathcal{L}}_1\partial_Z\mathbf{V_2} + \widetilde{\mathcal{L}}_2\partial_Z^2\mathbf{V_1} + \widetilde{\mathcal{G}}\mathbf{V_1} = \mathbf{N_3} \tag{2.20}$$

The partial differential equations that comprise Equations 2.18 to 2.20 are solved in succession. The practical advantage of our ansatz construction (Equation 2.16) is clear: the separable x-dependence means that the radial boundary conditions are solved in only one dimension. Thus our analytical framework is able to side-step many of the resolution issues faced by multidimensional simulations. We are able to resolve even small-scale structure in the boundary layers of our domain, because we need only resolve it in one dimension. We solve the radial component of each equation using the open source pseudospectral code Dedalus. We compute the radial components on a grid of Chebyshev polynomials, as is appropriate for bounded one-dimensional domains (e.g. Boyd 2001). The nonuniform spacing of the Chebyshev grid allows us to resolve the boundary layers well on a 128-point grid.

To close the perturbation series we enforce a solvability criterion on Equation 2.20 (see Appendix 2.A). This leads to an amplitude equation for $\alpha(T, Z)$ that governs the slow length- and timescale evolution of the system. This amplitude equation is

$$\partial_T \alpha = b\alpha + h\partial_Z^2 \alpha - c\alpha \left|\alpha^2\right|, \tag{2.21}$$

a real Ginzburg-Landau equation. The saturated solution to Equation 2.21 is evidently $\alpha_{saturation} = \pm\sqrt{b/c}$. We plot the first order, second order, and total perturbation structure of the fluid variables in Figures 2.3 and 2.4 with a constant $\alpha_{saturation}$. This is the Ginzburg-Landau equation that was previously found by URM07. Those authors investigated the behavior of this MRI system as a function of Pm. By analyzing the system over several orders of magnitude in Pm, we reproduce the URM07 result that the analytic saturation amplitude scales as $\alpha^2_{saturation} \propto \mathrm{Pm}^{4/3}$ in a thin-gap geometry when $\mathrm{Pm} \ll 1$.

2.4 Shearing box and ambipolar diffusion

Many studies of the MRI consider the instability in a shearing box, i.e. a wall-less local approximation that is meant to represent a small section of a disk. The shearing box is the limit in which Equations 2.7 - 2.10 are subjected to shear periodic radial boundary conditions rather than Equation 2.14 (e.g. Regev & Umurhan 2008). The periodic nature of the shearing box allows us to decompose the fluid perturbations into Fourier modes proportional to $e^{ik_x x + ik_z z}$. This makes the shearing box MRI straightforward to treat analytically. However, as noted above, the fastest-growing linear MRI modes in the shearing box are also exact solutions of the nonlinear MRI equations – that is, $J(\hat{\psi}_0, \hat{\psi}_0) = J(\hat{\psi}_0, \nabla^2 \hat{\psi}_0) = 0$ for $\hat{\psi}_0 \propto e^{ik_x x + ik_z z}$. While this may be an appealing trait for analytic simplicity, it leads to the unphysical conclusion that the fastest growing modes will never nonlinearly interact (Goodman & Xu 1994). This 'nonlinear property' will not be satisfied for two MRI modes with nonparallel wavenumbers, but with vertically periodic boundary conditions and a vertical background magnetic field the most unstable mode has a strictly axial vertical wavenumber. Thus a formal weakly nonlinear analysis cannot be conducted, as the most unstable mode will never nonlinearly interact with itself or its complex conjugate. Similarly, we cannot analytically examine interactions between MRI channel modes and damped eigenmodes belonging to other wave families. This is analytically examined for other plasma instabilities by tracking the amplitudes of growing, marginal, and damped eigenmodes simultaneously (e.g. Makwana et al. 2011). While the shearing box approximation allows the projection of the perturbed MRI equations into the basis set of linear eigenmodes, nonlinear coupling between modes will remain zero.

The nonlinear property of primary MRI modes in the shearing box motivates the addition of radial boundaries, such that the nonlinear evolution of the weakly nonlinear MRI can

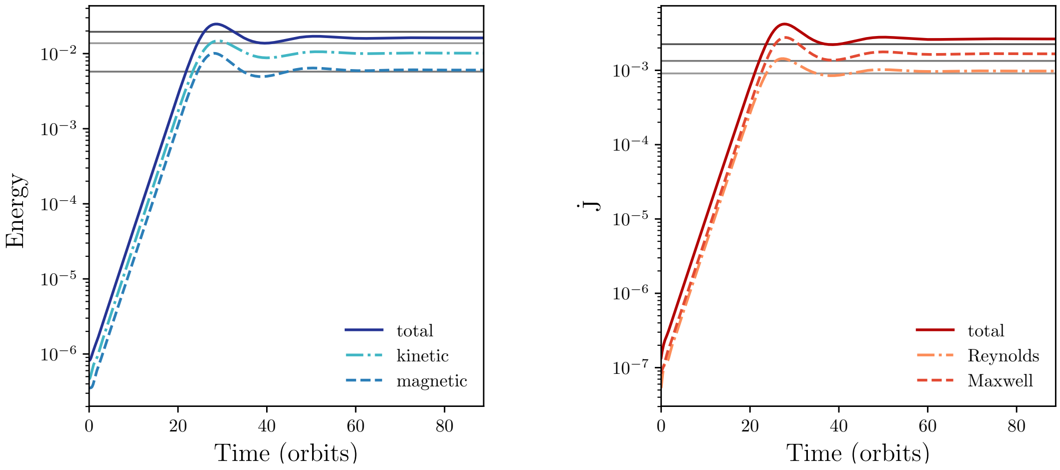

Figure 2.5: Average energy (left) and angular momentum transport (right) in the total, kinetic, and magnetic components of simulation data as a function of time. Gray lines show the weakly nonlinear theory values for each quantity.

be properly considered. It also raises the question of whether some additional nonlinear mechanism can be introduced such that the fastest-growing modes are no longer nonlinear solutions to the shearing box equations. It has already been shown that the Hall effect does not negate the nonlinear property of primary MRI modes (Kunz & Lesur 2013). However, it seems to have been overlooked in the literature that these linear modes are *not* solutions of the nonlinear ambipolar diffusion term, which is proportional to

$$\nabla \times ((\mathbf{J} \times \mathbf{B}) \times \mathbf{B}). \tag{2.22}$$

Furthermore, the radial wavenumber of the fastest-growing linear MRI mode in a shearing box with ambipolar diffusion is nonzero when a constant azimuthal background field is considered in addition to an axial one (Kunz & Balbus 2004). This means that, in the presence of ambipolar diffusion, we can derive the weakly nonlinear envelope equation for the MRI in the shearing box. Ambipolar diffusion adds both linear and nonlinear terms to Equations 2.18 to 2.20, but does not change their Z or T dependence. The constant azimuthal background field component does not contribute to any other terms in the local MRI equations. Thus, the slow-scale evolution of the MRI in a shearing box with ambipolar diffusion is also governed by a Ginzburg-Landau equation.

The Ginzburg-Landau form of the amplitude equation can be found in any system with Euclidean symmetry and a quadratic maximum in growth rate with respect to the wavenumber (Hoyle 2006). In this case, the Euclidean symmetry comes from axisymmetry in the x-z plane, and the quadratic maximum is a consequence of the linear dispersion relation given in Appendix 2.C. In Chapter 3, we show that the same symmetry occurs in the axisymmetric global geometry as well. The Ginzburg-Landau equation arises due to symmetries in the local MRI equations, irrespective of the boundary conditions to which they are subjected. This means that the local MRI is able to saturate via nonlinear mode interaction so long as the primary MRI modes are not exact solutions of the nonlinear terms. This can be achieved by considering the effects of ambipolar diffusion when the boundary conditions are shear periodic, or by enforcing wall-like radial boundary conditions. Both constructions require the most unstable mode to have nonconstant radial structure. Physically, this radial variation impedes the free exchange of angular momentum facilitated by the uniform stretching of channel modes.

2.5 Direct numerical simulation

Here, we make a preliminary test of our weakly nonlinear theory by comparing it to direct numerical simulation. Using Dedalus, we solved the full, nonlinear equations 2.7 - 2.10 with all parameters (Rm, Q) equal to their critical values except the background magnetic field, which we set to $B_0 = 1 + \epsilon^2$. We thus drive the system MRI unstable in the same way as in our theory. The computational requirements of low Pm simulations are quite intense in both time and space. Despite being virtually smooth, the solutions require a resolution of 192×1536 grid points at $\mathrm{Pm} = 10^{-2}$. Because the system has such a small growth rate, it takes hundreds of orbits for the system to reach saturation, as compared to the few orbits typical of high Rm simulations (e.g. Lesur & Longaretti 2007). As a result, we make our comparison at $\mathrm{Pm} = 10^{-2}$, which provides a good tradeoff between probing relatively low Pm while keeping the computational time for these exploratory simulations modest.

We initialize the runs with the linear eigenvectors of the MRI unstable mode (also computed by Dedalus; see section 2.3) multiplied by an initial amplitude $A_0 = 10^{-3}$. Doing so requires considerably less run time, as the MRI unstable mode starts growing immediately from A_0. By contrast, initializing random noise in ψ with amplitude A_0 would give the unstable mode a much smaller amplitude. Nevertheless, we have confirmed that simulations with eigenvector initial conditions have similar evolutions to those with noise initial conditions once each enter linear growth.

We analyze the average energy and angular momentum transport in the simulation domain (Figure 2.5). The saturation amplitude predicted by the weakly nonlinear theory depends on the choice of normalization of the linear eigenvectors. The eigenvectors of the linear problem are only determined up to an arbitrary normalization, and the nonlinear coefficient of the Ginzburg-Landau equation is sensitive to this normalization. The undetermined factor is typically assigned by comparison with direct numerical simulation or laboratory experiment (e.g. Recktenwald et al. 1993; Deyirmenjian et al. 1997). Here we determine the constant by requiring that the maximum amplitude of B_y be equal in both theory and simulation. With this normalization choice all plotted quantities agree to within $\sim 25\%$. The theory and simulation are thus in reasonably good agreement considering that the weakly nonlinear theory applies rigorously to a channel of infinite height, while the simulation was

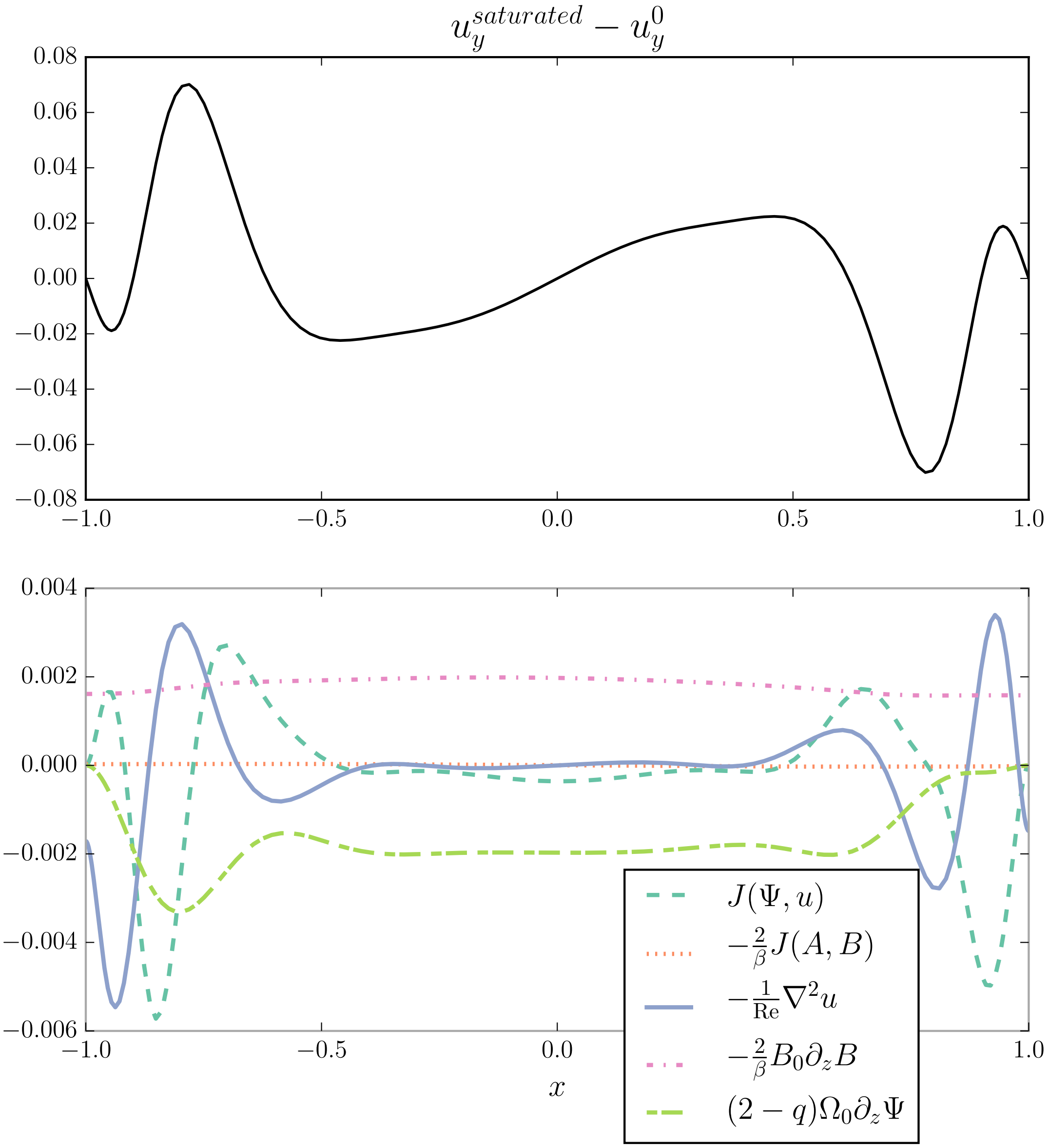

Figure 2.6: Top panel: radial profile for $u_y^{saturated} - u_y^0$, the difference between the saturated azimuthal velocity profile and the initial azimuthal velocity profile (TC flow). Bottom panel: each term in the steady state force balance (Equation 2.8 with $\partial_t u_y = 0$). Saturated quantities are computed with $\alpha_{saturation} = \sqrt{b/c}$ and $\epsilon = 0.5$. The saturated state shows reduced shear in the bulk of the flow, outside of the boundary layers.

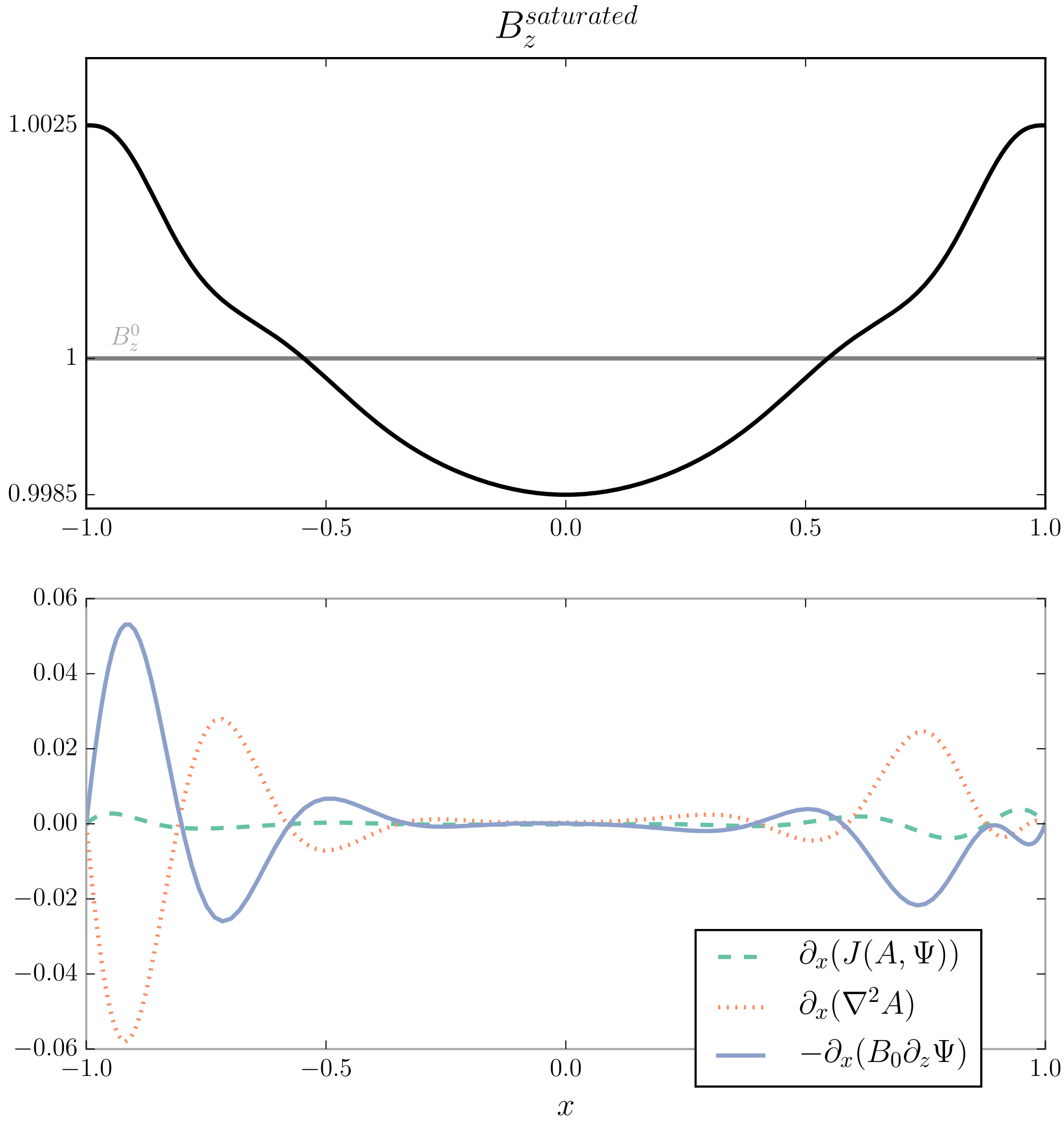

Figure 2.7: Top panel: radial profile for $B_z^{saturated}$, the saturated vertical magnetic field (black line). $B_z^0 = 1$ is the constant background magnetic field (gray line). Bottom panel: each term in the steady state inductive balance (∂_x of Equation 2.10 with $\partial_t B_y = 0$). Saturated quantities are computed with $\alpha_{saturation} = \sqrt{b/c}$ and $\epsilon = 0.5$. The saturated field is pushed to the radial domain boundaries.

carried out in a box with a vertical extent of only two critical wavelengths. We defer further comparisons between simulation and theory, including an analysis of the effect of the box height on the simulated flow, to future work.

2.6 Discussion

Here our focus is on a physical description of the saturation mechanism. Figure 2.6 shows saturated radial profiles of $u_0 - u_y = -q\Omega_0 x - u_y$ and each term in the steady state force balance (i.e. Equation 2.8 with $\partial_t u_y = 0$). In the bulk of the fluid away from the boundary layers, the saturated state shows reduced shear, with little diffusive contribution. This demonstrates that even in a case where diffusive effects are important, the bulk of the fluid saturates by balancing shear and magnetic tension. As discussed at length in Vasil (2015), when diffusive effects are not important, it is impossible to rearrange momentum without also rearranging the magnetic field. The Vasil (2015) model demonstrates saturation without diffusive effects; our results show that outside of the boundary layers, a simultaneous rearrangement of momentum and field occurs. In the boundary layers, the nonlinear advection balances viscous dissipation.

Figure 2.7 shows B_z and the terms corresponding to steady state inductive balance (∂_x of Equation 2.10 with $\partial_t B_y = 0$). Here, the instability acts to push the magnetic field toward the boundaries in both the bulk and the boundary layers. The radial average of the saturated B_z is B_0, i.e. B_z is marginally stable. Ebrahimi et al. (2009) considered the saturation of a single, strongly super-critical MRI mode allowed to interact nonlinearly only with itself and the mean. They considered two important cases, one in which the mean flow was forced to remain at its initial, quasi-Keplerian state for all time, and one in which the background flow was allowed to evolve. This is a crucial difference between the shearing box and our narrow-

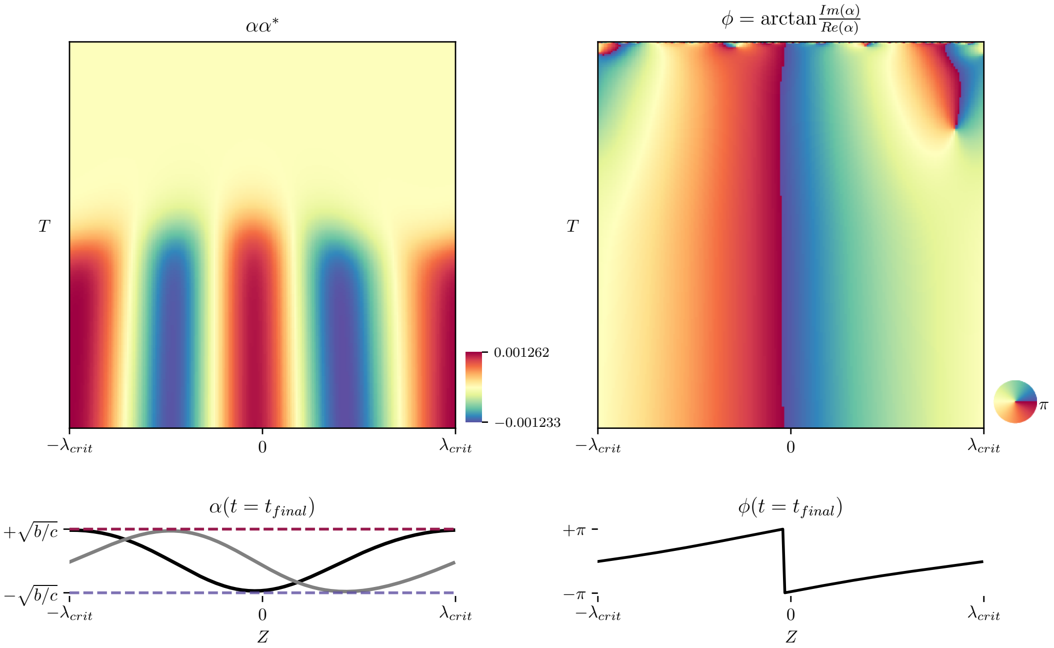

Figure 2.8: Evolution of the Ginzburg-Landau amplitude equation (Equation 2.21) on a Fourier Z domain of length $2\lambda_{crit}$, where $\lambda_{crit} = 2\pi/k_c$ is the critical wavelength of the system. Top left panel shows the evolution of the amplitude observable $\alpha\alpha^*$ on the full Z domain as a function of time T. Bottom left panel shows the amplitude α at the final timestep shown, where the black line is the real part $\mathrm{Re}\{\alpha(t = t_{final})\}$ and the gray line is the imaginary part $\mathrm{Im}\{\alpha(t = t_{final})\}$. The final amplitude is bounded by the analytic saturation amplitude $\alpha_{saturation} = \pm\sqrt{b/c}$. Top right panel shows the evolution of the phase angle $\phi = \arctan(\mathrm{Im}(\alpha)/\mathrm{Re}(\alpha))$ on the same domain. Bottom panel shows the phase angle as a function of Z for the final timestep. Note that the phase angle is wrapped on a 2π domain, such that $\pi = -\pi$, as indicated by the circular colorbar.

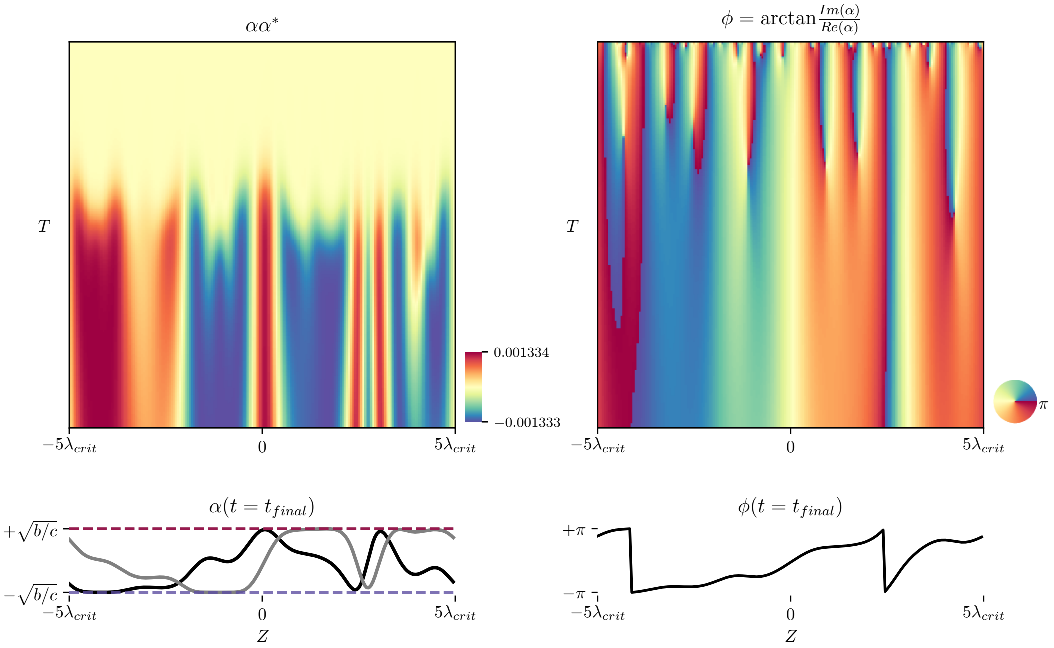

Figure 2.9: As in Figure 2.8 but for a Z domain of length $10\lambda_{crit}$.

gap TC flow: perturbations in our simulation can adjust the background flow, whereas in a shearing box, the shear periodicity forbids perturbations from affecting the mean flow. In the case with a freely evolving background flow, Ebrahimi et al. (2009) found a saturated state quite similar to ours: field pushed to the boundaries, and a reduction in shear in the bulk of the flow. Their flows have less pronounced boundary layers, likely because of their much larger $\mathrm{Pm} = 0.1 - 1$.

In the high Re and Rm limit, Vasil (2015) derives an amplitude equation considerably different than the one found here. By averaging in the z direction, the author computes a mean-field equation with striking similarity to the buckling of an elastic beam under load. The most salient feature of this equation is its *non-local* character. Unlike the present work, which focuses on Keplerian rotation profiles with $q = 3/2$ with a critical background magnetic field strength, Vasil (2015) focuses on a fixed field strength and a weakly destabilized shear profile. These differences are minor, however: the destabilizing parameter ϵ enters the analysis in the same quadratic proportion. Whether and how Vasil (2015)'s amplitude equation is equivalent to our own in the limit of dynamically important resistive and viscous effects is beyond the scope of this work. Nevertheless, the author identifies the nonlinear term responsible for saturation as consisting of flux and field transport and notes these are the only mechanisms able to produce saturation. Our results likewise demonstrate a combination of flux and field transport in the comparable region of our domain. This suggests that despite our formulation displaying different saturation dynamics (Ginzburg-Landau in our case; a network of coupled Duffing oscillators in Vasil 2015), there may indeed be an underlying unification.

The real Ginzburg-Landau equation describes the amplitude behavior of our system close to threshold. Although the form of the equation is generic to many systems, its coefficients depend on the specific physics of our system and govern its detailed evolution (see Appendix

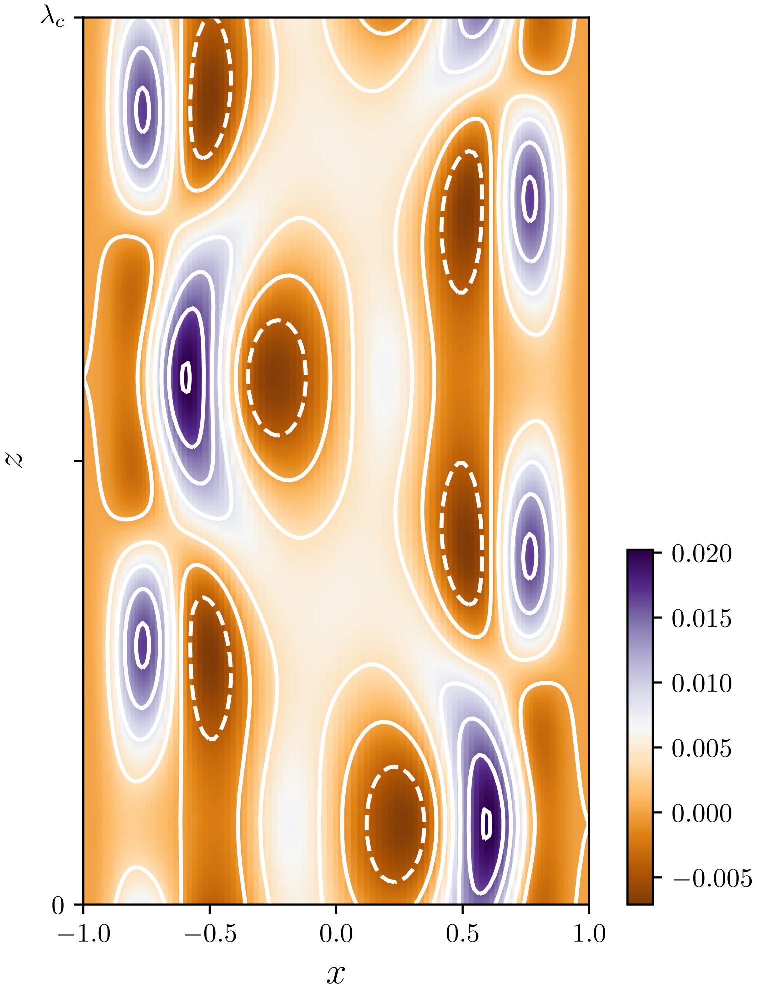

Figure 2.10: Total (Reynolds + Maxwell) stress in the domain as predicted from the weakly nonlinear theory at $\mathrm{Pm} = 10^{-2}$.

2.A). We simulate the evolution of the MRI amplitude equation by solving Equation 2.21 on a Fourier basis in Z using Dedalus. We initialize uniform random noise of amplitude -10^{-3} to $+10^{-3}$ in Z, and timestep the system using a four-stage, third-order Runge-Kutta integrator. We evolve the system for $100\Omega_0^{-1}$ in timesteps of $0.02\Omega_0^{-1}$. Results are shown in Figures 2.8 and 2.9, where the amplitude and phase structure over the vertical domain is plotted for every 20 timesteps. The system quickly organizes itself into rolls in Z bounded by the analytic saturation amplitude $\alpha_s = \sqrt{b/c}$. The specific geometry depends on the number of critical wavelengths $\lambda_{crit} = 2\pi/k_c$ that are initialized in Z. Figure 2.8 shows that a system with a height equal to two critical wavelengths will be modulated by simple rolls of sinusoidal amplitude. The saturation amplitude pattern becomes more complicated when more modes are allowed to interact. Figure 2.9 shows the evolution of a system of height $10\lambda_{crit}$. While still bounded by α_s, the saturation amplitude exhibits a nonlinear phase geometry due to the nonlinear interaction of modes in Z.

The weakly nonlinear theory predicts that the amplitude of the system is bounded by the saturation amplitude $\alpha_s = \sqrt{b/c}$, where b and c are coefficients corresponding to the linear growth term and nonlinear term of the Ginzburg-Landau equation, respectively. The coefficient b comes from the interaction between the background magnetic field and the linear MRI solution. The coefficient c describes the third-order nonlinear interaction between terms in the perturbation series. Physically, we see that the saturation amplitude is controlled by the strength of the mode interaction within our finite band of unstable modes. We stress that while the third-order nonlinear terms in the walled TC flow are strongly influenced by the boundary layers, this is not generically true of the MRI system. Indeed, in the shearing box MRI with ambipolar diffusion (the case sketched out in Section 2.4), boundary layers are impossible in the shear periodic flow. In this case the third-order nonlinear behavior of the system includes three-mode interactions from the cubic nonlinearity in the ambipolar diffusion term.

Figure 2.10 shows the total stress $u_x u_y - \mathrm{Co} B_x B_y$ for the $\mathrm{Pm} = 10^{-2}$ model with $\epsilon = 0.5$. The stress shows significantly more structure throughout the domain than the variables u_x, u_y, B_x and B_y that comprise it, demonstrating that a non-trivial correlation exists even in the weakly non-linear state. As in simulations at higher Rm, Figure 2.5 shows that the Maxwell stress dominates over the Reynolds stresses even though the kinetic energy significantly exceeds the magnetic energy.

2.7 Conclusion

In this paper we construct a weakly nonlinear analysis of the MRI using multiple scales analysis, leading to a real Ginzburg-Landau equation for the nonlinear amplitude, confirming the previous results of Umurhan et al. (2007b). We also confirm their results for the scaling of the analytic saturation amplitude with Pm. We extend their results by constructing a detailed force and inductive balance for the saturated u_y and B_z components. In doing so, we find that the saturated state is a complex balance in which reduction of shear and amplification and redistribution of B_z combine to saturate the instability. We perform numerical simulations of the amplitude equation and a direct numerical simulation of the MRI system. Using the former, we demonstrate that complex patterns can organize the flow on long length scales Z, though the maximum magnitude of the amplitude α is well predicted by the steady state solution. The latter show that there is rough agreement for both total energy and average angular momentum transport between the weakly nonlinear theory and simulation for a representative case at $\mathrm{Pm} = 10^{-2}$. We defer a full comparison between theory and simulation to later work. We describe the application of shear-periodic boundary conditions to the local MRI and find that with the inclusion of certain nonideal physical effects, namely ambipolar diffusion, our theory points to a new saturation avenue for the MRI in a shearing box. In Chapter 3, we make use of the techniques developed here to extend the weakly nonlinear analysis of the MRI to a full cylindrical geometry appropriate for a Taylor-Couette experiment.

Acknowledgments

S.E.C. was supported by a National Science Foundation Graduate Research Fellowship under grant No. DGE-16-44869. J.S.O. acknowledges support from NASA grant NNX16AC92G. We thank the anonymous referee for thoughtful comments that greatly improved the manuscript. We also thank Mordecai Mac Low, Jeremy Goodman, John Krommes, Geoff Vasil, and Ellen Zweibel for useful discussion.

2.A Detailed Equations

Here we detail the perturbation analysis described in Section 2.3. The perturbation series is described by Equations 2.18 - 2.20, where

$$\mathcal{L} = \mathcal{L}_0 + \mathcal{L}_1\partial_z + \mathcal{L}_2\partial_z^2 + \mathcal{L}_3\partial_z^3 + \mathcal{L}_4\partial_z^4, \tag{2.23}$$

$$\widetilde{\mathcal{L}}_1 = \mathcal{L}_1 + 2\mathcal{L}_2\partial_z + 3\mathcal{L}_3\partial_z^2 + 4\mathcal{L}_4\partial_z^3 \tag{2.24}$$

$$\widetilde{\mathcal{L}}_2 = \mathcal{L}_2 + 3\mathcal{L}_3\partial_z + 6\mathcal{L}_4\partial_z^2 \tag{2.25}$$

$$\widetilde{\mathcal{G}} = \mathcal{G}\partial_z + \mathcal{L}_3\partial_z^3, \tag{2.26}$$

and the constituent matrices are defined as

$$\mathcal{D} = \begin{bmatrix} \nabla^2 & 0 & 0 & 0 \\ 0 & 1 & 0 & 0 \\ 0 & 0 & 1 & 0 \\ 0 & 0 & 0 & 1 \end{bmatrix} \tag{2.27}$$

$$\mathcal{L}_0 = \begin{bmatrix} -\frac{1}{\mathrm{Re}}\partial_x^4 & 0 & 0 & 0 \\ 0 & -\frac{1}{\mathrm{Re}}\partial_x^2 & 0 & 0 \\ 0 & 0 & -\frac{1}{\mathrm{Rm}}\partial_x^2 & 0 \\ 0 & 0 & 0 & -\frac{1}{\mathrm{Rm}}\partial_x^2 \end{bmatrix} \tag{2.28}$$

$$\mathcal{L}_1 = \begin{bmatrix} 0 & -2 & -\mathrm{Co}\partial_x^2 & 0 \\ (2-q)\Omega_0 & 0 & 0 & -\mathrm{Co} \\ -1 & 0 & 0 & 0 \\ 0 & -1 & q\Omega_0 & 0 \end{bmatrix} \tag{2.29}$$

$$\mathcal{L}_2 = \begin{bmatrix} -2\frac{1}{\mathrm{Re}}\partial_x^2 & 0 & 0 & 0 \\ 0 & -\frac{1}{\mathrm{Re}} & 0 & 0 \\ 0 & 0 & -\frac{1}{\mathrm{Rm}} & 0 \\ 0 & 0 & 0 & -\frac{1}{\mathrm{Rm}} \end{bmatrix} \tag{2.30}$$

$$\mathcal{L}_3 = \begin{bmatrix} 0 & 0 & -\mathrm{Co} & 0 \\ 0 & 0 & 0 & 0 \\ 0 & 0 & 0 & 0 \\ 0 & 0 & 0 & 0 \end{bmatrix} \tag{2.31}$$

$$\mathcal{L}_4 = \begin{bmatrix} -\frac{1}{\mathrm{Re}} & 0 & 0 & 0 \\ 0 & 0 & 0 & 0 \\ 0 & 0 & 0 & 0 \\ 0 & 0 & 0 & 0 \end{bmatrix} \tag{2.32}$$

$$\mathcal{G} = \begin{bmatrix} 0 & 0 & -\mathrm{Co}\partial_x^2 & 0 \\ 0 & 0 & 0 & -\mathrm{Co} \\ -1 & 0 & 0 & 0 \\ 0 & -1 & 0 & 0 \end{bmatrix} \tag{2.33}$$

Once perturbed, the system is solved for successive orders of ϵ (Equations 2.18 - 2.20). $\mathcal{O}(\epsilon)$ is the linear system. At $\mathcal{O}(\epsilon^2)$, first-order MRI modes nonlinearly interact with themselves and with their complex conjugates, and so the term $\mathbf{N}_2$ in Equation 2.19 has the form

$$\mathbf{N}_2 = |\alpha|^2 \mathbf{N}_{20} + \alpha^2 \mathbf{N}_{22} e^{2ik_c z} \tag{2.34}$$

(see Appendix 2.B for the full form of $\mathbf{N}_{20}$ and $\mathbf{N}_{22}$).

Note that, following the notation of Umurhan et al. (2007b), the subscripts refer to ϵ order, z order, successively, such that $\mathbf{N}_{22}$ is the second-order nonlinear term which corresponds to $e^{2ik_c z}$ z-dependence.

Equation 2.19 is solved as three separate systems of equations, one for each possible z

resonance:

$$\mathcal{L}\mathbf{V}_{20} = \mathbf{N}_{20} \tag{2.35}$$

$$\mathcal{L}\mathbf{V}_{21} = -\widetilde{\mathcal{L}}_1 \partial_Z \mathbf{V}_{11} \tag{2.36}$$

$$\mathcal{L}\mathbf{V}_{22} = \mathbf{N}_{22} \tag{2.37}$$

Finally, at $\mathcal{O}(\epsilon^3)$ we eliminate secular terms to close the system. Secular terms are terms which are resonant with the solution to the homogenous linear equation (Equation 2.18), and which cause the higher-order solutions to grow without bound. The solvability criterion we enforce to eliminate these terms is the vanishing of the inner product of the solution to the adjoint linear homogenous equation $\mathcal{L}^\dagger \mathbf{V}^\dagger = 0$ with the nonhomogenous terms in Equation 2.20, namely

$$\langle \mathbb{V}^\dagger | \mathcal{D}\mathbb{V}_{11} \rangle \partial_T \alpha + \langle \mathbb{V}^\dagger | \widetilde{\mathcal{G}}\mathbb{V}_{11} \rangle \alpha + \langle \mathbb{V}^\dagger | \widetilde{\mathcal{L}}_1 \mathbb{V}_{21} + \widetilde{\mathcal{L}}_2 \mathbb{V}_{11} \rangle \partial_Z^2 \alpha = \langle \mathbb{V}^\dagger | \mathbf{N}_{31} \rangle \alpha |\alpha|^2. \tag{2.38}$$

This solvability criterion derives from a corollary to the Fredholm Alternative (see Chapter 3 for a formal definition).

Equation 2.38 can be rewritten as Equation 2.21, the Ginzburg-Landau equation, where the coefficients are

$$b = \langle \mathbb{V}^\dagger | \widetilde{\mathcal{G}}\mathbb{V}_{11} \rangle / \langle \mathbb{V}^\dagger | \mathcal{D}\mathbb{V}_{11} \rangle, \tag{2.39}$$

$$h = \langle \mathbb{V}^\dagger | \widetilde{\mathcal{L}}_1 \mathbb{V}_{21} + \widetilde{\mathcal{L}}_2 \mathbb{V}_{11} \rangle / \langle \mathbb{V}^\dagger | \mathcal{D}\mathbb{V}_{11} \rangle, \tag{2.40}$$

and

$$c = \langle \mathbb{V}^\dagger | \mathbf{N}_{31} \rangle / \langle \mathbb{V}^\dagger | \mathcal{D} \mathbb{V}_{11} \rangle. \tag{2.41}$$

We define the adjoint operator $\mathcal{L}^\dagger$ and solution $\mathbf{V}^\dagger$ as

$$\langle \mathbf{V}^\dagger | \mathcal{L} \mathbf{V} \rangle = \langle \mathcal{L}^\dagger \mathbf{V}^\dagger | \mathbf{V} \rangle, \tag{2.42}$$

where the inner product is defined as

$$\langle \mathbf{V}^\dagger | \mathcal{L} \mathbf{V} \rangle = \frac{k_c}{2\pi} \int_{-\pi/k_c}^{\pi/k_c} \int_{x_1}^{x_2} \mathbf{V}^{\dagger *} \cdot \mathcal{L} \mathbf{V} \, \mathrm{d}x \mathrm{d}z. \tag{2.43}$$

The solution to the adjoint homogenous equation has the form

$$\mathbf{V}^\dagger = \mathbb{V}^\dagger(x) e^{ik_c z} + c.c. \tag{2.44}$$

As noted by URM07, a second amplitude equation for a spatially constant azimuthal magnetic field mode arises from the terms in the $\mathcal{O}(\epsilon^3)$ equation which contain no z dependence. This is a diffusion equation, so the neutral mode simply decays away.

2.B Expansion of Nonlinear Terms

At each order in our perturbation series, lower-order MRI modes nonlinearly interact. Thus there is a nonlinear term contribution at $\mathcal{O}(\epsilon^2)$ and $\mathcal{O}(\epsilon^3)$. Here we detail the form of these nonlinear terms.

The overall nonlinear contribution to our system, written as a vector $\mathbf{N}$ in Equation 2.13, is

$$\mathbf{N} = \epsilon^2 \mathbf{N_2} + \epsilon^3 \mathbf{N_3} + \mathcal{O}(\epsilon^4) \tag{2.45}$$

where

$$N_2^{(\Psi)} = J(\Psi_1, \nabla^2 \Psi_1) - \mathrm{Co} J(A_1, \nabla^2 A_1) \tag{2.46}$$

$$N_2^{(u)} = J(\Psi_1, u_1) - \mathrm{Co} J(A_1, B_1) \tag{2.47}$$

$$N_2^{(A)} = -J(A_1, \Psi_1) \tag{2.48}$$

$$N_2^{(B)} = J(\Psi_1, B_1) - J(A_1, u_1) \tag{2.49}$$

and

$$\begin{aligned} N_3^{(\Psi)} = {} & J(\Psi_1, \nabla^2 \Psi_2) - \mathrm{Co} J(A_1, \nabla^2 A_2) + J(\Psi_2, \nabla^2 \Psi_1) - \mathrm{Co} J(A_2, \nabla^2 A_1) + \\ & 2J(\Psi_1, \partial_z \partial_Z \Psi_1) - 2\mathrm{Co} J(A_1, \partial_z \partial_Z A_1) + \widetilde{J}(\Psi_1, \nabla^2 \Psi_1) - \mathrm{Co} \widetilde{J}(A_1, \nabla^2 A_1) \end{aligned} \tag{2.50}$$

$$\begin{aligned} N_3^{(u)} = {} & J(\Psi_1, u_2) + J(\Psi_2, u_1) + \widetilde{J}(\Psi_1, u_1) - \mathrm{Co} J(A_1, B_2) - \mathrm{Co} J(A_2, B_1) \\ & - \mathrm{Co} \widetilde{J}(A_1, B_1) \end{aligned} \tag{2.51}$$

$$N_3^{(A)} = -J(A_1, \Psi_2) - J(A_2, \Psi_1) - \widetilde{J}(A_1, \Psi_1) \tag{2.52}$$

$$N_3^{(B)} = J(\Psi_1, B_2) + J(\Psi_2, B_1) + \widetilde{J}(\Psi_1, B_1) - J(A_1, u_2) - J(A_2, u_1) - \widetilde{J}(A_1, u_1). \tag{2.53}$$

$\mathbf{N_2}$ and $\mathbf{N_3}$ expand to become

$$\mathbf{N_2} = \alpha^2 \mathbb{N}_{22} e^{i2k_c z} + |\alpha|^2 \mathbb{N}_{20} + c.c. \tag{2.54}$$

and

$$\mathbf{N_3} = \alpha^3 \mathbb{N}_{33} e^{i3k_c z} + \alpha \partial_Z \alpha \mathbb{N}_{32} e^{i2k_c z} + \alpha |\alpha|^2 \mathbb{N}_{31} e^{ik_c z} + \alpha \partial_Z \beta \widetilde{\mathbb{N}}_{31} e^{ik_c z} + \alpha^* \partial_Z \alpha \mathbb{N}_{30} + c.c. \tag{2.55}$$

The second order nonlinear terms are

$$\begin{aligned} N_{22}^{(\Psi)} = & ik_c \Psi_{11} \cdot \left(\partial_x^3 \Psi_{11} - k_c^2 \partial_x \Psi_{11}\right) - \partial_x \Psi_{11} \cdot \left(ik_c \partial_x^2 \Psi_{11} - ik_c^3 \Psi_{11}\right) \\ & + \mathrm{Co} \partial_x A_{11} \cdot \left(ik_c \partial_x^2 A_{11} - ik_c^3 A_{11}\right) - \mathrm{Co} ik_c A_{11} \cdot \left(\partial_x^3 A_{11} - k_c^2 \partial_x A_{11}\right) \end{aligned} \tag{2.56}$$

$$N_{22}^{(u)} = ik_c \Psi_{11} \cdot \partial_x u_{11} - \partial_x \Psi_{11} \cdot ik_c u_{11} - \mathrm{Co} ik_c A_{11} \cdot \partial_x B_{11} + \mathrm{Co} \partial_x A_{11} \cdot ik_c B_{11} \tag{2.57}$$

$$N_{22}^{(A)} = -ik_c A_{11} \cdot \partial_x \Psi_{11} + \partial_x A_{11} \cdot ik_c \Psi_{11} \tag{2.58}$$

$$N_{22}^{(B)} = ik_c \Psi_{11} \cdot \partial_x B_{11} - \partial_x \Psi_{11} \cdot ik_c B_{11} - ik_c A_{11} \cdot \partial_x u_{11} + \partial_x A_{11} \cdot ik_c u_{11} \tag{2.59}$$

$$\begin{aligned} N_{20}^{(\Psi)} = & ik_c \Psi_{11} \cdot \left(\partial_x^3 \Psi_{11}^* - k_c^2 \partial_x \Psi_{11}^*\right) - \partial_x \Psi_{11} \cdot \left(ik_c^3 \Psi_{11}^* - ik_c \partial_x^2 \Psi_{11}^*\right) \\ & + \mathrm{Co} \partial_x A_{11} \cdot \left(ik_c^3 A_{11}^* - ik_c \partial_x^2 A_{11}^*\right) - \mathrm{Co} ik_c A_{11} \cdot \left(\partial_x^3 A_{11}^* - k_c^2 \partial_x A_{11}^*\right) \end{aligned} \tag{2.60}$$

$$N_{20}^{(u)} = ik_c \Psi_{11} \cdot \partial_x u_{11}^* + \partial_x \Psi_{11} \cdot ik_c u_{11}^* - \mathrm{Co} ik_c A_{11} \cdot \partial_x B_{11}^* - \mathrm{Co} \partial_x A_{11} \cdot ik_c B_{11}^* \tag{2.61}$$

$$N_{20}^{(A)} = -ik_c A_{11} \cdot \partial_x \Psi_{11}^* - \partial_x A_{11} \cdot ik_c \Psi_{11}^* \tag{2.62}$$

$$N_{20}^{(B)} = ik_c\Psi_{11} \cdot \partial_x B_{11}^* + \partial_x \Psi_{11} \cdot ik_c B_{11}^* - ik_c A_{11} \cdot \partial_x u_{11}^* - \partial_x A_{11} \cdot ik_c u_{11}^* \tag{2.63}$$

and the third order nonlinear terms become

$$\begin{aligned}
N_{31}^{(\Psi)} = {} & ik_c \left(\Psi_{11} \cdot \partial_x^3 \Psi_{20}\right) + ik_c \left(\Psi_{11} \cdot \partial_x^3 \Psi_{20}^*\right) - ik_c \left(\Psi_{11}^* \cdot \partial_x^3 \Psi_{22}\right) - i2k_c \left(\partial_x \Psi_{11}^* \cdot \partial_x^2 \Psi_{22}\right) \\
& + i8k_c^3 \left(\partial_x \Psi_{11}^* \cdot \Psi_{22}\right) + i4k_c^3 \left(\Psi_{11}^* \cdot \partial_x \Psi_{22}\right) + \mathrm{Co}\left[-ik_c \left(A_{11} \cdot \partial^3 A_{20}\right) - ik_c \left(A_{11} \cdot \partial_x^3 A_{20}^*\right)\right] \\
& + \mathrm{Co}\left[ik_c \left(A_{11}^* \cdot \partial_x^3 A_{22}\right) + i2k_c \left(\partial_x A_{11}^* \cdot \partial_x^2 A_{22}\right) - i8k_c^3 \left(\partial_x A_{11}^* \cdot A_{22}\right) - i4k_c^3 \left(A_{11}^* \cdot \partial_x A_{22}\right)\right] \\
& + i2k_c \left(\Psi_{22} \cdot \partial_x^3 \Psi_{11}^*\right) - i2k_c^3 \left(\Psi_{22} \cdot \partial_x \Psi_{11}^*\right) - ik_c \left(\partial_x \Psi_{20} \cdot \partial_x^2 \Psi_{11}\right) + ik_c \left(\partial_x \Psi_{22} \cdot \partial_x^2 \Psi_{11}^*\right) \\
& - ik_c \left(\partial_x \Psi_{20}^* \cdot \partial_x^2 \Psi_{11}\right) + ik_c^3 \left(\partial_x \Psi_{20} \cdot \Psi_{11}\right) + ik_c^3 \left(\partial_x \Psi_{20}^* \cdot \Psi_{11}\right) - ik_c^3 \left(\partial_x \Psi_{22} \cdot \Psi_{11}^*\right) \\
& + \mathrm{Co}\left[-i2k_c \left(A_{22} \cdot \partial_x^3 A_{11}^*\right) + i2k_c^3 \left(A_{22} \cdot \partial_x A_{11}^*\right) + ik_c \left(\partial_x A_{20} \cdot \partial_x^2 A_{11}\right) - ik_c \left(\partial_x A_{22} \cdot \partial_x^2 A_{11}^*\right)\right] \\
& + \mathrm{Co}\left[ik_c \left(\partial_x A_{20}^* \cdot \partial_x^2 A_{11}\right) - ik_c^3 \left(\partial_x A_{20} \cdot A_{11}\right) - ik_c^3 \left(\partial_x A_{20}^* \cdot A_{11}\right) + ik_c^3 \left(\partial_x A_{22} \cdot A_{11}^*\right)\right]
\end{aligned} \tag{2.64}$$

$$\begin{aligned}
N_{31}^{(u)} = {} & ik_c \left(\Psi_{11} \cdot \partial_x u_{20}\right) + ik_c \left(\Psi_{11} \cdot \partial_x u_{20}^*\right) - ik_c \left(\Psi_{11}^* \cdot \partial_x u_{22}\right) - i2k_c \left(\partial_x \Psi_{11}^* \cdot u_{22}\right) \\
& - ik_c \left(u_{11} \cdot \partial_x \Psi_{20}\right) - ik_c \left(u_{11} \cdot \partial_x \Psi_{20}^*\right) + ik_c \left(u_{11}^* \cdot \partial_x \Psi_{22}\right) + i2k_c \left(\partial_x u_{11}^* \cdot \Psi_{22}\right) \\
& + \mathrm{Co}\left[-ik_c \left(A_{11} \cdot \partial_x B_{20}\right) - ik_c \left(A_{11} \cdot \partial_x B_{20}^*\right) + ik_c \left(A_{11}^* \cdot \partial_x B_{22}\right) + i2k_c \left(\partial_x A_{11}^* \cdot B_{22}\right)\right] \\
& + \mathrm{Co}\left[ik_c \left(B_{11} \cdot \partial_x A_{20}\right) + ik_c \left(B_{11} \cdot \partial_x A_{20}^*\right) - ik_c \left(B_{11}^* \cdot \partial_x A_{20}\right) - i2k_c \left(\partial_x B_{11}^* \cdot A_{22}\right)\right]
\end{aligned} \tag{2.65}$$

$$\begin{aligned}
N_{31}^{(A)} = {} & - ik_c \left(A_{11} \cdot \partial_x \Psi_{20}\right) - ik_c \left(A_{11} \cdot \partial_x \Psi_{20}^*\right) + ik_c \left(A_{11}^* \cdot \partial_x \Psi_{22}\right) + i2k_c \left(\partial_x A_{11}^* \cdot \Psi_{22}\right) \\
& + ik_c \left(\Psi_{11} \cdot \partial_x A_{20}\right) + ik_c \left(\Psi_{11} \cdot \partial_x A_{20}^*\right) - ik_c \left(\Psi_{11}^* \cdot \partial_x A_{22}\right) - i2k_c \left(\partial_x \Psi_{11}^* \cdot A_{22}\right)
\end{aligned} \tag{2.66}$$

$$\begin{aligned}
N_{31}^{(B)} = & \, ik_c \left(\Psi_{11} \cdot \partial_x B_{20}\right) + ik_c \left(\Psi_{11} \cdot \partial_x B_{20}^*\right) - ik_c \left(\Psi_{11}^* \cdot \partial_x B_{22}\right) - i2k_c \left(\partial_x \Psi_{11}^* \cdot B_{22}\right) \\
& - ik_c \left(B_{11} \cdot \partial_x \Psi_{20}\right) - ik_c \left(B_{11} \cdot \partial_x \Psi_{20}^*\right) + ik_c \left(B_{11}^* \cdot \partial_x \Psi_{22}\right) + i2k_c \left(\partial_x B_{11}^* \cdot \Psi_{22}\right) \\
& - ik_c \left(A_{11} \cdot \partial_x u_{20}\right) - ik_c \left(A_{11} \cdot \partial_x u_{20}^*\right) + ik_c \left(A_{11}^* \cdot \partial_x u_{22}\right) + i2k_c \left(\partial_x A_{11}^* \cdot u_{22}\right) \\
& ik_c \left(u_{11} \cdot \partial_x A_{20}\right) + ik_c \left(u_{11} \cdot \partial_x A_{20}^*\right) - ik_c \left(u_{11}^* \cdot \partial_x A_{22}\right) - i2k_c \left(\partial_x u_{11}^* \cdot A_{22}\right)
\end{aligned} \tag{2.67}$$

2.C Linear dispersion relation

The linear dispersion relation, which determines the variable scalings in the multiple scales analysis. This relation is found by perturbing the linear system (Equation 2.18) with a small perturbation of the form $e^{\sigma t + ik_x x + ik_z z}$. Note that the spatial eigenvalues appear as k_z^2 and k_x^2 at lowest order.

$$\begin{aligned}
& \frac{B_0^4 k_x^2 k_z^4}{16\pi^2} + \frac{B_0^4 k_z^6}{16\pi^2} - \frac{B_0^2 \Omega_0 k_z^4 q}{2\pi} - 2\Omega_0 k_z^2 q \sigma^2 - \frac{4\sigma}{\mathrm{Rm}} \Omega_0 k_x^2 k_z^2 q - \frac{4\sigma}{\mathrm{Rm}} \Omega_0 k_z^4 q - \frac{2\Omega_0}{\mathrm{Rm}^2} k_x^4 k_z^2 q \\
& - \frac{4\Omega_0}{\mathrm{Rm}^2} k_x^2 k_z^4 q - \frac{2\Omega_0}{\mathrm{Rm}^2} k_z^6 q - k_x^2 \sigma^4 - k_z^2 \sigma^4 + 4k_z^2 \sigma^2 - \frac{2\sigma^3}{\mathrm{Rm}} k_x^4 - \frac{4\sigma^3}{\mathrm{Rm}} k_x^2 k_z^2 + \frac{8\sigma}{\mathrm{Rm}} k_x^2 k_z^2 - \frac{2\sigma^3}{\mathrm{Rm}} k_z^4 \\
& + \frac{8\sigma}{\mathrm{Rm}} k_z^4 - \frac{k_x^6 \sigma^2}{\mathrm{Rm}^2} - \frac{3\sigma^2}{\mathrm{Rm}^2} k_x^4 k_z^2 + \frac{4k_x^4}{\mathrm{Rm}^2} k_z^2 - \frac{3\sigma^2}{\mathrm{Rm}^2} k_x^2 k_z^4 + \frac{8k_x^2}{\mathrm{Rm}^2} k_z^4 - \frac{k_z^6 \sigma^2}{\mathrm{Rm}^2} + \frac{4k_z^6}{\mathrm{Rm}^2} - \frac{2\sigma^3}{\mathrm{Re}} k_x^4 \\
& - \frac{4\sigma^3}{\mathrm{Re}} k_x^2 k_z^2 - \frac{2\sigma^3}{\mathrm{Re}} k_z^4 - \frac{4k_x^6 \sigma^2}{\mathrm{ReRm}} - \frac{12k_x^4 k_z^2 \sigma^2}{\mathrm{ReRm}} - \frac{12k_x^2 k_z^4 \sigma^2}{\mathrm{ReRm}} - \frac{4k_z^6 \sigma^2}{\mathrm{ReRm}} - \frac{2k_x^8 \sigma}{\mathrm{ReRm}^2} - \frac{8k_x^6 k_z^2 \sigma}{\mathrm{ReRm}^2} \\
& - \frac{12k_x^4 k_z^4 \sigma}{\mathrm{ReRm}^2} - \frac{8k_x^2 k_z^6 \sigma}{\mathrm{ReRm}^2} - \frac{2k_z^8 \sigma}{\mathrm{ReRm}^2} - \frac{k_x^6 \sigma^2}{\mathrm{Re}^2} - \frac{3\sigma^2}{\mathrm{Re}^2} k_x^4 k_z^2 - \frac{3\sigma^2}{\mathrm{Re}^2} k_x^2 k_z^4 - \frac{k_z^6 \sigma^2}{\mathrm{Re}^2} - \frac{2k_x^8 \sigma}{\mathrm{Re}^2 \mathrm{Rm}} \\
& - \frac{8k_x^6 k_z^2 \sigma}{\mathrm{Re}^2 \mathrm{Rm}} - \frac{12k_x^4 k_z^4 \sigma}{\mathrm{Re}^2 \mathrm{Rm}} - \frac{8k_x^2 k_z^6 \sigma}{\mathrm{Re}^2 \mathrm{Rm}} - \frac{2k_z^8 \sigma}{\mathrm{Re}^2 \mathrm{Rm}} - \frac{k_x^{10}}{\mathrm{Re}^2 \mathrm{Rm}^2} - \frac{5k_x^8 k_z^2}{\mathrm{Re}^2 \mathrm{Rm}^2} - \frac{10k_x^6 k_z^4}{\mathrm{Re}^2 \mathrm{Rm}^2} - \frac{10k_x^4 k_z^6}{\mathrm{Re}^2 \mathrm{Rm}^2} \\
& - \frac{5k_x^2 k_z^8}{\mathrm{Re}^2 \mathrm{Rm}^2} - \frac{k_z^{10}}{\mathrm{Re}^2 \mathrm{Rm}^2} = 0.
\end{aligned} \tag{2.68}$$

Chapter 3

The weakly nonlinear magnetorotational instability in a global, cylindrical Taylor-Couette flow

3.1 Introduction

The magnetorotational instability (MRI) is believed to drive angular momentum transport in astrophysical disks. The MRI is a local instability excited by weak magnetic fields in differentially rotating fluids, and since first applied to an astrophysical context (Balbus & Hawley 1991) it has been invoked to explain accretion in protoplanetary disks (Armitage 2011) and disks around black holes (Blaes 2014), as well as jet and wind launching (Lesur et al. 2013), anisotropic turbulence (Murphy & Pessah 2015), and dynamo generation (Brandenburg et al. 1995; Vishniac 2009).

The diversity of astrophysical systems which may be MRI unstable yields an enormous

---

This section contains text from an article published in the Astrophysical Journal (Clark & Oishi 2017a).

Table 3.1: Fiducial parameters for MRI runs

	ξ	Pm	Co	Ω_2/Ω_1	R_1/R_2	radial magnetic b.c.
Standard MRI	0	1.6E-6	4.85E-2	0.121	0.33	conducting
Helical MRI	4	1E-6	118	0.27	0.5	insulating

parameter space to be explored. In protoplanetary disks, for example, the behavior and evolution of the MRI – and even its very existence – may change drastically depending on the properties of the magnetic field, the disk composition, disk geometry, and so forth. Multiphysics numerical simulations of such systems are currently an area of intense focus, enabling the study of nonideal MHD effects, disk stratification, nonequilibrium chemistry, and other complex physics that does not lend itself easily to analytic study (e.g. Fleming & Stone 2003; Bai 2011; Flock et al. 2013; Suzuki & Inutsuka 2014, among many others). Still, computational costs inevitably constrain numerical approaches. MRI saturation is a complicated nonlinear problem which may depend on the assumptions and approximations adopted by simulations in nonobvious ways. For example, the magnetic Prandtl number $\mathrm{Pm} = \nu/\eta \sim 10^{-8}$ in protoplanetary disks (e.g. Oishi & Mac Low 2011) and $\sim 10^{-6}$ in liquid metal experiments (e.g. Goodman & Ji 2002). Such extreme ratios of viscosity to resistivity far exceed current computational resources. However, we can construct asymptotic approximations valid for $\mathrm{Pm} \ll 1$ using analytic methods.

Analytic methods can also play a powerful role in elucidating the mechanisms responsible for MRI saturation. For instance, analytical approaches have revealed the mechanism that likely governs saturation in the "shearing box" approximation. The shearing box is an oft-invoked local approximation in which a section of a disk is represented by solving the MHD equations in a rotating, Cartesian box with a linearized background shear, subject to shear periodic boundary conditions in the radial direction. The shearing box is a convenient computational framework allowing extreme resolution for local MRI studies and has been extended to include vertical stratification and a wide variety of diffusive effects.

However, while the MRI is a local instability, there are a number of important problems that require a global treatment. Perhaps most importantly, linear evolution in the shearing box is dominated by channel modes, particularly when a net vertical magnetic field threads the box. These linear modes are exact solutions to the *nonlinear* local MRI equations. The shearing box MRI system avoids runaway growth by a secondary instability of the channel modes themselves (Goodman & Xu 1994; Pessah 2010). The growth of parasitic modes provides a saturation avenue for channel mode-dominated flows, yet this is unlikely to be the dominant saturation mechanism in laboratory experiments or astrophysical disks, as channel modes are artificially over-represented in the shearing box (Latter et al. 2015). Thus while the shearing box may accurately approximate many features of the global MRI, the saturation mechanism may not be among them. In Clark & Oishi (2017b, hereafter Chapter 2) we find that the fastest-growing MRI mode in the shearing box is not a channel mode when the effects of ambipolar diffusion are formally included. It is thus important to ask whether the symmetries that give rise to the weakly nonlinear saturation in the local geometry are also manifested in the global flow.

In this paper, we develop a weakly nonlinear, global theory for the MRI in a Taylor-Couette (TC) geometry. This system precludes channel modes, allowing us to develop an understanding of MRI saturation in their absence. A number of saturation mechanisms have been proposed for the MRI which do not rely on channel modes dominating the flow. The MRI feeds off of the free energy from differential rotation, and so a modification of the background shear may cause saturation (Knobloch & Julien 2005; Umurhan et al. 2007b). The MRI may transfer its free energy into the magnetic field, and saturate when the field is too strong to be susceptible to the MRI (Ebrahimi et al. 2009). The MRI may saturate differently depending on the particular parameter regime under investigation, and so our challenge is not only in identifying possible saturation mechanisms, but in understanding how and when each applies in different astrophysical environments.

Our investigation is astrophysically motivated, but we also intend our theory to be relevant to laboratory experiments. Several experimental efforts are attempting to observe the MRI in the laboratory, which will allow the study of a crucial astrophysical phenomenon in a controlled setting. Unfortunately, detection of the MRI has so far proven elusive. Sisan et al. (2004) claimed to detect the MRI in a spherical Couette flow, but most likely detected unrelated MHD instabilities instead (Hollerbach 2009; Gissinger et al. 2011). Most relevant to our work is the Princeton Plasma Physics Laboratory (PPPL) MRI Experiment, a liquid gallium TC flow with an axial magnetic field (Ji et al. 2001). There has been a significant amount of theoretical work designed to complement the Princeton MRI experiment involving direct numerical simulation of the experimental conditions, much of it focused on the specific challenges in identifying MRI signatures despite spurious, apparatus-driven flows (e.g. Gissinger et al. 2012). The vertical endcaps on a laboratory MRI apparatus drive meridional flows which both inhibit the excitement of MRI and obscure its detection. The Princeton MRI experiment employs split, independently rotating endcaps to mitigate these flows (Schartman et al. 2009). Our work assumes an infinite vertical domain, an idealization that is theoretically expedient but experimentally impractical. Such an approach changes the symmetry properties of the solution significantly, and in the much better studied hydrodynamic case this leads to significant differences even for TC devices with very large aspect ratios (Lopez & Marques 2005). Nevertheless, this study represents a first step in understanding the saturation of global, MRI unstable TC flow without the additional complication of vertical endcap effects.

Our radial treatment includes the curvature of the flow in a cylindrical apparatus. Many investigations of the MRI use the "narrow gap" approximation (the shearing box is a narrow

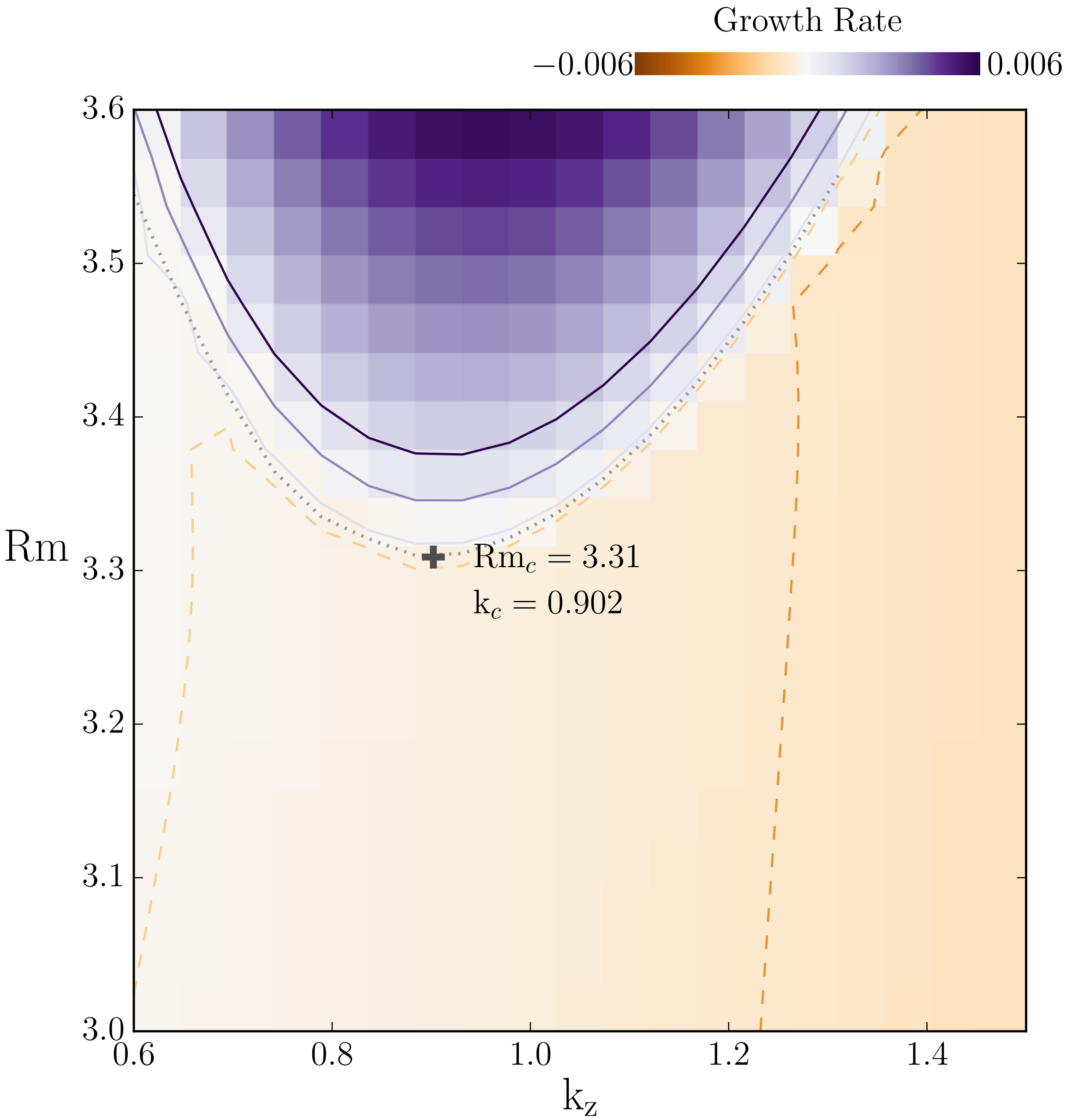

Figure 3.1: Growth rates in the (Rm, k_z) plane. Color map shows growth rate found by solving the linear eigenvalue problem for each (Rm, k_z) in the grid. The eigenvalue problem was solved for the widegap parameters listed in Table 3.1. Overlaid contours show growth rates at [-8E-4, -1.3E-4, 1.3E-4, 8E-4, 1.5E-3], where dashed contours represent negative values. The gray dotted line shows the interpolated marginal stability curve. The critical parameters $\mathrm{Rm}_c = 3.31$ and $k_c = 0.902$ correspond to the smallest parameter values that yield a zero growth rate.

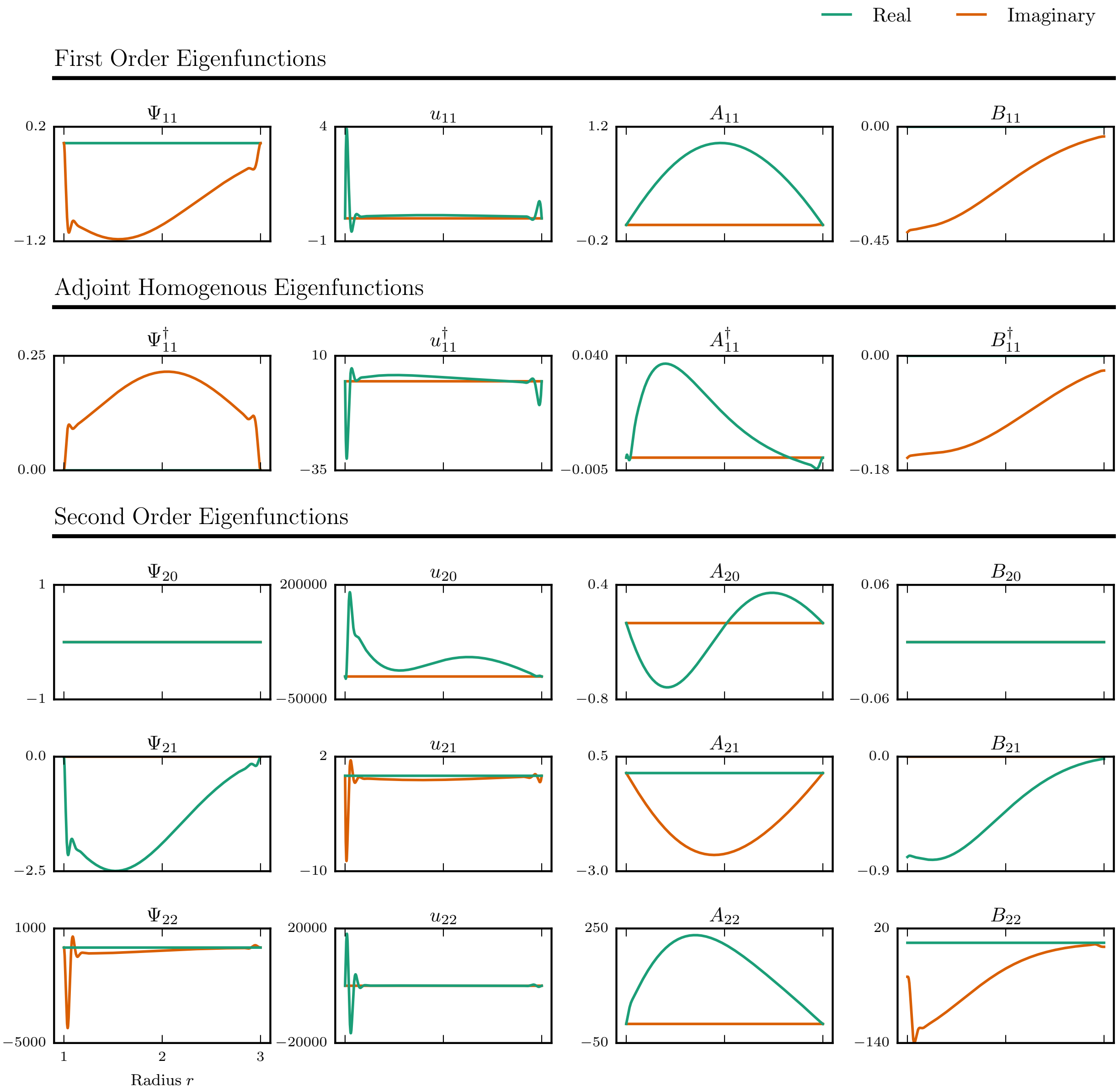

Figure 3.2: Eigenfunctions of the first order equations, first order adjoint homogenous equations, and second order equations. We use our fiducial parameters for the standard MRI ($\xi = 0$). Eigenfunctions are solved on a 512-element grid of Chebyshev polynomials. First-order eigenfunctions are normalized such that $A_{11}(r_0) = 1$. Adjoint homogenous eigenfunctions are normalized such that $\langle V^{\dagger}_{11} \cdot \mathcal{D} V_{11} \rangle = 1$.

gap without boundary walls), in which the radial extent of the fluid channel is taken to be much smaller than the radius of curvature. That is, for a center channel radius r_0 bounded by inner and outer radii r_1 and r_2, respectively, the narrow gap approximation applies when $r_0 \gg (r_2 - r_1)$. The narrow gap approximation simplifies the MRI equations by excluding curvature terms, because the flow through a narrow gap can be taken to be approximately linear in ϕ, i.e. Cartesian. Previous investigations into the weakly nonlinear behavior of the MRI have used this narrow gap approximation (Umurhan et al. 2007a,b; Clark & Oishi 2017b). Building on our work in Chapter 2, here we undertake the first (to our knowledge) weakly nonlinear analysis of the MRI in the wide gap regime, where the channel width may be comparable to or larger than its distance from the center of rotation.

Because we include curvature terms, our treatment also allows us to study the helical magnetorotational instability. The helical MRI is an overstability in which the background magnetic field is helical, $\mathbf{B} = B_0(\xi r/r_0 \hat{\phi} + \hat{\mathbf{z}})$ (Hollerbach & Rüdiger 2005). The helical MRI currently occupies a special place in the MRI puzzle. The helical MRI has been proposed as a method of awakening angular momentum transport in the "dead zones" of protoplanetary disks where the Rm becomes very small. However the rotation profiles needed to excite helical MRI may be steeper than Keplerian, depending on the boundary conditions, and so its role in astrophysical disks is currently a matter of debate (Liu et al. 2006; Rüdiger & Hollerbach 2007; Kirillov & Stefani 2013). Regardless of its astrophysical role, the helical MRI is significantly easier to excite in a laboratory setting than the standard MRI, and has already been detected by the Potsdam Rossendorf Magnetic Instability Experiment (PROMISE; Stefani et al. 2006, 2009).

In this work we explore the behavior of the viscous, dissipative MRI in a cylindrical geometry close to threshold, making explicit comparisons to the standard MRI behavior in the thin-gap regime. We investigate both the standard MRI, in which the background

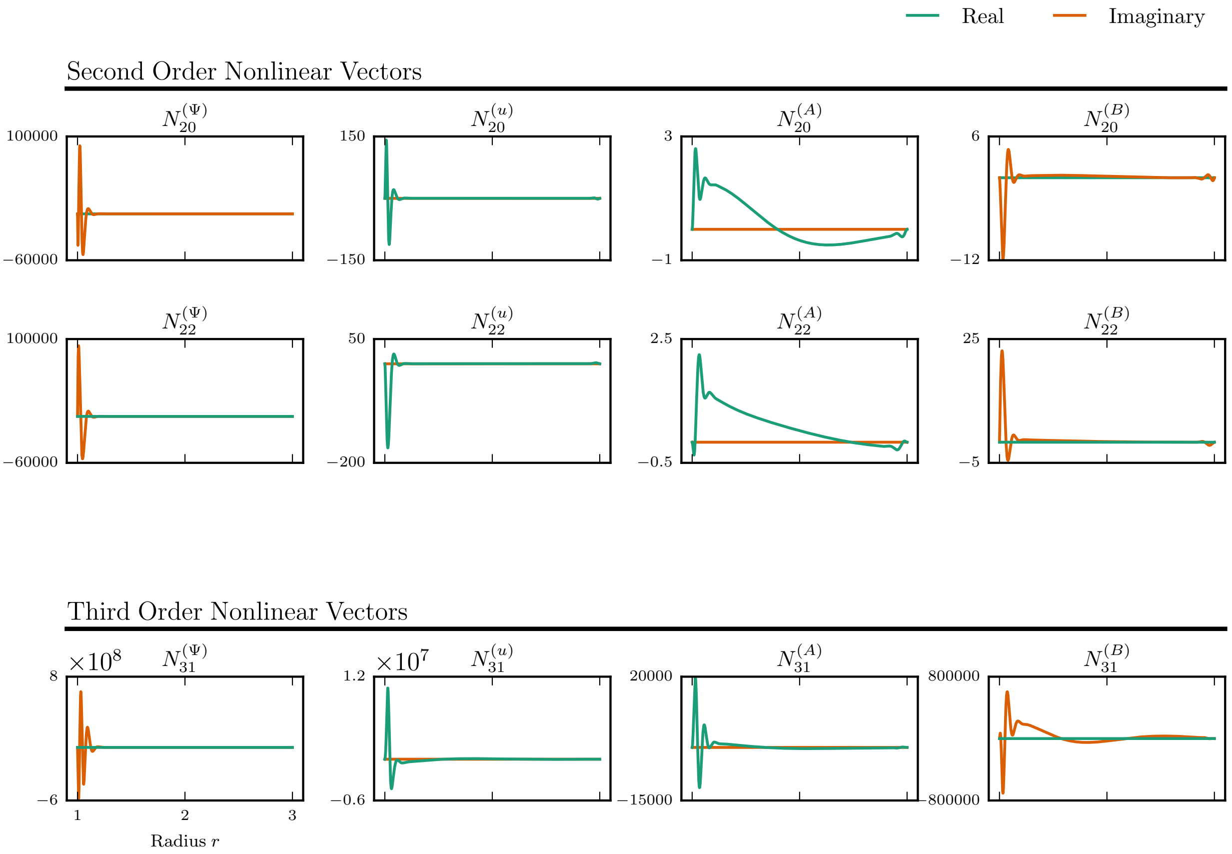

Figure 3.3: Nonlinear terms N_2 and N_3 for our fiducial standard MRI parameters. These are nonlinear combinations of lower-order eigenfunctions. At second order (N_2) the most unstable linear MRI mode interacts with itself and its complex conjugate. At third order (N_3) the first and second order MRI modes interact with each other.

magnetic field is purely axial, as well as the helical MRI. In section 3.2, we lay out the basic mathematical framework of the problem. In section 3.3, we introduce the method of multiple scales we use to construct our theory. In section 3.4 we describe the basic results, and in section 3.5 we place them in the context of previous work on other instabilities, discuss their relevance to experiments, and reiterate our final conclusions.

3.2 Basic framework

The basic equations solved are the momentum and induction equations,

$$\partial_t \mathbf{u} + \mathbf{u} \cdot \nabla \mathbf{u} = -\frac{1}{\rho} \nabla P - \nabla \Phi + \frac{1}{c\rho} (\mathbf{J} \times \mathbf{B}) + \nu \nabla^2 \mathbf{u} \tag{3.1}$$

and

$$\partial_t \mathbf{B} = \nabla \times (\mathbf{u} \times \mathbf{B}) + \eta \nabla^2 \mathbf{B}, \tag{3.2}$$

where P is the gas pressure, ν is the kinematic viscosity, η is the microscopic diffusivity, $\nabla\Phi$ is the gravitational force per unit mass, and the current density is $\mathbf{J} = c\nabla \times \mathbf{B}/4\pi$. We solve these equations subject to the incompressible fluid and solenoidal magnetic field constraints,

$$\nabla \cdot \mathbf{u} = 0 \tag{3.3}$$

and

$$\nabla \cdot \mathbf{B} = 0. \tag{3.4}$$

We perturb these equations axisymmetrically in a cylindrical (r, ϕ, z) geometry, i.e. $\mathbf{u} = \mathbf{u_0} + \mathbf{u_1}$ and $\mathbf{B} = \mathbf{B_0} + \mathbf{B_1}$, where $\mathbf{u_0}$ and $\mathbf{B_0}$ are defined below. We define a Stokes stream function Ψ such that

$$\mathbf{u_1} = \begin{bmatrix} \frac{1}{r}\partial_z \Psi \ \hat{\mathbf{r}} \\ u_\phi \ \hat{\phi} \\ -\frac{1}{r}\partial_r \Psi \ \hat{\mathbf{z}} \end{bmatrix}, \tag{3.5}$$

and the magnetic vector potential A is

$$\mathbf{B_1} = \begin{bmatrix} \frac{1}{r}\partial_z A \ \hat{\mathbf{r}} \\ B_\phi \ \hat{\phi} \\ -\frac{1}{r}\partial_r A \ \hat{\mathbf{z}} \end{bmatrix}. \tag{3.6}$$

These definitions automatically satisfy Equations 3.3 and 3.4 for axisymmetric disturbances. We note that in the linearized equations, streamfunctions of the form $u_x = \partial_z \Psi$, $u_z = -(\partial_r + \frac{1}{r})\Psi$, and the corresponding definitions of the magnetic vector potential, are convenient choices, but we define Equations 3.5 and 3.6 for this nonlinear investigation because of the incommutability of ∂_r and $\partial_r + \frac{1}{r}$.

The astrophysical magnetorotational instability operates in accretion disks and in stellar interiors, environments where fluid rotation is strongly regulated by gravity. In accretion disks, differential rotation is imposed gravitationally by a central body, so the rotation profile is forced to be Keplerian. Clearly a gravitationally enforced Keplerian flow is inaccessible to laboratory study, so differential rotation is created by rotating an inner cylinder faster than an outer cylinder (a TC setup). For a nonideal fluid subject to no-slip boundary conditions, the base flow is

$$\Omega(r) = c_1 + \frac{c_2}{r^2}, \tag{3.7}$$

where $c_1 = (\Omega_2 r_2^2 - \Omega_1 r_1^2)/(r_2^2 - r_1^2)$, $c_2 = r_1^2 r_2^2 (\Omega_1 - \Omega_2)/(r_2^2 - r_1^2)$, and Ω_1 and Ω_2 are the rotation rates at the inner and outer cylinder radii, respectively. In the laboratory, r_1 and r_2 are typically fixed by experimental design. However Ω_1 and Ω_2 may be chosen such that the flow in the center of the channel is approximately Keplerian. Defining a shear parameter q, we see that for Couette flow,

$$q(r) \equiv -\frac{d \ln \Omega}{d \ln r} = \frac{2c_2}{c_1 r^2 + c_2}. \tag{3.8}$$

Thus through judicious choice of cylinder rotation rates, one can set $q(r_0) = 3/2$, for quasi-Keplerian flow. Note that the narrow gap approximation imposes a linear shear (constant q), and so the interaction of fluid perturbations with the base velocity profile differs significantly from the case considered here. Our base velocity is

$$\mathbf{u_0} = r\Omega(r)\hat{\phi}. \tag{3.9}$$

We initialize a magnetic field

$$\mathbf{B_0} = B_0\hat{\mathbf{z}} + B_0\xi\frac{r_0}{r}\hat{\phi}, \tag{3.10}$$

so that the base magnetic field is axial when $\xi = 0$ and otherwise helical.

In this work we will focus our findings on two fiducial parameter sets, one for the standard MRI where $\xi = 0$ and one for the helical MRI. We choose the standard MRI parameters to be comparable to the case considered in Goodman & Ji (2002). The helical MRI parameters were chosen to be comparable to Hollerbach & Rüdiger (2005). Our fiducial parameters are described in Table 3.1.

Our perturbed system is

$$\begin{aligned} &\frac{1}{r}\partial_t(\nabla^2\Psi - \frac{2}{r}\partial_r\Psi) - \mathrm{Co}\frac{1}{r}B_0\partial_z(\nabla^2 A - \frac{2}{r}\partial_r A) - \frac{2}{r}u_0\partial_z u_\phi + \mathrm{Co}\frac{2}{r^2}B_0\xi\partial_z B_\phi \\ &- \frac{1}{\mathrm{Re}}\left[\nabla^2(\frac{1}{r}\nabla^2\Psi - \frac{2}{r^2}\partial_r\Psi) - \frac{1}{r^3}\nabla^2\Psi + \frac{2}{r^4}\partial_r\Psi\right] = N^{(\Psi)} \end{aligned} \tag{3.11}$$

$$\partial_t u_\phi + \frac{1}{r^2}u_0\partial_z\Psi + \frac{1}{r}\partial_r u_0\partial_z\Psi - \mathrm{Co}B_0\partial_z B_\phi - \frac{1}{\mathrm{Re}}(\nabla^2 u_\phi - \frac{1}{r^2}u_\phi) = N^{(u)} \tag{3.12}$$

$$\partial_t A - B_0\partial_z\Psi - \frac{1}{\mathrm{Rm}}(\nabla^2 A - \frac{2}{r}\partial_r A) = N^{(A)} \tag{3.13}$$

$$\partial_t B_\phi + \frac{1}{r^2}u_0\partial_z A - B_0\partial_z u_\phi - \frac{1}{r}\partial_r u_0\partial_z A - \frac{2}{r^3}B_0\xi\partial_z\Psi - \frac{1}{\mathrm{Rm}}(\nabla^2 B_\phi - \frac{1}{r^2}B_\phi) = N^{(B)} \tag{3.14}$$

The righthand side of the equations contain the nonlinear terms

$$N^{(\Psi)} = -J(\Psi, \frac{1}{r^2}(\nabla^2\Psi - \frac{2}{r}\partial_r\Psi)) + \mathrm{Co}J(A, \frac{1}{r^2}(\nabla^2 A - \frac{2}{r}\partial_r A)) - \mathrm{Co}\frac{2}{r}B_\phi\partial_z B_\phi + \frac{2}{r}u_\phi\partial_z u_\phi \quad (3.15)$$

$$N^{(u)} = \mathrm{Co}\frac{1}{r}J(A, B_\phi) - \frac{1}{r}J(\Psi, u_\phi) + \mathrm{Co}\frac{1}{r^2}B_\phi\partial_z A - \frac{1}{r^2}u_\phi\partial_z\Psi \quad (3.16)$$

$$N^{(A)} = \frac{1}{r}J(A, \psi) \quad (3.17)$$

$$N^{(B)} = \frac{1}{r}J(A, u_\phi) + \frac{1}{r}J(B_\phi, \psi) + \frac{1}{r^2}B_\phi\partial_z\psi - \frac{1}{r^2}u_\phi\partial_z A \quad (3.18)$$

where J is the Jacobian $J(f,g) \equiv \partial_z f \partial_r g - \partial_r f \partial_z g$. Note that in the above, $\nabla^2 f \equiv \partial_r^2 f + \partial_z^2 f + \frac{1}{r}\partial_r f$. Equations 3.11 - 3.18 are nondimensionalized by inner cylinder quantities: lengths have been scaled by r_1, velocities by $r_1\Omega_1$, and densities by ρ_0, where ρ_0 is the constant density. Magnetic fields are scaled by B_0, the constant strength of the initial background field; where B_0 appears in the above it is formally unity. $\Omega_1 = \Omega(r_1)$ is the rotation rate of the inner cylinder. We introduce the Reynolds number $\mathrm{Re} = \Omega_1 r_1^2/\nu$, the magnetic Reynolds number $\mathrm{Rm} = \Omega_1 r_1^2/\eta$, and a plasma beta parameter $\mathrm{Co} = 2B_0^2/\Omega_1^2 r_1^2 \rho_0$. Note that if we define the dimensional cylindrical coordinate $r = r_1(1+\delta x)$, we recover the narrow gap approximation of the system in the limit $\delta \to 0$.

We solve the standard MRI system subject to the same boundary conditions used in Goodman & Ji (2002). These are periodic vertical boundary conditions and no-slip, perfectly conducting radial boundary conditions, namely

$$\Psi = \partial_r\Psi = u = A = \partial_r(rB) = 0 \quad (3.19)$$

at $r = r_1, r_2$. To the helical MRI system we apply insulating boundary conditions as used in Hollerbach & Rüdiger (2005):

$$\partial_r A = k\frac{I_0(kr)}{I_1(kr)}A \text{ at } r = r_1 \tag{3.20}$$

$$\partial_r A = -k\frac{K_0(kr)}{K_1(kr)}A \text{ at } r = r_2 \tag{3.21}$$

and $B = 0$ at $r = r_1, r_2$ (see Willis & Barenghi 2002). Here, I_n and K_n are the modified Bessel functions of the first and second kind, respectively.

We note that Equations 3.11 - 3.14 are written in a nonstandard form, with the nonlinear terms on the righthand side. This choice has a practical motivation. As detailed in §3.3, we expand these equations in a perturbation series and solve them order by order using a pseudospectral code. The code solves partial differential equations of the form $\mathrm{M}\partial_t\mathbf{V}+\mathrm{L}\mathbf{V} = \mathbf{F}$, where M and L are matrices and $\mathbf{F}$ is a vector containing any nonhomogenous terms. The nonlinear terms in our perturbation analysis become nonhomogenous term inputs to the solver.

3.3 Weakly nonlinear perturbation analysis

We find the marginal system as a function of the dimensionless parameters. The marginal stability curve for our standard MRI system is a hyperplane in $(\mathrm{Rm}, \mathrm{Pm}, \mathrm{Co}, \Omega_2/\Omega_1, \mathrm{R}_1/\mathrm{R}_2)$, but we hold all of these constant except for Rm. To analyze the MRI system at marginality, we fix the parameters listed in Table 3.1 and determine the critical Rm and vertical wavenumber k_z by repeatedly solving the linear MRI system to determine the smallest parameter values for which the fastest growing mode has zero growth rate. That is, we solve the linear eigenvalue problem for eigenvalues $\sigma = \gamma + i\omega$ and determine the parameters which yield $\gamma = 0$. Figure 3.1 shows linear MRI growth rates γ in the (Rm, k_z) plane. For the

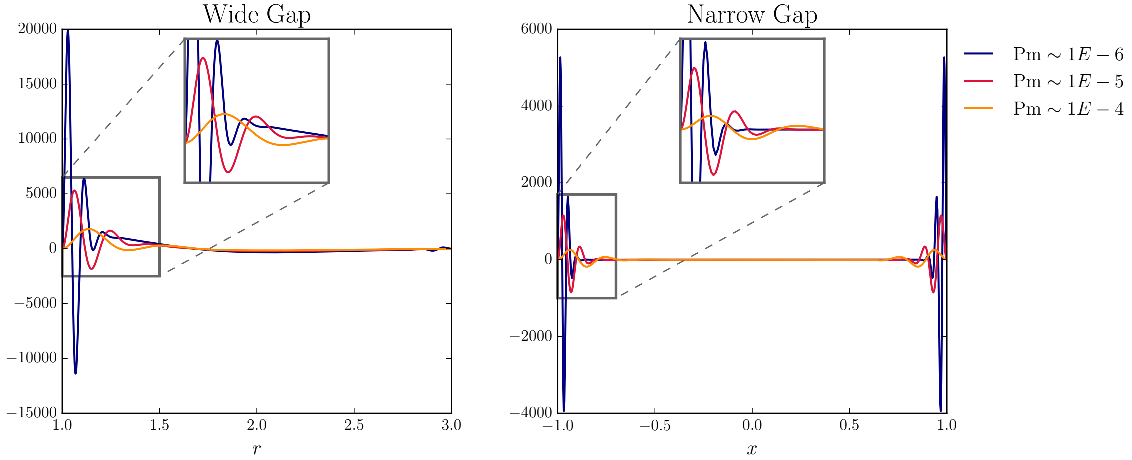

Figure 3.4: Nonlinear term $N_{31}^{(A)}$ for the wide gap (left) and narrow gap (right) standard MRI, where the wide gap is the TC flow considered in this work. Terms shown span three orders of magnitude in Pm. The wide gap vectors represent runs using the parameters in Table 3.1 and Pm $= 1.6E-4, 1.6E-5, 1.6E-6$. The narrow gap MRI runs use the fiducial parameters in Umurhan et al. (2007b), with Pm $= 1E-4, 1E-5, 1E-6$. Inlaid plots show zoomed-in views of boundary layers at the inner boundary. The wide gap case displays dramatic boundary layers only at the inner boundary, but boundary layers in the thin gap approximation are symmetric about the origin because MRI modes in the narrow gap approximation are eigenstates of parity.

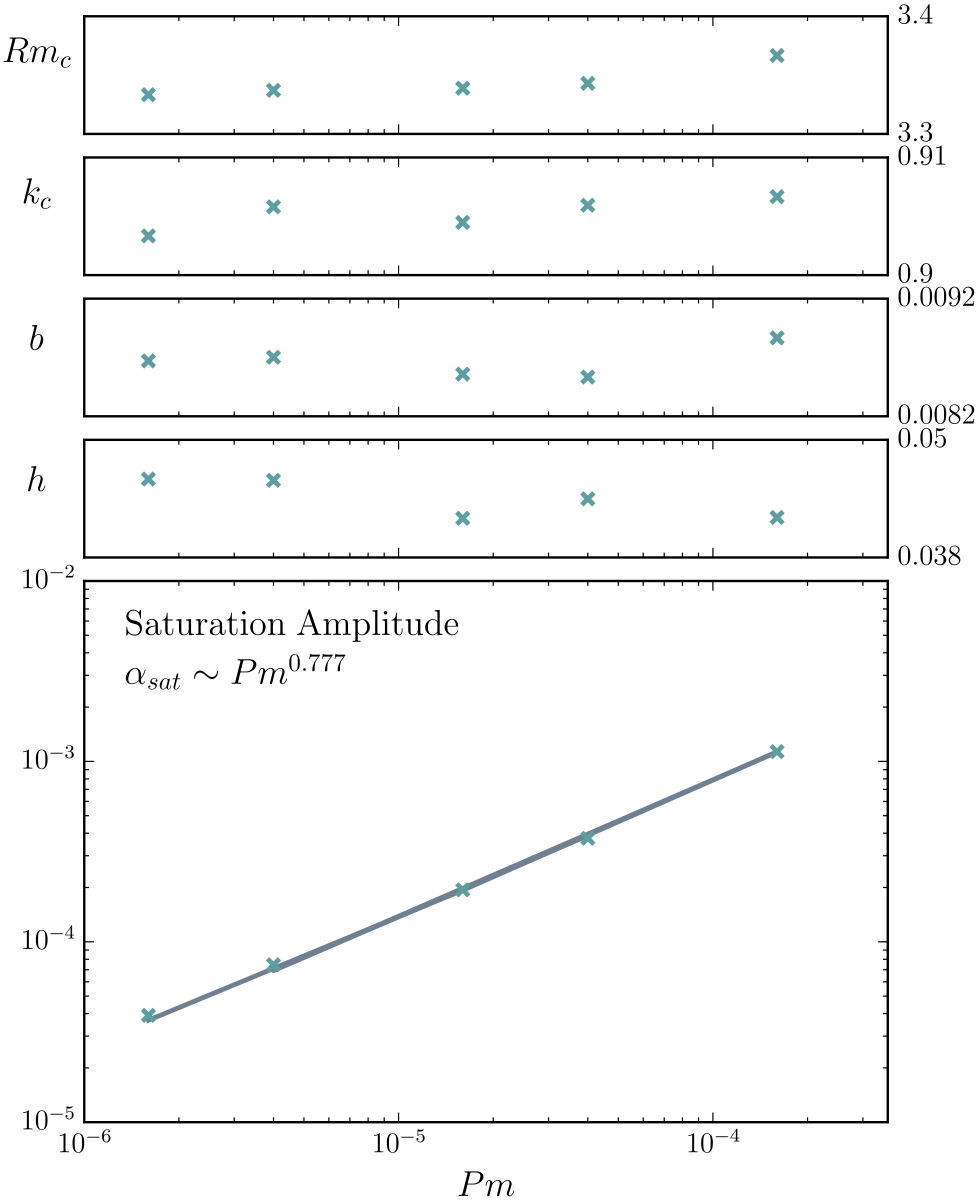

Figure 3.5: Critical parameters Rm_c and k_c, and coefficients of the Ginzburg-Landau equation (Equation 3.28) as a function of Pm. Note the very weak dependence of the linear (b) and diffusive (h) coefficients on Pm. The saturation amplitude $\alpha_{sat} = \sqrt{b/c}$ of the standard MRI system has a power law dependence on Pm which we measure to be $\alpha_{sat} \sim \mathrm{Pm}^{0.777}$. This scaling is driven by the Pm dependence of the nonlinear coefficient c.

fiducial standard MRI parameters in Table 3.1 we find critical parameters $\mathrm{Rm}_c = 3.30$ and $k_c = 0.901$.

As in the weakly nonlinear analysis of Chapter 2, we tune the system away from marginality by taking $B_0 \rightarrow B_0\,(1+\epsilon^2)$, where the small parameter $\epsilon \ll 1$. We parameterize scale separation as $Z = \epsilon z$ and $T = \epsilon^2 t$, where Z and T are slowly varying spatial and temporal scales, respectively. We group the fluid variables into a state vector $\mathbf{V} = [\Psi, u, A, B]^{\mathrm{T}}$, such that the full nonlinear system in Equations 3.11 - 3.18 can be expressed as

$$\mathcal{D}\partial_t \mathbf{V} + \mathcal{L}\mathbf{V} + \epsilon^2 \widetilde{\mathcal{G}}\mathbf{V} + \xi\widetilde{\mathcal{H}}\mathbf{V} + \mathbf{N} = 0, \tag{3.22}$$

where $\mathcal{D}$, $\mathcal{L}$, and $\widetilde{\mathcal{G}}$ are matrices defined in Appendix 3.A, and $\mathbf{N}$ is a vector containing all nonlinear terms. We expand the variables in a perturbation series

$$\mathbf{V} = \epsilon\mathbf{V}_1 + \epsilon^2\mathbf{V}_2 + \epsilon^3\mathbf{V}_3 + h.o.t. \tag{3.23}$$

The perturbed system can then be expressed at each order by the equations

$$\mathcal{O}(\epsilon) : \mathcal{L}\mathbf{V}_1 + \xi\widetilde{\mathcal{H}}\mathbf{V}_1 + \mathcal{D}\partial_t\mathbf{V}_1 = 0 \tag{3.24}$$

$$\mathcal{O}(\epsilon^2) : \mathcal{L}\mathbf{V}_2 + \xi\widetilde{\mathcal{H}}\mathbf{V}_2 + \mathcal{D}\partial_t\mathbf{V}_2 + \widetilde{\mathcal{L}}_1\partial_Z\mathbf{V}_1 + \xi\mathcal{H}\partial_Z\mathbf{V}_1 + \mathbf{N}_2 = 0 \tag{3.25}$$

$$\begin{aligned}\mathcal{O}(\epsilon^3) : {} & \mathcal{L}\mathbf{V}_3 + \xi\widetilde{\mathcal{H}}\mathbf{V}_3 + \mathcal{D}\partial_t\mathbf{V}_3 + \mathcal{D}\partial_T\mathbf{V}_1 + \widetilde{\mathcal{L}}_1\partial_Z\mathbf{V}_2 + \xi\mathcal{H}\partial_Z\mathbf{V}_2 + \widetilde{\mathcal{L}}_2\partial_Z^2\mathbf{V}_1 \\ & - \xi\widetilde{\mathcal{H}}\mathbf{V}_1 + \widetilde{\mathcal{G}}\mathbf{V}_1 + \mathbf{N}_3 = 0.\end{aligned} \tag{3.26}$$

The nonlinear terms $\mathbf{N}_2$ and $\mathbf{N}_3$ which appear at $\mathcal{O}(\epsilon^2)$ and $\mathcal{O}(\epsilon^3)$, respectively, contain the nonlinear interaction between MRI modes. The system is weakly nonlinear because this mode interaction occurs in a controlled way. At $\mathcal{O}(\epsilon^2)$, the nonlinear terms represent the interaction of linear ($\mathcal{O}(\epsilon)$) MRI modes with themselves and their complex conjugates.

At $\mathcal{O}(\epsilon^3)$, the nonlinear terms contain the interaction between first- and second-order MRI modes. See Appendix 3.A for the definition of matrices and a thorough derivation, and Appendix 3.B for the detailed form of the nonlinear vectors. We emphasize that Equations 3.24 - 3.26 have the same form as these equations in the narrow gap case, although the matrices, which contain all radial derivatives, are significantly different in this wide gap formulation. This is because we do not have slow variation in the radial dimension. In the standard MRI case, $\sigma = 0$ at marginality and so the ∂_t terms drop out of the equations. For the helical MRI case, however, σ has a nonzero imaginary component even at threshold, so we must formally include these terms in our perturbation expansion. The slow variation in Z and T are parameterized as an amplitude function $\alpha(Z, T)$ which modulates the flow in these dimensions. This parameterization coupled with the boundary conditions lead us to an ansatz linear solution

$$\mathbf{V}_1 = \alpha(Z, T)\mathbb{V}_{11}(r)e^{ik_z z + \sigma t} + c.c., \tag{3.27}$$

where the radial variation is contained in $\mathbb{V}_{11}$, and $\sigma = \gamma + i\omega$.

We solve the equations at each order using Dedalus, an open source pseudospectral code. We solve the radial portion of the eigenvectors on a basis of Chebyshev polynomials subject to our radial boundary conditions. We use a 512-component Chebyshev grid, and confirm numerical convergence at 1.5× the resolution. This is sufficient to determine convergence because of the faster-than-exponential convergence of spectral methods (Boyd 2001). We solve Equation 3.24 as a linear eigenvalue problem, and Equation 3.25 as a linear boundary value problem. The result of the weakly nonlinear analysis is a single amplitude equation for α. This amplitude equation is found by enforcing a solvability condition on Equation 3.26.

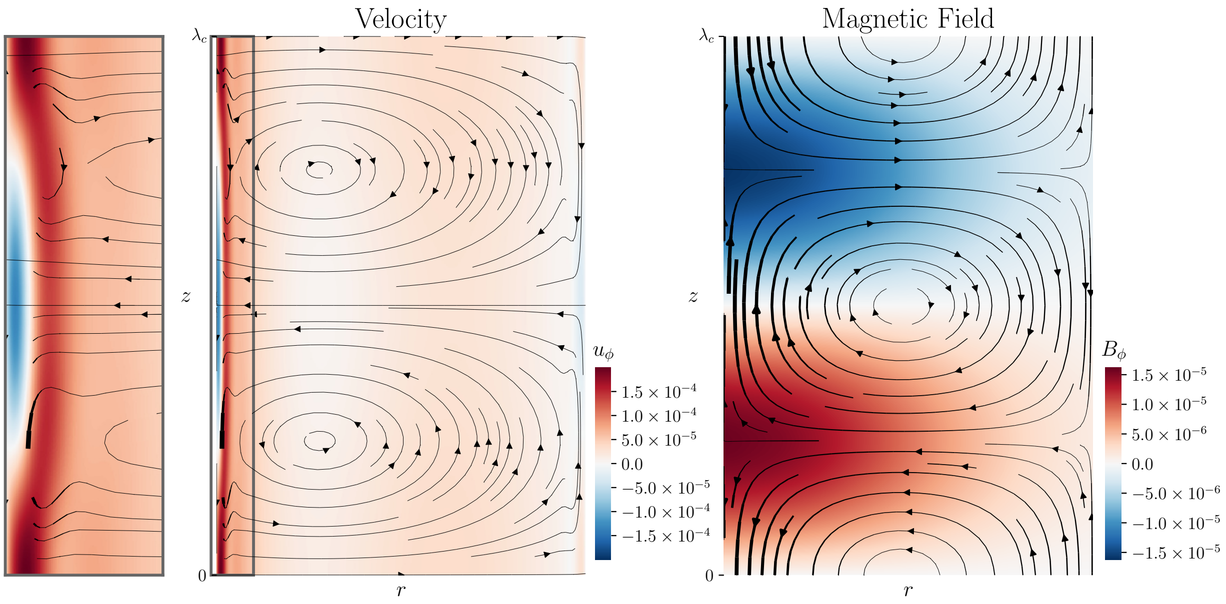

Figure 3.6: Perturbation structure for the velocity and magnetic field of the fiducial standard MRI case, including first and second order perturbations. Leftmost panel is a radially zoomed-in section of the velocity perturbation structure, to better show the boundary layer-driven structure at the inner cylinder. Colors are azimuthal velocity and magnetic field perturbations, and streamfunctions show the perturbation structure in the r, z plane. The width of the streamfunctions is proportional to the speed and magnetic field strength in the r, z plane for the velocity and magnetic field, respectively. Vertical domain covers one critical wavelength $\lambda_c = 2\pi/k_c$. We use the constant saturation amplitude $\alpha_s = 3.9 \times 10^{-5}$ derived for this case, and a small parameter $\epsilon = 0.5$.

We find

$$\partial_T \alpha = b\alpha + d\partial_Z^2 \alpha - c\alpha \left|\alpha^2\right|, \tag{3.28}$$

a Ginzburg-Landau equation (GLE). The GLE governs the weakly nonlinear amplitude behavior in a wide range of physical systems, including the narrow gap MRI (Umurhan et al. 2007b), Rayleigh-Bénard convection (Newell & Whitehead 1969), and hydrodynamic TC flow (e.g. Recktenwald et al. 1993). We emphasize that this is a model equation, valid only near marginality (Cross & Hohenberg 1993). The dynamics of the GLE are determined by its coefficients, which are in turn determined by the linear eigenfunctions and nonlinear vectors plotted in Figures 3.2 and 3.3. Equation 3.28 contains three coefficients: b, which determines the linear growth rate of the system, d, a diffusion coefficient, and c, the coefficient of the nonlinear term. When all of the coefficients of Equation 3.28 are real, this is known as the real GLE, although the amplitude α is in general complex. The real GLE is subject to several well-studied instabilities, including the Ekhaus and Zig-Zag instabilities. When the coefficients are complex, we have the complex GLE, a source of even richer phase dynamics than its real counterpart (see Aranson & Kramer 2002) for a thorough review.

3.4 Results

3.4.1 Standard MRI

For the standard MRI we derive a real GLE. Here we note a departure from the behavior of the narrow gap system. The purely conducting boundary condition states that the axial component of the current ($\mathbf{J}_z = [\nabla \times \mathbf{B}]_z$) must be zero at the walls. In the thin gap geometry, the purely conducting boundary condition on the azimuthal magnetic field is $\partial_x(B_y) = 0$ for axisymmetric perturbations. A spatially constant azimuthal field satisfies both the thin-gap

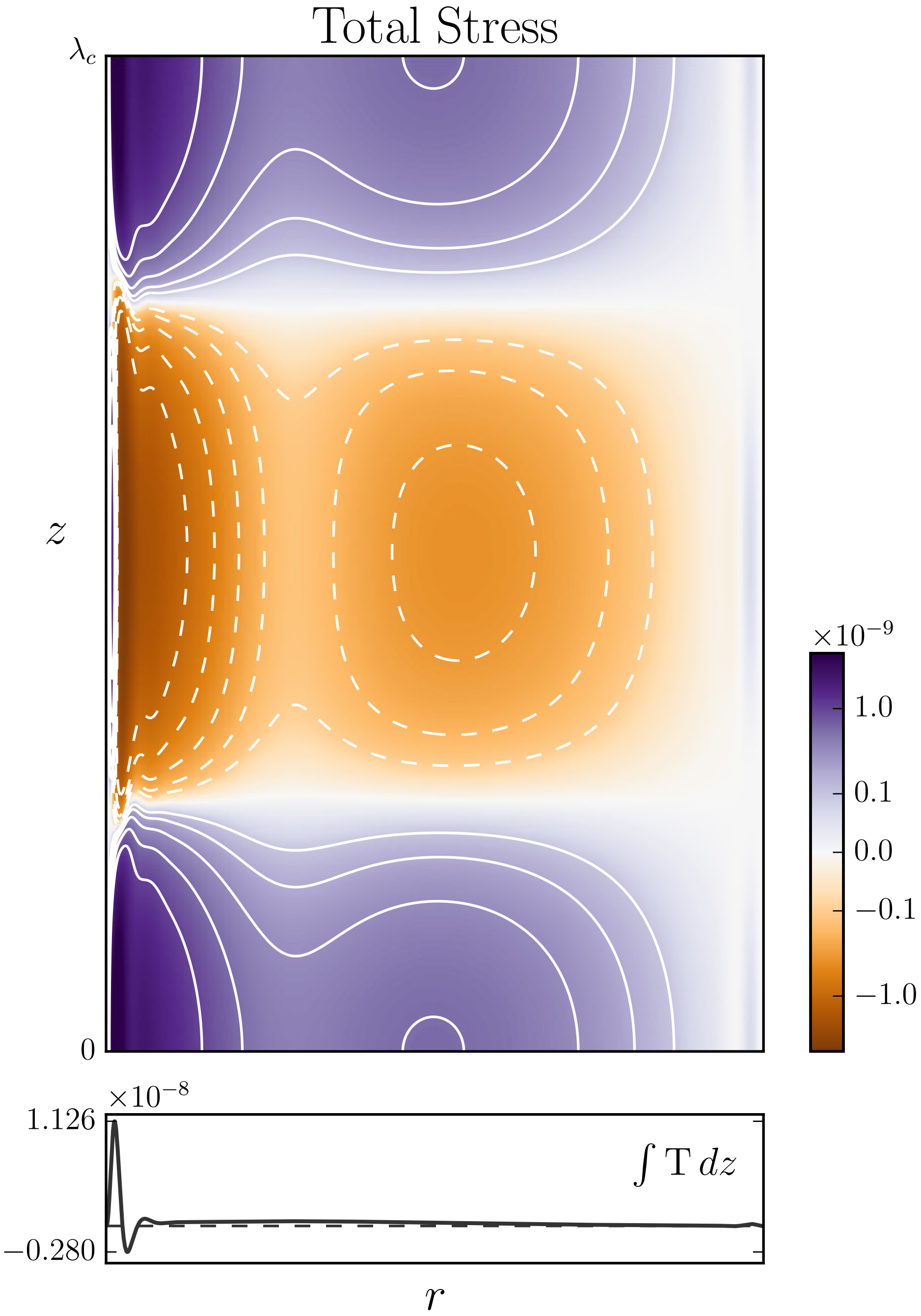

Figure 3.7: Total stress $\mathrm{T}(r, z) = u_r u_\phi - \mathrm{Co} B_r B_\phi$, i.e. the sum of the Reynolds and Maxwell stresses for the fiducial standard MRI parameters (top panel). Bottom panel shows the vertically integrated stress $\int \mathrm{T}(r, z)\, dz$.

MRI equations and this boundary condition. This neutral mode is formally included in the analysis of Umurhan et al. (2007b) and yields a second amplitude equation in the form of a simple diffusion equation. This amplitude equation decouples from the GLE because of the translational symmetry of the thin-gap geometry. Because that symmetry is not preserved in the wide-gap case, Umurhan et al. (2007b) postulate that slow variation in the wide-gap geometry will be governed by two coupled amplitude equations. However, the purely geometric term in Equation 3.14 prevents the wide-gap geometry from sustaining a neutral mode. We note that a neutral mode of the form $B_\phi(r) \propto \frac{1}{r}$ would exist in a resistance-free approximation. Here, however, this mode does not exist and we derive a single real GLE as the amplitude equation of the standard MRI.

The preservation of symmetries in the thin-gap geometry is worth a closer look, as its absence in the wide gap case is the source of many differences in the systems. Latter et al. (2015) point out that in the ideal limit ($\nu, \eta \to 0$), the linearized system described by the lefthand side of Equations 3.11 - 3.14 can be expressed as a Schrödinger equation for the radial velocity. Similarly combining equations to obtain a single expression for Ψ, we find that the thin-gap limit, linear, ideal MRI can be expressed as

$$\partial_x^2 \Psi + k_z^2 \mathrm{U}(x) \Psi = 0 \tag{3.29}$$

where $\mathrm{U}(x) = 3/v_A^2 k_z^2 + 1$ at marginality. This form is not unique to the ideal MHD case, though the ideal approximation simplifies the expression considerably. When no-slip radial boundary conditions are applied, the thin-gap MRI system resembles a particle in a box with a radially constant potential well. Thus thin-gap linear MRI modes must be eigenstates of parity. These symmetries are preserved in the nonlinear MRI vectors because they are nonlinear combinations of lower-order eigenfunctions. In the wide gap case, the “potential” $\mathrm{U}(r)$ varies with r, so symmetric and antisymmetric modes are no longer required. This lack

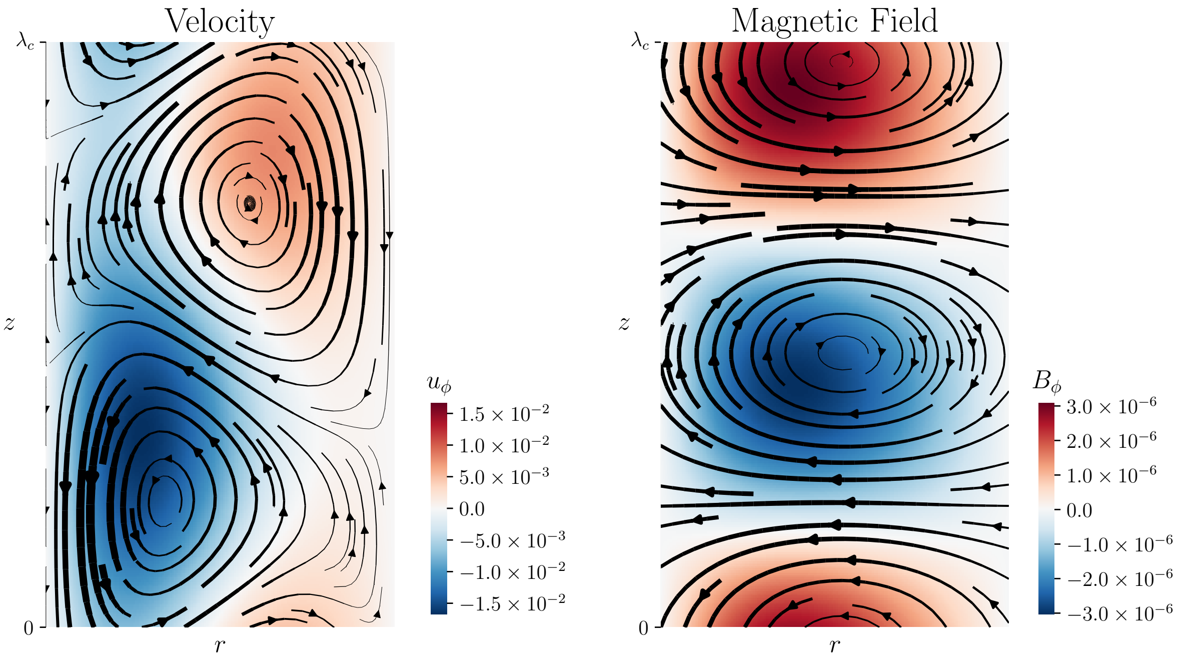

Figure 3.8: As in Figure 3.6 but for the fiducial helical MRI case, including first and second order perturbations.

of symmetry is readily apparent in the eigenfunctions and nonlinear vectors in Figures 3.2 and 3.3, both of which display enhanced boundary layer activity at the inner boundary as compared to the outer boundary. The inner and outer boundary layers are symmetric in the thin gap case (see Figure 3.4).

The form of the nonlinear terms, detailed in Appendix 3.B, represent a departure from the thin-gap theory. The narrow gap nonlinear terms at both second and third orders are linear combinations of Jacobians. The nonlinear terms in the wide-gap case differ from their thin-gap analogues with the addition of vertical advective terms. These terms derive from the advective derivatives in the momentum and induction equations, but are filtered out in the thin-gap approximation. The nonlinear terms ultimately determine the saturation amplitude of the system, as described below.

We examine the behavior of the wide gap MRI system as a function of Pm in the regime

$\mathrm{Pm} \ll 1$. Figure 3.5 shows the critical parameters k_c and Rm as a function of Pm, as well as the GLE linear coefficient b and the diffusion coefficient d. From Equation 3.28 it is apparent that the asymptotic saturation amplitude is $\alpha_s = \pm\sqrt{b/c}$, and we plot the dependence of α_s on Pm in the bottom panel of Figure 3.5. Note that because Rm is essentially constant as a function of Pm, the saturation amplitude is equivalently sensitive to Re^{-1}. We find by fitting the data that the saturation amplitude scales as $\alpha_s \sim \mathrm{Pm}^{0.777}$. For these same boundary conditions, Umurhan et al. (2007b) find that the narrow gap saturation amplitude scales as $\mathrm{Pm}^{2/3}$. They find that this amplitude dependence is driven by the $\mathrm{Pm}^{1/3}$ dependence of the linear boundary layer. Boundary layer analysis similarly reveals a $\nu^{1/3}$ dependence for the radial extent of the boundary layer in TC flow (Goodman & Ji 2002). Figure 3.4 shows the structure of the third-order nonlinear term $N_{31}^{(A)}$ as a function of Pm for both the narrow and wide gap standard MRI. N_{31} is the vector that determines the GLE coefficient c, and thus the scaling of the saturation amplitude because of the insensitivity of b to Pm (see Appendix 3.A for the wide gap case, and Umurhan et al. (2007b) and Chapter 2 for the narrow gap equations). Clearly, the width of the boundary layers scales with Pm in both the wide and narrow gap MRI. This translates to a steeper saturation amplitude Pm dependence in the wide gap case.

Because it is governed by a real GLE, the saturated standard MRI state may be unstable to the Eckhaus instability, in which the wavelength of the large-scale pattern is adjusted (e.g. Hoyle 2006). Preliminary investigation of the GLE behavior for the standard MRI coefficients derived here indicates that when the simulated vertical domain is large (i.e. spans multiple critical wavelengths), the amplitude function is modulated in Z, but always be bounded by $\alpha_s = \pm\sqrt{b/c}$, as must be the case for the one-dimensional real GLE. In Figure 3.6 we plot the saturated state perturbation structure of the fiducial standard MRI, up to and including second order disturbances. We use a constant saturation amplitude, but note that a nonconstant α_s would introduce more vertical structure. We similarly plot the total stress, i.e. the sum of the Reynolds and Maxwell stresses in our domain (Figure 3.7). As in Chapter 2, we find that the saturation mechanism for weakly nonlinear TC flow is a combination of reduced shear and redistributed and amplified background B_z. This strongly suggests that the underlying physics remains the same in the wide gap geometry, despite the addition of curvature terms.

3.4.2 Helical MRI

When ξ in Equation 3.22 is nonzero, the helical MRI arises. We examine a single fiducial helical MRI case, for the parameters used by Hollerbach & Rüdiger (2005), listed in Table 3.1. The helical MRI is an overstability, so the ansatz linear eigenvector we consider (Equation 3.27) is characterized by a complex temporal eigenvalue σ. For our fiducial parameters, the marginal mode has a frequency $\omega = 0.153$. This means that the helical MRI modes are traveling waves, moving in the z direction with a phase velocity ω/k_c.

At the conclusion of the weakly nonlinear analysis, we find that the coefficients of Equation 3.28 are complex. The marginal helical MRI is thus described by a complex GLE. This difference in character between the amplitude equations that modulate the weakly nonlinear standard and helical MRI is a consequence of the same property that makes the helical MRI an overstability. With the introduction of an azimuthal component, the background magnetic field acquires a handedness that is not present in a purely axial field. The helical MRI eigenvectors are therefore free to be out of phase with one another. In our perturbation series, the helical MRI modes interact within and between orders with modes which carry different phases, leading to complex GLE coefficients.

The phase dynamics of the complex GLE are well-studied in a variety of systems, and depend on the values of the GLE coefficients. The complex GLE may be unstable to traveling wave instabilities such as the Benjamin-Feir instability, a generalization of the Ekhaus instability. The complex GLE can also admit spatiotemporal chaos, and various classes of coherent structures (Aranson & Kramer 2002). Although a detailed description of the phase dynamics in the helical MRI is beyond the scope of this work, we note that such long-wavelength, long-timescale behavior may be observed in liquid metal helical MRI experiments.

3.5 Discussion

In this work we carry out a formal weakly nonlinear multiscale analysis of the MRI in a Taylor-Couette flow. We analyze both the standard and helical MRI, which differ only in the geometry of their imposed background magnetic fields. We find that the amplitude function, which governs the behavior of the system on long length- and timescales, obeys a real GLE for the case of the standard MRI, and a complex GLE for the helical MRI. These two systems are thus subject to different large-scale phase dynamics.

Our work should be placed in the broader context of emergent pattern formation in physical systems. The real Ginzburg-Landau equation derived here governs the slow-parameter evolution of the standard MRI close to threshold. The GLE arises in a number of other physical systems, and in each case it is a consequence not of the particular physics at hand, but of the underlying symmetries in the problem. Here we make a phenomenological comparison to two other systems that give rise to a GLE. The first and perhaps most famous is Rayleigh-Bénard convection, in which a fluid between two plates is heated from below (Newell & Whitehead 1969). If we take the plane of the fluid to be infinite in the horizontal plane, the system is initially translationally symmetric. At the onset of convection the system undergoes a symmetry breaking, forming rolls, or convection cells, which break the horizontal translational invariance. Analogously, the standard MRI system considered here is initially vertically translationally symmetric, because we idealize the TC device as an infinitely long cylinder. The MRI breaks this symmetry, forming cells along the vertical length of the domain. Just as Rayleigh-Bénard cells transport heat vertically, the MRI cells transport angular momentum horizontally. The symmetry breaking of each of these systems is described near onset by the real GLE.

A real GLE has also been found to describe the formation of zonal flows out of magnetized turbulence in a model system (Parker & Krommes 2013, 2017). Zonal flows are axisymmetric structures, large-scale and long-lived, which form spontaneously out of turbulence. They have recently been observed in some numerical studies of the MRI, and have generated considerable interest for their possible role in planet formation in protoplanetary disks (Johansen et al. 2009; Kunz & Lesur 2013). The present work is of course an idealized geometry, and we make no attempt to model a realistic protoplanetary disk environment. However, it is worth noting that the GLE we derive implies that axisymmetric, large-scale, long-lived structures are a generic feature of the MRI in the weakly nonlinear regime. This work provides a mathematical description of the MRI as a pattern-forming process, but much remains to be understood, particularly involving the application of this model system to realistic astrophysical disks. Chapter 2 establishes that the GLE will arise in the shearing box approximation in the presence of ambipolar diffusion, and this work demonstrates that the pattern-forming behavior is not an artifact of the local geometry. The stage is thus set to apply this theory to more astrophysical conditions in either the global geometry or a local approximation. Of course our current model is most directly relevant to TC flows, and we emphasize that laboratory MRI experiments stand poised to observe the MRI-driven pattern formation predicted here.

We detail several avenues for future work, which highlight the application of this theory to both laboratory experiments and astrophysical disks:

- Our theory may be applied to a specific experimental apparatus to model the predicted saturated state. One can then ask whether GLE dynamics should be detectable, especially over endcap-driven flows.
- The saturation properties of different rotation profiles may be compared by direct application of the theory developed here.
- Vertical stratification may be added to the base state, constructing a more realistic model of global vertical disk structure.
- Other nonideal MHD effects such as the Hall effect and ambipolar diffusion are straightforward additions to this model, and are of particular interest for understanding protoplanetary disks.
- The background magnetic field geometry may be generalized to include radial variation, another feature relevant to astrophysical disks.
- The radial boundary conditions considered here may be expanded to mimic astrophysical disks rather than TC devices.
- Our theory can be compared to simulations in both the weakly and strongly nonlinear regimes: both the pattern selection at saturation and the $\mathrm{Pm}^{0.777}$ scaling can be directly tested.

This is the first weakly nonlinear analysis of the MRI in a cylindrical geometry, and is thus the global analogue of similar analyses in local approximations (Umurhan et al. 2007b; Vasil 2015). Understanding the connection between local and global MRI modes is crucial for interpreting simulation results across domain geometries. (The relationship between local and global *linear* MRI modes is investigated in Latter et al. 2015.) Phenomena such as saturation and the development of turbulence depend critically on the nature of the underlying MRI modes. The formalism presented here describes analytically the weakly nonlinear behavior of global MRI modes. This treatment should be expanded to encompass more astrophysically relevant conditions, so that our understanding of complicated MRI phenomena may continue to make contact with analytical theory.

Acknowledgments

S.E.C. was supported by a National Science Foundation Graduate Research Fellowship under grant No. DGE-16-44869. J.S.O. acknowledges support from NASA grant NNX16AC92G. We thank the anonymous referee for many thoughtful comments. We also thank Mordecai Mac Low, Jeremy Goodman, John Krommes, Geoff Vasil, and Ellen Zweibel for useful discussion.

3.A Detailed Equations

Here we detail the perturbation analysis described in Section 3.3. The perturbation series is described by Equations 3.24 - 3.26, where

$$\mathcal{L} = \mathcal{L}_0 + \mathcal{L}_1\partial_z + \mathcal{L}_2\partial_z^2 + \mathcal{L}_3\partial_z^3 + \mathcal{L}_4\partial_z^4, \tag{3.30}$$

$$\widetilde{\mathcal{L}}_1 = \mathcal{L}_1 + 2\mathcal{L}_2\partial_z + 3\mathcal{L}_3\partial_z^2 + 4\mathcal{L}_4\partial_z^3 \tag{3.31}$$

$$\widetilde{\mathcal{L}}_2 = \mathcal{L}_2 + 3\mathcal{L}_3\partial_z + 6\mathcal{L}_4\partial_z^2 \tag{3.32}$$

$$\widetilde{\mathcal{G}} = \mathcal{G}\partial_z + \mathcal{L}_3\partial_z^3, \tag{3.33}$$

$$\widetilde{\mathcal{H}} = \mathcal{H}\partial_z, \tag{3.34}$$

and the constituent matrices are defined as

$$\mathcal{L}_0 = \begin{bmatrix} \mathcal{L}_0^{\Psi\Psi} & 0 & 0 & 0 \\ 0 & -\tfrac{1}{\mathrm{Re}}(\partial_r^2 + \tfrac{1}{r}\partial_r - \tfrac{1}{r^2}) & 0 & 0 \\ 0 & 0 & -\tfrac{1}{\mathrm{Rm}}(\partial_r^2 - \tfrac{1}{r}\partial_r) & 0 \\ 0 & 0 & 0 & -\tfrac{1}{\mathrm{Rm}}(\partial_r^2 + \tfrac{1}{r}\partial_r - \tfrac{1}{r^2}) \end{bmatrix} \tag{3.35}$$

where

$$\mathcal{L}_0^{\Psi\Psi} = -\frac{1}{\mathrm{Re}}(-\frac{3}{r^4}\partial_r + \frac{3}{r^3}\partial_r^2 - \frac{2}{r^2}\partial_r^3 + \frac{1}{r}\partial_r^4), \tag{3.36}$$

$$\mathcal{L}_1 = \begin{bmatrix} 0 & -\tfrac{2}{r}u_0 & \mathrm{Co}(\tfrac{1}{r^2}\partial_r - \tfrac{1}{r}\partial_r^2) & 0 \\ \tfrac{1}{r^2}u_0 + \tfrac{1}{r}\partial_r u_0 & 0 & 0 & -\mathrm{Co} \\ -1 & 0 & 0 & 0 \\ 0 & -1 & \tfrac{1}{r^2}u_0 - \tfrac{1}{r}\partial_r u_0 & 0 \end{bmatrix} \tag{3.37}$$

$$\mathcal{L}_2 = \begin{bmatrix} -\tfrac{1}{\mathrm{Re}}(-\tfrac{2}{r^2}\partial_r + \tfrac{2}{r}\partial_r^2) & 0 & 0 & 0 \\ 0 & -\tfrac{1}{\mathrm{Re}} & 0 & 0 \\ 0 & 0 & -\tfrac{1}{\mathrm{Rm}} & 0 \\ 0 & 0 & 0 & -\tfrac{1}{\mathrm{Rm}} \end{bmatrix} \tag{3.38}$$

$$\mathcal{L}_3 = \begin{bmatrix} 0 & 0 & -\mathrm{Co}\frac{1}{r} & 0 \\ 0 & 0 & 0 & 0 \\ 0 & 0 & 0 & 0 \\ 0 & 0 & 0 & 0 \end{bmatrix} \tag{3.39}$$

$$\mathcal{L}_4 = \begin{bmatrix} -\frac{1}{\mathrm{Re}}\frac{1}{r} & 0 & 0 & 0 \\ 0 & 0 & 0 & 0 \\ 0 & 0 & 0 & 0 \\ 0 & 0 & 0 & 0 \end{bmatrix} \tag{3.40}$$

$$\mathcal{G} = \begin{bmatrix} 0 & 0 & \mathrm{Co}(\frac{1}{r^2}\partial_r - \frac{1}{r}\partial_r^2) & 0 \\ 0 & 0 & 0 & -\mathrm{Co} \\ -1 & 0 & 0 & 0 \\ 0 & -1 & 0 & 0 \end{bmatrix} \tag{3.41}$$

$$\mathcal{H} = \begin{bmatrix} 0 & 0 & 0 & \mathrm{Co}\frac{2}{r^2} \\ 0 & 0 & 0 & 0 \\ 0 & 0 & 0 & 0 \\ -\frac{2}{r^3} & 0 & 0 & 0 \end{bmatrix} \tag{3.42}$$

$$\mathcal{D} = \begin{bmatrix} \frac{1}{r}\partial_r^2 + \frac{1}{r}\partial_z^2 - \frac{1}{r^2}\partial_r & 0 & 0 & 0 \\ 0 & 1 & 0 & 0 \\ 0 & 0 & 1 & 0 \\ 0 & 0 & 0 & 1 \end{bmatrix}. \tag{3.43}$$

We solve the $\mathcal{O}(\epsilon)$ (linear) system, followed by the $\mathcal{O}(\epsilon^2)$ system in Equation 3.25. At second order in ϵ, nonlinear terms arise which are formed by the interaction of first-order

MRI modes with themselves and their complex conjugates. This mode interaction means that the second-order nonlinear term is

$$\mathbf{N}_2 = |\alpha|^2 \mathbf{N}_{20} + \alpha^2 \mathbf{N}_{22} e^{2ik_c z}, \tag{3.44}$$

where terms are grouped by z-dependence. See Appendix 3.B for the full form of the nonlinear terms. Equation 3.25 must therefore be solved as three separate systems of equations, one for each possible z resonance:

$$\mathcal{L}\mathbf{V}_{20} + \xi \partial_z \mathcal{H} \mathbf{V}_{20} = \mathbf{N}_{20} \tag{3.45}$$

$$\mathcal{L}\mathbf{V}_{21} + \xi \partial_z \mathcal{H} \mathbf{V}_{21} = -\widetilde{\mathcal{L}}_1 \partial_Z \mathbf{V}_{11} - \xi \partial_Z \mathcal{H} \mathbf{V}_{11} \tag{3.46}$$

$$\mathcal{L}\mathbf{V}_{22} + \xi \partial_z \mathcal{H} \mathbf{V}_{22} = \mathbf{N}_{22} \tag{3.47}$$

To find a bounded solution at $\mathcal{O}(\epsilon^3)$ we must eliminate secular terms: terms which are resonant with the solution to the linear homogenous equation $(\mathcal{L} + \xi \widetilde{\mathcal{H}})\mathbf{V} = 0$ and cause the solution to grow without bound. Secular terms in our system are those that are resonant with the linear ansatz (Equation 3.27), i.e. terms with $e^{ik_c z}$ z-dependence. To eliminate these terms we enforce a solvability condition, which arises from a corollary to the Fredholm alternative. The Fredholm alternative states that if we consider a system of equations $\mathcal{L}\mathbf{V} = \mathbf{b}$ and its adjoint homogenous system $\mathcal{L}^\dagger \mathbf{V}^\dagger = 0$, only one of two conditions holds. Either there exists one and only one solution to the nonhomogenous system, or the homogenous adjoint equation has a nontrivial solution. The relevant corollary arises as a consequence of the second condition: if $\mathcal{L}^\dagger \mathbf{V}^\dagger = 0$ has a nontrivial solution, then $\mathcal{L}\mathbf{V} = \mathbf{b}$ has a solution if and only if $\langle \mathbf{V}^\dagger | b \rangle = 0$.

We define the adjoint operator $\mathcal{L}^\dagger$ and solution $\mathbf{V}^\dagger$ as

$$\langle \mathbf{V}^\dagger | (\mathcal{L} + \xi \widetilde{\mathcal{H}}) \mathbf{V} \rangle = \langle (\mathcal{L}^\dagger + \xi \widetilde{\mathcal{H}}^\dagger) \mathbf{V}^\dagger | \mathbf{V} \rangle, \tag{3.48}$$

where the inner product is defined as

$$\langle \mathbf{V}^\dagger | \mathcal{L} \mathbf{V} \rangle = \frac{k_c}{2\pi} \int_{-\pi/k_c}^{\pi/k_c} \int_{r_1}^{r_2} \mathbf{V}^{\dagger *} \cdot \mathcal{L} \mathbf{V} \, r \mathrm{d}r \mathrm{d}z \tag{3.49}$$

We derive the adjoint operator by successive integration by parts, to find

$$\mathcal{L}^\dagger = \mathcal{L}_0^\dagger - \partial_z \mathcal{L}_1^\dagger + d_z^2 \mathcal{L}_2^\dagger - \partial_z^3 \mathcal{L}_3^\dagger + \partial_z^4 L_4^\dagger \tag{3.50}$$

and

$$\mathcal{H}^\dagger = -d_z \mathcal{H}^{\mathrm{T}}, \tag{3.51}$$

where

$$\mathcal{L}_0^\dagger = \begin{bmatrix} \mathcal{L}_0^{\dagger,\Psi\Psi} & 0 & 0 & 0 \\ 0 & -\frac{1}{\mathrm{Re}}(\frac{1}{r}\partial_r + \partial_r^2 - \frac{1}{r^2}) & 0 & 0 \\ 0 & 0 & -\frac{1}{\mathrm{Rm}}(\frac{3}{r}\partial_r + \partial_r^2) & 0 \\ 0 & 0 & 0 & -\frac{1}{\mathrm{Rm}}(\frac{1}{r}\partial_r + \partial_r^2 - \frac{1}{r^2}) \end{bmatrix}, \tag{3.52}$$

where

$$\mathcal{L}_0^{\dagger,\Psi\Psi} = -\frac{1}{\mathrm{Re}}(-\frac{3}{r^5} + \frac{3}{r^4}\partial_r - \frac{3}{r^3}\partial_r^2 + \frac{2}{r^2}\partial_r^3 + \frac{1}{r}\partial_r^4), \tag{3.53}$$

$$\mathcal{L}_1^\dagger = \begin{bmatrix} 0 & \frac{1}{r^2}u_0 + \frac{1}{r}\partial_r u_0 & -1 & 0 \\ -\frac{2}{r}u_0 & 0 & 0 & -1 \\ \mathrm{Co}(\frac{1}{r^3} - \frac{1}{r^2}\partial_r - \frac{1}{r}\partial_r^2) & 0 & 0 & \frac{1}{r^2}u_0 - \frac{1}{r}\partial_r u_0 \\ 0 & -\mathrm{Co} & 0 & 0 \end{bmatrix}, \tag{3.54}$$

$$\mathcal{L}_2^\dagger = \begin{bmatrix} -\frac{1}{\mathrm{Re}}(-\frac{2}{r^3} + \frac{2}{r^2}\partial_r + \frac{2}{r}\partial_r^2) & 0 & 0 & 0 \\ 0 & -\frac{1}{\mathrm{Re}} & 0 & 0 \\ 0 & 0 & -\frac{1}{\mathrm{Rm}} & 0 \\ 0 & 0 & 0 & -\frac{1}{\mathrm{Rm}} \end{bmatrix}, \tag{3.55}$$

and $\mathcal{L}_3^\dagger = \mathcal{L}_3^{\mathrm{T}}$, $\mathcal{L}_4^\dagger = \mathcal{L}_4^{\mathrm{T}}$. The adjoint boundary conditions are selected to satisfy Equation 3.49, and differ depending on the boundary conditions enforced on the homogenous system. Specifically, the boundary conditions arise from the requirement that the integrands in Equation 3.49 are zero at r_1 and r_2. For the conducting boundary conditions we apply to the standard MRI, the adjoint equation

$$(\mathcal{L}^\dagger + \xi\widetilde{\mathcal{H}}^\dagger)\mathbf{V}^\dagger = 0 \tag{3.56}$$

must be solved subject to the boundary conditions

$$\Psi^\dagger = \partial_r\Psi^\dagger = u^\dagger = A^\dagger = \partial_r(rB^\dagger) = 0. \tag{3.57}$$

For the insulating case, the adjoint boundary conditions are

$$k\frac{I_0(kr)}{I_1(kr)}rA^\dagger - 2A^\dagger - r\partial_r A^\dagger = 0 \text{ at } r = r_1 \tag{3.58}$$

$$-k\frac{K_0(kr)}{K_1(kr)}rA^\dagger - 2A^\dagger - r\partial_r A^\dagger = 0 \text{ at } r = r_2 \tag{3.59}$$

We take the inner product of the adjoint homogenous solution with the terms in Equation 3.26 that are resonant with e^{ik_cz}. This gives us

$$\begin{aligned}&\langle \mathbb{V}^\dagger|\mathcal{D}\mathbb{V}_{11}\rangle\partial_T\alpha + \langle \mathbb{V}^\dagger|\widetilde{\mathcal{G}}\mathbb{V}_{11} + \xi\widetilde{\mathcal{H}}\mathbb{V}_{11}\rangle\alpha + \langle \mathbb{V}^\dagger|\widetilde{\mathcal{L}}_1\mathbb{V}_{21} + \widetilde{\mathcal{L}}_2\mathbb{V}_{11} + \xi\mathcal{H}\mathbb{V}_{21}\rangle\partial_Z^2\alpha\\ &= \langle \mathbb{V}^\dagger|\mathbf{N}_{31}\rangle\alpha|\alpha|^2,\end{aligned} \tag{3.60}$$

or Equation 3.28, the Ginzburg-Landau Equation, where the coefficients are

$$b = \langle \mathbb{V}^\dagger|\widetilde{\mathcal{G}}\mathbb{V}_{11} + \xi\widetilde{\mathcal{H}}\mathbb{V}_{11}\rangle/\langle \mathbb{V}^\dagger|\mathcal{D}\mathbb{V}_{11}\rangle, \tag{3.61}$$

$$h = \langle \mathbb{V}^\dagger|\widetilde{\mathcal{L}}_1\mathbb{V}_{21} + \widetilde{\mathcal{L}}_2\mathbb{V}_{11} + \xi\mathcal{H}\mathbb{V}_{21}\rangle/\langle \mathbb{V}^\dagger|\mathcal{D}\mathbb{V}_{11}\rangle, \tag{3.62}$$

and

$$c = \langle \mathbb{V}^\dagger|\mathbf{N}_{31}\rangle/\langle \mathbb{V}^\dagger|\mathcal{D}\mathbb{V}_{11}\rangle. \tag{3.63}$$

3.B Nonlinear Terms

Here we detail the perturbative expansion of the nonlinear vector $\mathbf{N}$ in Equation 3.22,

$$\mathbf{N} = \epsilon^2\mathbf{N}_2 + \epsilon^3\mathbf{N}_3. \tag{3.64}$$

The nonlinear terms are as follows.

$$\begin{aligned}N_2^\Psi =& - J(\Psi_1, \frac{1}{r^2}\nabla^2\Psi_1) - J(\Psi_1, -\frac{2}{r^3}\partial_r\Psi_1) + \mathrm{Co}J(A_1, \frac{1}{r^2}\nabla^2 A_1)\\ &+ \mathrm{Co}J(A_1, -\frac{2}{r^3}\partial_r A_1) + \frac{2}{r}u_1\partial_z u_1 - \mathrm{Co}\frac{2}{r}B_1\partial_z B_1\end{aligned} \tag{3.65}$$

$$N_2^u = -\frac{1}{r}J\left(\Psi_1, u_1\right) + \frac{1}{r}\mathrm{Co}J\left(A_1, B_1\right) - \frac{1}{r^2}u_1\partial_z\Psi_1 + \mathrm{Co}\frac{1}{r^2}B_1\partial_z A_1 \tag{3.66}$$

$$N_2^A = \frac{1}{r}J\left(A_1, \Psi_1\right) \tag{3.67}$$

$$N_2^B = \frac{1}{r}J\left(A_1, u_1\right) - \frac{1}{r}J\left(\Psi_1, B_1\right) + \frac{1}{r^2}B_1\partial_z\Psi_1 - \frac{1}{r^2}u_1\partial_z A_1 \tag{3.68}$$

$$\begin{aligned}N_3^\Psi =& - J(\Psi_1, \frac{1}{r^2}\nabla^2\Psi_2) - J(\Psi_2, \frac{1}{r^2}\nabla^2\Psi_1) - 2J(\Psi_1, \frac{1}{r^2}\partial_Z\partial_z\Psi_1) - J(\Psi_1, -\frac{2}{r^3}\partial_r\Psi_2)\\ &- J(\Psi_2, -\frac{2}{r^3}\partial_r\Psi_1) - \widetilde{J}(\Psi_1, \frac{1}{r^2}\nabla^2\Psi_1) - \widetilde{J}(\Psi_1, -\frac{2}{r^3}\partial_r\Psi_1) + \mathrm{Co}J(A_1, \frac{1}{r^2}\nabla^2 A_2)\\ &+ \mathrm{Co}J(A_2, \frac{1}{r^2}\nabla^2 A_1) + 2\mathrm{Co}J(A_1, \frac{1}{r^2}\partial_Z\partial_z A_1) + \mathrm{Co}J(A_1, -\frac{2}{r^3}\partial_r A_2)\\ &+ \mathrm{Co}J(A_2, -\frac{2}{r^3}\partial_r A_1) + \mathrm{Co}\widetilde{J}(A_1, \frac{1}{r^2}\nabla^2 A_1) + \mathrm{Co}\widetilde{J}(A_1, -\frac{2}{r^3}\partial_r A_1) + \frac{2}{r}u_1\partial_z u_2\\ &+ \frac{2}{r}u_2\partial_z u_1 + \frac{2}{r}u_1\partial_Z u_1 - \mathrm{Co}\frac{2}{r}B_1\partial_z B_2 - \mathrm{Co}\frac{2}{r}B_2\partial_z B_1 - \mathrm{Co}\frac{2}{r}B_1\partial_Z B_1\end{aligned} \tag{3.69}$$

$$\begin{aligned}N_3^u =& - \frac{1}{r}J\left(\Psi_1, u_2\right) - \frac{1}{r}J\left(\Psi_2, u_1\right) - \frac{1}{r}\widetilde{J}\left(\Psi_1, u_1\right) + \frac{1}{r}\mathrm{Co}J\left(A_1, B_2\right) + \frac{1}{r}\mathrm{Co}J\left(A_2, B_1\right)\\ &+ \frac{1}{r}\mathrm{Co}\widetilde{J}\left(A_1, B_1\right) - \frac{1}{r^2}u_1\partial_z\Psi_2 - \frac{1}{r^2}u_2\partial_z\Psi_1 - \frac{1}{r^2}u_1\partial_Z\Psi_1 + \mathrm{Co}\frac{1}{r^2}B_1\partial_z A_2\\ &+ \mathrm{Co}\frac{1}{r^2}B_2\partial_z A_1 + \mathrm{Co}\frac{1}{r^2}B_1\partial_Z A_1\end{aligned} \tag{3.70}$$

$$N_3^A = \frac{1}{r}J\left(A_1, \Psi_2\right) + \frac{1}{r}J\left(A_2, \Psi_1\right) + \frac{1}{r}\widetilde{J}\left(A_1, \Psi_1\right) \tag{3.71}$$

$$
\begin{aligned}
N_3^B =& \frac{1}{r}J\left(A_1, u_2\right) + \frac{1}{r}J\left(A_2, u_1\right) + \frac{1}{r}\widetilde{J}\left(A_1, u_1\right) + \frac{1}{r}J\left(B_1, \Psi_2\right) + \frac{1}{r}J\left(B_2, \Psi_1\right) + \frac{1}{r}\widetilde{J}\left(B_1, u_1\right) \\
&+ \frac{1}{r^2}B_1\partial_z\Psi_2 + \frac{1}{r^2}B_2\partial_z\Psi_1 + \frac{1}{r^2}B_1\partial_Z\Psi_1 - \frac{1}{r^2}u_1\partial_z A_2 - \frac{1}{r^2}u_2\partial_z A_1 - \frac{1}{r^2}u_1\partial_Z A_1 \quad (3.72)
\end{aligned}
$$

Chapter 4

Magnetically Aligned HI Fibers and the Rolling Hough Transform

4.1 Introduction

Magnetic fields, radiation, turbulence, and cosmic rays are major players that mold the diffuse interstellar medium (ISM). The prevalence of starlight photons and cosmic rays partially ionizes the largely neutral medium, and causes magnetic fields and gas to move together (i.e., flux freezing). We therefore expect the geometry and strength of the interstellar magnetic field to affect the shape of the ISM. Studies of the magnetic field in diffuse HI (n $\sim$ 0.1 - 100 cm^{-3}) suggest that the field strength is relatively independent of volume density, in contrast to magnetic fields in molecular clouds (e.g. Heiles & Crutcher 2005). The role of magnetic fields in molecular cloud and star formation is an area of active research (see Crutcher 2012, for a recent review). A better understanding of the magnetic structure of the diffuse ISM, the medium from which denser structures form, may elucidate the processes at work on all

---

This section contains text from an article published in the Astrophysical Journal (Clark et al. 2014).

scales.

Sensitive, high spatial dynamic range HI observations allow us to observe the structure of the diffuse ISM in unprecedented detail. These observations have resolved the previously "blobby" ISM into a complex network of filaments, clumps, and shells. Even a cursory inspection of these data indicates that the ISM is not a simple, self-similar, turbulent medium easily described by a few parameters, but rather an enormously complex structure affected by many discrete processes on a wide range of scales. Traditionally, such features within the ISM have been identified by eye (e.g. McClure-Griffiths 2006; Begum et al. 2010), though there have been some attempts to automate the process for relatively simple structures (e.g. Saul et al. 2012). Many numerical investigations of ISM data have revolved around functions that either strip out Fourier phase information and rely heavily on power spectra, or examine the hierarchical clustering of gas (e.g. Burkhart & Lazarian 2011). Some work has been done to build metrics that quantify morphology (Adams 1992; Khalil et al. 2004; Robitaille et al. 2010), though these metrics are designed to be general, rather than to capture information about specific observed features. There are very few methods that have quantified shape information in the ISM and use it as a predictor of an underpinning physical property.

The Galactic Arecibo L-Band Feed Array HI (GALFA-HI) Survey is mapping 13,000 square degrees of sky at 4′ resolution. At this high spatial resolution, we observe that the diffuse, high-latitude HI is organized into high aspect ratio structures we call fibers (Figure 4.1). We often find them in groups largely parallel to each other. We use the term "fibers" to evoke the slender, parallel nature of these HI features. They are visually similar to slender molecular fibers identified in star forming regions (e.g. André et al. 2013; Hacar et al. 2013). While the term "filaments" is used in the literature to describe a wide range of linear structure, we reserve it in this work to refer to networks of gravitationally bound structures found by other authors.

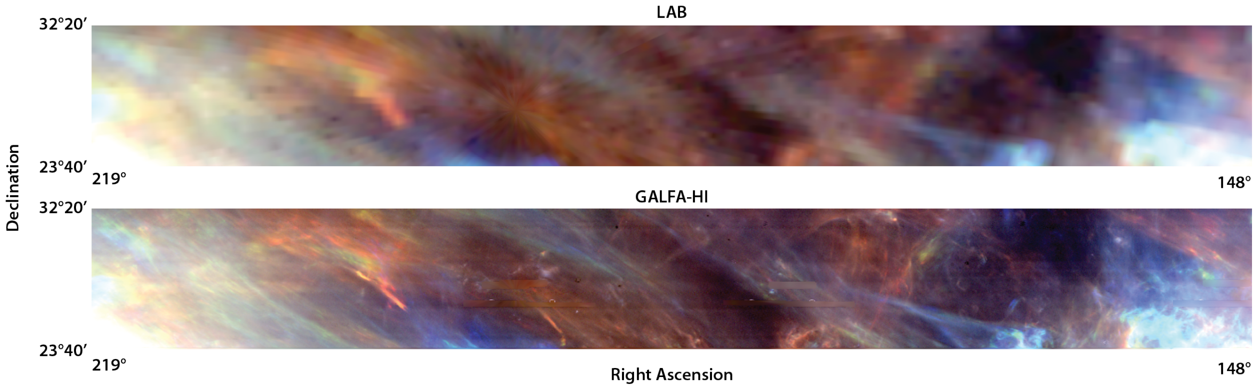

Figure 4.1: HI data at high Galactic latitude. Top panel is taken from the 36′ resolution Leiden-Argentina-Bonn survey (Kalberla et al. 2005, LAB), bottom panel from a section of the 4′ resolution GALFA-HI DR1 data analyzed in this work. Red, blue, and green channels represent -7 to -4 km s^{-1}, -3 to -1 km s^{-1}, and 0 to 3 km s^{-1}, respectively. Brightnesses are shown in a logarithmic stretch in brightness temperature from 0.5 K (dark) to 5 K (light), or an HI column density range of 3×10^{18} cm^{-2} to 3×10^{19} cm^{-2}. The slender fiber features can be seen in the bottom panel but are washed out by low resolution of the LAB survey in the top panel.

Why does such striking linear structure pervade the high-latitude ISM? The elongation we see in these fibers suggests that magnetic fields may play a crucial role in determining the structure of the diffuse ISM. In this work we explore the correlation between the orientation of the magnetic field, as traced by starlight polarization, and the orientation of these gaseous fibers. Starlight polarization traces the orientation of the plane-of-sky magnetic field because the starlight is polarized by magnetically aligned interstellar grains (Goldsmith et al. 2008). To examine this correlation quantitatively, we require a method for detecting and parameterizing linear structure. In Section 4.2 we develop a machine vision algorithm, the Rolling Hough Transform (RHT), designed for this purpose. This powerful new technique allows us to quantify the alignment of HI fibers with the magnetic field using diagnostics we develop in Section 4.3. In Section 4.4 we detail the data used in this study. We investigate the gas-magnetic field alignment in diffuse HI in Section 4.5, and apply the same analysis to the Riegel-Crutcher HI self-absorption feature in Section 4.6. The success of the RHT at mapping the detailed structure of the magnetic field in the Riegel-Crutcher cloud suggests a technique for resolved field strength estimation, which we propose in Section 4.7. We discuss the implications of the work in Section 4.8 and conclude with a summary and prospects for future work in Section 4.9.

4.2 The Rolling Hough Transform (RHT)

The detection of astronomical linear structure is approached in various ways depending on the context. In cosmic web data, filaments are described as structures linking local density maxima (e.g. the DisPerSE method of Sousbie (2011) and the SHMAFF method of Bond et al. (2010)). DisPerSE has also been used in the context of filaments in the molecular ISM, as in the *Herschel* filaments analyzed in Arzoumanian et al. (2011). A rich methodology for linear and curvilinear feature detection has been developed for analysis of solar data (see Aschwanden (2009) for a broad review of solar image processing and feature detection). The curvelet transform as described by Starck et al. (2003) has been used across a number of sub-disciplines to highlight and enhance linear features in astronomical images. Hennebelle (2013) uses the inertia matrix to isolate filaments in simulation data.

We wish to quantify the linearity and spatial coherence of HI structures. Because these structures are not objects with distinct boundaries (see Figure 4.1), we are tackling a problem that is fundamentally different from solar feature detection and filament identification. Additionally, the filament detection algorithms used in solar observations (and Starck et al. 2003) report images as their results, which do not directly produce a quantitative measure of linearity in the image. As these diffuse HI fibers were not formed by gravitational forces, there is no reason to require that they must be, or bridge, local overdensities. Indeed, we find the fibers often to be in groups of parallel structures, very unlike the cosmic web. Thus, methods developed for gravitationally-dominated systems are not optimal for our purposes.

The RHT is, as its name suggests, a modification of the Hough transform. The Hough transform was first introduced in a patent for the detection of complex patterns in bubble chamber photographs (Hough 1962). It was soon recognized as a powerful line detection technique, and has found wide applications in image processing and machine vision (for an excellent review, see Illingworth and Kitler 1988). The adaption of the Hough transform described here is a rolling version that is particularly well suited to the detection and quantization of specific linear features in astronomical data. The RHT does not merely identify fibers; it encodes the probability that any given image pixel is part of a coherent linear structure. This allows the user to quantify the linearity of regions of sky without specifying fibers as discrete entities.

4.2.1 RHT procedure

The RHT operates on two-dimensional data and is designed to be sensitive to linear structure irrespective of the overall brightness of the region. The first step is to unsharp mask the image. The image is convolved with a two-dimensional top-hat smoothing kernel of a user-defined diameter, D_K (Figure 4.2, step 1). The smoothed data is then subtracted from the original data (Figure 4.2, step 2), and the resulting map is thresholded at 0 to obtain a bitmask (Figure 4.2, step 3). The subtraction of the smoothed component can be considered a suppression of large-scale structure, or a high-pass Fourier filter.

Our implementation of the Hough transform follows that of Duda and Hart (1972), where a straight line is parameterized in terms of the angle θ of its normal, and its minimum Euclidean distance from the origin, ρ:

$$\rho = x \cos\theta + y \sin\theta. \tag{4.1}$$

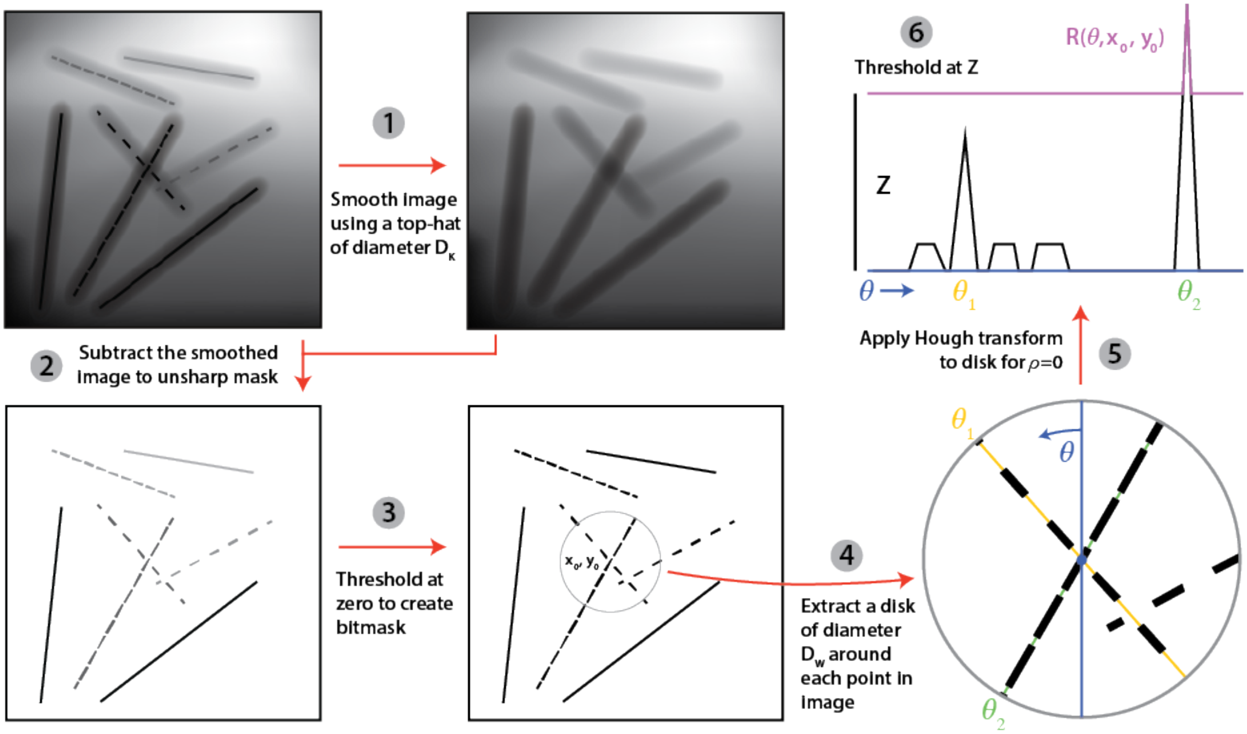

Figure 4.2: A diagram of the RHT procedure (Section 4.2.1). Steps 1-3 are preprocessing of the image. Step 4 shows the selection of a disk of diameter D_W. This window rolls across the data, centered on each pixel in turn. Step 5 shows the Hough transform applied to cartoon data, and step 6 illustrates that only data above a defined threshold is recorded. Note that this cartoon data contains three linear features, two of which (green and yellow) are centered on the selected window center (x_0, y_0), and contribute the most intensity to the Hough transform. The dashed lines are representative of different levels of coherence in the data. Here, only the green line (with $\theta = \theta_2$ orientation) has RHT intensity $R(\theta, x_0, y_0)$ over the threshold Z.

This parameterization avoids the computationally problematic singularities that can arise in a point-slope description of a line.

Every possible line in the image space is uniquely specified by a point in the ρ-θ space. The standard Hough transform maps each (x, y) pixel in the image space to all $(\rho,\ \theta)$ line parameters possible for that pixel in the ρ-θ space. The Hough transform is thus a one-to-many mapping between image space and parameter space. The Hough transform stores in a $(\rho,\ \theta)$ "accumulator array" the number of "on" pixels in image space that contribute to each pixel in the ρ-θ space. All values in the $(\rho,\ \theta)$ accumulator array over a set threshold are then identified as a line in the image space.

The RHT performs a similar mapping from image space to parameter space, with several key differences. The RHT mapping is performed on a circular domain, diameter D_W, centered on each image-space pixel (x_0, y_0) in turn (Figure 4.2, step 4). Then a Hough transform is performed on this area, limited to $\rho = 0$ (Figure 4.2, step 5). Thus the ρ-θ space is reduced to a one-dimensional space on θ for each pixel. All intensity over a set intensity threshold Z is stored as $R(\theta, x_0, y_0)$: RHT intensity as a function of θ for that pixel (Figure 4.2, step 6). Z is a percentage. In every direction θ, $Z \times D_W$ pixels must contain signal in order for the transform to record the data in that direction. We use the canonical binning for the number of theta bins:

$$n_\theta = \left\lceil \pi \frac{\sqrt{2}}{2} \left(D_W - 1 \right) \right\rceil \tag{4.2}$$

The mapping of each pixel in the circular region to the reduced domain $(\rho = 0,\ \theta)$ is defined by the Hough transform. As the Hough transform is distributive over image coadditon, we tabulate this mapping in advance for each pixel within the circular region to optimize the RHT. By iterating ("rolling") over the entire image space we produce the RHT output, $R\left(\theta, x, y\right)$. A visualization of the linear structures identified by the RHT, the backprojection

$R\,(x, y)$, is obtained by integrating $R(\theta, x, y)$ over θ:

$$R(x, y) = \int R(\theta, x, y)\, d\theta. \tag{4.3}$$

The bottom panels of Figures 4.7 and 4.8 show RHT backprojections.

4.2.2 Parameter space

One advantage of the RHT is that the input parameters of the transform can be chosen to highlight specific linear features of interest. One defines, for a given run of the RHT, a smoothing kernel diameter (D_K), window diameter (D_W), and intensity threshold (Z), as described above. The rolling nature of the RHT ensures that linear structure at least as long as D_W will be identified. Thus D_W, along with the Z, sets a lower limit for the spatial length of the linear features. Thresholding below 100% ($Z < 1$) reflects the fact that structures can be physically coherent even if they are not visibly connected (see Figure 4.2). With Galactic HI data we have radial velocity as well as spatial information, so we choose a specific velocity (v) and velocity range (δv) to generate an image on which to run the RHT.

4.3 RHT-starlight polarization methods

We describe two metrics for quantifying the degree of alignment between RHT output, hereafter $R(\theta, x, y)$, and starlight polarization angle, hereafter $\theta^\star$. $R(\theta, x, y)$ is intensity as a function of angle on a domain $\theta \in [0, \pi)$, as a 0° orientation is equivalent to a 180° orientation. Similarly, 0° and 180° are equivalent starlight polarization angles.

In what follows, we sample $R(\theta, x, y)$ in a circular region around each star in the field:

$$R_\star(\theta) = \iint\limits_{disk} R(\theta, x, y)\, dxdy. \tag{4.4}$$

We visualize this on a half-polar plot, such that perfect alignment between $R_\star(\theta)$ and $\theta^\star$ lies at 0, and orthogonal alignment lies at $\theta = \pi/2$ or $-\pi/2$. This amounts to shifting $R_\star\left(\theta\right)$ to $R_\star\left(\phi\right)$, where:

$$\phi \equiv \theta - \theta^*, \tag{4.5}$$

and this subtraction occurs on the domain $\theta \in [0, \pi)$, such that $\phi \in [-\pi/2, \pi/2]$.

We are interested in the total $R_\star\left(\phi\right)$ of all stars in a field. We sum each star's $R_\star\left(\phi\right)$ and normalize by correcting for the total RHT intensity and the total area sampled, as follows:

$$\hat{R}\left(\phi\right) = \frac{\sum\limits_{n_\star} R_\star(\phi)}{\frac{1}{n_\theta}\int\limits_\theta\int\limits_x\int\limits_y R\left(\theta, x, y\right)\, d\theta dxdy}\left(\frac{\Omega}{n_\star \pi r^2}\right) \tag{4.6}$$

Where $n_\star$ is the number of stars sampled in the field, r is the sampling radius around each star, and Ω is the total area in the field.

4.3.1 RHT angle expectation value

In this section we describe a point estimator that quantifies the direction of a given region of $R(\theta)$. We choose the region $R_\star\left(\theta\right)$.

We compute the angle

$$\langle\theta_{RHT}\rangle' = \frac{1}{2}\arctan\left[\frac{\int \sin(2\theta) R_\star(\theta)\, d\theta}{\int \cos(2\theta) R_\star(\theta)\, d\theta}\right] \tag{4.7}$$

and find the equivalent value on the interval $\theta \in [0, \pi)$,

$$\langle \theta_{RHT} \rangle = \pi - \mathrm{mod}(\langle \theta_{RHT} \rangle' + \pi, \pi). \tag{4.8}$$

This is the RHT angle expectation value, a measure of the orientation of the gas around a particular star. To compare this to the starlight polarization angle $\theta^\star$, one can simply take the difference in the two values:

$$\langle \phi_{RHT} \rangle = \langle \theta_{RHT} \rangle - \theta^\star, \tag{4.9}$$

where, again, this subtraction must take place on the domain $\theta \in [0, \pi)$, such that $\langle \phi_{RHT} \rangle \in [-\pi/2, \pi/2]$. Thus, if $\langle \phi_{RHT} \rangle \simeq 0$, $R_\star(\theta)$ is well aligned with its starlight polarization angle.

4.3.2 RHT distribution widths

The RHT angle expectation value $\langle \theta_{RHT} \rangle$ is a useful metric for generalizing the orientation of the gas, but ignores all information about the strength and shape of $R_\star(\theta)$. A narrowly peaked $R_\star(\theta)$ and a much broader $R_\star(\theta)$ can have the same $\langle \theta_{RHT} \rangle$. Similarly, the amount of intensity detected by the RHT is ignored in calculating $\langle \theta_{RHT} \rangle$, which could be useful in determining the certainty of our angle estimation.

Another approach is to characterize the spread in the distribution. We report the interquartile range IQR($\hat{R}(\phi)$) as a metric for the width of $\hat{R}(\phi)$. One can also report the IQR of the $\langle \phi_{RHT} \rangle$ measures around all stars in a field, IQR($\langle \phi_{RHT} \rangle$).

We note that IQR($\hat{R}(\phi)$) and IQR($\langle \phi_{RHT} \rangle$) for a collection of stars are qualitatively different metrics. Assuming the linear structure is aligned with the magnetic field as traced by starlight polarization in a given region, the IQR($\langle \phi_{RHT} \rangle$) reports how accurately one could predict the starlight polarization angle for the given RHT data, independent of RHT intensity. The IQR($\hat{R}(\phi)$) is inherently biased toward higher RHT intensity, and thus is a measure of how well one could predict the starlight polarization angle weighted by RHT intensity. Thus, if the strength of the RHT is a measure of the reliability of our prediction of the starlight polarization angles, IQR($\hat{R}(\phi)$) will typically be narrower than IQR($\langle\phi_{RHT}\rangle$).

4.4 Data

We present an analysis of diffuse HI from two surveys, each sensitive to a broad range of spatial scales. The Galactic Arecibo L-Band Feed Array HI Survey (GALFA-HI; Peek et al. 2011a) maps 13,000 deg^2 with $4'$ spatial resolution, 0.18 km s^{-1} spectral resolution, and ~60 mK rms brightness temperature noise for a 1 km s^{-1} velocity bin. We analyze a region of sky with $115.0° \leq \text{RA} \leq 245.0°$, and $23.0° \leq \delta \leq 33.0°$: a 1,300 deg^2 region of sky relatively devoid of telescope scan artifacts in the first data release, DR1. This is a strip of sky from l, $b \sim (45°, 45°)$ to $(190°, 20°)$ that encompasses Galactic zenith. For GALFA-HI data we present an analysis of the velocity range from -7.0 km s^{-1} to -1.1 km s^{-1} where the fibers are most evident. We note that modifying this velocity range does not dramatically change the RHT-starlight polarization correlation.

The second survey we analyze is the Parkes Galactic All Sky Survey (GASS; McClure-Griffiths et al. 2009). GASS maps the southern celestial sky at all declinations $\delta \leq 1°$ with $16'$ spatial resolution, 1 km s^{-1} spectral resolution, and 57 mK rms brightness temperature noise per 1 km s^{-1} channel. We analyze the entire spatial area of GASS, excluding the region $|b| < 30°$ to remain focused on high latitude features. GASS data is analyzed from 1.6 km s^{-1} to 5.8 km s^{-1}. Again, the RHT-starlight polarization correlation is insensitive to the exact velocity range.

In addition to these two surveys, we present an analysis of an HI cold cloud in the Galactic plane with previously identified filaments in Section 4.6. Observations of the Riegel-Crutcher cloud were obtained by (McClure-Griffiths et al. 2006, hereafter McC-G06) as part of an extension to the Southern Galactic Plane Survey (McClure-Griffiths et al. 2005). The data have a resolution of $100''$ (0.06 pc at the 125 pc distance of the cloud) and a channel spacing of 0.82 km s^{-1}. The data are analyzed from +3.30 km s^{-1} to +7.42 km s^{-1}.

The starlight polarization data corresponding to the GASS survey area are from the Heiles (2000) compilation, an aggregation of starlight polarization catalogs that contains 9,286 stars. In the GALFA-HI region, the Heiles (2000) compilation is supplemented with stars from Berdyugin et al. (2001) and Berdyugin & Teerikorpi (2002) which catalog 336 stars and 116 stars in the region of the North Galactic Pole, respectively. In cases where the same star is measured in more than one catalog, we defer to the more modern measurement. All catalogs contain optical measurements of starlight polarization angles. We exclude any stars in the catalogs that were part of targeted polarization studies of clusters, in order to have a star sample that is well distributed across the sky. We did not apply a distance or polarization intensity cut for the stars used with GALFA-HI and GASS, though we did exclude stars with quoted errors on the starlight polarization angle greater than 25°. This leaves us with 153 stars in the GALFA-HI region, and 3,206 stars in the GASS region. The stars used in the GALFA-HI region have a median distance of 253 pc and an interquartile range of 133–442 pc. The stars used for the GASS correlation have a median distance of 1140 pc and an interquartile range of 291-2218 pc.

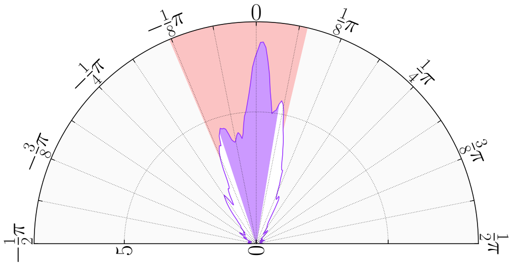

Figure 4.3: Integrated RHT output $\hat{R}\,(\phi)$ (see Section 4.3) for all stars in the GALFA-HI field (purple line). The velocity range is -7.0 km s^{-1} to -1.1 km s^{-1}, analyzed in two equal channels (see Section 4.5.1). The RHT was run with $(D_W, D_K, Z) = (100', 10', 70\%)$. $R(\theta, x, y)$ is sampled in regions of radius 0.5° around each star. IQR($\hat{R}\,(\phi)$) is 27° (purple shading). IQR($\langle\phi_{RHT}\rangle$) is 37° (red shading).

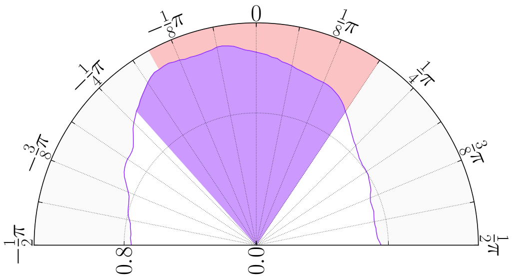

Figure 4.4: Same as Figure 4.3, but $\hat{R}\,(\phi)$ for all stars with $|b| > 30°$ in the GASS field. The RHT was run on data integrated over the velocity range 1.6 km s^{-1} to 5.8 km s^{-1}. The RHT was run with $(D_W, D_K, Z) = (245', 53', 70\%)$. $R(\theta, x, y)$ is sampled in regions of radius 2° around each star. IQR($\hat{R}\,(\phi)$) is 77° (purple shading). IQR($\langle\phi_{RHT}\rangle$) is 65° (red shading).

4.5 Fibers in diffuse HI

Fibers in the diffuse, high latitude HI are examined using the GALFA-HI and GASS data sets. We find that $\hat{R}\,(\phi)$ is well-centered on zero in both data sets, with IQR($\hat{R}\,(\phi)$) = 27° for GALFA-HI and 77° for GASS (Figures 4.3 and 4.4). These IQR($\hat{R}\,(\phi)$) are measured for $(D_W, D_K, Z) = (100', 10', 70\%)$ and sampling radius $r = 0.5°$ for GALFA-HI, and $(D_W, D_K, Z) = (245',\ 53',\ 70\%)$ and sampling radius $r = 2°$ for GASS. This correlation indicates that the magnetic field is indeed aligned with the observed fibers. This result is

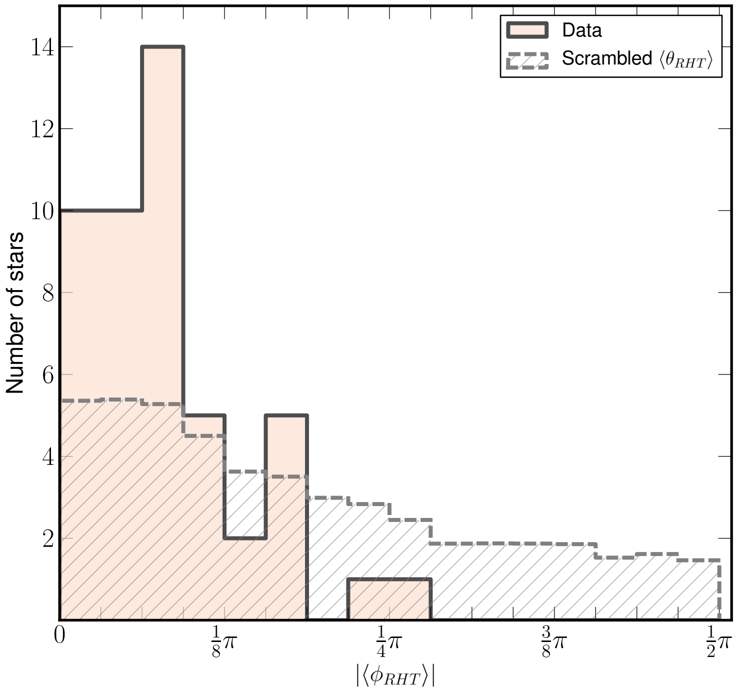

Figure 4.5: Histograms of the difference between the measured starlight polarization angle and the RHT angle expectation value for all GALFA-HI stars in the top quintile of RHT intensity (filled pink) and the same stars with scrambled $\langle\theta_{RHT}\rangle$ values (hatched grey). Scrambled histogram is an average of 10^4 random samples of $\langle\theta_{RHT}\rangle$. The RHT-starlight polarization correlation is highly statistically significant ($p < 0.0001$). See Section 4.5.2.

robust to variation in RHT parameters (see Figure 4.6).

The alignment between $R_\star(\theta)$ and $\theta^\star$ in both GASS and GALFA-HI data suggests that HI-magnetic field alignment is a pervasive feature of the high-latitude ISM. However, fibers are not a scale-independent feature of the ISM; detection of the HI-magnetic field alignment is much improved with better spatial resolution. By eye, and in the backprojection, the slender fibers in GALFA-HI (Figure 4.7) are largely absent from GASS (Figure 4.8). This point is echoed by our study of the Riegel-Crutcher cloud in Section 4.6.

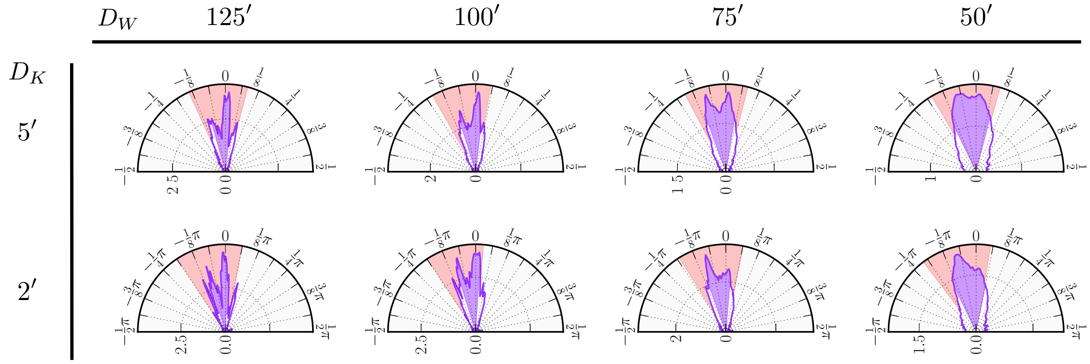

Figure 4.6: A sample of the parameter space for GALFA. Smoothing kernel diameter (D_K) and window diameter (D_W) are indicated. All runs use an intensity threshold $Z = 70\%$. Red shading indicates IQR($\langle\phi_{RHT}\rangle$), purple shading indicates IQR($\hat{R}\,(\phi)$).

4.5.1 Parameter space

We conduct a thorough exploration of the parameter space for the GALFA-Hɪ data. Rolling window diameters (D_W) from 50′ to 125′, smoothing kernel diameters (D_K) from 2′ to 10′, and intensity thresholds from Z = 50% to 90% (see Figure 4.2) were applied to the GALFA-Hɪ data. All combinations of parameters visually identify the same linear features in backprojection, and every $\hat{R}\,(\phi)$ displays a strong correlation with starlight polarization. This correlation is therefore robust to the variation of the RHT input parameters. Low intensity thresholds are computationally expensive because they require the storage of uniform background intensity. We select Z = 70% for the duration of this work because lower intensity thresholds find the same linear features but store too much low-intensity background. Variation of the sampling radius r does not significantly alter the observed RHT-starlight polarization correlation.

Figure 4.6 shows a representative sampling of the parameter space. We find that increasing D_W narrows IQR($\hat{R}\,(\phi)$), indicating that the longest, most linear features are the most well aligned with starlight polarization. However, IQR($\langle\phi_{RHT}\rangle$) remains consistent

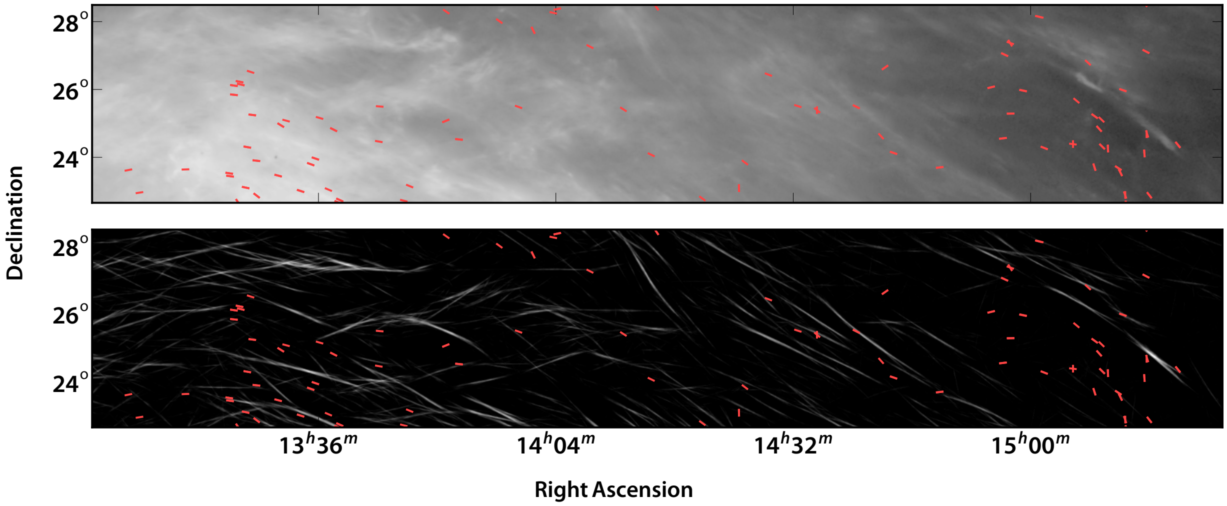

Figure 4.7: A representative region of the GALFA-HI data analyzed in Section 4.5, shown in HI emission (top) and RHT backprojection $R(x, y)$ (bottom; see Equation 4.3). The images are integrated over the velocity range -7.0 km s^{-1} to -1.1 km s^{-1}. Overlaid pseudovectors represent polarization angle measurements from the Heiles (2000), Berdyugin et al. (2001), and (Berdyugin & Teerikorpi 2002) catalogs. In the top panel, the intensity scale is linear in log(N_{HI}), where black represents a column density of 2×10^{18} cm^{-2}, and white is 2×10^{20} cm^{-2}.

across parameter space, as this metric gives equal weight to the RHT-starlight polarization alignment around each star, regardless of RHT intensity.

We also explore the effects of data channelization, δv. In the GASS data, we find the alignment is insensitive to whether we bin the data in advance of the RHT, or sum the $R_\star(\theta)$ from each channel. In the case of GALFA-HI, it is possible to bin the data so finely (0.18 km s^{-1}) that noise washes out the observed fibers, or to integrate over so many channels that fibers are less visually evident. In these cases the signal is detectably diminished. We split the velocity range -7.0 km s^{-1} to -1.1 km s^{-1} into two channels, run the RHT on each, and sum the $R_\star(\theta)$ from each channel, though the result is not sensitive to the exact channelization.

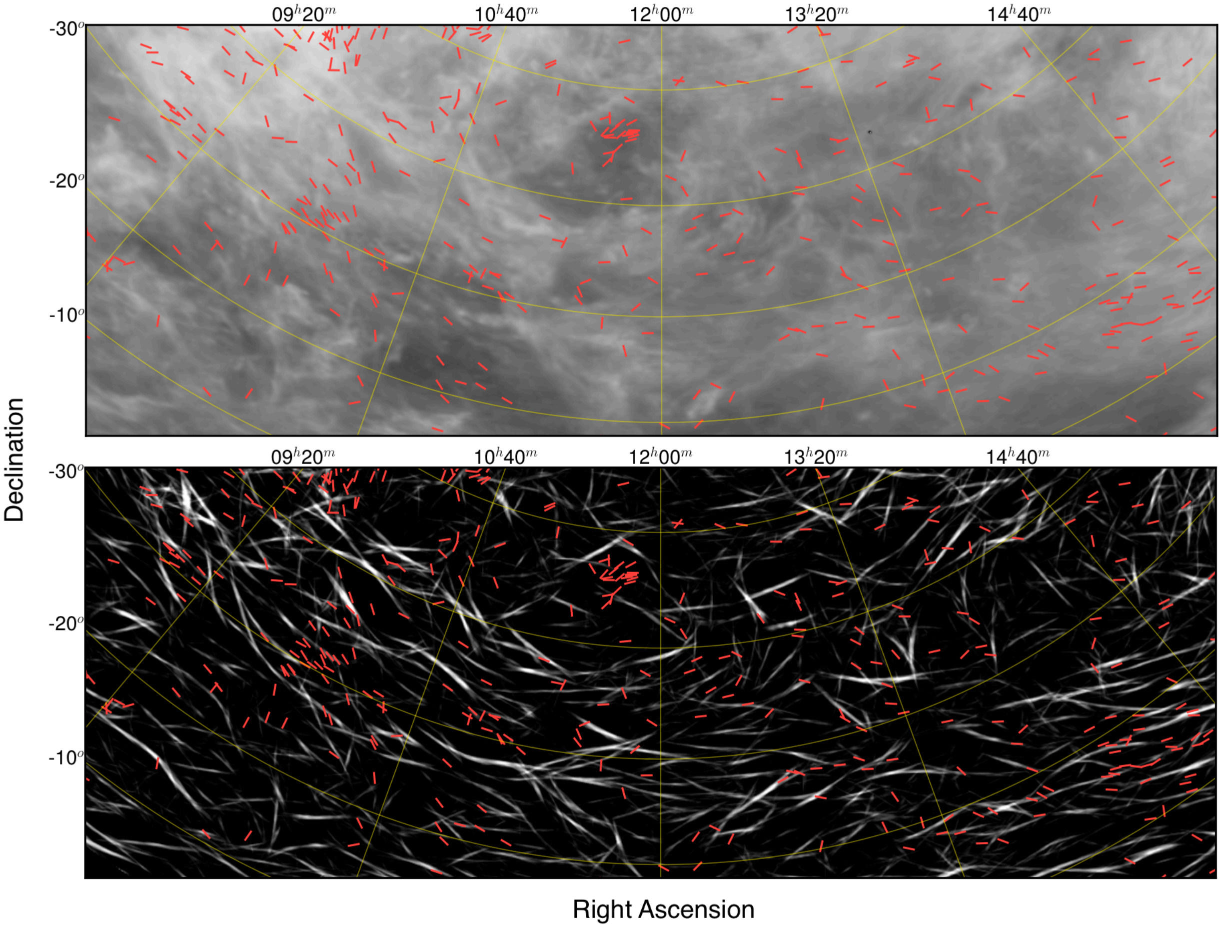

Figure 4.8: A representative region of the GASS data analyzed in Section 4.5, as in Figure 4.7. The images are integrated over the velocity range 1.6 km s^{-1} to 5.8 km s^{-1}. In the top panel, the intensity scale is linear in $\log(N_{HI})$, where black represents a column density of 2×10^{18} cm^{-2}, and white is 2×10^{21} cm^{-2}.

4.5.2 Correlation with starlight polarization

We examine the star-by-star correlation between the measured starlight polarization angles $\theta^\star$ and the RHT angle expectation value $\langle\theta_{RHT}\rangle$ in GALFA-HI (Figure 4.5). This allows us to determine whether the RHT-starlight polarization correlation exists on a fine scale, or simply in the large-scale orientation of the stars and gas, and to test the correlation robustness. We select the stars that sample regions in the top quintile of RHT intensity in

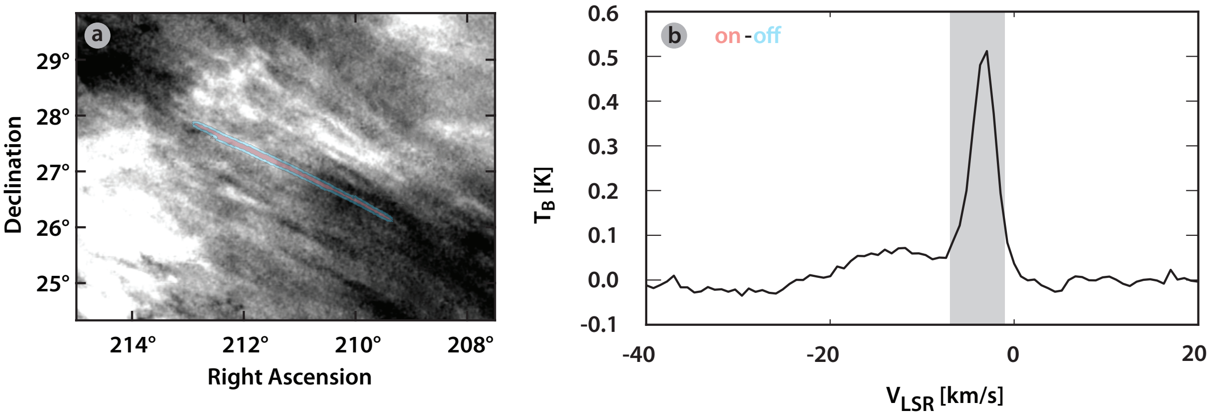

Figure 4.9: (a) "On" fiber and "off" fiber fields overlaid on GALFA-HI data. The image is integrated over the velocities indicated in (b). The fiber was selected from the RHT backprojection. Black represents a column density of 10^{19} cm^{-2}, white is 3×10^{19} cm^{-2}. (b) The difference between the average spectrum in the on and off fields. Grey region indicates the velocity range analyzed for GALFA-HI data, -7.0 km s^{-1} to -1.1 km s^{-1}. See Section 4.5 for a discussion of fiber properties.

each velocity channel (δv from above), 48 stars in total. We expect the regions with the strongest RHT intensity to trace the most visually evident fibers. We calculate $|\langle\phi_{RHT}\rangle|$ for each star (Equation 4.9). We then scramble the $\langle\theta_{RHT}\rangle$ values and recompute $|\langle\phi_{RHT}\rangle|$ for each star. The scrambling is performed 10^4 times and the results are averaged. The scrambled angle differences exhibit only a slight skew toward zero, indicating only a slight large-scale trend in fiber orientation. The unscrambled data is sharply skewed toward zero. The RHT-starlight polarization correlation is determined by a Monte Carlo analysis of the median to be highly statistically significant ($p < 0.0001$).

4.5.3 Fiber properties

We measure the properties of a GALFA-HI fiber highlighted by the RHT backprojection. We note that the exact boundary of the fiber is dependent on the RHT input parameters, and that measured properties depend on the interpretation of the fiber as a distinct physical

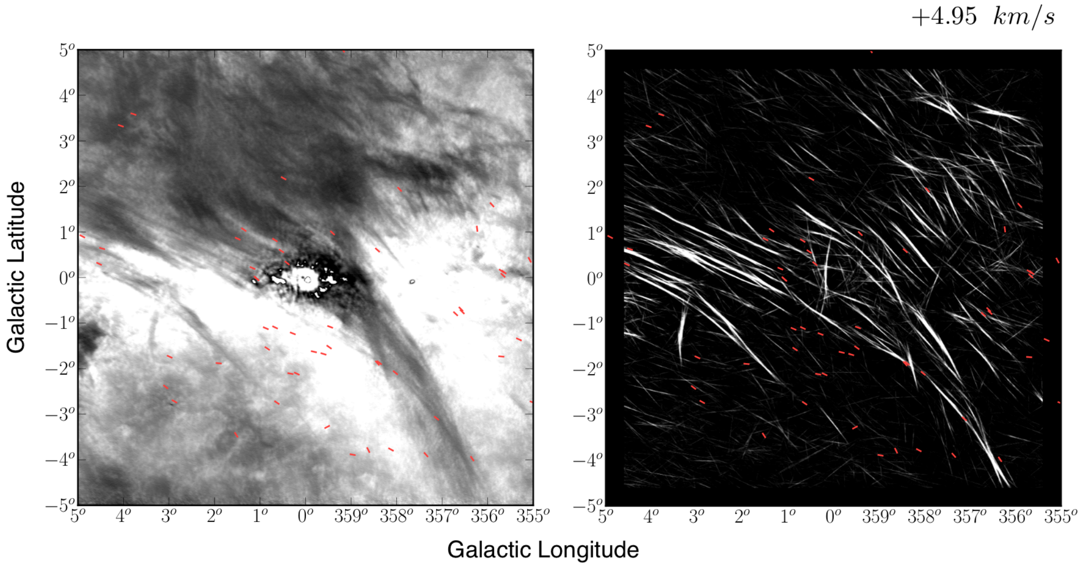

Figure 4.10: The Riegel-Crutcher cloud (Section 4.6) in HI absorption (left) and RHT backprojection (right). Overlaid pseudovectors represent polarization angle measurements from the Heiles (2000) compilation. In the left panel, the intensity scale is linear from -20 K (white) to -120 K (black).

structure. We use the RHT backprojection to mask an "on" fiber and "off" fiber region, each of equal area, on the sky. Figure 4.9 shows the average on minus average off spectrum and the selected regions of sky. We determine the line width of the spectrum to be 3.4 km s^{-1} (FWHM) using a Gaussian fit. This fiber has a column density of 5.3×10^{18} cm^{-2}, roughly typical of the GALFA-HI fibers.

It is worth noting here that the column densities of the fibers discussed above are far too low to create the measured starlight polarization. To induce starlight polarization that can be measured accurately in the Heiles (2000) catalog, a selective extinction of ~ 0.01 is needed, equivalent to a column of $\sim 5 \times 10^{19}$ cm^{-2}. Given the correlation between the magnetic field orientation and the fiber orientation, the fibers must be features of (or objects within) a dusty medium with a coaligned magnetic field, rather than the only elements

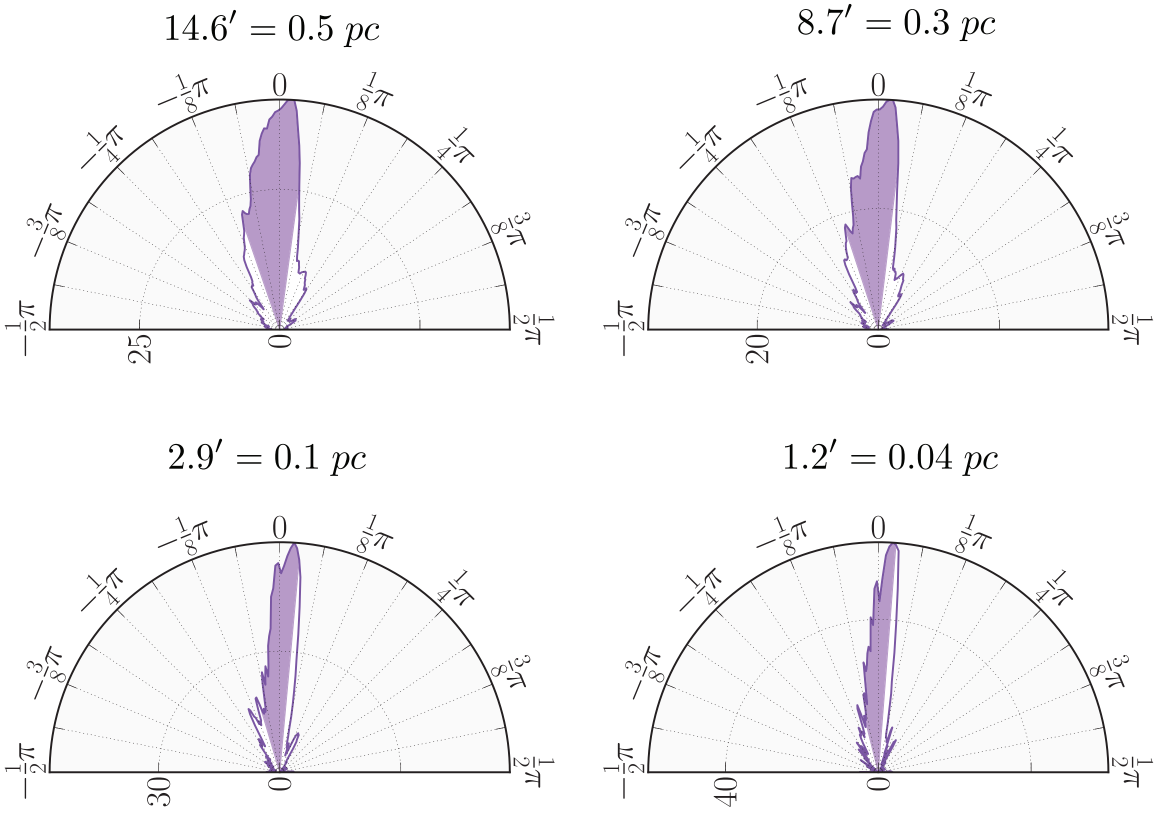

14.6′ = 0.5 *pc*

8.7′ = 0.3 *pc*

2.9′ = 0.1 *pc*

1.2′ = 0.04 *pc*

Figure 4.11: $\hat{R}(\phi)$ for all stars in the Riegel-Crutcher cloud (Section 4.6). The radius of the sampling beam around each star is labeled above each figure, with sampling beam decreasing left to right from 14.6′ to 1.2′. Spatial radii of the sampling beams are calculated using the cloud distance of 125 pc. The width of the distribution decreases with decreasing beam size. As beam size decreases (top left to lower right): IQR($\hat{R}(\phi)$) = 27.3°, 26.2°, 22.9°, 19.9°.

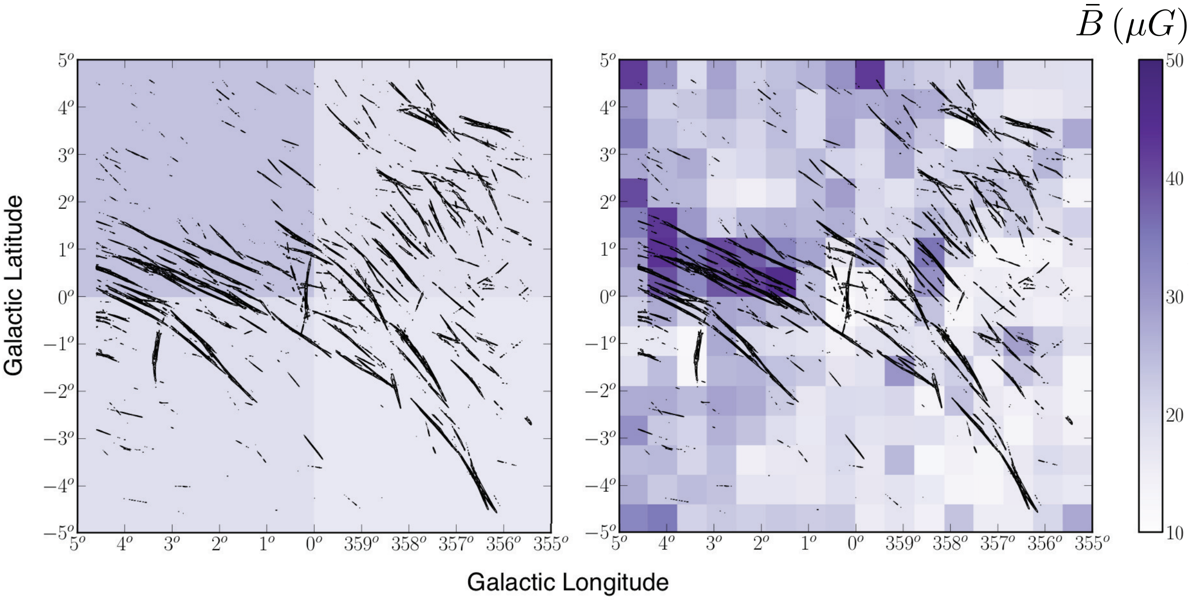

Figure 4.12: Mean magnetic field strength B_{RHT} calculated using the modified Chandrasekhar-Fermi method (Section 4.7) for 4 and 256 sections of the Riegel-Crutcher cloud. Density contours of the RHT backprojection are overlaid to give an idea of the fiber geometry (see Figure 4.10).

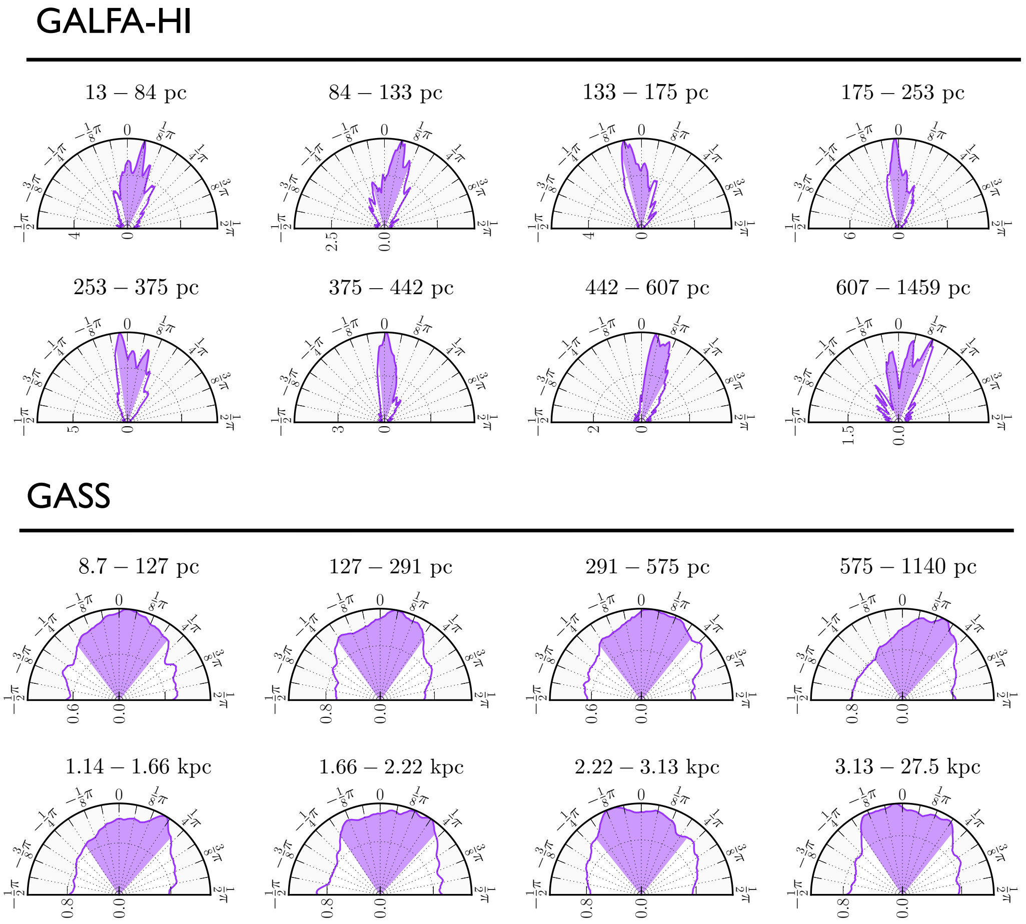

Figure 4.13: $\hat{R}(\phi)$ binned in star distance octiles for GALFA-HI and GASS data (see Section 4.5). There are approximately 18 stars in each GALFA-HI distance octile, and 394 stars in each GASS distance octile. The median values of the $\hat{R}(\phi)$ distributions are consistent with a random sampling of distances.

of the medium. Indeed, because the starlight polarization angle represents the cumulative polarization of all material between observer and star, the discovery that the fiber orientation is correlated with the magnetic field orientation indicates that the fibers trace a structure that is co-aligned for a significant fraction of the dust along the line of sight. This correlation is discussed in the context of the local ISM morphology in Section 4.8.2.

4.6 Fibers in the Riegel-Crutcher cloud

The RHT can be applied to many different environments. We apply the method to a region of cold neutral medium: the Riegel-Crutcher cloud, an HI self-absorption (HISA) feature at 125 pc toward the Galactic center (Heeschen 1955; Riegel & Crutcher 1972). The cloud was mapped in high resolution ($100'' = 0.06$ pc at 125 pc) in McC-G06, who first resolved its exquisite filamentary structure and characterized the region as magnetically dominated. In the same work, the authors comment on the visibly apparent alignment of starlight polarization pseudovectors in the plane of the sky with the linearly elongated HISA structure. The RHT allows us to quantify this alignment.

Figure 4.10 shows the Riegel-Crutcher (hereafter R-C) cloud with polarization pseudovectors from the Heiles (2000) catalog overlaid. Following McC-G06, we include all stars with $-5^\circ < l < +5^\circ$ and $-5^\circ < b < +5^\circ$, distances of less than 2 kpc, and polarization intensities of greater than 1%. This leaves 56 stars in the region.

As the R-C cloud is composed of many thin linear features that are believed to be dominantly shaped by magnetic forces, the RHT-starlight polarization correlation should be very strong. Indeed, the degree of alignment is striking for a broad range of RHT input parameters. We run the RHT for a single velocity channel at a time to preserve all velocity information. All channels individually show strong RHT-starlight polarization alignment. Each panel in Figure 4.11 shows $\hat{R}(\phi)$ for the velocity channels $+3.30$ km s$^{-1} \leq v \leq +7.42$ km s^{-1}, a range that encompasses the cloud visually (again following McC-G06).

The sharp alignment of $R_\star(\theta)$ with $\theta^\star$ in Figure 4.11 demonstrates that the filaments trace the magnetic field, as expected. As the radius of the sampling beam decreases, IQR($\hat{R}(\phi)$) decreases. For sampling beam radii of ($14.6'$, $8.7'$, $2.9'$, $1.2'$), we find IQR($\hat{R}(\phi)$) = (27.3°, 26.2°, 22.9°, 19.9°). As the alignment is significantly better with a smaller sampling beam for

$R(\theta, x, y)$, we infer that the RHT is not simply confirming the evident large-scale orientation of the magnetic field, but actually tracing the fine magnetic structure in the region. We have checked and confirmed that the alignment of $\hat{R}(\phi)$ is not dominated by a few stars.

4.7 Toward a resolved Chandrasekhar-Fermi method

The result that the RHT traces small-scale variation in the magnetic field in the R-C suggests that the RHT may provide a reasonable proxy for starlight polarization measurements in regions where the RHT and starlight polarization are in close alignment. For such regions we propose an extension of the Chandrasekhar-Fermi method for estimating the magnetic field strength in the plane of the sky.

Originally proposed by Chandrasekhar and Fermi (1953) to estimate the field strength in spiral arms, the Chandrasekhar-Fermi method uses starlight polarization to estimate the average field strength $\langle B \rangle$ in a region. The method relates the line-of-sight velocity dispersion (v_{los}) to the dispersion of starlight polarization angles about a mean component. Assuming that turbulence isotropically randomizes the magnetic field in the region, the mean field strength is given by

$$B_{CF}^2 \equiv \overline{B}^2 = \xi 4\pi\rho \, \frac{\sigma(v_{los})^2}{\sigma(\tan(\delta^\star))^2}, \tag{4.10}$$

where

$$\delta^\star \equiv \theta^\star - \overline{\theta^\star}, \tag{4.11}$$

ρ is the gas density, $\overline{\theta^\star}$ is the mean starlight polarization angle, and ξ is a correction factor representing the ratio of turbulent magnetic to turbulent kinetic energy (e.g. Heitsch et al. 2001). The validity of the method depends critically on the presence of a significant mean field component.

We apply a modified Chandrasekhar-Fermi method to the R-C cloud described in Section 4.6. Following McC-G06, we adopt $\xi = 0.5$, $\rho = 1.4 m_H n_H = 1.1 \text{ x } 10^{-21}$ g cm^{-3}, and $\sigma_{v_{los}} = \sigma_{turb} = 1.4$ km s^{-1}. Instead of $\theta^\star$ we substitute the expectation value of the RHT evaluated at every pixel in the image, $\langle\theta_{RHT}\rangle_{\text{pixel}}$, where $\langle\theta_{RHT}\rangle_{\text{pixel}}$ is the equivalent of $\langle\theta_{RHT}\rangle$, substituting $R\left(\theta, x_0, y_0\right)$ for $R_\star\left(\theta\right)$ in Equation 4.7. Thus we are evaluating:

$$B_{RHT}^2 \equiv \overline{B}^2 = \xi 4\pi\rho \, \frac{\sigma(v_{los})^2}{\sigma(tan(\delta_{RHT}))^2} \tag{4.12}$$

where

$$\delta_{RHT} \equiv \langle\theta_{RHT}\rangle_{\text{pixel}} - \overline{\langle\theta_{RHT}\rangle_{\text{pixel}}} \tag{4.13}$$

Because we obtain a $\langle\theta_{RHT}\rangle_{\text{pixel}}$ value for every pixel in the image space, $\overline{\langle\theta_{RHT}\rangle_{\text{pixel}}}$ can be evaluated over a region of any size that contains significant RHT signal.

Evaluating $\overline{\langle\theta_{RHT}\rangle_{\text{pixel}}}$ over the full extent of the R-C cloud, we obtain $B_{RHT} = 19$ μG. McC-G06 report $B_{CF} = 60$ μG for the region -3° < l $\leq$ 5°, -3° < b $\leq$ 5°. In this same region, we obtain $B_{RHT} = 23$ μG. Figure 4.12 shows B_{RHT} evaluated over smaller regions of sky, to demonstrate the possibility of a resolved Chandrasekhar-Fermi method. Each colored square in Figure 4.12 represents B_{RHT} calculated using all $\langle\theta_{RHT}\rangle_{\text{pixel}}$ values in that square. Pixels containing no RHT power are not included in the computation of Equation 4.13. The strongest B_{RHT} we find in a subregion of the cloud is ~50 μG, near $(l, b) \sim (1.5°, 0.25°)$ (see Figure 4.12).

This should be considered a preliminary step in the development of a resolved Chandrasekhar-Fermi method. A thorough analysis of the limitations and error in the RHT point estimator $\langle\theta_{RHT}\rangle_{\text{pixel}}$, as well as testing with simulations, will be pursued in the future. Indeed we expect $\langle\theta_{RHT}\rangle_{\text{pixel}}$ to overestimate the true variability of magnetic field orientation, and thus underestimate $\bar{B}$. A weighting scheme based on $R_\star(\theta, x, y)$ would reduce this bias. We caution that the same assumptions hold as in the classical Chandrasekhar-Fermi method, in particular that a significant mean field element must be present for the field estimate to have meaning. Nevertheless, the naïve application of the method outlined here to the R-C cloud does achieve the same typical field-strength estimate as the classical Chandrasekhar-Fermi method.

4.8 Discussion

The RHT is a powerful new tool for characterizing linear structure. This work quantifies for the first time the strong alignment between diffuse HI fibers and the interstellar magnetic field. In this section we discuss the physical properties of the diffuse fibers, their relationship to the local cavity, and their significance in the context of modern magnetohydrodynamic simulations.

4.8.1 Physical properties of fibers

The GALFA-HI and GASS surveys cover similar column density and latitude regimes, but differ by a factor of four in angular resolution ($4'$ for GALFA, $16'$ for GASS). The strikingly collinear HI fibers that prompted this investigation are visually evident in GALFA-HI data (Figure 4.7), and are not as apparent in the GASS data (Figure 4.8). The fiber widths are in many cases visually unresolved even in the GALFA-HI data, and so are on the order of or thinner than the GALFA-HI spatial resolution. We find that the RHT-starlight polarization correlation is significantly higher in the GALFA-HI data. Thus, the data are consistent with a model in which fine, magnetically aligned HI fibers are ubiquitous in the high-latitude sky, but washed out at lower resolutions.

The GALFA-HI fibers have typical column densities that range from $\sim 10^{19}$ cm^{-2} down to our sensitivity limit of $\sim 10^{18}$ cm^{-2}. A typical total Galactic HI column density at high latitude is $\sim 3\times 10^{20}$ cm^{-2}, so an individual fiber does not dominate the column. Assuming a cylindrical geometry, we calculate an HI volume density of n $\sim$ 14 cm^{-3} for the fiber shown in Figure 4.9. If we interpret the linewidth as purely thermal, we find a temperature of 220 K; some of this linewidth may in fact be driven by turbulence within the cloud, so we consider this an upper limit on the temperature. The thermodynamic pressure is then P/k_B = nT = 3200 K cm^{-3}, consistent with the standard pressure found in the ISM at the solar circle (Wolfire et al. 2003). The angular length of the fiber identified by the RHT backprojection in Figure 4.9 is about 5°, although a typical fiber length is difficult to identify as they often exist in complexes of fibers up to 15° long and they may extend past the boundaries of the surveyed area. The physical scale of the fibers depends on the distance to the gas. If we choose a fiducial distance of 100 pc, the distance to the wall of the local cavity (Sfeir et al. 1999), the physical resolution of GALFA-HI is 0.12 pc, and the length of the fiber in Figure 4.9 is 8.7 pc. As mentioned above, the widths are largely unresolved and therefore correspond to < 0.12 pc for the GALFA-HI fibers. We investigate correlations between the polarization alignment and the location on the sky, extinction level, and polarization intensity and find no relationship.

McC-G06 put a constraint on the magnetic field strength of the R-C cloud as $B_{tot} > 30\ \mu$G through the assumption that the magnetic energy density should dominate over the kinetic energy density to maintain the distinct linear nature of the filaments. If we apply this argument to a typical GALFA-HI fiber we find $B_{tot} > 5\ \mu$G. This number is consistent with expectations for the magnetic field in the diffuse ISM (Heiles & Crutcher 2005).

4.8.2 Fibers and the Local Cavity wall

The Sun resides inside a largely evacuated volume of the ISM called the local cavity (LC). While the original theory that the LC is a bubble filled with hot, overpressurized, X-ray emitting gas has largely been overturned (Koutroumpa et al. 2009; Welsh & Shelton 2009; Peek et al. 2011b), there is strong evidence that very little neutral gas and dust exists on this side of the LC wall, approximately 100 pc away (see Lallement et al. 2014, for a detailed map). In Figure 4.13 we show that the orientation of polarized starlight is well aligned with $\hat{R}(\phi)$, independent of the distance to the stars. Our stellar compilation only includes stars with relatively low errors in polarization angle measurement ($\Delta\theta < 25°$, see Section 4.4), which tend to have higher polarization percentages, and thus are behind more polarizing material. The median distance to stars $|b| > 30°$ that meet this criterion is 144 pc, while the median distance to stars that fail this criterion is 43 pc. The wall of the LC is often defined as the distance at which $N_{HI} > 10^{19}$ cm^{-2} (Cox & Reynolds 1987), which is equivalent to an extinction $E(B-V)$ of only 0.002 (Peek 2013), too low to produce well-measured polarization angles in our compiled data set. Thus, essentially by definition, all of the stars we consider in this analysis are outside of the LC. If the fibers are a part of the wall of the LC, this explains why we do not see a marked decrease in correlation as we examine farther stars; they too are being polarized by the gas in the LC wall.

If there were a signficant column of dust-bearing gas beyond the LC wall, unaffected by the structure of the LC itself, it would presumably have a relatively uncorrelated magnetic field orientation. This would generate a decreased RHT-starlight polarization angle correlation. Since no such decorrelation is detected (Figure 4.13), we find that the vast majority of the high Galactic latitude column is in or near the LC wall. This is consistent with modern tomographic maps of the local ISM (Vergely et al. 2010; Lallement et al. 2014).

The thickness of the wall is not yet well constrained. We note that there may be a hint of decorrelation in the farthest distance bin in the GALFA-HI data. This may be due to the presence of the intermediate-velocity arch, which covers much of the GALFA-HI area and resides at approximately 1 kpc above the disk (Kuntz & Danly 1996).

This result points towards a formation and alignment mechanism for the fibers similar to that described in Weaver (1979) and further quantitatively developed in Heiles (1998) for the Sco-Cen association and Radio Loop I. To paraphrase, many megayears ago a collection of massive stars produced outflows, and in the case of the LC, supernovae (Cox & Reynolds 1987). These winds and explosions inflated a bubble of gas and dust and stretched the cavity wall to create the aligned fibers and magnetic field lines we detect. Whether or not this description fully explains the fibers and their magnetic alignment, any explanation must take into account the formation and structure of the local ISM.

4.8.3 Simulations of linear structures

Much of the simulation work linking gas morphology to magnetic field structure is focused on understanding molecular clouds. Observational evidence for magnetic influence on gravitational collapse includes regions where the magnetic field is oriented orthogonal to the densest structures in a molecular cloud, but parallel to the surrounding lower density medium, apparently owing to self-gravitational collapse along the field lines (e.g. Goldsmith et al. 2008; Nakamura & Li 2008). Recent *Herschel* observations (Molinari et al. 2010; Peretto et al. 2012; André et al. 2010) have sparked an interest in modeling the formation of more diffuse molecular filaments, where a complex interplay between turbulence, gravity, and magnetism determine the alignment between filaments and magnetic fields. Soler et al. (2013) modeled turbulent molecular clouds and found a link between the gas morphology and the orientation of the magnetic field. For diffuse, high-latitude HI, gravity is unlikely to play a role in fiber formation and magnetic alignment.

Major progress has been made in this low density regime by Hennebelle (2013), who showed that linear features can be created and maintained in a turbulent ISM without appealing to gravity. Arzoumanian et al. (2011) detected a typical width for dust filaments of 0.1 pc in *Herschel* data. In simulations conducted in Hennebelle (2013; see also Hennebelle & André (2013)) they reproduce this characteristic width in regions shielded from UV radiation, the scale being set by the dissipative process of ion-neutral friction. Exposed, non-gravitating features, such as the fibers examined in this paper, are expected to have widths at least 10 times smaller due to higher ionization and lower densities. This prediction is consistent with our finding that we are increasingly resolving the fibers that are aligned with the magnetic field with higher resolution observations. The fibers are more apparent and better aligned with the field in the GALFA-HI data than in the GASS data, or a resolution of 0.12 pc vs. 0.47 pc (at 100 pc), respectively. For the HI absorption filaments probed in the R-C cloud again the alignment improves as we decrease the radius of the sampling beam. This is consistent with the width of the filaments largely being unresolved, or < 0.06 pc at the cloud's distance of 125 pc. We can test the prediction of 0.01 pc wide fibers with yet higher resolution, highly sensitive observations enabled by instruments like the JVLA and the SKA pathfinder telescopes.

4.9 Conclusions

This paper used HI surveys of the Galactic ISM to study the relationship between gas morphology and the structure of the interstellar magnetic field. The highlights are summarized as follows.

- We identified a novel set of features in the diffuse, high Galactic latitude HI ISM: slender, linear, clustered features we call HI fibers.
- We developed a method for quantifying the coherent linearity of structures in images called the Rolling Hough Transform.
- We used the RHT to demonstrate that the orientation of the fibers is correlated with the orientation of starlight polarization. This result is largely independent of the RHT input parameters D_W, D_K, and Z, as well as velocity binning δv.
- The magnetic fields and linear HI features are aligned throughout the high Galactic latitude ISM, but this effect is not scale free. Higher resolution observations show a much higher correlation between the fibers and the field. The fibers are largely unresolved even with the highest resolution observations at 0.06 pc.
- The GALFA-HI and GASS fiber features are most likely a component of the local cavity wall and their derived physical properties at 100 pc are consistent with this environment.
- We propose a technique based on the Chandrasekhar-Fermi method to measure the magnetic field strength in regions with strong, pervasive fields using only the RHT.

The results of this work suggest a number of avenues for future exploration. The most obvious is to expand the work to larger areas of sky at higher resolution. In the northern celestial sky, EBHIS (Kerp et al. 2011) will provide a map similar to that of GASS with slightly higher resolution ($9'$) and slightly lower sensitivity. The GALFA-HI second data release will provide ten times more area at $4'$ resolution than the region examined here. In the future, SKA pathfinders APERTIF (Verheijen et al. 2009) and ASKAP (Duffy et al. 2012; Dickey et al. 2013) will provide sub-arcminute resolution observations of the entire sky. The RHT can also be applied to observations of other phases of the magnetized ISM, for instance in molecular gas and dust, and likely would be an appropriate tool for any region not strongly dominated by gravity. Indeed, the RHT may even be a useful tool for finding stellar stream features in the Galactic halo. Furthermore, since the Hough transform can be generalized to find practically any template in the image plane (Duda & Hart 1972), the RHT could be extended to search for shells, cometary structures, or any other pervasive morphological feature of the ISM.

Another clear direction is the pursuit of comparable structures in simulations of the ISM. To date, we know of no examples in the ISM simulation literature in which magnetic fields are shown to be aligned with linear, neutral structures in diffuse media similar to that discussed here. This may be because multi-phase, magnetized simulations of a realistic Galactic ISM (e. g. Hill et al. 2012) are never conducted at high enough resolution to resolve the features we detect. We suggest that a zoom-in of such a simulation near the Galactic disk at higher resolution or an implementation with an adaptive mesh (or both) may be able to resolve the HI fibers. If simulations were to be unable to generate these kinds of features and correlations, it would suggest that the fibers are dependent on physics we are still incapable of capturing in simulations.

The discovery that the RHT can, at least in magnetically dominated regions, trace fine magnetic field structure, invites further investigation of the relationship between RHT angle dispersion and the magnetic field strength, and the efficacy of a resolved Chandrasekhar-Fermi method. To do this properly, we suggest the simulation work discussed above could be used to determine any bias or scaling that are needed to apply our method to other data accurately (as in Heitsch et al. 2001).

Acknowledgments

The authors thank Destry Saul, Snežana Stanimirović, Carl Heiles, Erik Rosolowsky, Patrick Hennebelle, Fabian Heitsch, and François Levrier for useful discussion, Naomi McClure-Griffiths for providing the Riegel-Crutcher cloud data, and the anonymous referee for many helpful comments. We also thank other members of the GALFA-HI team and members of the ALFALFA team for their role in making the survey possible. We acknowledge support from the Luce Foundation. S.E.C. was supported by a National Science Foundation Graduate Research Fellowship under Grant No. DGE-11-44155. J.E.G.P. was supported by HST-HF-51295.01A, provided by NASA through a Hubble Fellowship grant from STScI, which is operated by AURA under NASA contract NAS5-26555.

Chapter 5

Neutral Hydrogen Structures Trace Dust Polarization Angle: Implications for Cosmic Microwave Background Foregrounds

5.1 Introduction

The cosmic microwave background (CMB) is the pervasive residual radiation from the formation of the Universe. The detection of primordial B-mode polarization in the CMB is a major goal of contemporary cosmology. This signal is imprinted at the surface of last scattering by perturbations from gravitational waves generated during the epoch of inflation, a period of rapid expansion in the early Universe (Seljak & Zaldarriaga 1997; Seljak 1997; Kamionkowski et al. 1997). An inflationary gravitational wave (IGW) B-mode measure-

---

This section contains text from an article published in Physical Review Letters (Clark et al. 2015).

ment would be the first direct evidence of inflation. A number of experiments are pursuing the signal, using ground-based (e.g. ABS, Essinger-Hileman et al. 2010; Advanced ACT, Niemack et al. 2010; BICEP2/*Keck* Array, Ade et al. 2015d; CLASS, Essinger-Hileman et al. 2014; POLARBEAR, Kermish et al. 2012; SPT-3G, Benson et al. 2014), balloon-borne (EBEX, Reichborn-Kjennerud et al. 2010; SPIDER, Fraisse et al. 2013), and space telescopes (*Planck*, Adam et al. 2015a).

Unfortunately, our view of the polarized CMB is obscured by contaminating foregrounds. For IGW B-mode searches at frequencies $\gtrsim$ 100 GHz, the largest foreground is Galactic polarized dust emission. Aspherical dust grains in the Milky Way align their short axes with the ambient magnetic field, and interstellar radiation is absorbed and reradiated by the dust as partially polarized light. The BICEP2 collaboration claimed a measurement of primordial B-modes (Ade et al. 2014b), but subsequent analyses determined that the detection could be attributed entirely to Galactic dust (Flauger et al. 2014; Ade et al. 2015a). A detailed understanding of the foreground polarization signal is required before a definitive IGW B-mode detection can be achieved. Pursuant to that goal, the *Planck* satellite recently mapped the full sky at 353 GHz, a frequency dominated by thermal dust emission. These data can be used to subtract the foreground polarization pattern from lower-frequency CMB observations. To optimize the chance of primordial B-mode detection, experiments should target the "cleanest" regions of sky: areas where there is relatively little polarized dust, and where the dust polarization structure is measured with high signal-to-noise. The *Planck* maps are limited in this regard, because the *Planck* polarized signal is noise-limited at high Galactic latitudes, where the dust column is lowest. Thus IGW B-mode searches are plagued by a trade-off: the regions of lowest foreground amplitude are also the regions with the poorest foreground constraints.

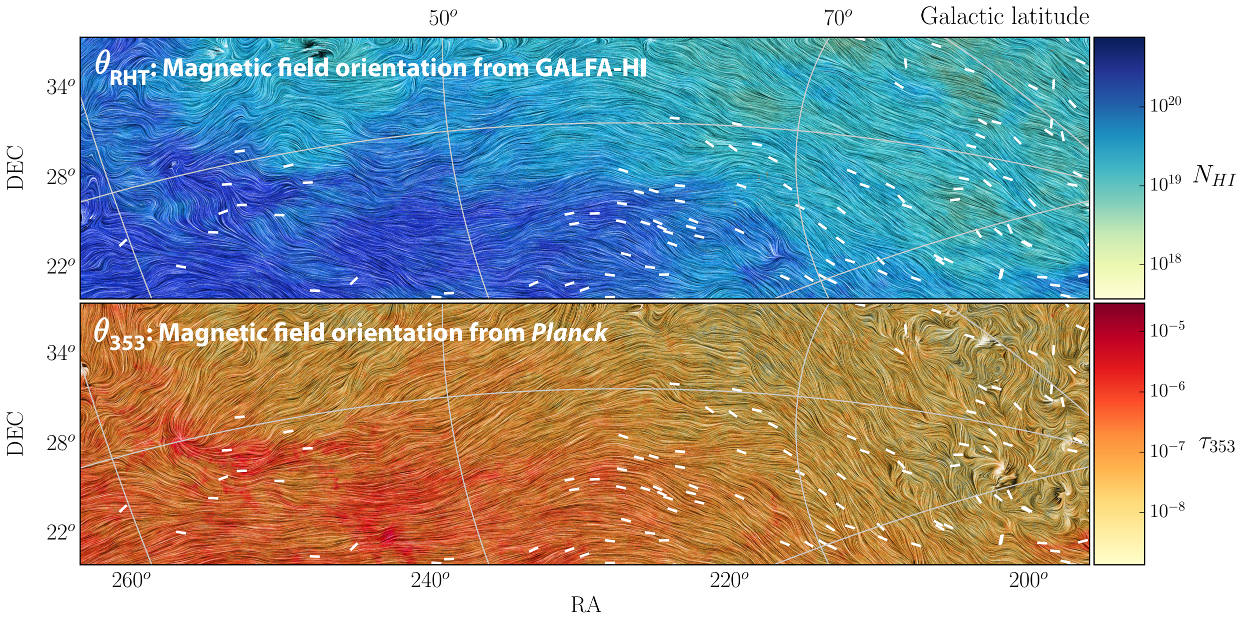

Figure 5.1: Plane-of-sky magnetic field orientation as predicted by θ_{RHT} (top) and θ_{353} (bottom). Color maps are integrated HI column density from $v = -61.5$ km s^{-1} to $+61.5$ km s^{-1} (N_{HI} [cm^{-2}]), and dust opacity (τ_{353}). *Planck* and RHT Q and U values are smoothed with a FWHM = 1° Gaussian kernel, then used to construct θ_{353} and θ_{RHT}, which are visualized using line integral convolution (LIC; Cabral & Leedom 1993). The high latitude ($b \gtrsim 70$) behavior of the θ_{353} LIC pattern is due to *Planck* noise. White pseudovectors represent starlight polarization angles. Galactic latitude lines lie at $b = 30°, 50°, 70°$, from left to right. Galactic longitude lines lie at $l = 80°, 50°, 20°$, from top to bottom.

5.2 A new constraint on polarized foregrounds

We present an entirely new method for constraining Galactic foregrounds. Using only the morphology of diffuse neutral hydrogen (HI) structures, we predict the orientation of polarized dust emission at high precision over a range of angular scales. In parallel with existing measurements of polarized CMB foregrounds, our recovery of the dust polarization angle will increase the precision of foreground models. This is especially valuable in regions where the *Planck* 353 GHz data are noise-limited.

This work follows the discovery that linear structures in HI are elongated in the direction of the interstellar magnetic field as probed by starlight polarization (Clark et al. 2014). Here, we demonstrate that HI orientation is well correlated with the *Planck* 353 GHz polarization angle across a region of high Galactic latitude sky. Note that the *Planck* data enable quantitative conclusions beyond the previous work, which considered only 153 sparsely sampled starlight polarization measures over 1,300 $\deg^2$ of sky. Also, polarized dust emission samples the full line of sight, whereas starlight polarization only traces the magnetic field out to the distance of the star. The relationship between dust and HI in the interstellar medium (ISM) is deeper than their correlation in column density (e.g. Burstein & Heiles 1982), which is already used to estimate the amplitude of polarized dust emission (Flauger et al. 2014; Ade et al. 2014a). Small dust grains and long plumes of HI are both aligned by the magnetic field, though the mechanism for aligned HI structure formation is not yet well understood.

The slender linear features that best trace the orientation of the Galactic magnetic field are only revealed by high spatial and spectral resolution HI maps (see Clark et al. 2014, for details). We use data from the Galactic Arecibo L-Band Feed Array HI survey (GALFA-HI; Peek et al. 2011a) with the Arecibo 305m radio antenna. GALFA-HI has an angular resolution of FWHM $\simeq 4'$, a spectral resolution of 0.18 km s^{-1}, and a brightness temperature noise of ~ 140 mK rms per 1 km s^{-1} integrated channel over 13,000 $\deg^2$ of sky. This work uses data from the forthcoming second data release (Peek et al. 2017).

We analyze 353 GHz polarization data obtained by the *Planck* satellite's High Frequency Instrument (HFI; Ade et al. 2014a). These data have an angular resolution of FWHM $\simeq 5'$, comparable to GALFA-HI. We transform the *Planck* data from Galactic to Equatorial coordinates [1]. For all analyses, we apply a mask constructed from the union of all point source masks provided for each HFI channel in both temperature and polarization.

We additionally consider 126 optical starlight polarization measures in this region (Heiles

---

[1] Using HEALPix, `http://healpix.jpl.nasa.gov`

2000). Starlight is polarized parallel to the magnetic field by the preferential absorption of aligned grains.

We quantify the orientation of GALFA-HI structures using the Rolling Hough Transform (RHT), a machine vision technique (Clark et al. 2014). The RHT runs on image data, and outputs $R(\theta)$, linear intensity as a function of angle, for every pixel in the input map. For a detailed description of the RHT we refer the reader to (Clark et al. 2014).

For this work we select a 1,278 deg^2 region of the GALFA-HI sky. The region, which spans right ascension 195° to 265° and declination 19.1° to 38.3°, stretches from $b = 30°$ above the Galactic plane to $b = 81.7°$, nearly Galactic zenith. We analyze this GALFA-HI region from -13.5 km s^{-1} to $+13.5$ km s^{-1}, binned in 3.0 km s^{-1} integrated velocity channels.

Linear polarization data can be fully described by either a polarization angle ψ and polarized intensity P or by the Stokes parameters Q and U, where $\psi = 1/2\arctan(U/Q)$ and $P^2 = Q^2 + U^2$. We define from the RHT output

$$\begin{aligned} Q_{RHT} &= \int \cos(2\theta) \cdot R(\theta)\; d\theta \\ U_{RHT} &= \int \sin(2\theta) \cdot R(\theta)\; d\theta, \end{aligned} \tag{5.1}$$

where values are calculated for each point in the image data. We process each velocity channel with the RHT and add the resulting Q_{RHT} and U_{RHT} maps.

We define $\theta_{RHT} = \frac{1}{2}\arctan(U_{RHT}/Q_{RHT})$, an estimate for the orientation of the magnetic field derived solely from HI data. We compare this value to θ_{353}, a 90° rotation of the polarization angle obtained from Q_{353} and U_{353} (we use the IAU polarization definition). The polarization angle of dust emission is conventionally taken to be 90° from the orientation of the local Galactic magnetic field (however, see Lazarian 2007, and references therein).

We calculate θ_{353} and θ_{RHT} for the region described. Figure 5.1 shows a map of each

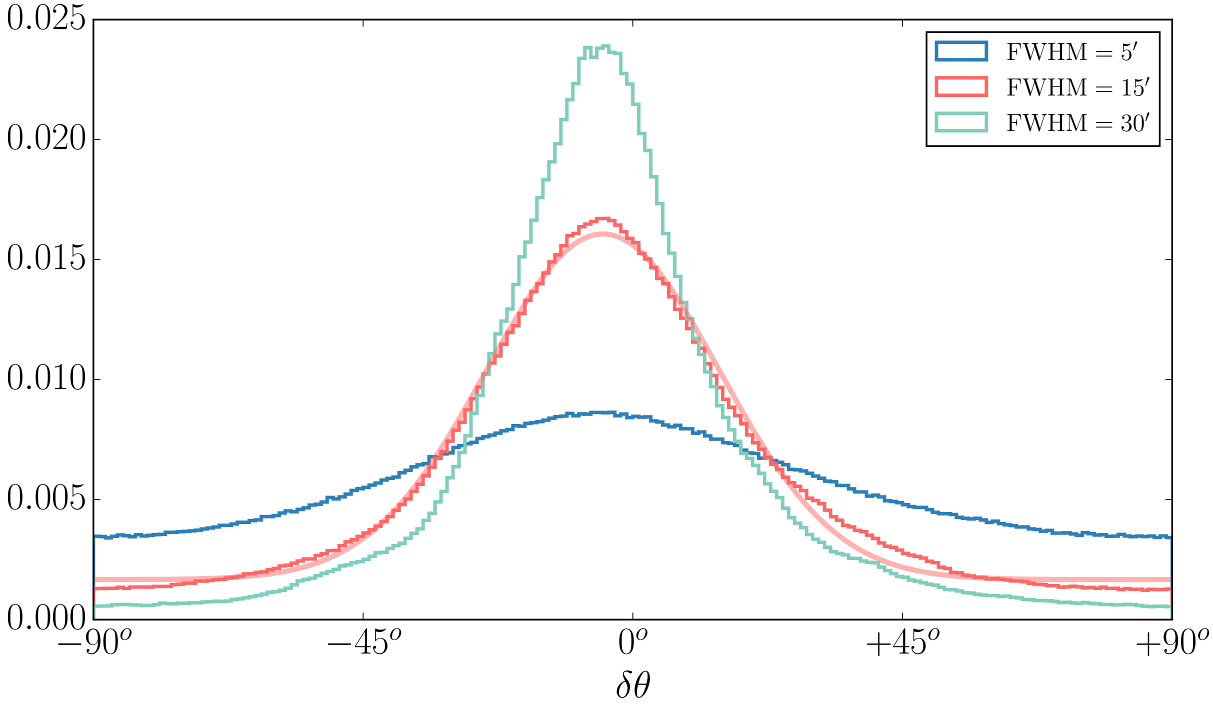

Figure 5.2: Normalized histograms of $\delta\theta = \theta_{353} - \theta_{RHT}$ in 1° bins at resolutions of FWHM $= 5'$, $15'$, and $30'$. The Gaussian fit to the FWHM $= 15'$ histogram shown has a standard deviation $\sigma = 19.4°$.

of these quantities on the sky, along with starlight polarization angles. Although derived from independent data, these three estimates for the plane-of-sky magnetic field orientation trace one another remarkably well. Figure 5.2 shows histograms of $\delta\theta \equiv \theta_{353} - \theta_{RHT}$. We construct θ_{353} and θ_{RHT} from Q and U maps smoothed to three different resolutions. For Gaussian smoothing kernels of FWHM $= 5'$, $15'$, and $30'$, we find Gaussian fits to the $\delta\theta$ histogram with standard deviation $\sigma = 30.2°$, $\sigma = 19.4°$, and $\sigma = 14.4°$, respectively. We run a Monte Carlo analysis to determine the pure *Planck* noise contribution to $\delta\theta$, and find this noise is responsible for a Gaussian component with $\sigma = 16.0°$, $\sigma = 6.1°$, and $\sigma = 3.5°$ for each respective smoothing kernel. Thus as the data are smoothed to larger angular scales, θ_{353} and θ_{RHT} obtain ever better agreement, and a non-negligible fraction of the $\delta\theta$ scatter is solely due to Q_{353} and U_{353} measurement noise. The $\delta\theta$ histograms are centered at about $-3°$ to $-4°$. This small offset from zero may be due to either residual systematics in the 353 GHz map (Adam et al. 2015b) or true systematic differences between θ_{353} and θ_{RHT}.

To further characterize the relationship between RHT, *Planck*, and starlight polarization angles, we construct simple template maps and compute cross-power spectra between them. We construct the templates using the *Planck* 353 GHz intensity, I_{353}. A full polarization template would also require an estimate of the polarization fraction, $p = P/I$, but since our goal is to isolate the polarization angle information, we set $p = 1$ in all templates. (Over a small patch of sky, $p \approx$ constant is a reasonable approximation, and one can simply rescale our power spectra for a given value of p.) Furthermore, measuring P from the *Planck* data is non-trivial, as simple estimators are noise-biased (e.g. Plaszczynski et al. 2013). The templates are

$$\begin{aligned} Q &= I_{353}\cos(2\psi) \\ U &= I_{353}\sin(2\psi), \end{aligned} \tag{5.2}$$

where ψ is either the RHT, *Planck*, or starlight polarization angle. For all templates, we smooth the Q and U data to a common resolution of FWHM $= 4°$ before computing ψ. This prohibits small-scale noise in Q and U from contaminating the templates on large scales via the harmonic-space convolution implied by the real-space map multiplication in Eq. (5.2). To avoid noise biases, we measure cross-correlations between templates constructed from independent half-mission splits of the *Planck* data.

We apply a common mask to all template maps, consisting of the *Planck* point source mask and a mask removing regions that are more than 7° from starlight data, regions where the integrated RHT intensity is zero, and the edges of the region, where RHT artifacts could arise. The total unmasked sky subtends 1,181 deg^2, 92% of the original area. We apodize the mask with a Gaussian taper of FWHM $= 15'$. We use `polspice` (Chon et al. 2004) to compute EE and BB power spectra (C_ℓ, where multipole ℓ is the harmonic variable conjugate to angular scale), corresponding to the usual curl-free and divergence-free decompositions of polarization data (Seljak & Zaldarriaga 1997; Kamionkowski et al. 1997), respectively. We calibrate the `polspice` internal parameters using 100 simulations of polarized dust power spectra with properties matching recent *Planck* measurements (Ade et al. 2014a; Adam et al. 2014). We bin the measured power spectra in four logarithmically spaced multipole bins between $\ell = 40$ and $\ell = 600$ (centered at $\ell = 59, 116, 229,$ and 451). Error bars are calculated in the Gaussian approximation from the auto-power spectra of the template maps used in each cross-correlation. Sample variance is not included in the error bars, as our interest is in comparing measurements of the same modes on the sky.

Figure 5.3 shows cross-power spectra for the template maps constructed from RHT, *Planck*, and starlight data. We refrain from fitting a model to the data, as we have not considered p in our templates, but instead consider the relative amplitudes of the cross-power spectra. For the *Planck*-only templates and the *Planck*–RHT, *Planck*–starlight, and RHT–starlight cross-correlations, respectively, we detect the E-mode power spectrum at 70σ, 55σ, 40σ, and 40σ significance. We detect the B-mode power spectrum at 65σ, 60σ, 50σ, and 40σ significance. We verify that template maps constructed with random angles yield a cross-power spectrum consistent with zero (even when using the true I_{353} data in the random-angle templates). We compare the template cross-power spectra with the actual EE and BB power spectra measured directly from Q_{353} and U_{353} and infer a mean $p \sim 5\%$, which is reasonable for this region (Ade et al. 2014a).

Although significant cross-correlations are detected for all templates in Figure 5.3, the *Planck*-only templates yield higher amplitudes than the cross-correlations with RHT- or

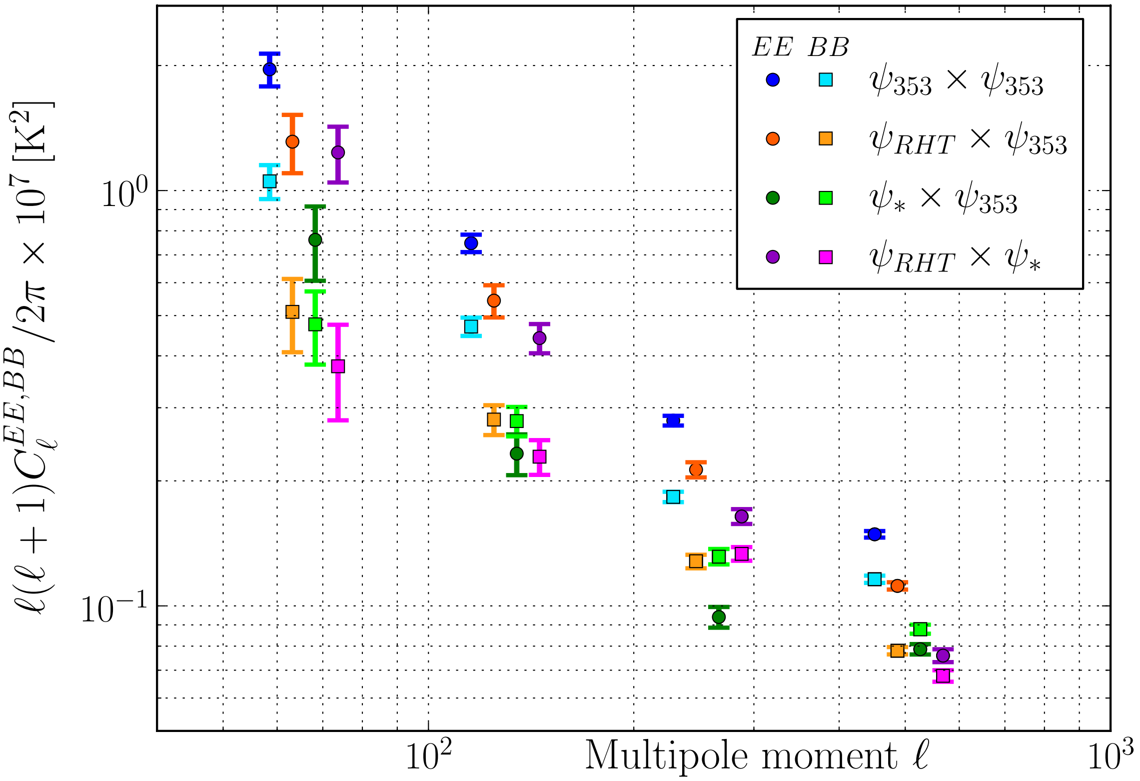

Figure 5.3: Cross-power spectra of polarization template maps constructed from I_{353} and either *Planck* (ψ_{353}), RHT (ψ_{RHT}), or starlight polarization (ψ_*) data (Eq. 5.2). Shown are E-mode (circles) and B-mode (squares) components. Significant (40–70σ) cross-correlations are detected in all cases.

starlight-based templates. While this could be due to physical differences between angles, we note that the RHT–*Planck* and RHT–starlight cross-correlations yield similar results (especially at low-ℓ), suggesting that the *Planck*-only templates' power spectra could be systematically biased. Because the angle construction relies on the U_{353}/Q_{353} ratio, it is sensitive to any effect that modifies the zero point of the maps. Such effects could include gain calibration drifts or intensity-to-polarization leakage that varies over the sky, both of which are known to be present in the *Planck* data at some level (Adam et al. 2015b). Indeed, scan-synchronous systematics have been detected in *Planck* temperature data (Aghanim et al. 2016; Kim & Komatsu 2013), and maps of $\delta\theta = \theta_{353} - \theta_{RHT}$ present clear visual evidence

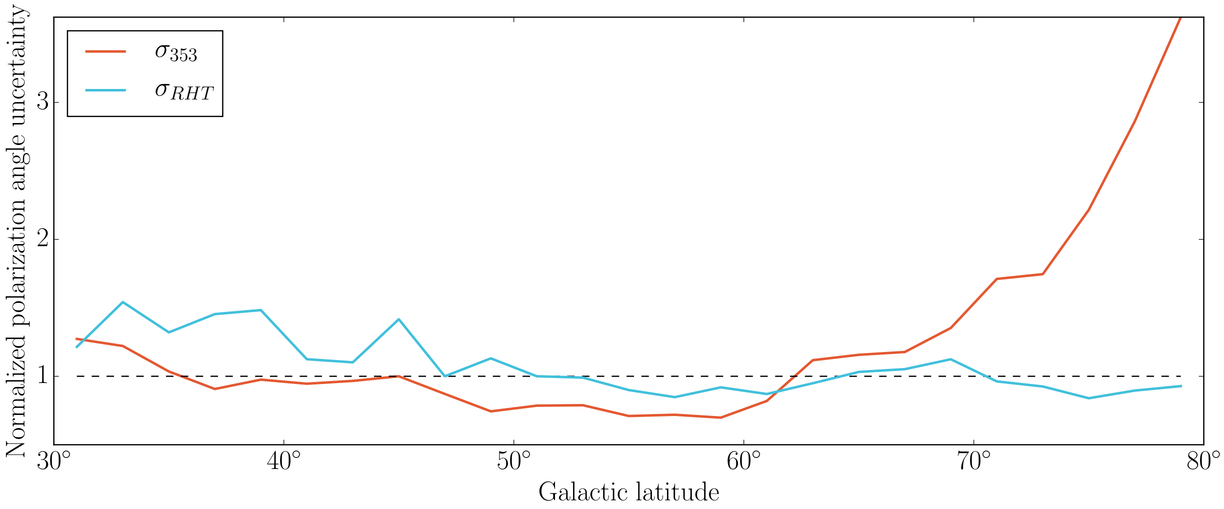

Figure 5.4: Angle uncertainties averaged over 2° Galactic latitude bins, normalized by their respective median values (dashed line).

of residuals that are highly correlated with the *Planck* scan directions. We leave a detailed consideration of these systematic effects on the *Planck* angles to future work. Note that direct measurements of EE and BB power spectra from Q_{353} and U_{353} are more immune to these systematics than the angle construction, but we require the latter method to compare *Planck* data in a straightforward way to the RHT- and starlight-based templates.

The RHT–*Planck* cross-power spectra yield an amplitude ratio $C_l^{EE}/C_l^{BB} \approx 2$, a result consistent with the *Planck* 353 GHz measurement (Adam et al. 2014), though this must be interpreted with caution as we have not modeled p in our templates. Many current models of the dust polarized sky (O'Dea et al. 2011; Delabrouille et al. 2013) predict equal E- and B-mode amplitudes (Adam et al. 2014). HI orientation preserves the nonunity EE/BB ratio, suggesting that ISM structure is a crucial missing component of these models. The preferential alignment of *Planck* filamentary dust structures with the magnetic field (Ade et al. 2015c) supports this conclusion. Our work underscores the need for a deeper understanding of the interplay between ISM phenomena and polarized dust.

IGW B-mode experiments often target the high Galactic latitude sky, where *Planck* data cannot distinguish between the most promising potential targets (Kovetz & Kamionkowski 2015). Figure 5.4 shows the relative Galactic latitude dependence of uncertainties in θ_{353} and θ_{RHT}, where the θ_{RHT} uncertainty is propagated from the variance in $R(\theta)$. With sensitive measurements at high latitudes, θ_{RHT} maps can be used to assess the structure of the magnetic field in targeted regions of sky.

Our results indicate that full foreground templates with higher signal-to-noise than the Q_{353} and U_{353} maps can be constructed by combining θ_{RHT} with other data describing P. A scale-dependent modeling of p and I from a combination of I_{353}, P_{353}, and HI data may enable the extension of this work to full polarized dust foreground maps. Such templates should remove CMB and cosmic infrared background emission from I_{353}, which we neglect here. We can also replace I_{353} in Eq. 5.2 with an unbiased estimator of P_{353} (e.g. Plaszczynski et al. 2013; Vidal et al. 2014). P is theoretically determined by the dust column along the line of sight, traced by I, and the tangledness of the magnetic field along the line of sight, where more tangled fields cause greater depolarization. N_{HI} is a powerful proxy for I_{353}, particularly at high Galactic latitudes where dust emission is low and the expected depletion of HI into a molecular state is minimal. Changes in θ_{RHT} for different HI velocity channels may indicate line-of-sight field tangling, and may elucidate the physical origin of variations in p by isolating components of the magnetic field. This will be the subject of future work, and may lead to further HI constraints on P_{353}.

5.3 Conclusions

In this work we demonstrate that HI orientation correlates with *Planck* 353 GHz polarization angle. We will process HI data from the full Arecibo sky in a forthcoming work, as it overlaps with several CMB experiments. Lower resolution HI surveys such as GASS (McClure-Griffiths et al. 2009) and EBHIS (Kerp et al. 2011) can be used on other regions of the sky, although they do not trace the Galactic magnetic field as precisely as the high resolution GALFA-HI data (Clark et al. 2014). Soon, Galactic all-sky maps from Square Kilometer Array pathfinders (Duffy et al. 2012) will be ideal for HI-based foreground maps.

Acknowledgments

The authors thank David Spergel, Amber Miller, Blake Sherwin, Raphael Flauger, and Kendrick Smith for enlightening discussion of the work presented here. We thank the other members of the GALFA-HI team for their role in producing that data. We also thank Akito Kusaka and Tobias Marriage for providing survey coordinates on behalf of the PolarBear and CLASS teams, respectively. We thank the anonymous referees for their thoughtful comments. S. E. C. was supported by a National Science Foundation Graduate Research Fellowship under Grant No. DGE-11-44155. This work was partially supported by a Junior Fellow award from the Simons Foundation to J.C.H. M.E.P. acknowledges support from NSF Grant No. AST-1410800.

5.A Supplemental material

In this work we run the RHT using an unsharp mask kernel diameter $D_K = 15'$, a rolling window size $D_W = 75'$, and an intensity threshold $Z = 70\%$ (see Clark et al. 2014). Under variation of these parameters, both the velocity channel binning as well as the RHT parameters, our results remain qualitatively unchanged.

Uncertainties for P and ψ are defined by

$$\sigma_P = \frac{1}{P}\sqrt{Q^2{\sigma_{QQ}}^2 + U^2{\sigma_{UU}}^2} \tag{5.3}$$

and

$$\sigma_\psi = 28.65^\circ \sqrt{\frac{Q^2{\sigma_{UU}}^2 + U^2{\sigma_{QQ}}^2}{Q^2{\sigma_{QQ}}^2 + U^2{\sigma_{UU}}^2}} \cdot \frac{\sigma_P}{P}, \tag{5.4}$$

where we neglect QU covariance. We compute σ_{QQ}^{353} and σ_{UU}^{353} from half-mission splits of the *Planck* data, following the procedure outlined in (Adam et al. 2015b). The analogous quantities σ_{QQ}^{RHT} and σ_{UU}^{RHT} are computed from the variance in the RHT spectrum, as

$${\sigma_{QQ}^{RHT}}^2 = \int \cos^2(2\theta) \cdot R(\theta)\ d\theta \tag{5.5}$$

and

$${\sigma_{UU}^{RHT}}^2 = \int \sin^2(2\theta) \cdot R(\theta)\ d\theta. \tag{5.6}$$

We define the difference between θ_{353} and θ_{RHT} as

$$\delta\theta = \frac{1}{2}\arctan\left[\frac{\sin(2\theta_{353})\cos(2\theta_{RHT}) - \cos(2\theta_{353})\sin(2\theta_{RHT})}{\cos(2\theta_{353})\cos(2\theta_{RHT}) + \sin(2\theta_{353})\sin(2\theta_{RHT})}\right]. \tag{5.7}$$

This equation properly accounts for the 180° degeneracy in polarization angle.

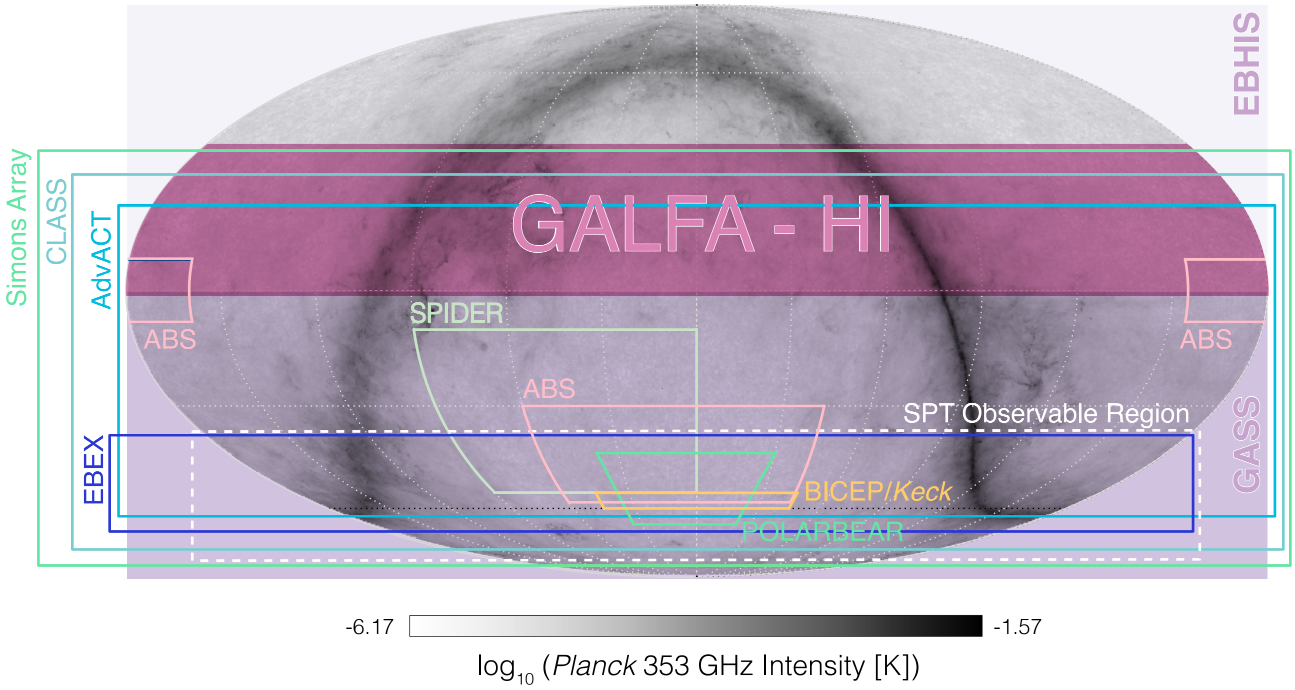

Figure 5.5: Approximate observing regions of various CMB B-mode experiments in Equatorial coordinates. Background image is the log of the *Planck* 353 GHz dust intensity [K]. The GALFA-HI full-sky region is overlaid. The Effelsberg-Bonn HI Survey (EBHIS) and the Galactic All-Sky Survey (GASS) cover the entire Northern and Southern Equatorial skies, respectively.

Chapter 6

Toward Higher Fidelity Maps of Polarized CMB Foregrounds

6.1 Introduction

The search for inflationary gravitational wave B-mode polarization is currently hindered by the foreground polarized dust emission, as discussed in previous chapters. Improved maps of the plane-of-sky magnetic field will be invaluable for the study of the ISM, as well as for the search for inflation. An improved map of the foreground polarization will also benefit studies of CMB lensing. The large-scale structure of the Universe gravitationally lenses the CMB signal, measurably affecting the structure of CMB anisotropies (Blanchard & Schneider 1987). Lensing also deforms the CMB polarization pattern, generating a lensing B-mode signal from intrinsically E-mode polarization (Zaldarriaga & Seljak 1998). Sensitive measurements of CMB temperature and polarization anisotropies can thus be used to reconstruct the projected matter density of the Universe between the surface of last scattering and the present day (Zaldarriaga & Seljak 1999; Hu & Okamoto 2002). Astrophysical foregrounds can bias the CMB lensing reconstruction, an effect that is currently better-understood in temperature than in polarization (van Engelen et al. 2014). Improved maps of the foreground polarization signal can be used to study foreground biases for CMB lensing reconstruction.

We construct a flexible Bayesian pipeline for estimating dust polarization properties from 353 GHz and HI data. The likelihood of the data is constructed from *Planck* 353 GHz dust polarization measurements. We implement and test a number of different priors, with the goal of understanding how to best create maps that self-consistently incorporate polarized emission and HI data. The Bayesian priors use the orientation of HI, measured with the Rolling Hough Transform (RHT; Chapter 4), to inform the true plane-of-sky polarization angle. The resulting Bayesian posteriors are sampled to obtain new maps of the polarized sky. We cross-correlate these maps with *Planck* 217 GHz data; independent observations of the polarized dust emission. We compare the resulting cross-power spectra with the cross-power spectra of 217 GHz data and maps that contain no HI information.

6.2 Methods

The objective is to estimate the true polarization properties – Stokes I_0, Q_0, and U_0 – from the data. In what follows we denote the true values I_0, Q_0, and U_0, and the measured values of these quantities I, Q, U. The polarized intensity $P_0 \equiv \sqrt{Q_0^2 + U_0^2}$, the polarization fraction $p_0 \equiv P_0/I_0$, and the polarization angle $\psi_0 \equiv \frac{1}{2}\mathrm{arctan}(\frac{U_0}{Q_0})$, and the measured values of these quantities are defined analogously.

The total intensity I is generally measured with higher signal to noise than the linear polarization parameters Q and U. In this initial study we assume the intensity is perfectly known, i.e. $I = I_0$ and $\sigma_I = 0$. This assumption allows us to work in two-dimensional (p, ψ) space.

6.2.1 Likelihood

The likelihood of the data is constructed from the *Planck* 353 GHz measurements of p, ψ, and noise properties. Because of the assumption that $\sigma_I = 0$, the covariances $\sigma_{II} = \sigma_{IQ} = \sigma_{IU} = 0$, and the covariance matrix reduces to

$$\Sigma = \begin{bmatrix} \sigma_{QQ} & \sigma_{QU} \\ \sigma_{QU} & \sigma_{UU} \end{bmatrix}. \tag{6.1}$$

Following Montier et al. (2015) we define

$$\Sigma_p = \frac{1}{I_0^2}\Sigma \tag{6.2}$$

and

$$\sigma_{p,G}^4 = \det(\Sigma_p). \tag{6.3}$$

The likelihood is then

$$f_{2D}\left(p, \psi | p_0, \psi_0, \Sigma_p\right) = \frac{p}{\pi\sigma_{p,G}^2} \exp\left(-\frac{1}{2}\,\mathbb{C}^{\mathrm{T}}\,\Sigma_p^{-1}\,\mathbb{C}\right), \tag{6.4}$$

where

$$\mathbb{C} = \begin{bmatrix} p\cos(2\psi) - p_0\cos(2\psi_0) \\ p\sin(2\psi) - p_0\sin(2\psi_0) \end{bmatrix}. \tag{6.5}$$

In the more general case where $I \neq I_0$, we will need to include the full I, Q, U covariance matrix, and the likelihood becomes three-dimensional.

6.2.2 Prior

We construct priors on the (p, ψ) plane for each pixel. In all cases we use the *Planck* polarization angle convention in Galactic coordinates. Because the RHT is run on H I data in Equatorial coordinates, this conversion is nontrivial. The RHT records linear intensity as a function of angle, binned by θ such that the linear power in a single angle bin is $R(\theta_i)$. We project the amplitude R into Galactic coordinates as a scalar. We then project and rotate each angle bin $\theta_i \rightarrow \psi_i$ such that it is in the desired projection and angle convention.

We use a flat prior in p, i.e.

$$\kappa(p_0') = \begin{cases} 1, & \text{if } p_a \leq p_0 \leq p_b \\ 0, & \text{otherwise} \end{cases} \tag{6.6}$$

prior to normalization.

Theoretically the polarized intensity cannot exceed the total intensity, and the total intensity must be nonnegative, i.e. $p_0 \in [0, 1]$. However in practice, $p_0 \in (-\infty, \infty)$ because of measurement noise. The imposition of $p_a = 0$ and $p_b = 1$ in Equation 6.6 constrains the polarization fraction to a physically realizable quantity, but we can do better when the polarization is measured with high signal to noise. We create an adaptive p_0 prior from the naive *Planck* measurement of p and its uncertainty. The variance in p is

$$\sigma_p^2 = \frac{1}{p^2 I_0^4} \left(Q^2 \sigma_{QQ} + U^2 \sigma_{UU} + 2QU\sigma_{QU} \right), \tag{6.7}$$

where, again, we have taken I to be perfectly known (Ade et al. 2015b). We then define the adaptive p_0 grid

$$\begin{aligned} p_a &= \max\{0, p - 7\sigma_p\} \\ p_b &= \min\{1, p + 7\sigma_p\}, \end{aligned} \tag{6.8}$$

such that p_0 is bounded by a minimum value of $p - 7\sigma_p$ or 0 and a maximum value of $p + 7\sigma_p$ or 1, whichever is the most restrictive bound in each case. Using a fixed number of sampling elements n_{sample}, this approach imposes a grid element size $\delta p_0 = (p_b - p_a)/n_{sample}$. The coarsest possible grid resolution is $\delta p_0 = 1/n_{sample}$, but the grid resolution becomes finer for pixels with lower uncertainties in p.

The prior is normalized over the (p_0, ψ_0) domain such that

$$\int_{\psi_a}^{\psi_b} \int_{p_a}^{p_b} \kappa(p_0, \psi_0) dp_0 d\psi_0 = 1. \tag{6.9}$$

We note that a flat prior in p is not an uninformative prior, and may not be the best choice if some sightlines are expected to be unpolarized (Quinn 2012). The maximum prior domain $p_0 \in [0, 1]$ is a reasonable first guess, but in reality the maximum theoretical polarization fraction is probably sub-unity, just as it is for synchrotron radiation. Better a priori knowledge can be used to improve Equation 6.6.

The ψ-dependence of the prior is based on the RHT analysis of GALFA-HI data. The implicit assumption is that the RHT distribution contains information about the true distribution of polarization angles. Chapters 4 and 5 support this assumption by demonstrating the alignment between HI and various probes of the plane-of-sky polarization angle.

The HI information can be encoded into a prior in many ways. We broadly consider two categories of HI-informed prior: a prior based on $R(\psi)$, the full RHT output, and a prior based on ψ_{RHT}, an RHT-based point estimate for the orientation of HI (see Equation 5.1).

The prior based on ψ_{RHT} is an axial von Mises distribution, the axial analogue to a circular normal distribution (Arnold & SenGupta 2006).

$$\kappa(\psi_0) = \frac{1}{\pi I_0(w)} \cosh\left(w \cos\left(\psi_0 - \psi_{RHT}\right)\right), \tag{6.10}$$

where $I_0(\cdot)$ is the modified Bessel function of the first kind, order 0, and w is a width parameter for which we use $w = 1/{\sigma_{\psi}}_{RHT}^2$, the inverse of the RHT angle variance computed from Equations 5.5 and 5.6. This allows the strength of the prior to vary based on the variance of the RHT distribution. We can instead use $w = 1/\sigma_{\delta\theta}^2$, the inverse variance of the angle difference histogram shown in Figure 5.2. This keeps the strength of the prior fixed, but is motivated by the data based on the dispersion in δ_θ in a given region of sky at a given angular resolution.

The ψ_{RHT}-based approach only uses the point estimate of the RHT data rather than the full RHT spectrum $R(\psi)$. We can instead define

$$\kappa(\psi_0) = R(\psi) + Z, \tag{6.11}$$

where Z is a variable that can be used to tune the relative strength of the HI information. When $Z = 0$, the prior is the raw RHT data. The final normalization of the prior (Equation 6.9) means that as $Z \to \infty$, the prior converges to a flat prior in (p_0, ψ_0). Z can be constant or vary spatially on the sky. One motivation for a non-zero Z is that the amplitude of $R(\psi)$ contains information that can be destroyed in the normalization. Consider an $R(\psi)$ with a single peak at a ψ value of $\pi/2$. If $R(\psi = \pi/2) = 1$, the HI data contains a stronger linear feature oriented at $\pi/2$ through that pixel than if $R(\psi = \pi/2) = 0.1$. Once normalized, however, these two $R(\psi)$ distributions will yield the same prior. We can mitigate this by choosing an $R(\psi)$ amplitude-dependent Z. We find that one reasonable choice is

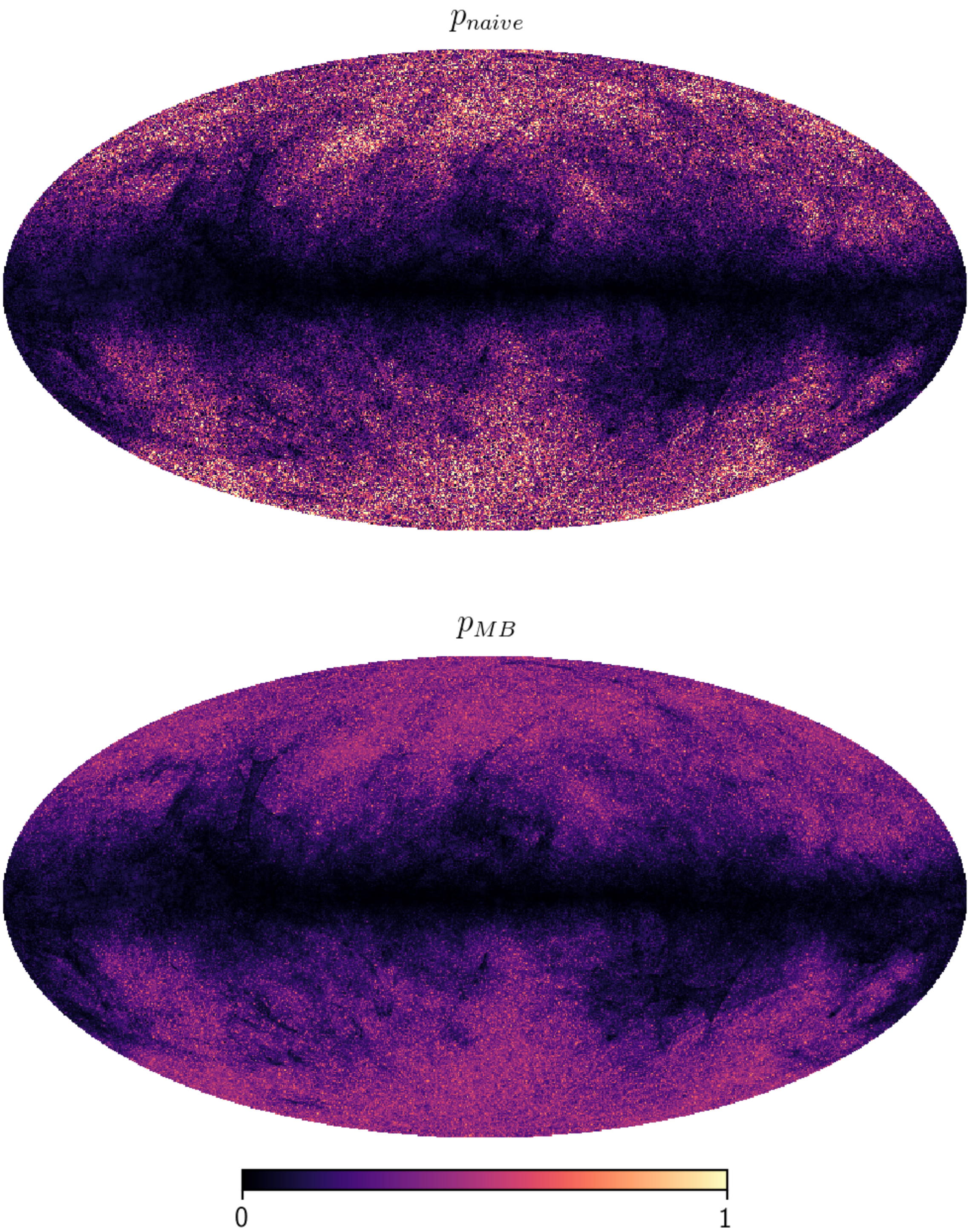

Figure 6.1: Naive *Planck* polarization fraction p (top) and mean Bayesian posterior estimate p_{MB} after application of a flat prior on $[p_a, p_b]$ as defined in Equations 6.6 and 6.8 (bottom). Data are plotted on $[0, 1]$, but p_{naive} values reach > 900.

$$Z = \max(R(\psi, x, y)) - \max(R(\psi)), \tag{6.12}$$

where $\max(R(\psi, x, y))$ is the global maximum of all $R(\psi)$ distributions in the region of sky considered, and $\max(R(\psi))$ is the maximum amplitude that the RHT distribution reaches for a particular pixel. We note that for a single velocity slice, the theoretical $\max(R(\psi))$ is 1, but we sum $R(\psi)$ data over multiple velocity channels so the theoretical maximum is $n_{channels}$.

As a point of comparison, we can use a flat $\kappa(\psi_0)$ in addition to the flat $\kappa(p_0)$ dependence, such that our total, normalized prior becomes

$$\kappa(p_0, \psi_0) = \begin{cases} \frac{1}{\pi(p_b - p_a)}, & \text{if } p_a \leq p_0 \leq p_b \\ 0, & \text{otherwise.} \end{cases} \tag{6.13}$$

Again, although this prior is flat, it is not uninformative. Because this prior is uniform in (p, ψ), it prefers points closer to the origin in (Q, U) space, as discussed in Quinn (2012). The effect of this flat prior on the all-sky distribution of the *Planck* 353 GHz polarization fraction is shown in Figure 6.1.

6.2.3 Posterior estimation

The posterior is defined from the likelihood and normalized prior using Bayes theorem:

$$B_{2D}(p_0, \psi_0 | p, \psi, \Sigma_p) = \frac{f_{2D}\left(p, \psi | p_0, \psi_0, \Sigma_p\right) \cdot \kappa(p_0, \psi_0)}{\int_0^\pi \int_{p_a}^{p_b} f_{2D}\left(p, \psi | p_0', \psi_0', \Sigma_p\right) \kappa(p_0', \psi_0') dp_0' d\psi_0'} \tag{6.14}$$

where both the prior and the posterior are normalized over the sampled domain $p_0 \in [p_a, p_b]$, $\psi_0 \in [0, \pi)$.

We then compute the mean Bayesian posterior estimator, the first moments of the pos-

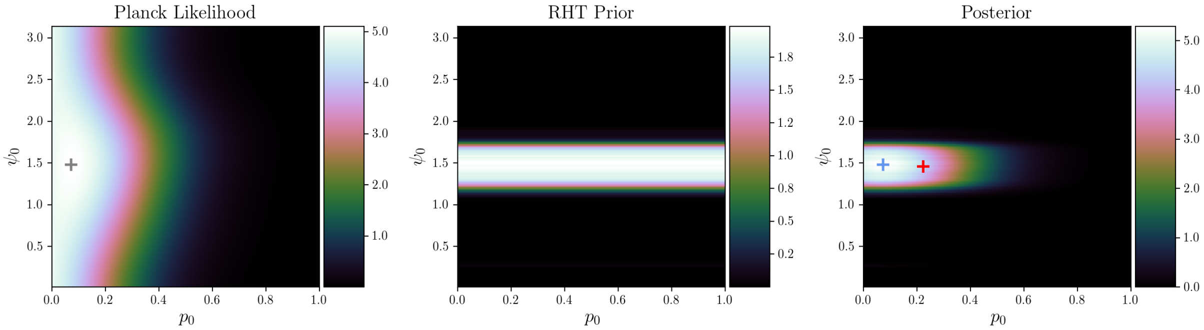

Figure 6.2: Demonstration of the Bayesian posterior construction for a single pixel. Left: the likelihood of the data, constructed from *Planck* 353 GHz linear polarization data and noise properties, including covariance information (Section 6.2.1). Gray cross shows the naive (p, ψ) *Planck* measurements. Middle: the HI-based prior. The ψ dependence of the prior is defined by the raw $R(\psi)$ distribution (Equation 6.11 with $Z = 0$). The p dependence is flat (Equation 6.6). Right: the resulting Bayesian posterior (Equation 6.14). Blue cross shows the maximum a posteriori values (p_{MAP}, ψ_{MAP}) (Equation 6.20). Red cross shows mean Bayesian estimator values (p_{MB}, ψ_{MB}) (Equations 6.15 and 6.16).

terior PDF:

$$\hat{p}_{MB} \equiv \int_{p_a}^{p_b} \int_0^{\pi} p_0 B_{2D}(p_0, \psi_0 | p, \psi, \Sigma_p) \mathrm{d}\psi_0 \mathrm{d}p_0 \tag{6.15}$$

$$\hat{\psi}_{MB} \equiv \int_{p_a}^{p_b} \int_0^{\pi} \psi_0 B_{2D}(p_0, \psi_0 | p, \psi, \Sigma_p) \mathrm{d}\psi_0 \mathrm{d}p_0. \tag{6.16}$$

Some care is required in the calculation of $\hat{\psi}_{MB}$ because of the circularity of the ψ integral (Montier et al. 2015). Rather than integrate Equation 6.16 directly, we compute separate Q and U first moment components,

$$\hat{q}_{MB} = \int_{p_a}^{p_b} \int_0^{\pi} \cos(2\psi_0) B_{2D}(p_0, \psi_0 | p, \psi, \Sigma_p) \mathrm{d}\psi_0 \mathrm{d}p_0 \tag{6.17}$$

$$\hat{u}_{MB} = \int_{p_a}^{p_b} \int_0^{\pi} \sin(2\psi_0) B_{2D}(p_0, \psi_0 | p, \psi, \Sigma_p) \mathrm{d}\psi_0 \mathrm{d}p_0 \tag{6.18}$$

and then find

$$\hat{\psi}_{MB} = \frac{1}{2}\mathrm{arctan}\frac{\hat{u}_{MB}}{\hat{q}_{MB}}. \tag{6.19}$$

An alternative approach discussed in Montier et al. (2015) is to simply compute the maximum a posteriori value

$$(\hat{p}_{MAP}, \hat{\psi}_{MAP}) = \underset{(p_0,\psi_0)}{\mathrm{argmax}}\, B_{2D}. \tag{6.20}$$

Figure 6.2 shows an example of these values computed for one pixel on the sky. For two-dimensional posteriors on (p, ψ), it is efficient to compute the posterior on a grid and sample it directly. For posterior estimation on (I, p, ψ), it may be more efficient to sample the posterior using a Markov Chain Monte Carlo (MCMC) method. Uncertainties for the $\hat{p}_{MB}, \hat{\psi}_{MB}$ estimators can be estimated from the second moments of the posterior distribution (Montier et al. 2015).

6.3 New foreground maps: progress and future directions

We follow the procedures outlined in Section 6.2 for the region of sky analyzed in Chapter 5. We test several methods of constructing an HI-based prior. The best way to test our method is to compare the resulting maps with independent probes of the polarized dust emission. We compute cross-power spectra between maps derived from our procedure and *Planck* 217 GHz polarization maps. By cross-correlating our maps with lower-frequency *Planck* data, we can ask whether the priors we introduce produce maps that are lower-noise representations of the true polarized dust foreground.

Our Bayesian pipeline computes foreground maps in the (p, ψ) plane, assuming $I = I_0 =$

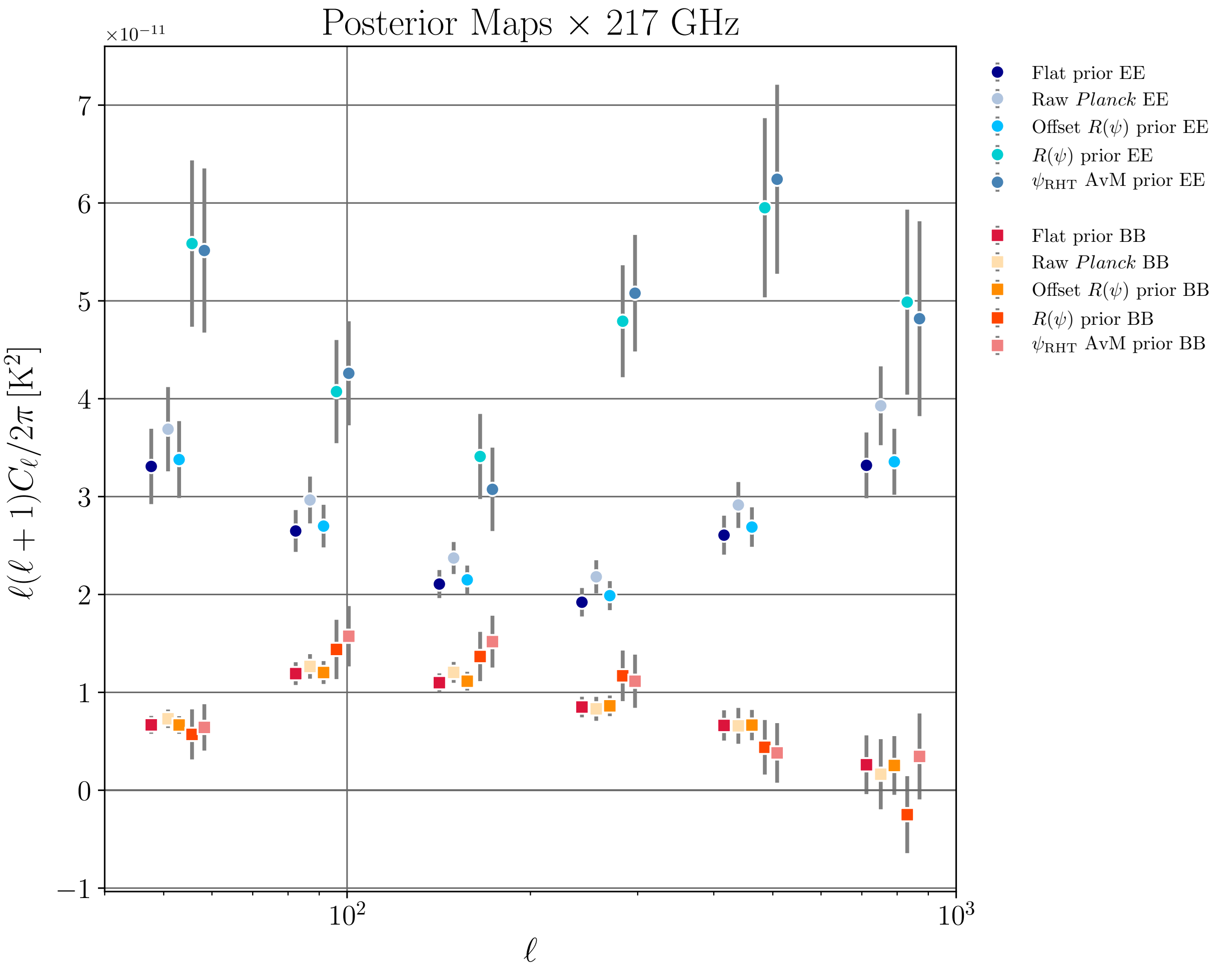

Figure 6.3: *EE* and *BB* cross-power spectra for various input maps × *Planck* 217 GHz polarization maps. Error bars are computed from the corresponding autocorrelation spectra. Data are shown for six logarithmically-spaced multipole bins centered at $l = [53, 91.5, 157.5, 270, 462, 791.5]$. "Flat prior" indicates the use of a uniform prior over (p, ψ), i.e. Equation 6.13. "Raw *Planck*" indicates the cross-power spectra for the raw Q_{353}, U_{353} data, with no Bayesian estimation. "Offset $R(\psi)$ prior" uses the prior from Equation 6.11 with Z as defined in Equation 6.12. "$R(\psi)$ prior" is the raw RHT output applied as the prior on ψ, i.e. Equation 6.11 with $Z = 0$. "ψ_{RHT} AvM prior" is the prior constructed from ψ_{RHT} using the axial von Mises distribution, i.e. Equation 6.10 with $w = 1/\sigma_{\psi_{RHT}}^2$. All templates except the "raw" data are constructed from the mean Bayesian estimator of the posterior.

I_{353}. We combine these components into Q, U template maps by combining the posterior estimators $\hat{p}$ and $\hat{\psi}$ with the 353 GHz total intensity I_{353}

$$\begin{aligned} \hat{Q} &= I_{353}\,\hat{p}\,\cos(2\hat{\psi}) \\ \hat{U} &= I_{353}\,\hat{p}\,\sin(2\hat{\psi}). \end{aligned} \qquad (6.21)$$

From these we compute EE and BB power spectra using `polspice` (Chon et al. 2004).

We show some representative examples of the cross-power spectra between maps constructed from our Bayesian posterior estimation and *Planck* 217 GHz data in Figure 6.3. The error bars are computed from the autocorrelation spectrum of each template in the Gaussian approximation. All of the templates used to compute the cross-power spectra are computed using Equation 6.21 with the mean Bayesian estimator of the posterior, i.e. $\hat{p}_{MB}$ and $\hat{\psi}_{MB}$. The one exception is the "raw *Planck*" data, which are simply the Q_{353}, U_{353} maps, with no prior applied.

We find that using an $R(\psi)$ prior (Equation 6.11) with Z as defined in Equation 6.12 leads to a modestly more significant cross-correlation with the 217 GHz data than using a flat prior (Equation 6.13). Both this $R(\psi)$ prior and the flat prior yield error bars that are smaller than those for the raw *Planck* data. Using Equation 6.11 with $Z = 0$ and constructing the prior from ψ_{RHT} using the axial von Mises distribution (Equation 6.10) both generally lead to larger error bars, presumably because the prior is too strong relative to the likelihood in pixels where the RHT data is dominated by noise.

It appears promising that HI-based priors can improve the polarized foreground map, but the optimal formulation of an HI-based prior is still being pursued. There are a number of avenues to explore. One is the spatial resolution of the maps. Currently we do not apply any type of spatial smoothing to the RHT data. The RHT data by nature has a very variable signal-to-noise, because regions that lie in between well-detected linear features may have noisy, low-amplitude RHT spectra (see Chapter 4 for a description of the algorithm). One remedy for this may be to smooth the RHT data, and build priors based on lower angular resolution RHT data. From a Bayesian perspective, this means that the prior would articulate a belief that the polarization angle does not physically vary on angular scales smaller than the smoothing scale of the RHT data.

Both the shape and the amplitude of the RHT prior contain information on the underlying HI distribution. The introduction of an RHT amplitude-dependent Z in Equation 6.11 is an attempt to encode both of these aspects of the RHT distribution in a way that will not be destroyed by the normalization of the prior. Other choices of Z, or other constructions of the prior that achieve this same end, should be explored. These priors should be tested on different, and larger, areas of sky. We can also cross-correlate the new foreground maps with *Planck* 143 GHz data, or data from other CMB experiments.

Further afield, there are a number of ways that this Bayesian procedure can be extended. As mentioned above, the assumption that I is perfectly known can be relaxed, and this pipeline can be run in three-dimensional I, Q, U space. In that case HI data can enter as a prior on I, as well, as N_{HI} is a strong predictor of I in the diffuse ISM. As mentioned in Chapter 5, changes in the orientation of HI as a function of velocity may trace line-of-sight field tangling, and therefore be useful as a predictor of p. It may also be beneficial to weight the RHT contribution in each velocity channel by the intensity of the HI emission at that channel. Eventually, we can introduce additional data into the priors, such as starlight polarization measurements. Indeed, as long as the significance of the cross-correlation with lower-frequency data is an accurate measure of how well a given foreground map reflects the underlying truth, this method can be used to test data-driven models of how the ISM affects the polarized sky.

Chapter 7

Conclusion

The study of interstellar magnetism provides no lack of mystery. Our understanding of the interstellar magnetic field has dramatically expanded since its discovery, but many foundational questions remain. The magnetic field's origin, structure, and role in ISM processes remain poorly understood, and present a formidable challenge. The abstruse nature of cosmic magnetism means that insights are hard-won but far-reaching in their implications. Hence the broad scope of this Thesis, which advances our understanding of the role of magnetism in accretion disks, in the diffuse ISM, and as a foreground for cosmology experiments. Along the way we employ analytical theory, numerical simulations, and observations: the full toolbox of astrophysical investigation.

7.1 Summary of results

In Chapters 2 and 3 we analyze the MRI, a plasma instability that drives accretion and turbulence in astrophysical disks. We study the MRI using the mathematical framework of pattern formation, in which nonlinear interactions give rise to the spontaneous selection of certain spatial features. We conduct a multiscale perturbative treatment of the nonideal, axisymmetric MRI, in the limit where nonlinear interactions are weak. In Chapter 2 we analyze the MRI in a local approximation, and in Chapter 3 we consider a fully cylindrical geometry. In both cases we derive the behavior of the MRI on long spatial and temporal scales, and find that the amplitude of the magnetohydrodynamic variables are modulated by a Ginzburg-Landau equation. For the standard MRI, when the initialized magnetic field is purely vertical, we derive a real Ginzburg-Landau equation. For the helical MRI, an overstability that arises when the initialized field has both vertical and azimuthal components, we derive a complex Ginzburg-Landau equation. This indicates that the saturated state of the MRI system will be unstable on long space- and timescales to various instabilities, whose character will depend on whether the background field is helical or only poloidal.

In Chapter 4 we introduce a new algorithm, the Rolling Hough Transform, for measuring the linear intensity of image features as a function of orientation. We use the RHT to characterize the orientation of slender linear features in high-dynamic range observations of the diffuse ISM. We demonstrate for the first time that the cold neutral medium of the ISM is generically organized into linear "fibers" that are well aligned with the interstellar magnetic field as probed by starlight polarization.

With the release of *Planck* 353 GHz dust polarization maps, our view of the plane-of-sky magnetic field orientation in the diffuse ISM was no longer limited to sparse starlight polarization measurements. In Chapter 5 we show that linear features in the diffuse HI trace the magnetic field measured in polarized dust emission extremely well. We demonstrate that the structure of the cold neutral medium is more tightly coupled to the magnetic field than previously known. Because the orientation of neutral hydrogen is an independent predictor of the local dust polarization angle, our work provides a new tool in the search for inflationary gravitational wave B-mode polarization in the cosmic microwave background, which is currently limited by foreground dust contamination. In Chapter 6 we develop a

Bayesian method for creating CMB foreground maps that self-consistently incorporate dust polarization data and HI orientation measurements. The use of HI orientation as a prior on the dust polarization angle appears to be a promising method for generating higher-fidelity maps of the polarized CMB foreground.

7.2 Impact of the Rolling Hough Transform

Much of the work in this Dissertation (Chapters 2 - 5) is already published in the literature, but as these contributions are relatively recent we do not purport to know what their full influence on the field will be. However Chapter 4 was published first, in 2014, and the Rolling Hough Transform algorithm was made public at the same time.[1] The RHT is a general-purpose machine vision code, in that it can be applied to any image data. It has since been adopted by researchers in several areas of astrophysics, and here we briefly highlight some applications of the RHT in the recent literature.

The RHT was used to study L1642, an unusually high-latitude star-forming cloud (Malinen et al. 2016). The authors used the RHT to compare the orientation of *Herschel* dust emission structures to the orientation of the magnetic field as probed by *Planck* 353 GHz polarized dust emission. A principal component analysis of the histogram of relative orientations of density structures and the magnetic field revealed that the diffuse molecular gas is preferentially organized into striations that are aligned with the field. In the denser gas, there is some evidence for a bimodal distribution of structure orientation parallel and perpendicular to the field.

Koch & Rosolowsky (2015) develop a method for isolating filaments in image data that uses the RHT to measure the orientations of identified filaments. Their algorithm, "Fil-

---

[1] The RHT webpage can be found at http://seclark.github.io/RHT/.

Finder", identifies filamentary structure based on local changes in brightness, and successfully identifies both bright molecular filaments and fainter structures in more diffuse gas. The authors applied FilFinder to *Herschel* observations of Gould Belt molecular clouds, and used the RHT to analyze the distribution of orientation of the filaments (relative to one another, not relative to the magnetic field). They found that the diffuse molecular striations in some clouds are preferentially oriented parallel to one another, while other regions display no preferred orientation.

The RHT can also be applied to synthetic observations of simulations. Inoue & Inutsuka (2016) show that the alignment of synthetic density structures with the magnetic field in simulations of turbulence depends on the strength of the local shear strain. The level of shear strain in a region is mediated by the angles between the propagation direction of shocks and the orientation of the magnetic field. The authors demonstrate that HI density structures in the ISM that form after shocks compress the diffuse warm neutral medium will be preferentially aligned with the magnetic field as long as the simulated shocks propagate into a realistic level of upstream turbulence.

Recently the RHT was used to analyze fibrils, fine linear features in the solar chromosphere. Fibrils extend radially from photospheric magnetic field concentrations, and so have long been assumed to trace the magnetic field lines. Asensio Ramos et al. (2017) use the RHT to demonstrate that the fibrils are indeed tracing the local magnetic field, measured using Zeeman observations of the CaII 8542 Å line. The authors quantify the degree of dispersion between fibril orientation and the field orientation, and show that the dispersion increases in weakly magnetized regions. Magnetohydrodynamic simulations indicate that ambipolar diffusion can cause fibrils to be misaligned with the magnetic field (Martínez-Sykora et al. 2016). Thus Asensio Ramos et al. (2017) suggest that RHT analyses of fibril observations may be used to determine the role of ambipolar diffusion in the chromosphere.

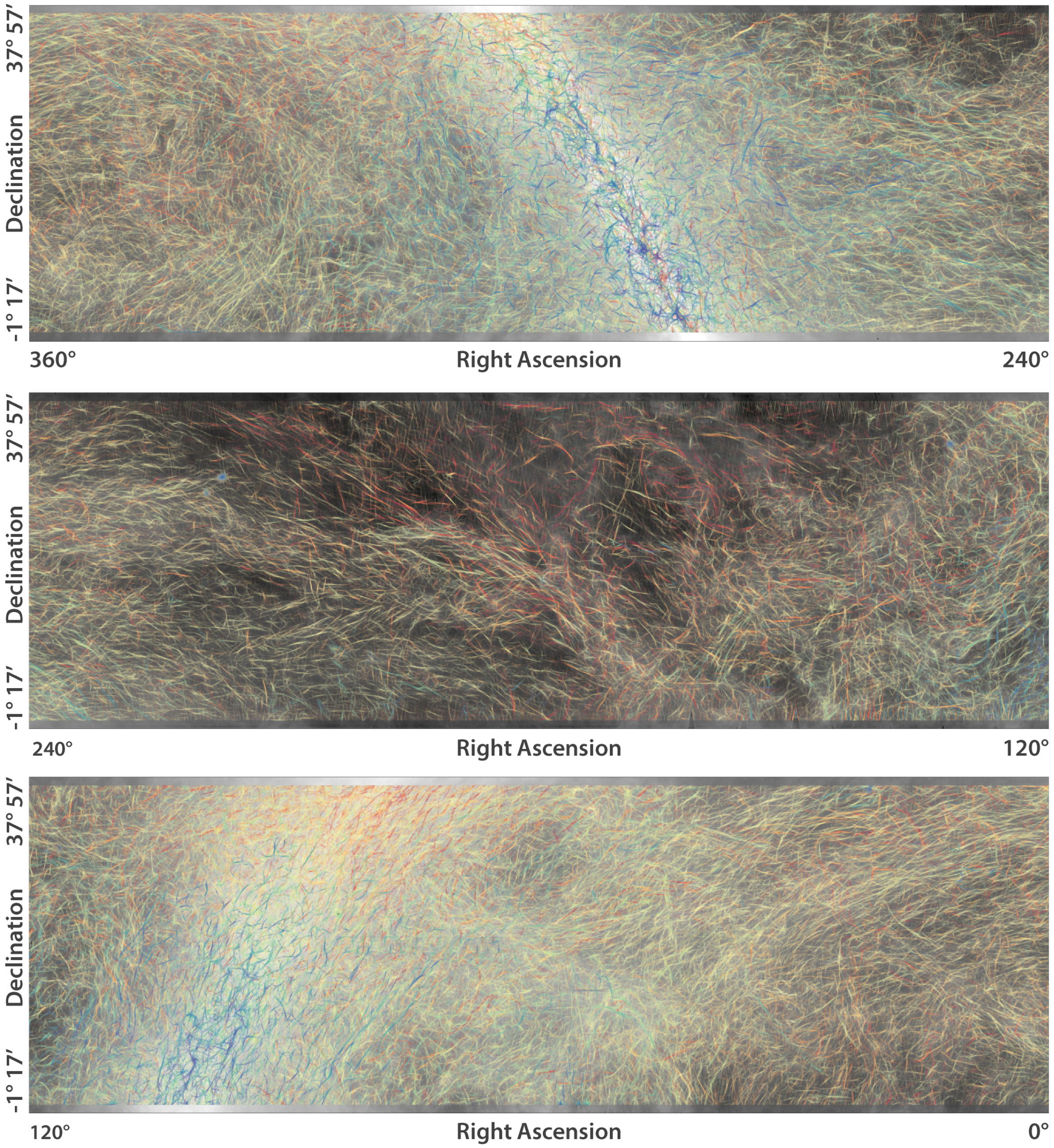

Figure 7.1: Visualization of the Rolling Hough Transform of the entire GALFA-HI sky. Background grayscale image is the integrated over the velocity interval $|\mathrm{v}_{\mathrm{lsr}}| \leq 90$ km s^{-1} corrected for stray radiation. Overlaid structures show the RHT backprojection, colored by velocity channel, from -36.4 km s^{-1} (purple) to $+37.2$ km s^{-1} (red). The opacity of the features in each velocity channel represents the amplitude of the RHT backprojection $\int R(\theta, x, y)\, d\theta$ (see Section 4.2.1). A version of this Figure will appear in Peek et al. (2017).

We have applied the RHT to the entire Arecibo sky over a range of velocity channels (Figure 7.1), and RHT data will be provided to the public along with the second data release of GALFA-HI (Peek et al. 2017). This will encourage exploration of the orientation of high-resolution HI by other authors.

7.3 Future work

A number of avenues for future work have already been presented in each preceding Chapter. There are many more applications of the weakly nonlinear MRI framework developed in Chapters 2 and 3, and of the RHT presented in Chapter 4. The discovery that linear structures in the diffuse neutral medium are well aligned with the local magnetic field, presented in Chapters 4 and 5, is the basis for the ongoing development of polarized CMB foreground maps discussed in Chapter 6. Still, there is more to be done. The work presented in this Thesis has far-reaching applications, and here we present several novel directions that remain to be explored.

7.3.1 Damped eigenmode saturation of the MRI

In Section 2.4 we presented the realization that the fastest-growing linear modes in the shearing box MRI are no longer solutions to the nonlinear MRI equations in the presence of ambipolar diffusion. This means that nonlinear interaction between primary MRI modes is no longer precluded as a saturation mechanism in this setup. For the first time, we can analytically investigate whether nonlinear saturation in an MRI shearing box can occur via some mechanism other than parasitic modes.

One such mechanism that can now be explored is the role of damped eigenmodes in MRI saturation. Typical treatments of turbulence-mediated saturation invoke an energy cascade down a wavenumber spectrum that ends at some dissipation scale. A weakly nonlinear approach like the one presented in Chapters 2 and 3 analyzes a finite band of excited modes. In both treatments, damped modes – eigenmodes of the system that are linearly damped for all wavenumbers – are ignored. Because the linear time evolution of damped Fourier modes is simple exponential decay, one might assume that all pertinent nonlinear interactions occur in the wavevector plane of the unstable mode, e.g. in the (k_x, k_z) plane for axisymmetric perturbations. However, analyses restricted to this plane represent an incomplete sample of the interactions – and therefore fluid motions – available to the system. A complete description would allow nonlinear interactions between not only different wavevectors, but different mode families at different wavevectors (see Figure 1 in Hatch et al. 2011, for a schematic depiction of inter-mode coupling).

Nonlinear coupling between damped and unstable eigenmodes has been studied extensively in the plasma literature, and these interactions are important for the saturation of a number of plasma instabilities (e.g. Terry et al. 2006; Makwana et al. 2011; Hatch et al. 2011; Fraser et al. 2017). The techniques developed in the plasma literature can be applied to the local MRI system described in Section 2.4. Rather than analyzing only the evolution of the most unstable eigenmode, we can project the MRI equations into the basis set of the linear eigenmodes. The nonlinear terms in the MRI equations will then couple the four mode families of incompressible, rotational MHD, and we can analyze the contribution of damped eigenmodes to MRI saturation. We can also compare this analysis with direct numerical simulations of the shearing box MRI with ambipolar diffusion.

7.3.2 Asymmetry in the polarized sky

B-mode polarization is one of two rotational invariants into which we decompose the polarized sky, along with E-mode polarization. Naively, one might expect that the power in the E-mode and B-mode dust polarization signal is equal. This is what would arise for a randomly oriented polarization field, or for a constant magnetic field with fluctuating polarized intensities (Zaldarriaga 2001). This parity is predicted by the state-of-the-art models of the polarized dust foreground (Delabrouille et al. 2013; O'Dea et al. 2011). But *Planck* revealed that in fact there is a significant asymmetry in the E- and B-mode cross-correlation amplitudes, $C_l^{EE}/C_l^{BB} \sim 2$. This ratio seems to hold over the whole sky (Adam et al. 2014).

In Chapter 5, we find $EE/BB \sim 2$ using E- and B-mode template maps constructed using only HI orientation. This suggests that the missing physics in the polarization models is the alignment between ISM density structures and the magnetic field. We can investigate this idea phenomenologically, by calculating the EE/BB ratio produced by models of the polarized foreground with different degrees of alignment between intensity structures and the magnetic field. These can be toy models, but we can also use simulations to relate structure-field alignment to the governing physics of the turbulent ISM. Observations indicate an apparent turnover in the alignment of *Planck* density structures, from preferentially oriented parallel to the magnetic field to preferentially oriented perpendicular to the field, at column densities of $\sim 10^{21}$. The promise of using density alignment as a constraint for theories of star formation is driving an interest in analyzing the structure alignment in high-resolution simulations of star-forming molecular clouds. Whether or not structure alignment is driving the EE/BB asymmetry, this ratio provides an additional constraint on synthetic observations of the polarized dust emission in simulations.

The physics responsible for intensity structure-field alignment and the EE/BB asymmetry can also be explored analytically. A first step toward connecting the EE/BB ratio to the physics of the ISM was recently made by Caldwell et al. (2017). The authors calculated the expected EE/BB and TE (temperature-E-mode) correlations for basic magnetohydrodynamic waves. They found that the observations cannot be explained by simple MHD turbulence – and indeed, neither can the degree of alignment between ISM structures and the magnetic field observed in the ISM (Clark et al. 2014). We can move beyond this simple picture by deriving the expected EE/BB ratio for an ISM that includes nonideal effects, as well as for an ISM dominated by various instabilities, which should contribute to the E- and B-mode power via linear combinations of the simple waves derived in Caldwell et al. (2017). A direct link between statistical observations like the EE/BB ratio to the physics of magnetically aligned filament formation would be an extremely powerful diagnostic.

7.3.3 Toward magnetic tomography

Our understanding of the magnetic fields in the interstellar medium is ultimately limited by our position within it. We view the ISM in projection, and a truly three-dimensional picture of the magnetized ISM remains elusive. However, new techniques for synthesizing large datasets are changing this. The combination of stellar distance and reddening measurements has enabled the first three-dimensional dust maps: estimates of the distribution of dust as a function of distance from the Sun (Lallement et al. 2014; Green et al. 2015). The three-dimensional distribution of HI can be inferred from the Galactic rotation profile and from dust extinction measurements (e.g. Levine 2006).

Starlight polarization measurements, which individually give only the projected plane-of-sky field orientation, can in principle be combined with three-dimensional dust maps to probe the change in this field component along the line of sight. The properties of polarized dust, which currently trace the entire line of sight, can be mapped onto this three-dimensional picture: for example, the dust polarization fraction can constrain the degree of field disorder along the line of sight. In Chapters 4 and 5 we link the orientation of diffuse HI to starlight polarization and dust polarization measurements, respectively. The realization that HI morphology is a powerful diagnostic of the ambient magnetic field provides an additional probe of the plane-of-sky magnetic field that can be linked to the three-dimensional gas distribution in the Galaxy.

In combination with traditional probes of the magnetic field, particularly Faraday rotation measures, these techniques will enable a clearer picture of the Galactic magnetic field. Only with clever multi-wavelength methods can we hope to de-project our observations back into their full three-dimensional context. The power of this type of "magnetic tomography" will only be amplified as the Square Kilometer Array and other next-generation telescopes come online. Planned observations of the ISM, both for its own sake and for CMB foreground removal, will provide an influx of new data over the coming decades. If we can develop theoretical models capable of taking full advantage of these observations, the future is bright for continued progress in our knowledge of cosmic magnetism. Dedicated study must continue, that magnetic fields might no longer represent a measure of our ignorance, but a triumph of our understanding of the interstellar medium.

Bibliography

Adam, R., Ade, P. A. R., Aghanim, N., Akrami, Y., Alves, M. I. R., Arnaud, M., Arroja, F., Aumont, J., Baccigalupi, C., Ballardini, M., Banday, A. J., Barreiro, R. B., Bartlett, J. G., Bartolo, N., Basak, S., Battaglia, P., Battaner, E., Battye, R., Benabed, K., Benoît, A., Benoit-Lévy, A., Bernard, J. P., Bersanelli, M., Bertincourt, B., Bielewicz, P., Bonaldi, A., Bonavera, L., Bond, J. R., Borrill, J., Bouchet, F. R., Boulanger, F., Bucher, M., Burigana, C., Butler, R. C., Calabrese, E., Cardoso, J. F., Carvalho, P., Casaponsa, B., Castex, G., Catalano, A., Challinor, A., Chamballu, A., Chary, R. R., Chiang, H. C., Chluba, J., Christensen, P. R., Church, S., Clemens, M., Clements, D. L., Colombi, S., Colombo, L. P. L., Combet, C., Comis, B., Contreras, D., Couchot, F., Coulais, A., Crill, B. P., Cruz, M., Curto, A., Cuttaia, F., Danese, L., Davies, R. D., Davis, R. J., de Bernardis, P., de Rosa, A., de Zotti, G., Delabrouille, J., Delouis, J. M., Désert, F. X., Di Valentino, E., Dickinson, C., Diego, J. M., Dolag, K., Dole, H., Donzelli, S., Doré, O., Douspis, M., Ducout, A., Dunkley, J., Dupac, X., Efstathiou, G., Eisenhardt, P. R. M., Elsner, F., Enßlin, T. A., Eriksen, H. K., Falgarone, E., Fantaye, Y., Farhang, M., Feeney, S., Fergusson, J., Fernandez-Cobos, R., Feroz, F., Finelli, F., Florido, E., Forni, O., Frailis, M., Fraisse, A. A., Franceschet, C., Franceschi, E., Frejsel, A., Frolov, A., Galeotta, S., Galli, S., Ganga, K., Gauthier, C., Génova-Santos, R. T., Gerbino, M., Ghosh, T., Giard, M., Giraud-Héraud, Y., Giusarma, E., Gjerløw, E., González-

Nuevo, J., Górski, K. M., Grainge, K. J. B., Gratton, S., Gregorio, A., Gruppuso, A., Gudmundsson, J. E., Hamann, J., Handley, W., Hansen, F. K., Hanson, D., Harrison, D. L., Heavens, A., Helou, G., Henrot-Versillé, S., Hernández-Monteagudo, C., Herranz, D., Hildebrandt, S. R., Hivon, E., Hobson, M., Holmes, W. A., Hornstrup, A., Hovest, W., Huang, Z., Huffenberger, K. M., Hurier, G., Jaffe, A. H., Jaffe, T. R., Jin, T., Jones, W. C., Juvela, M., Karakci, A., Keihänen, E., Keskitalo, R., Kiiveri, K., Kim, J., Kisner, T. S., Kneissl, R., Knoche, J., Krachmalnicoff, N., Kunz, M., Kurki-Suonio, H., Lacasa, F., Lagache, G., Lähteenmäki, A., Lamarre, J. M., Langer, M., Lasenby, A., Lattanzi, M., Lawrence, C. R., Le Jeune, M., Leahy, J. P., Lellouch, E., Leonardi, R., León-Tavares, J., Lesgourgues, J., Levrier, F., Lewis, A., Liguori, M., Lilje, P. B., Linden-Vørnle, M., Lindholm, V., Liu, H., Lopez-Caniego, M., Lubin, P. M., Ma, Y. Z., Macias-Pérez, J. F., Maggio, G., Mak, D. S. Y., Mandolesi, N., Mangilli, A., Marchini, A., Marcos-Caballero, A., Marinucci, D., Marshall, D. J., Martin, P. G., Martinelli, M., Martinez-González, E., Masi, S., Matarrese, S., Mazzotta, P., McEwen, J. D., McGehee, P., Mei, S., Meinhold, P. R., Melchiorri, A., Melin, J. B., Mendes, L., Mennella, A., Migliaccio, M., Mikkelsen, K., Mitra, S., Miville-Deschênes, M. A., Molinari, D., Moneti, A., Montier, L., Moreno, R., Morgante, G., Mortlock, D., Moss, A., Mottet, S., Müenchmeyer, M., Munshi, D., Murphy, J. A., Narimani, A., Naselsky, P., Nastasi, A., Nati, F., Natoli, P., Negrello, M., Netterfield, C. B., Nørgaard-Nielsen, H. U., Noviello, F., Novikov, D., Novikov, I., Olamaie, M., Oppermann, N., Orlando, E., Oxborrow, C. A., Paci, F., Pagano, L., Pajot, F., Paladini, R., Pandolfi, S., Paoletti, D., Partridge, B., Pasian, F., Patanchon, G., Pearson, T. J., Peel, M., Peiris, H. V., Pelkonen, V. M., Perdereau, O., Perotto, L., Perrott, Y. C., Perrotta, F., Pettorino, V., Piacentini, F., Piat, M., Pierpaoli, E., Pietrobon, D., Plaszczynski, S., Pogosyan, D., Pointecouteau, E., Polenta, G., Popa, L., Pratt, G. W., Prezeau, G., Prunet, S., Puget, J. L., Rachen, J. P., Racine, B., Reach, W. T., Rebolo, R., Reinecke, M., Remazeilles, M., Renault, C., Renzi, A., Ristorcelli, I., Rocha, G., Roman, M., Romelli, E., Rosset, C., Rossetti, M., Rotti, A., Roudier, G., d'Orfeuil, B. R., Rowan-Robinson, M., Rubiño-Martín, J. A., Ruiz-Granados, B., Rumsey, C., Rusholme, B., Said, N., Salvatelli, V., Salvati, L., Sandri, M., Sanghera, H. S., Santos, D., Saunders, R. D. E., Sauvé, A., Savelainen, M., Savini, G., Schaefer, B. M., Schammel, M. P., Scott, D., Seiffert, M. D., Serra, P., Shellard, E. P. S., Shimwell, T. W., Shiraishi, M., Smith, K., Souradeep, T., Spencer, L. D., Spinelli, M., Stanford, S. A., Stern, D., Stolyarov, V., Stompor, R., Strong, A. W., Sudiwala, R., Sunyaev, R., Sutter, P., Sutton, D., Suur-Uski, A. S., Sygnet, J. F., Tauber, J. A., Tavagnacco, D., Terenzi, L., Texier, D., Toffolatti, L., Tomasi, M., Tornikoski, M., Tristram, M., Troja, A., Trombetti, T., Tucci, M., Tuovinen, J., Türler, M., Umana, G., Valenziano, L., Valiviita, J., Van Tent, B., Vassallo, T., Vidal, M., Viel, M., Vielva, P., Villa, F., Wade, L. A., Walter, B., Wandelt, B. D., Watson, R., Wehus, I. K., Welikala, N., Weller, J., White, M., White, S. D. M., Wilkinson, A., Yvon, D., Zacchei, A., Zibin, J. P., Zonca, A., & Planck Collaboration. 2015a, Astronomy and Astrophysics, 594, A1

Adam, R., Ade, P. A. R., Aghanim, N., Arnaud, M., Ashdown, M., Aumont, J., Baccigalupi, C., Banday, A. J., Barreiro, R. B., Bartolo, N., Battaner, E., Benabed, K., Benoît, A., Benoit-Lévy, A., Bernard, J. P., Bersanelli, M., Bertincourt, B., Bielewicz, P., Bonavera, L., Bond, J. R., Borrill, J., Bouchet, F. R., Boulanger, F., Bucher, M., Burigana, C., Calabrese, E., Cardoso, J. F., Catalano, A., Challinor, A., Chamballu, A., Chiang, H. C., Christensen, P. R., Clements, D. L., Colombi, S., Colombo, L. P. L., Combet, C., Couchot, F., Coulais, A., Crill, B. P., Curto, A., Cuttaia, F., Danese, L., Davies, R. D., Davis, R. J., de Bernardis, P., de Rosa, A., de Zotti, G., Delabrouille, J., Delouis, J. M., Désert, F. X., Diego, J. M., Dole, H., Donzelli, S., Doré, O., Douspis, M., Ducout, A., Dupac, X., Efstathiou, G., Elsner, F., Enßlin, T. A., Eriksen, H. K., Falgarone, E., Fergusson, J., Finelli, F., Forni, O., Frailis, M., Fraisse, A. A., Franceschi, E., Frejsel, A., Galeotta, S., Galli, S., Ganga, K., Ghosh, T., Giard, M., Giraud-Héraud, Y., Gjerløw, E., González-Nuevo, J., Górski, K. M., Gratton, S., Gruppuso, A., Gudmundsson, J. E., Hansen, F. K., Hanson, D., Harrison, D. L., Henrot-Versillé, S., Herranz, D., Hildebrandt, S. R., Hivon, E., Hobson, M., Holmes, W. A., Hornstrup, A., Hovest, W., Huffenberger, K. M., Hurier, G., Jaffe, A. H., Jaffe, T. R., Jones, W. C., Juvela, M., Keihänen, E., Keskitalo, R., Kisner, T. S., Kneissl, R., Knoche, J., Kunz, M., Kurki-Suonio, H., Lagache, G., Lamarre, J. M., Lasenby, A., Lattanzi, M., Lawrence, C. R., Le Jeune, M., Leahy, J. P., Lellouch, E., Leonardi, R., Lesgourgues, J., Levrier, F., Liguori, M., Lilje, P. B., Linden-Vørnle, M., Lopez-Caniego, M., Lubin, P. M., Macias-Pérez, J. F., Maggio, G., Maino, D., Mandolesi, N., Mangilli, A., Martin, P. G., Martinez-González, E., Masi, S., Matarrese, S., Mazzotta, P., McGehee, P., Melchiorri, A., Mendes, L., Mennella, A., Migliaccio, M., Mitra, S., Miville-Deschênes, M. A., Moneti, A., Montier, L., Moreno, R., Morgante, G., Mortlock, D., Moss, A., Mottet, S., Munshi, D., Murphy, J. A., Naselsky, P., Nati, F., Natoli, P., Netterfield, C. B., Nørgaard-Nielsen, H. U., Noviello, F., Novikov, D., Novikov, I., Oxborrow, C. A., Paci, F., Pagano, L., Pajot, F., Paoletti, D., Pasian, F., Patanchon, G., Pearson, T. J., Perdereau, O., Perotto, L., Perrotta, F., Pettorino, V., Piacentini, F., Piat, M., Pierpaoli, E., Pietrobon, D., Plaszczynski, S., Pointecouteau, E., Polenta, G., Pratt, G. W., Prezeau, G., Prunet, S., Puget, J. L., Rachen, J. P., Reinecke, M., Remazeilles, M., Renault, C., Renzi, A., Ristorcelli, I., Rocha, G., Rosset, C., Rossetti, M., Roudier, G., Rusholme, B., Sandri, M., Santos, D., Sauvé, A., Savelainen, M., Savini, G., Scott, D., Seiffert, M. D., Shellard, E. P. S., Spencer, L. D., Stolyarov, V., Stompor, R., Sudiwala, R., Sutton, D., Suur-Uski, A. S., Sygnet, J. F., Tauber, J. A., Terenzi, L., Toffolatti, L., Tomasi, M., Tristram, M., Tucci, M., Tuovinen, J., Valenziano, L., Valiviita, J., Van Tent, B., Vielva, P., Villa, F., Wade, L. A., Wandelt, B. D., Watson, R., Wehus, I. K., Yvon, D., Zacchei, A., Zonca, A., & Planck Collaboration. 2015b, Astronomy and Astrophysics, 594, A8

Adam, R., Ade, P. A. R., Aghanim, N., Arnaud, M., Aumont, J., Baccigalupi, C., Banday, A. J., Barreiro, R. B., Bartlett, J. G., Bartolo, N., Battaner, E., Benabed, K., Benoit-Lévy, A., Bernard, J. P., Bersanelli, M., Bielewicz, P., Bonaldi, A., Bonavera, L., Bond, J. R., Borrill, J., Bouchet, F. R., Boulanger, F., Bracco, A., Bucher, M., Burigana, C., Butler, R. C., Calabrese, E., Cardoso, J. F., Catalano, A., Challinor, A., Chamballu, A., Chary, R. R., Chiang, H. C., Christensen, P. R., Clements, D. L., Colombi, S., Colombo, L. P. L., Combet, C., Couchot, F., Coulais, A., Crill, B. P., Curto, A., Cuttaia, F., Danese, L., Davies, R. D., Davis, R. J., de Bernardis, P., de Zotti, G., Delabrouille, J., Delouis, J. M., Désert, F. X., Dickinson, C., Diego, J. M., Dolag, K., Dole, H., Donzelli, S., Doré, O., Douspis, M., Ducout, A., Dunkley, J., Dupac, X., Efstathiou, G., Elsner, F., Enßlin, T. A., Eriksen, H. K., Falgarone, E., Finelli, F., Forni, O., Frailis, M., Fraisse, A. A., Franceschi, E., Frejsel, A., Galeotta, S., Galli, S., Ganga, K., Ghosh, T., Giard, M., Giraud-Héraud, Y., Gjerløw, E., González-Nuevo, J., Górski, K. M., Gratton, S., Gregorio, A., Gruppuso, A., Guillet, V., Hansen, F. K., Hanson, D., Harrison, D. L., Helou, G., Henrot-Versillé, S., Hernández-Monteagudo, C., Herranz, D., Hivon, E., Hobson, M., Holmes, W. A., Huffenberger, K. M., Hurier, G., Jaffe, A. H., Jaffe, T. R., & Planck Collaboration. 2014, Astronomy and Astrophysics, 586, A133

Adam, R., Ade, P. A. R., Alves, M. I. R., Ashdown, M., Aumont, J., Baccigalupi, C., Banday, A. J., Barreiro, R. B., Bartolo, N., Battaner, E., Benabed, K., Benoit-Lévy, A., Bernard, J. P., Bersanelli, M., Bielewicz, P., Bonavera, L., Bond, J. R., Borrill, J., Bouchet, F. R., Boulanger, F., Bucher, M., Burigana, C., Butler, R. C., Calabrese, E., Cardoso, J. F., Catalano, A., Chiang, H. C., Christensen, P. R., Colombo, L. P. L., Combet, C., Couchot, F., Crill, B. P., Curto, A., Cuttaia, F., Danese, L., Davis, R. J., de Bernardis, P., de Rosa, A., de Zotti, G., Delabrouille, J., Dickinson, C., Diego, J. M., Dolag, K., Doré, O., Ducout, A., Dupac, X., Elsner, F., Enßlin, T. A., Eriksen, H. K., Ferrière, K., Finelli, F., Forni, O., Frailis, M., Fraisse, A. A., Franceschi, E., Galeotta, S., Ganga, K., Ghosh, T., Giard, M., Gjerløw, E., González-Nuevo, J., Górski, K. M., Gregorio, A., Gruppuso, A., Gudmundsson, J. E., Hansen, F. K., Harrison, D. L., Hernández-Monteagudo, C., Herranz, D., Hildebrandt, S. R., Hobson, M., Hornstrup, A., Hurier, G., Jaffe, A. H., Jaffe, T. R., Jones, W. C., Juvela, M., Keihänen, E., Keskitalo, R., Kisner, T. S., Knoche, J., Kunz, M., Kurki-Suonio, H., Lamarre, J. M., Lasenby, A., Lattanzi, M., Lawrence, C. R., Leahy, J. P., Leonardi, R., Levrier, F., Liguori, M., Lilje, P. B., Linden-Vørnle, M., Lopez-Caniego, M., Lubin, P. M., Macias-Pérez, J. F., Maggio, G., Maino, D., Mandolesi, N., Mangilli, A., Maris, M., Martin, P. G., Martinez-González, E., Masi, S., Matarrese, S., Melchiorri, A., Mennella, A., Migliaccio, M., Miville-Deschênes, M. A., Moneti, A., Montier, L., Morgante, G., Munshi, D., Murphy, J. A., Naselsky, P., Nati, F., Natoli, P., Nørgaard-Nielsen, H. U., Oppermann, N., Orlando, E., Pagano, L., Pajot, F., Paladini, R., Paoletti, D., Pasian, F., Perotto, L., Pettorino, V., Piacentini, F., Piat, M., Pierpaoli, E., Plaszczynski, S., Pointecouteau, E., Polenta, G., Ponthieu, N., Pratt, G. W., Prunet, S., Puget, J. L., Rachen, J. P., Reinecke, M., Remazeilles, M., Renault, C., Renzi, A., Ristorcelli, I., Rocha, G., Rossetti, M., Roudier, G., Rubiño-Martín, J. A., Rusholme, B., Sandri, M., Santos, D., Savelainen, M., Scott, D., Spencer, L. D., Stolyarov, V., Stompor, R., Strong, A. W., Sudiwala, R., Sunyaev, R., Suur-Uski, A. S., Sygnet, J. F., Tauber, J. A., Terenzi, L., Toffolatti, L., Tomasi, M., Tristram, M., Tucci, M., Valenziano, L., Valiviita, J., Van Tent, F., Vielva, P., Villa, F., Wade, L. A., Wandelt, B. D., Wehus, I. K., Yvon, D., Zacchei, A., Zonca, A., & Planck Collaboration. 2016, Astronomy and Astrophysics, 596, A103

Adams, F. C. 1992, The Astrophysical Journal, 387, 572

Ade, P. A. R., Aghanim, N., Ahmed, Z., Aikin, R. W., Alexander, K. D., Arnaud, M., Aumont, J., Baccigalupi, C., Banday, A. J., Barkats, D., Barreiro, R. B., Bartlett, J. G., Bartolo, N., Battaner, E., Benabed, K., Benoît, A., Benoit-Lévy, A., Benton, S. J., Bernard, J. P., Bersanelli, M., Bielewicz, P., Bischoff, C. A., Bock, J. J., Bonaldi, A., Bonavera, L., Bond, J. R., Borrill, J., Bouchet, F. R., Boulanger, F., Brevik, J. A., Bucher, M., Buder, I., Bullock, E., Burigana, C., Butler, R. C., Buza, V., Calabrese, E., Cardoso, J. F., Catalano, A., Challinor, A., Chary, R. R., Chiang, H. C., Christensen, P. R., Colombo, L. P. L., Combet, C., Connors, J., Couchot, F., Coulais, A., Crill, B. P., Curto, A., Cuttaia, F., Danese, L., Davies, R. D., Davis, R. J., de Bernardis, P., de Rosa, A., de Zotti, G., Delabrouille, J., Delouis, J. M., Désert, F. X., Dickinson, C., Diego, J. M., Dole, H., Donzelli, S., Doré, O., Douspis, M., Dowell, C. D., Duband, L., Ducout, A., Dunkley, J., Dupac, X., Dvorkin, C., Efstathiou, G., Elsner, F., Enßlin, T. A., Eriksen, H. K., Falgarone, E., Filippini, J. P., Finelli, F., Fliescher, S., Forni, O., Frailis, M., Fraisse, A. A., Franceschi, E., Frejsel, A., Galeotta, S., Galli, S., Ganga, K., Ghosh, T., Giard, M., Gjerløw, E., Golwala, S. R., González-Nuevo, J., Górski, K. M., Gratton, S., Gregorio, A., Gruppuso, A., Gudmundsson, J. E., Halpern, M., Hansen, F. K., Hanson, D., Harrison, D. L., Hasselfield, M., Helou, G., Henrot-Versillé, S., Herranz, D., Hildebrandt, S. R., Hilton, G. C., Hivon, E., Hobson, M., Holmes, W. A., Hovest, W., Hristov, V. V., Huffenberger, K. M., Hui, H., Hurier, G., Irwin, K. D., Jaffe, A. H., Jaffe, T. R., Jewell, J., Jones, W. C., Juvela, M., Karakci, A., Karkare, K. S., Kaufman, J. P., Keating, B. G., Kefeli, S., Keihänen, E., Kernasovskiy, S. A., Keskitalo, R., Kisner, T. S., Kneissl, R., Knoche, J., Knox, L., Kovac, J. M., Krachmalnicoff, N., Kunz, M., Kuo, C. L., Kurki-Suonio, H., Lagache, G., Lähteenmäki, A., Lamarre, J. M., Lasenby, A., Lattanzi, M., Lawrence, C. R., Leitch, E. M., Leonardi, R., Levrier, F., Lewis, A., Liguori, M., Lilje, P. B., Linden-Vørnle, M., Lopez-Caniego, M., Lubin, P. M., Lueker, M., Macias-Pérez, J. F., Maffei, B., Maino, D., Mandolesi, N., Mangilli, A., Maris, M., Martin, P. G., Martinez-González, E., Masi, S., Mason, P., Matarrese, S., Megerian, K. G., Meinhold, P. R., Melchiorri, A., Mendes, L., Mennella, A., Migliaccio, M., Mitra, S., Miville-Deschênes, M. A., Moneti, A., Montier, L., Morgante, G., Mortlock, D., Moss, A., Munshi, D., Murphy, J. A., Naselsky, P., Nati, F., Natoli, P., Netterfield, C. B., Nguyen, H. T., Nørgaard-Nielsen, H. U., Noviello, F., Novikov, D., Novikov, I., O'Brient, R., Ogburn, R. W., Orlando, A., Pagano, L., Pajot, F., Paladini, R., Paoletti, D., Partridge, B., Pasian, F., Patanchon, G., Pearson, T. J., Perdereau, O., Perotto, L., Pettorino, V., Piacentini, F., Piat, M., Pietrobon, D., Plaszczynski, S., Pointecouteau, E., Polenta, G., Ponthieu, N., Pratt, G. W., Prunet, S., Pryke, C., Puget, J. L., Rachen, J. P., Reach, W. T., Rebolo, R., Reinecke, M., Remazeilles, M., Renault, C., Renzi, A., Richter, S., Ristorcelli, I., Rocha, G., Rossetti, M., Roudier, G., Rowan-Robinson, M., Rubiño-Martín, J. A., Rusholme, B., Sandri, M., Santos, D., Savelainen, M., Savini, G., Schwarz, R., Scott, D., Seiffert, M. D., Sheehy, C. D., Spencer, L. D., Staniszewski, Z. K., Stolyarov, V., Sudiwala, R., Sunyaev, R., Sutton, D., Suur-Uski, A. S., Sygnet, J. F., Tauber, J. A., Teply, G. P., Terenzi, L., Thompson, K. L., Toffolatti, L., Tolan, J. E., Tomasi, M., Tristram, M., Tucci, M., Turner, A. D., Valenziano, L., Valiviita, J., Van Tent, B., Vibert, L., Vielva, P., Vieregg, A. G., Villa, F., Wade, L. A., Wandelt, B. D., Watson, R., Weber, A. C., Wehus, I. K., White, M., White, S. D. M., Willmert, J., Wong, C. L., Yoon, K. W., Yvon, D., Zacchei, A., Zonca, A., BICEP2/Keck Array, & Planck Collaboration. 2015a, Physical Review Letters, 114, 101301

Ade, P. A. R., Aghanim, N., Alina, D., Alves, M. I. R., Armitage-Caplan, C., Arnaud, M., Arzoumanian, D., Ashdown, M., Atrio-Barandela, F., Aumont, J., Baccigalupi, C., Banday, A. J., Barreiro, R. B., Battaner, E., Benabed, K., Benoit-Lévy, A., Bernard,

J. P., Bersanelli, M., Bielewicz, P., Bock, J. J., Bond, J. R., Borrill, J., Bouchet, F. R., Boulanger, F., Bracco, A., Burigana, C., Butler, R. C., Cardoso, J. F., Catalano, A., Chamballu, A., Chary, R. R., Chiang, H. C., Christensen, P. R., Colombi, S., Colombo, L. P. L., Combet, C., Couchot, F., Coulais, A., Crill, B. P., Curto, A., Cuttaia, F., Danese, L., Davies, R. D., Davis, R. J., de Bernardis, P., Pino, E. M. d. G. D., de Rosa, A., de Zotti, G., Delabrouille, J., Désert, F. X., Dickinson, C., Diego, J. M., Donzelli, S., Doré, O., Douspis, M., Dunkley, J., Dupac, X., Enßlin, T. A., Eriksen, H. K., Falgarone, E., Ferrière, K., Finelli, F., Forni, O., Frailis, M., Fraisse, A. A., Franceschi, E., Galeotta, S., Ganga, K., Ghosh, T., Giard, M., Giraud-Héraud, Y., González-Nuevo, J., Górski, K. M., Gregorio, A., Gruppuso, A., Guillet, V., Hansen, F. K., Harrison, D. L., Helou, G., Hernández-Monteagudo, C., Hildebrandt, S. R., Hivon, E., Hobson, M., Holmes, W. A., Hornstrup, A., Huffenberger, K. M., Jaffe, A. H., Jaffe, T. R., Jones, W. C., Juvela, M., Keihänen, E., Keskitalo, R., Kisner, T. S., Kneissl, R., Knoche, J., Kunz, M., Kurki-Suonio, H., Lagache, G., Lähteenmäki, A., Lamarre, J. M., Lasenby, A., Lawrence, C. R., Leahy, J. P., Leonardi, R., Levrier, F., Liguori, M., Lilje, P. B., Linden-Vørnle, M., Lopez-Caniego, M., Lubin, P. M., Macias-Pérez, J. F., Maffei, B., Magalhães, A. M., Maino, D., Mandolesi, N., Maris, M., Marshall, D. J., Martin, P. G., Martinez-González, E., Masi, S., Matarrese, S., Mazzotta, P., Melchiorri, A., Mendes, L., Mennella, A., Migliaccio, M., Miville-Deschênes, M. A., Moneti, A., Montier, L., Morgante, G., Mortlock, D., Munshi, D., Murphy, J. A., Naselsky, P., Nati, F., Natoli, P., Netterfield, C. B., Noviello, F., Novikov, D., Novikov, I., Oxborrow, C. A., Pagano, L., Pajot, F., Paladini, R., Paoletti, D., Pasian, F., Pearson, T. J., Perdereau, O., Perotto, L., Perrotta, F., Piacentini, F., Piat, M., Pietrobon, D., Plaszczynski, S., Poidevin, F., Pointecouteau, E., Polenta, G., Popa, L., Pratt, G. W., Prunet, S., Puget, J. L., Rachen, J. P., Reach, W. T., Rebolo, R., Reinecke, M., Remazeilles, M., Renault, C., Ricciardi, S., Riller, T., Ristorcelli, I., Rocha, G., Rosset, C., Roudier, G., Rubiño-Martín, J. A., Rusholme, B., Sandri, M., Savini, G., Scott, D., Spencer, L. D., Stolyarov, V., Stompor, R., Sudiwala, R., Sutton, D., Suur-Uski, A. S., Sygnet, J. F., Tauber, J. A., Terenzi, L., Toffolatti, L., Tomasi, M., Tristram, M., Tucci, M., Umana, G., Valenziano, L., Valiviita, J., Van Tent, B., Vielva, P., Villa, F., Wade, L. A., Wandelt, B. D., Zacchei, A., Zonca, A., & Planck Collaboration. 2014a, Astronomy and Astrophysics, 576, A104

Ade, P. A. R., Aghanim, N., Alina, D., Alves, M. I. R., Armitage-Caplan, C., Arnaud, M., Arzoumanian, D., Ashdown, M., Atrio-Barandela, F., Aumont, J., Baccigalupi, C., Banday, A. J., Barreiro, R. B., Battaner, E., Benabed, K., Benoit-Lévy, A., Bernard, J. P., Bersanelli, M., Bielewicz, P., Bock, J. J., Bond, J. R., Borrill, J., Bouchet, F. R., Boulanger, F., Bracco, A., Burigana, C., Butler, R. C., Cardoso, J. F., Catalano, A., Chamballu, A., Chary, R. R., Chiang, H. C., Christensen, P. R., Colombi, S., Colombo, L. P. L., Combet, C., Couchot, F., Coulais, A., Crill, B. P., Curto, A., Cuttaia, F., Danese, L., Davies, R. D., Davis, R. J., de Bernardis, P., de Gouveia Dal Pino, E. M., de Rosa, A., de Zotti, G., Delabrouille, J., Désert, F. X., Dickinson, C., Diego, J. M., Donzelli, S., Doré, O., Douspis, M., Dunkley, J., Dupac, X., Efstathiou, G., Enßlin, T. A., Eriksen, H. K., Falgarone, E., Ferrière, K., Finelli, F., Forni, O., Frailis, M., Fraisse, A. A., Franceschi, E., Galeotta, S., Ganga, K., Ghosh, T., Giard, M., Giraud-Héraud, Y., González-Nuevo, J., Górski, K. M., Gregorio, A., Gruppuso, A., Guillet, V., Hansen, F. K., Harrison, D. L., Helou, G., Hernández-Monteagudo, C., Hildebrandt, S. R., Hivon, E., Hobson, M., Holmes, W. A., Hornstrup, A., Huffenberger, K. M., Jaffe, A. H., Jaffe, T. R., Jones, W. C., Juvela, M., Keihänen, E., Keskitalo, R., Kisner, T. S., Kneissl, R., Knoche, J., Kunz, M., Kurki-Suonio, H., Lagache, G., Lähteenmäki, A., Lamarre, J. M., Lasenby, A., Lawrence, C. R., Leahy, J. P., Leonardi, R., Levrier, F., Liguori, M., Lilje, P. B., Linden-Vørnle, M., Lopez-Caniego, M., Lubin, P. M., Macias-Pérez, J. F., Maffei, B., Magalhães,

A. M., Maino, D., Mandolesi, N., Maris, M., Marshall, D. J., Martin, P. G., Martinez-González, E., Masi, S., Matarrese, S., Mazzotta, P., Melchiorri, A., Mendes, L., Mennella, A., Migliaccio, M., Miville-Deschênes, M. A., Moneti, A., Montier, L., Morgante, G., Mortlock, D., Munshi, D., Murphy, J. A., Naselsky, P., Nati, F., Natoli, P., Netterfield, C. B., Noviello, F., Novikov, D., Novikov, I., Oxborrow, C. A., Pagano, L., Pajot, F., Paladini, R., Paoletti, D., Pasian, F., Pearson, T. J., Perdereau, O., Perotto, L., Perrotta, F., Piacentini, F., Piat, M., Pietrobon, D., Plaszczynski, S., Poidevin, F., Pointecouteau, E., Polenta, G., Popa, L., Pratt, G. W., Prunet, S., Puget, J. L., Rachen, J. P., Reach, W. T., Rebolo, R., Reinecke, M., Remazeilles, M., Renault, C., Ricciardi, S., Riller, T., Ristorcelli, I., Rocha, G., Rosset, C., Roudier, G., Rubiño-Martín, J. A., Rusholme, B., Sandri, M., Savini, G., Scott, D., Spencer, L. D., Stolyarov, V., Stompor, R., Sudiwala, R., Sutton, D., Suur-Uski, A. S., Sygnet, J. F., Tauber, J. A., Terenzi, L., Toffolatti, L., Tomasi, M., Tristram, M., Tucci, M., Umana, G., Valenziano, L., Valiviita, J., Van Tent, B., Vielva, P., Villa, F., Wade, L. A., Wandelt, B. D., Zacchei, A., Zonca, A., & Planck Collaboration. 2015b, Astronomy and Astrophysics, 576, A104

Ade, P. A. R., Aghanim, N., Armitage-Caplan, C., Arnaud, M., Ashdown, M., Atrio-Barandela, F., Aumont, J., Baccigalupi, C., Banday, A. J., Barreiro, R. B., Bartlett, J. G., Bartolo, N., Battaner, E., Benabed, K., Benoît, A., Benoit-Lévy, A., Bernard, J. P., Bersanelli, M., Bielewicz, P., Bobin, J., Bock, J. J., Bonaldi, A., Bond, J. R., Borrill, J., Bouchet, F. R., Bridges, M., Bucher, M., Burigana, C., Butler, R. C., Calabrese, E., Cardoso, J. F., Catalano, A., Challinor, A., Chamballu, A., Chiang, H. C., Chiang, L. Y., Christensen, P. R., Church, S., Clements, D. L., Colombi, S., Colombo, L. P. L., Couchot, F., Coulais, A., Crill, B. P., Curto, A., Cuttaia, F., Danese, L., Davies, R. D., Davis, R. J., de Bernardis, P., de Rosa, A., de Zotti, G., Delabrouille, J., Delouis, J. M., Désert, F. X., Dickinson, C., Diego, J. M., Dole, H., Donzelli, S., Doré, O., Douspis, M., Dunkley, J., Dupac, X., Efstathiou, G., Enßlin, T. A., Eriksen, H. K., Finelli, F., Forni, O., Frailis, M., Franceschi, E., Galeotta, S., Ganga, K., Gauthier, C., Giard, M., Giardino, G., Giraud-Hiraud, Y., González-Nuevo, J., Górski, K. M., Gratton, S., Gregorio, A., Gruppuso, A., Hamann, J., Hansen, F. K., Hanson, D., Harrison, D., Henrot-Versillé, S., Hernández-Monteagudo, C., Herranz, D., Hildebrandt, S. R., Hivon, E., Hobson, M., Holmes, W. A., Hornstrup, A., Hovest, W., Huffenberger, K. M., Jaffe, A. H., Jaffe, T. R., Jones, W. C., Juvela, M., Keihänen, E., Keskitalo, R., Kisner, T. S., Kneissl, R., Knoche, J., Knox, L., Kunz, M., Kurki-Suonio, H., Lagache, G., Lähteenmäki, A., Lamarre, J. M., Lasenby, A., Laureijs, R. J., Lawrence, C. R., Leach, S., Leahy, J. P., Leonardi, R., Lesgourgues, J., Lewis, A., Liguori, M., Lilje, P. B., Linden-Vernle, M., Lopez-Caniego, M., Lubin, P. M., Macias-Pérez, J. F., Maffei, B., Maino, D., Mandolesi, N., Maris, M., Marshall, D. J., Martin, P. G., Martinez-González, E., Masi, S., Massardi, M., Matarrese, S., Matthai, F., Mazzotta, P., Meinhold, P. R., Melchiorri, A., Mendes, L., Mennella, A., Migliaccio, M., Mitra, S., Miville-Deschênes, M. A., Moneti, A., Montier, L., Morgante, G., Mortlock, D., Moss, A., Munshi, D., Murphy, J. A., Naselsky, P., Nati, F., Natoli, P., Netterfield, C. B., Nørgaard-Nielsen, H. U., Noviello, F., Novikov, D., Novikov, I., O'Dwyer, I. J., Osborne, S., Oxborrow, C. A., Paci, F., Pagano, L., Pajot, F., Paladini, R., Pandolfi, S., Paoletti, D., Partridge, B., Pasian, F., Patanchon, G., Peiris, H. V., Perdereau, O., Perotto, L., Perrotta, F., Piacentini, F., Piat, M., Pierpaoli, E., Pietrobon, D., Plaszczynski, S., Pointecouteau, E., Polenta, G., Ponthieu, N., Popa, L., Poutanen, T., Pratt, G. W., Prezeau, G., Prunet, S., Puget, J. L., Rachen, J. P., Rebolo, R., Reinecke, M., Remazeilles, M., Renault, C., Ricciardi, S., Riller, T., Ristorcelli, I., Rocha, G., Rosset, C., Roudier, G., Rowan-Robinson, M., Rubiño-Martín, J. A., Rusholme, B., Sandri, M., Santos, D., Savelainen, M., Savini, G., Scott, D., Seiffert, M. D., Shellard, E. P. S., Spencer, L. D., Starck, J. L., Stolyarov, V., Stompor, R., Sudiwala, R., Sunyaev, R., Sureau, F., Sutton, D., Suur-Uski, A. S., Sygnet, J. F., Tauber, J. A., Tavagnacco, D., Terenzi, L., Toffolatti, L., Tomasi, M., Treguer-Goudineau, J., Tristram, M., Tucci, M., Tuovinen, J., Valenziano, L., Valiviita, J., Van Tent, B., Varis, J., Vielva, P., Villa, F., Vittorio, N., Wade, L. A., Wandelt, B. D., White, M., Wilkinson, A., Yvon, D., Zacchei, A., Zibin, J. P., Zonca, A., & Planck Collaboration. 2013, Astronomy and Astrophysics, 571, A22

Ade, P. A. R., Aghanim, N., Arnaud, M., Ashdown, M., Aumont, J., Baccigalupi, C., Banday, A. J., Barreiro, R. B., Bartolo, N., Battaner, E., Benabed, K., Benoit-Lévy, A., Bernard, J. P., Bersanelli, M., Bielewicz, P., Bonaldi, A., Bonavera, L., Bond, J. R., Borrill, J., Bouchet, F. R., Boulanger, F., Bracco, A., Burigana, C., Calabrese, E., Cardoso, J. F., Catalano, A., Chamballu, A., Chary, R. R., Chiang, H. C., Christensen, P. R., Colombo, L. P. L., Combet, C., Crill, B. P., Curto, A., Cuttaia, F., Danese, L., Davies, R. D., Davis, R. J., de Bernardis, P., de Rosa, A., de Zotti, G., Delabrouille, J., Delouis, J. M., Dickinson, C., Diego, J. M., Dole, H., Donzelli, S., Doré, O., Douspis, M., Dunkley, J., Dupac, X., Efstathiou, G., Elsner, F., Enßlin, T. A., Eriksen, H. K., Falgarone, E., Ferrière, K., Finelli, F., Forni, O., Frailis, M., Fraisse, A. A., Franceschi, E., Frolov, A., Galeotta, S., Galli, S., Ganga, K., Ghosh, T., Giard, M., Gjerløw, E., González-Nuevo, J., Górski, K. M., Gruppuso, A., Guillet, V., Hansen, F. K., Harrison, D. L., Helou, G., Hernández-Monteagudo, C., Herranz, D., Hildebrandt, S. R., Hivon, E., Hornstrup, A., Hovest, W., Huang, Z., Huffenberger, K. M., Hurier, G., Jaffe, T. R., Jones, W. C., Juvela, M., Keihänen, E., Keskitalo, R., Kisner, T. S., Kneissl, R., Knoche, J., Kunz, M., Kurki-Suonio, H., Lamarre, J. M., Lasenby, A., Lattanzi, M., Lawrence, C. R., Leonardi, R., León-Tavares, J., Levrier, F., Liguori, M., Lilje, P. B., Linden-Vørnle, M., Lopez-Caniego, M., Lubin, P. M., Macias-Pérez, J. F., Maffei, B., Maino, D., Mandolesi, N., Maris, M., Martin, P. G., Martinez-González, E., Masi, S., Matarrese, S., McGehee, P., Melchiorri, A., Mennella, A., Migliaccio, M., Miville-Deschênes, M. A., Moneti, A., Montier, L., Morgante, G., Mortlock, D., Munshi, D., Murphy, J. A., Naselsky, P., Nati, F., Natoli, P., Novikov, D., Novikov, I., Oppermann, N., Oxborrow, C. A., Pagano, L., Pajot, F., Paoletti, D., Pasian, F., Perdereau, O., Pettorino, V., Piacentini, F., Piat, M., Pierpaoli, E., Plaszczynski, S., Pointecouteau, E., Polenta, G., Ponthieu, N., Pratt, G. W., Prunet, S., Puget, J. L., Rachen, J. P., Reach, W. T., Rebolo, R., Reinecke, M., Remazeilles, M., Renault, C., Renzi, A., Ristorcelli, I., Rocha, G., Rosset, C., Rossetti, M., Roudier, G., Rubiño-Martín, J. A., Rusholme, B., Sandri, M., Santos, D., Savelainen, M., Savini, G., Scott, D., Serra, P., Soler, J. D., Stolyarov, V., Sudiwala, R., Sunyaev, R., Suur-Uski, A. S., Sygnet, J. F., Tauber, J. A., Terenzi, L., Toffolatti, L., Tomasi, M., Tristram, M., Tucci, M., Umana, G., Valenziano, L., Valiviita, J., Van Tent, B., Vielva, P., Villa, F., Wade, L. A., Wandelt, B. D., Wehus, I. K., Yvon, D., Zacchei, A., Zonca, A., & Planck Collaboration. 2015c, Astronomy and Astrophysics, 586, A141

Ade, P. A. R., Ahmed, Z., Aikin, R. W., Alexander, K. D., Barkats, D., Benton, S. J., Bischoff, C. A., Bock, J. J., Brevik, J. A., Buder, I., Bullock, E., Buza, V., Connors, J., Crill, B. P., Dowell, C. D., Dvorkin, C., Duband, L., Filippini, J. P., Fliescher, S., Golwala, S. R., Halpern, M., Harrison, S., Hasselfield, M., Hildebrandt, S. R., Hilton, G. C., Hristov, V. V., Hui, H., Irwin, K. D., Karkare, K. S., Kaufman, J. P., Keating, B. G., Kefeli, S., Kernasovskiy, S. A., Kovac, J. M., Kuo, C. L., Leitch, E. M., Lueker, M., Mason, P., Megerian, K. G., Netterfield, C. B., Nguyen, H. T., O'Brient, R., Ogburn, R. W. I., Orlando, A., Pryke, C., Reintsema, C. D., Richter, S., Schwarz, R., Sheehy, C. D., Staniszewski, Z. K., Sudiwala, R. V., Teply, G. P., Thompson, K. L., Tolan, J. E., Turner, A. D., Vieregg, A. G., Weber, A. C., Willmert, J., Wong, C. L., Yoon, K. W., & BICEP2/Keck Collaborations. 2015d, The Astrophysical Journal, 811, 126

Ade, P. A. R., Aikin, R. W., Barkats, D., Benton, S. J., Bischoff, C. A., Bock, J. J., Brevik,

J. A., Buder, I., Bullock, E., Dowell, C. D., Duband, L., Filippini, J. P., Fliescher, S., Golwala, S. R., Halpern, M., Hasselfield, M., Hildebrandt, S. R., Hilton, G. C., Hristov, V. V., Irwin, K. D., Karkare, K. S., Kaufman, J. P., Keating, B. G., Kernasovskiy, S. A., Kovac, J. M., Kuo, C. L., Leitch, E. M., Lueker, M., Mason, P., Netterfield, C. B., Nguyen, H. T., O'Brient, R., Ogburn, R. W., Orlando, A., Pryke, C., Reintsema, C. D., Richter, S., Schwarz, R., Sheehy, C. D., Staniszewski, Z. K., Sudiwala, R. V., Teply, G. P., Tolan, J. E., Turner, A. D., Vieregg, A. G., Wong, C. L., Yoon, K. W., & BICEP2 Collaboration. 2014b, Physical Review Letters, 112, 241101

Aghanim, N., Arnaud, M., Ashdown, M., Aumont, J., Baccigalupi, C., Banday, A. J., Barreiro, R. B., Bartlett, J. G., Bartolo, N., Battaner, E., Battye, R., Benabed, K., Benoît, A., Benoit-Lévy, A., Bernard, J. P., Bersanelli, M., Bielewicz, P., Bock, J. J., Bonaldi, A., Bonavera, L., Bond, J. R., Borrill, J., Bouchet, F. R., Burigana, C., Butler, R. C., Calabrese, E., Cardoso, J. F., Catalano, A., Challinor, A., Chiang, H. C., Christensen, P. R., Churazov, E., Clements, D. L., Colombo, L. P. L., Combet, C., Comis, B., Coulais, A., Crill, B. P., Curto, A., Cuttaia, F., Danese, L., Davies, R. D., Davis, R. J., de Bernardis, P., de Rosa, A., de Zotti, G., Delabrouille, J., Désert, F. X., Dickinson, C., Diego, J. M., Dolag, K., Dole, H., Donzelli, S., Doré, O., Douspis, M., Ducout, A., Dupac, X., Efstathiou, G., Elsner, F., Enßlin, T. A., Eriksen, H. K., Fergusson, J., Finelli, F., Forni, O., Frailis, M., Fraisse, A. A., Franceschi, E., Frejsel, A., Galeotta, S., Galli, S., Ganga, K., Génova-Santos, R. T., Giard, M., González-Nuevo, J., Górski, K. M., Gregorio, A., Gruppuso, A., Gudmundsson, J. E., Hansen, F. K., Harrison, D. L., Henrot-Versillé, S., Hernández-Monteagudo, C., Herranz, D., Hildebrandt, S. R., Hivon, E., Holmes, W. A., Hornstrup, A., Huffenberger, K. M., Hurier, G., Jaffe, A. H., Jones, W. C., Juvela, M., Keihänen, E., Keskitalo, R., Kneissl, R., Knoche, J., Kunz, M., Kurki-Suonio, H., Lacasa, F., Lagache, G., Lähteenmäki, A., Lamarre, J. M., Lasenby, A., Lattanzi, M., Leonardi, R., Lesgourgues, J., Levrier, F., Liguori, M., Lilje, P. B., Linden-Vørnle, M., Lopez-Caniego, M., Macias-Pérez, J. F., Maffei, B., Maggio, G., Maino, D., Mandolesi, N., Mangilli, A., Maris, M., Martin, P. G., Martinez-González, E., Masi, S., Matarrese, S., Melchiorri, A., Melin, J. B., Migliaccio, M., Miville-Deschênes, M. A., Moneti, A., Montier, L., Morgante, G., Mortlock, D., Munshi, D., Murphy, J. A., Naselsky, P., Nati, F., Natoli, P., Noviello, F., Novikov, D., Novikov, I., Paci, F., Pagano, L., Pajot, F., Paoletti, D., Pasian, F., Patanchon, G., Perdereau, O., Perotto, L., Pettorino, V., Piacentini, F., Piat, M., Pierpaoli, E., Pietrobon, D., Plaszczynski, S., Pointecouteau, E., Polenta, G., Ponthieu, N., Pratt, G. W., Prunet, S., Puget, J. L., Rachen, J. P., Reinecke, M., Remazeilles, M., Renault, C., Renzi, A., Ristorcelli, I., Rocha, G., Rossetti, M., Roudier, G., Rubiño-Martín, J. A., Rusholme, B., Sandri, M., Santos, D., Sauvé, A., Savelainen, M., Savini, G., Scott, D., Spencer, L. D., Stolyarov, V., Stompor, R., Sunyaev, R., Sutton, D., Suur-Uski, A. S., Sygnet, J. F., Tauber, J. A., Terenzi, L., Toffolatti, L., Tomasi, M., Tramonte, D., Tristram, M., Tucci, M., Tuovinen, J., Valenziano, L., Valiviita, J., Van Tent, B., Vielva, P., Villa, F., Wade, L. A., Wandelt, B. D., Wehus, I. K., Yvon, D., Zacchei, A., Zonca, A., & Planck Collaboration. 2016, Astronomy and Astrophysics, 594, A22

Ahlers, M. & Mertsch, P. 2017, Progress in Particle and Nuclear Physics, 94, 184

Andersson, B. G., Lazarian, A., & Vaillancourt, J. E. 2015, Annual Review of Astronomy and Astrophysics, 53, 501

André, P., Di Francesco, J., Ward-Thompson, D., Inutsuka, S.-i., Pudritz, R. E., & Pineda, J. 2013, in Protostars and Planets VI, ed. H. Beuther, R. S. Klessen, C. P. Dullemond, & T. K. Henning, 27–51

André, P., Men'shchikov, A., Bontemps, S., Konyves, V., Motte, F., Schneider, N., Didelon, P., Minier, V., Saraceno, P., Ward-Thompson, D., Di Francesco, J., White, G., Molinari, S., Testi, L., Abergel, A., Griffin, M., Henning, T., Royer, P., Merín, B., Vavrek, R., Attard, M., Arzoumanian, D., Wilson, C. D., Ade, P., Aussel, H., Baluteau, J. P., Benedettini, M., Bernard, J. P., Blommaert, J. A. D. L., Cambrésy, L., Cox, P., Di Giorgio, A., Hargrave, P., Hennemann, M., Huang, M., Kirk, J., Krause, O., Launhardt, R., Leeks, S., Le Pennec, J., Li, J. Z., Martin, P. G., Maury, A., Olofsson, G., Omont, A., Peretto, N., Pezzuto, S., Prusti, T., Roussel, H., Russeil, D., Sauvage, M., Sibthorpe, B., Sicilia-Aguilar, A., Spinoglio, L., Waelkens, C., Woodcraft, A., & Zavagno, A. 2010, Astronomy and Astrophysics, 518, L102

Aranson, I. S. & Kramer, L. 2002, Reviews of Modern Physics, 74, 99

Armitage, P. J. 2011, Annual Review of Astronomy and Astrophysics, 49, 195

Arnold, B. C. & SenGupta, A. 2006, Environmental and Ecological Statistics, 13, 271

Arzoumanian, D., André, P., Didelon, P., Konyves, V., Schneider, N., Men'shchikov, A., Sousbie, T., Zavagno, A., Bontemps, S., Di Francesco, J., Griffin, M., Hennemann, M., Hill, T., Kirk, J., Martin, P., Minier, V., Molinari, S., Motte, F., Peretto, N., Pezzuto, S., Spinoglio, L., Ward-Thompson, D., White, G., & Wilson, C. D. 2011, Astronomy and Astrophysics, 529, L6

Aschwanden, M. J. 2009, Solar Physics, 262, 235

Asensio Ramos, A., de la Cruz Rodriguez, J., Martínez González, M. J., & Socas-Navarro, H. 2017, Astronomy and Astrophysics, 599, A133

Bai, X.-N. 2011, The Astrophysical Journal, 739, 50

—. 2015, The Astrophysical Journal, 798, 84

Balbus, S. & Hawley, J. 1998, Reviews of Modern Physics, 70, 1

Balbus, S. A. 2001, The Astrophysical Journal, 562, 909

—. 2003, Annual Review of Astronomy and Astrophysics, 41, 555

Balbus, S. A. & Hawley, J. F. 1991, The Astrophysical Journal, 376, 214

Beck, R. 2001, Space Science Reviews, 99, 243

—. 2015, The Astronomy and Astrophysics Review, 24, 4

Begum, A., Stanimirović, S., Peek, J. E., Ballering, N. P., Heiles, C., Douglas, K. A., Putman, M., Gibson, S. J., Grcevich, J., Korpela, E. J., Lee, M.-Y., Saul, D., & Gallagher, III, J. S. 2010, The Astrophysical Journal, 722, 395

Bender, C. M. & Orszag, S. A. 1978, Advanced Mathematical Methods for Scientists and Engineers (New York: Advanced Mathematical Methods for Scientists and Engineers)

Benoît, A., Ade, P., Amblard, A., Ansari, R., Aubourg, É., Bargot, S., Bartlett, J. G., Bernard, J. P., Bhatia, R. S., Blanchard, A., Bock, J. J., Boscaleri, A., Bouchet, F. R., Bourrachot, A., Camus, P., Couchot, F., de Bernardis, P., Delabrouille, J., Désert, F. X., Doré, O., Douspis, M., Dumoulin, L., Dupac, X., Filliatre, P., Fosalba, P., Ganga, K., Gannaway, F., Gautier, B., Giard, M., Giraud-Héraud, Y., Gispert, R., Guglielmi, L., Hamilton, J. C., Hanany, S., Henrot-Versillé, S., Kaplan, J., Lagache, G., Lamarre, J. M., Lange, A. E., Macias-Pérez, J. F., Madet, K., Maffei, B., Magneville, C., Marrone, D. P., Masi, S., Mayet, F., Murphy, A., Naraghi, F., Nati, F., Patanchon, G., Perrin, G., Piat, M., Ponthieu, N., Prunet, S., Puget, J. L., Renault, C., Rosset, C., Santos, D., Starobinsky, A., Strukov, I., Sudiwala, R. V., Teyssier, R., Tristram, M., Tucker, C., Vanel, J. C., Vibert, D., Wakui, E., & Yvon, D. 2004, Astronomy and Astrophysics, 424, 571

Benson, B. A., Ade, P. A. R., Ahmed, Z., Allen, S. W., Arnold, K., Austermann, J. E., Bender, A. N., Bleem, L. E., Carlstrom, J. E., Chang, C. L., Cho, H. M., Cliche, J. F., Crawford, T. M., Cukierman, A., de Haan, T., Dobbs, M. A., Dutcher, D., Everett, W., Gilbert, A., Halverson, N. W., Hanson, D., Harrington, N. L., Hattori, K., Henning, J. W., Hilton, G. C., Holder, G. P., Holzapfel, W. L., Irwin, K. D., Keisler, R., Knox, L., Kubik, D., Kuo, C. L., Lee, A. T., Leitch, E. M., Li, D., McDonald, M., Meyer, S. S., Montgomery, J., Myers, M., Natoli, T., Nguyen, H., Novosad, V., Padin, S., Pan, Z., Pearson, J., Reichardt, C., Ruhl, J. E., Saliwanchik, B. R., Simard, G., Smecher, G., Sayre, J. T., Shirokoff, E., Stark, A. A., Story, K., Suzuki, A., Thompson, K. L., Tucker, C., Vanderlinde, K., Vieira, J. D., Vikhlinin, A., Wang, G., Yefremenko, V., & Yoon, K. W. 2014, in SPIE Astronomical Telescopes + Instrumentation, ed. W. S. Holland & J. Zmuidzinas (SPIE), 91531P

Berdyugin, A. & Teerikorpi, P. 2002, Astronomy and Astrophysics, 384, 1050

Berdyugin, A., Teerikorpi, P., Haikala, L., Hanski, M., Knude, J., & Markkanen, T. 2001, Astronomy and Astrophysics, 372, 276

Blaes, O. 2014, Space Science Reviews, 183, 21

Blanchard, A. & Schneider, J. 1987, Astronomy and Astrophysics, 184, 1

Bond, N. A., Strauss, M. A., & Cen, R. 2010, Monthly Notices of the Royal Astronomical Society, 409, 156

Boulares, A. & Cox, D. P. 1990, The Astrophysical Journal, 365, 544

Boyd, J. P. 2001, Chebyshev and Fourier Spectral Methods, 2nd edn. (Dover Books on Mathematics)

Brandenburg, A., Nordlund, A., Stein, R. F., & Torkelsson, U. 1995, The Astrophysical Journal, 446, 741

Brown, J. C., Haverkorn, M., Gaensler, B. M., Taylor, A. R., Bizunok, N. S., McClure-Griffiths, N. M., Dickey, J. M., & Green, A. J. 2007, The Astrophysical Journal, 663, 258

Burkhart, B. & Lazarian, A. 2011, Proceedings of the International Astronomical Union, 6, 365

Burstein, D. & Heiles, C. 1982, The Astronomical Journal, 87, 1165

Cabral, B. & Leedom, L. C. 1993, SIGGRAPH '93 Proceedings of the 20th annual conference on Computer graphics and interactive techniques, 263

Caldwell, R. R., Hirata, C., & Kamionkowski, M. 2017, The Astrophysical Journal, 839, 91

Chandrasekhar, S. 1960, Proceedings of the National Academy of Sciences of the United States of America, 46, 137

Chandrasekhar, S. & Fermi, E. 1953, Astrophysical Journal, 118, 113

Chon, G., Challinor, A., Prunet, S., Hivon, E., & Szapudi, I. 2004, Monthly Notices of the Royal Astronomical Society, 350, 914

Clark, S. E., Hill, J. C., Peek, J. E. G., Putman, M. E., & Babler, B. L. 2015, Physical Review Letters, 115, 241302

Clark, S. E. & Oishi, J. S. 2017a, The Astrophysical Journal, 841, 2

—. 2017b, The Astrophysical Journal, 841, 1

Clark, S. E., Peek, J. E. G., & Putman, M. E. 2014, The Astrophysical Journal, 789, 82

Clemens, D. P., Pavel, M. D., & Cashman, L. R. 2012, The Astrophysical Journal Supplement Series, 200, 21

Cox, D. P. 2005, Annual Review of Astronomy and Astrophysics, 43, 337

Cox, D. P. & Reynolds, R. J. 1987, Annual Review of Astronomy and Astrophysics, 25, 303

Cross, M. C. & Hohenberg, P. C. 1993, Reviews of Modern Physics, 65, 851

Crutcher, R. M. 2012, Annual Review of Astronomy and Astrophysics, 50, 29

Crutcher, R. M. & Kazes, I. 1983, Astronomy and Astrophysics, 125, L23

Crutcher, R. M., Troland, T. H., Lazareff, B., Paubert, G., & Kazès, I. 1999, The Astrophysical Journal, 514, L121

Crutcher, R. M., Wandelt, B., Heiles, C., Falgarone, E., & Troland, T. H. 2010, The Astrophysical Journal, 725, 466

Davis, L. 1951, Physical Review, 81, 890

Davis, L. J. & Greenstein, J. L. 1951, The Astrophysical Journal, 114, 206

Deguchi, S. & Watson, W. D. 1984, The Astrophysical Journal, 285, 126

Delabrouille, J., Betoule, M., Melin, J. B., Miville-Deschênes, M. A., González-Nuevo, J., Le Jeune, M., Castex, G., de Zotti, G., Basak, S., Ashdown, M., Aumont, J., Baccigalupi, C., Banday, A. J., Bernard, J. P., Bouchet, F. R., Clements, D. L., da Silva, A., Dickinson, C., Dodu, F., Dolag, K., Elsner, F., Fauvet, L., Faÿ, G., Giardino, G., Leach, S., Lesgourgues, J., Liguori, M., Macias-Pérez, J. F., Massardi, M., Matarrese, S., Mazzotta, P., Montier, L., Mottet, S., Paladini, R., Partridge, B., Piffaretti, R., Prezeau, G., Prunet, S., Ricciardi, S., Roman, M., Schaefer, B. M., & Toffolatti, L. 2013, Astronomy and Astrophysics, 553, A96

Deyirmenjian, V. B., Daya, Z. A., & Morris, S. W. 1997, Physical Review E, 56, 1706

Dicke, R. H., Peebles, P. J. E., Roll, P. G., & Wilkinson, D. T. 1965, The Astrophysical Journal, 142, 414

Dickey, J. M., McClure-Griffiths, N., Gibson, S. J., Gomez, J. F., Imai, H., Jones, P., Stanimirovic, S., van Loon, J. T., Walsh, A., Alberdi, A., Anglada, G., Uscanga, L., Arce, H., Bailey, M., Begum, A., Wakker, B., Ben Bekhti, N., Kalberla, P., Winkel, B., Bekki, K., For, B. Q., Staveley-Smith, L., Westmeier, T., Burton, M., Cunningham, M., Dawson, J., Ellingsen, S., Diamond, P., Green, J. A., Hill, A. S., Koribalski, B., McConnell, D., Rathborne, J., Voronkov, M., Douglas, K. A., English, J., Ford, H. A., Foster, T., Gomez, Y., Green, A., Bland-Hawthorn, J., Gulyaev, S., Hoare, M., Joncas, G., Kang, J.-H., Kerton, C. R., Koo, B.-C., Leahy, D., Lo, N., Lockman, F. J., Migenes, V., Nakashima, J., Zhang, Y., Nidever, D., Peek, J. E. G., Tafoya, D., Tian, W., & Wu, D. 2013, Publications of the Astronomical Society of Australia, 30, e003

Draine, B. T. 2003, Annual Review of Astronomy and Astrophysics, 41, 241

Duda, R. O. & Hart, P. E. 1972, Communications of the ACM, 15, 11

Duffy, A. R., Meyer, M. J., Staveley-Smith, L., Bernyk, M., Croton, D. J., Koribalski, B. S., Gerstmann, D., & Westerlund, S. 2012, Monthly Notices of the Royal Astronomical Society, 426, 3385

Durrer, R. & Neronov, A. 2013, The Astronomy and Astrophysics Review, 21, 62

Ebrahimi, F., Prager, S. C., & Schnack, D. D. 2009, The Astrophysical Journal, 698, 233

Essinger-Hileman, T., Ali, A., Amiri, M., Appel, J. W., Araujo, D., Bennett, C. L., Boone, F., Chan, M., Cho, H.-M., Chuss, D. T., Colazo, F., Crowe, E., Denis, K., Dünner, R., Eimer, J., Gothe, D., Halpern, M., Harrington, K., Hilton, G., Hinshaw, G. F., Huang, C., Irwin, K., Jones, G., Karakla, J., Kogut, A. J., Larson, D., Limon, M., Lowry, L., Marriage, T., Mehrle, N., Miller, A. D., Miller, N., Moseley, S. H., Novak, G., Reintsema, C., Rostem, K., Stevenson, T., Towner, D., U-Yen, K., Wagner, E., Watts, D., Wollack, E., Xu, Z., & Zeng, L. 2014, in Proceedings of SPIE

Essinger-Hileman, T., Appel, J. W., Beall, J. A., Cho, H. M., Fowler, J., Halpern, M., Hasselfield, M., Irwin, K. D., Marriage, T. A., Niemack, M. D., Page, L., Parker, L. P., Pufu, S., Staggs, S. T., Stryzak, O., Visnjic, C., Yoon, K. W., & Zhao, Y. 2010, in Proceedings of the Thirteenth International Conference on Low-Temperature Detectors

Federrath, C. & Klessen, R. S. 2012, The Astrophysical Journal, 761, 156

Ferrière, K. M. 2001, Reviews of Modern Physics, 73, 1031

Flauger, R., Hill, J. C., & Spergel, D. N. 2014, Journal of Cosmology and Astroparticle Physics, 8, 039

Fleming, T. & Stone, J. M. 2003, The Astrophysical Journal, 585, 908

Flock, M., Fromang, S., González, M., & Commerçon, B. 2013, Astronomy and Astrophysics, 560, A43

Fosalba, P., Lazarian, A., Prunet, S., & Tauber, J. A. 2002, The Astrophysical Journal, 564, 762

Fraisse, A. A., Ade, P. A. R., Amiri, M., Benton, S. J., Bock, J. J., Bond, J. R., Bonetti, J. A., Bryan, S., Burger, B., Chiang, H. C., Clark, C. N., Contaldi, C. R., Crill, B. P., Davis, G., Doré, O., Farhang, M., Filippini, J. P., Fissel, L. M., Gandilo, N. N., Golwala, S., Gudmundsson, J. E., Hasselfield, M., Hilton, G., Holmes, W., Hristov, V. V., Irwin, K., Jones, W. C., Kuo, C. L., MacTavish, C. J., Mason, P. V., Montroy, T. E., Morford, T. A., Netterfield, C. B., O'Dea, D. T., Rahlin, A. S., Reintsema, C., Ruhl, J. E., Runyan, M. C., Schenker, M. A., Shariff, J. A., Soler, J. D., Trangsrud, A., Tucker, C., Tucker, R. S., Turner, A. D., & Wiebe, D. 2013, Journal of Cosmology and Astroparticle Physics, 4, 047

Fraser, A. E., Terry, P. W., Zweibel, E. G., & Pueschel, M. J. 2017, Physics of Plasmas, 24, 062304

Gardner, F. F. & Whiteoak, J. B. 1966, Annual Review of Astronomy and Astrophysics, 4, 245

Gissinger, C., Goodman, J., & Ji, H. 2012, Physics of Fluids, 24, 074109

Gissinger, C., Ji, H., & Goodman, J. 2011, Physical Review E, 84, 026308

Glenn, J., Walker, C. K., Bieging, J. H., & Jewell, P. R. 1997, The Astrophysical Journal, 487, L89

Goldreich, P. & Kylafis, N. D. 1981, The Astrophysical Journal, 243, L75

Goldsmith, P. F., Heyer, M., Narayanan, G., Snell, R., Li, D., & Brunt, C. 2008, The Astrophysical Journal, 680, 428

Gomez, G. C. & Cox, D. P. 2004, The Astrophysical Journal, 615, 744

Goodman, A. A. 1996, in Polarimetry of the Interstellar Medium, 325–344

Goodman, J. & Ji, H. 2002, Journal of Fluid Mechanics, 462, 365

Goodman, J. & Xu, G. 1994, The Astrophysical Journal, 432, 213

Greaves, J. S., Holland, W. S., Friberg, P., & Dent, W. R. F. 1999, The Astrophysical Journal, 512, L139

Green, G. M., Schlafly, E. F., Finkbeiner, D. P., Rix, H.-W., Martin, N., Burgett, W., Draper, P. W., Flewelling, H., Hodapp, K., Kaiser, N., Kudritzki, R. P., Magnier, E., Metcalfe, N., Price, P., Tonry, J., & Wainscoat, R. 2015, The Astrophysical Journal, 810, 25

Griffiths, D. J. 2005, Introduction to Quantum Mechanics (Pearson Prentice Hall)

Guth, A. H. 1981, Physical Review D, 23, 347

Hacar, A., Tafalla, M., Kauffmann, J., & Kovacs, A. 2013, Astronomy and Astrophysics, 554, A55

Hale, G. E. 1908, The Astrophysical Journal, 28, 315

Han, J. L., Manchester, R. N., Lyne, A. G., Qiao, G. J., & van Straten, W. 2006, The Astrophysical Journal, 642, 868

Hanson, D., Hoover, S., Crites, A., Ade, P. A. R., Aird, K. A., Austermann, J. E., Beall, J. A., Bender, A. N., Benson, B. A., Bleem, L. E., Bock, J. J., Carlstrom, J. E., Chang, C. L., Chiang, H. C., Cho, H. M., Conley, A., Crawford, T. M., de Haan, T., Dobbs, M. A., Everett, W., Gallicchio, J., Gao, J., George, E. M., Halverson, N. W., Harrington, N., Henning, J. W., Hilton, G. C., Holder, G. P., Holzapfel, W. L., Hrubes, J. D., Huang, N., Hubmayr, J., Irwin, K. D., Keisler, R., Knox, L., Lee, A. T., Leitch, E., Li, D., Liang, C., Luong-Van, D., Marsden, G., McMahon, J. J., Mehl, J., Meyer, S. S., Mocanu, L., Montroy, T. E., Natoli, T., Nibarger, J. P., Novosad, V., Padin, S., Pryke, C., Reichardt,

C. L., Ruhl, J. E., Saliwanchik, B. R., Sayre, J. T., Schaffer, K. K., Schulz, B., Smecher, G., Stark, A. A., Story, K. T., Tucker, C., Vanderlinde, K., Vieira, J. D., Viero, M. P., Wang, G., Yefremenko, V., Zahn, O., & Zemcov, M. 2013, Physical Review Letters, 111, 141301

Hatch, D. R., Terry, P. W., Jenko, F., Merz, F., Pueschel, M. J., Nevins, W. M., & Wang, E. 2011, Physics of Plasmas, 18, 055706

Haverkorn, M. 2015, in Magnetic Fields in Diffuse Media, ed. A. Lazarian, E. M. d. G. D. Pino, & C. Melioli (Springer), 483–506

Hawley, J. F., Gammie, C. F., & Balbus, S. A. 1996, The Astrophysical Journal, 464, 690

Hawley, J. F., Guan, X., & Krolik, J. H. 2011, The Astrophysical Journal, 738, 84

Heeschen, D. S. 1955, The Astrophysical Journal, 121, 569

Heiles, C. 1998, in The Local Bubble and Beyond Lyman-Spitzer-Colloquium, ed. D. Breitschwerdt, M. Freyberg, & J. Trümper (Springer Berlin Heidelberg), 227–238

Heiles, C. 2000, The Astronomical Journal, 119, 923

Heiles, C. & Crutcher, R. 2005, in Cosmic Magnetic Fields, ed. R. Wielebinski & R. Beck (Lecture Notes in Physics), 137

Heiles, C., Goodman, A. A., McKee, C. F., & Zweibel, E. G. 1993, In: Protostars and planets III (A93-42937 17-90), 279

Heitsch, F., Zweibel, E. G., Mac Low, M. M., Li, P., & Norman, M. L. 2001, The Astrophysical Journal, 561, 800

Hennebelle, P. 2013, Astronomy and Astrophysics, 556, A153

Hennebelle, P. & André, P. 2013, Astronomy and Astrophysics, 560, A68

Hill, A. S., Joung, M. R., Mac Low, M. M., Benjamin, R., Haffner, L. M., Kingenberg, C., & Waagan, K. 2012, The Astrophysical Journal, 750, 104

Hiltner, W. A. 1949, Science, 109, 165

Hollerbach, R. 2009, Proceedings of the Royal Society A: Mathematical, Physical and Engineering Sciences, 465, 2003

Hollerbach, R. & Rüdiger, G. 2005, Physical Review Letters, 95, 124501

Houde, M., Hezareh, T., Jones, S., & Rajabi, F. 2013, The Astrophysical Journal, 764, 24

Hough, P. V. C. 1962, Method and Means for Recognizing Complex Patterns, US Patent

Hoyle, R. 2006, Pattern Formation, An Introduction to Methods (Cambridge: Cambridge University Press)

Hu, W. & Okamoto, T. 2002, The Astrophysical Journal, 574, 566

Illingworth, J. & Kittler, J. 1988, Computer Vision, Graphics, and Image Processing, 44, 87

Inoue, T. & Inutsuka, S.-i. 2016, The Astrophysical Journal, 833, 10

Jaffe, T. R., Ferrière, K. M., Banday, A. J., Strong, A. W., Orlando, E., Macias-Pérez, J. F., Fauvet, L., Combet, C., & Falgarone, E. 2013, Monthly Notices of the Royal Astronomical Society, 431, 683

Jaffe, T. R., Leahy, J. P., Banday, A. J., Leach, S. M., Lowe, S. R., & Wilkinson, A. 2010, Monthly Notices of the Royal Astronomical Society, 401, 1013

Jansson, R. & Farrar, G. R. 2012, The Astrophysical Journal, 757, 14

Ji, H., Goodman, J., & Kageyama, A. 2001, Monthly Notices of the Royal Astronomical Society, 325, L1

Johansen, A., Youdin, A., & Klahr, H. 2009, The Astrophysical Journal, 697, 1269

Kalberla, P. M. W., Burton, W. B., Hartmann, D., Arnal, E. M., Bajaja, E., Morras, R., & Pöppel, W. G. L. 2005, Astronomy and Astrophysics, 440, 775

Kamionkowski, M., Kosowsky, A., & Stebbins, A. 1997, Physical Review Letters, 78, 2058

Kermish, Z., Ade, P., Anthony, A., Arnold, K., Arnold, K., Barron, D., Boettger, D., Borrill, J., Chapman, S., Chinone, Y., Dobbs, M. A., Errard, J., Fabbian, G., Flanigan, D., Fuller, G., Ghribi, A., Grainger, W., Halverson, N., Hasegawa, M., Hattori, K., Hazumi, M., Holzapfel, W. L., Howard, J., Hyland, P., Jaffe, A., Keating, B., Kisner, T., Lee, A. T., Le Jeune, M., Linder, E., Lungu, M., Matsuda, F., Matsumura, T., Meng, X., Miller, N. J., Morii, H., Moyerman, S., Myers, M. J., Nishino, H., Paar, H., Quealy, E., Reichardt, C. L., Richards, P. L., Ross, C., Shimizu, A., Shimon, M., Shimmin, C., Sholl, M., Siritanasak, P., Spieler, H., Stebor, N., Steinbach, B., Stompor, R., Suzuki, A., Tomaru, T., Tucker, C., & Zahn, O. 2012, in Millimeter, Submillimeter, and Far-Infrared Detectors and Instrumentation for Astronomy VI, 84521C

Kerp, J., Winkel, B., Ben Bekhti, N., Floeer, L., & Kalberla, P. 2011, Astronomische Nachrichten, 332, 637

Khalil, A., Joncas, G., & Nekka, F. 2004, The Astrophysical Journal, 601, 352

Kim, J. & Komatsu, E. 2013, Physical Review D, 88, 101301

Kirillov, O. N. & Stefani, F. 2013, Physical Review Letters, 111, 061103

Knobloch, E. & Julien, K. 2005, Physics of Fluids, 17, 094106

Koch, E. W. & Rosolowsky, E. W. 2015, Monthly Notices of the Royal Astronomical Society, 452, 3435

Koutroumpa, D., Lallement, R., Raymond, J. C., & Kharchenko, V. 2009, The Astrophysical Journal, 696, 1517

Kovac, J., Leitch, E. M., Pryke, C., Carlstrom, J. E., Halverson, N. W., & Holzapfel, W. L. 2002, Nature, 420, 772

Kovetz, E. D. & Kamionkowski, M. 2015, Physical Review D, 91, 081303

Kuntz, K. D. & Danly, L. 1996, The Astrophysical Journal, 457, 703

Kunz, M. W. & Balbus, S. A. 2004, Monthly Notices of the Royal Astronomical Society, 348, 355

Kunz, M. W. & Lesur, G. 2013, Monthly Notices of the Royal Astronomical Society, 434, 2295

Kylafis, N. D. 1983, The Astrophysical Journal, 267, 137

Lallement, R., Vergely, J. L., Valette, B., & Puspitarini, L. 2014, Astronomy and Astrophysics, 561, A91

Latter, H. N., Fromang, S., & Faure, J. 2015, Monthly Notices of the Royal Astronomical Society, 453, 3257

Latter, H. N., Fromang, S., & Gressel, O. 2010, Monthly Notices of the Royal Astronomical Society, 406, 848

Lazarian, A. 2007, Journal of Quantitative Spectroscopy & Radiative Transfer, 106, 225

Lesur, G., Ferreira, J., & Ogilvie, G. I. 2013, Astronomy and Astrophysics, 550, A61

Lesur, G. & Longaretti, P. Y. 2007, Monthly Notices of the Royal Astronomical Society, 378, 1471

Levine, E. S. 2006, Science, 312, 1773

Liu, W., Goodman, J., Herron, I., & Ji, H. 2006, Physical Review E, 74, 056302

Lopez, J. M. & Marques, F. 2005, Physica D: Nonlinear Phenomena, 211, 168

Mac Low, M. M. & Klessen, R. S. 2004, Reviews of Modern Physics, 76, 125

Makwana, K. D., Terry, P. W., Kim, J. H., & Hatch, D. R. 2011, Physics of Plasmas, 18, 012302

Malinen, J., Montier, L., Montillaud, J., Juvela, M., Ristorcelli, I., Clark, S. E., Berné, O., Bernard, J. P., Pelkonen, V. M., & Collins, D. C. 2016, Monthly Notices of the Royal Astronomical Society, 460, 1934

Martínez-Sykora, J., Pontieu, B. D., Carlsson, M., & Hansteen, V. 2016, The Astrophysical Journal, 831, L1

McClure-Griffiths, N. M. 2006, New Horizons in Astronomy: Frank N. Bash Symposium ASP Conference Series, 352, 95

McClure-Griffiths, N. M., Dickey, J. M., Gaensler, B. M., Green, A. J., & Haverkorn, M. 2006, The Astrophysical Journal, 652, 1339

McClure-Griffiths, N. M., Dickey, J. M., Gaensler, B. M., Green, A. J., Haverkorn, M., & Strasser, S. 2005, The Astrophysical Journal Supplement Series, 158, 178

McClure-Griffiths, N. M., Pisano, D. J., Calabretta, M. R., Ford, H. A., Lockman, F. J., Staveley-Smith, L., Kalberla, P. M. W., Bailin, J., Dedes, L., Janowiecki, S., Gibson, B. K., Murphy, T., Nakanishi, H., & Newton-McGee, K. 2009, The Astrophysical Journal Supplement Series, 181, 398

McKee, C. F. & Ostriker, E. C. 2007, Annual Review of Astronomy and Astrophysics, 45, 565

McKee, C. F. & Ostriker, J. P. 1977, The Astrophysical Journal, 218, 148

Mitra, D., Wielebinski, R., Kramer, M., & Jessner, A. 2003, Astronomy and Astrophysics, 403, 585

Molinari, S., Swinyard, B., Bally, J., Barlow, M., Bernard, J. P., Martin, P., Moore, T., Noriega-Crespo, A., Plume, R., Testi, L., Zavagno, A., Abergel, A., Ali, B., Anderson, L., André, P., Baluteau, J. P., Battersby, C., Beltrán, M. T., Benedettini, M., Billot, N., Blommaert, J., Bontemps, S., Boulanger, F., Brand, J., Brunt, C., Burton, M., Calzoletti, L., Carey, S., Caselli, P., Cesaroni, R., Cernicharo, J., Chakrabarti, S., Chrysostomou, A., Cohen, M., Compiegne, M., de Bernardis, P., de Gasperis, G., di Giorgio, A. M., Elia, D., Faustini, F., Flagey, N., Fukui, Y., Fuller, G. A., Ganga, K., Garcia-Lario, P., Glenn, J., Goldsmith, P. F., Griffin, M. J., Hoare, M., Huang, M., Ikhenaode, D., Joblin, C., Joncas, G., Juvela, M., Kirk, J. M., Lagache, G., Li, J. Z., Lim, T. L., Lord, S. D., Marengo, M., Marshall, D. J., Masi, S., Massi, F., Matsuura, M., Minier, V., Miville-Deschênes, M. A., Montier, L. A., Morgan, L., Motte, F., Mottram, J. C., Mueller, T. G., Natoli, P., Neves, J., Olmi, L., Paladini, R., Paradis, D., Parsons, H., Peretto, N., Pestalozzi, M., Pezzuto, S., Piacentini, F., Piazzo, L., Polychroni, D., Pomarès, M., Popescu, C. C., Reach, W. T., Ristorcelli, I., Robitaille, J. F., Robitaille, T., Rodón, J. A., Roy, A., Royer, P., Russeil, D., Saraceno, P., Sauvage, M., Schilke, P., Schisano, E., Schneider, N., Schuller, F., Schulz, B., Sibthorpe, B., Smith, H. A., Smith, M. D., Spinoglio, L., Stamatellos, D., Strafella, F., Stringfellow, G. S., Sturm, E., Taylor, R., Thompson, M. A., Traficante, A., Tuffs, R. J., Umana, G., Valenziano, L., Vavrek, R., Veneziani, M., Viti, S., Waelkens, C., Ward-Thompson, D., White, G., Wilcock, L. A., Wyrowski, F., Yorke, H. W., & Zhang, Q. 2010, Astronomy and Astrophysics, 518, L100

Montier, L., Plaszczynski, S., Levrier, F., Tristram, M., Alina, D., Ristorcelli, I., Bernard, J. P., & Guillet, V. 2015, Astronomy and Astrophysics, 574, A136

Mouschovias, T. C. 1991, The Astrophysical Journal, 373, 169

Murphy, G. C. & Pessah, M. E. 2015, The Astrophysical Journal, 802, 139

Nakamura, F. & Li, Z. Y. 2008, The Astrophysical Journal, 687, 354

Newell, A. C. & Whitehead, J. A. 1969, Journal of Fluid Mechanics, 38, 279

Niemack, M. D., Ade, P. A. R., Aguirre, J., Barrientos, F., Beall, J. A., Bond, J. R., Britton, J., Cho, H. M., Das, S., Devlin, M. J., Dicker, S., Dunkley, J., Dunner, R., Fowler, J. W., Hajian, A., Halpern, M., Hasselfield, M., Hilton, G. C., Hilton, M., Hubmayr, J., Hughes, J. P., Infante, L., Irwin, K. D., Jarosik, N., Klein, J., Kosowsky, A., Marriage, T. A., McMahon, J., Menanteau, F., Moodley, K., Nibarger, J. P., Nolta, M. R., Page, L. A., Partridge, B., Reese, E. D., Sievers, J., Spergel, D. N., Staggs, S. T., Thornton, R., Tucker, C., Wollack, E., & Yoon, K. W. 2010, in Millimeter, Submillimeter, and Far-Infrared Detectors and Instrumentation for Astronomy VI, 77411S

O'Dea, D. T., Clark, C. N., Contaldi, C. R., & MacTavish, C. J. 2011, Monthly Notices of the Royal Astronomical Society, 419, 1795

Oishi, J. S. & Mac Low, M. M. 2011, The Astrophysical Journal, 740, 18

Parker, J. B. & Krommes, J. A. 2013, Physics of Plasmas, 20, 100703

—. 2017, in Zonal Jets, ed. B. Galperin & P. L. Read (eprint arXiv:1503.07498)

Parkin, E. R. 2014, Monthly Notices of the Royal Astronomical Society, 438, 2513

Parkin, E. R. & Bicknell, G. V. 2013, Monthly Notices of the Royal Astronomical Society, 435, 2281

Peek, J. E. G. 2013, The Astrophysical Journal Letters, 766, L6

Peek, J. E. G., Babler, B. L., Zheng, X. W., Clark, S. E., Douglas, K. A., Korpela, E. J., Putman, M. E., Stanimirovic, S., Gibson, S. J., & Heiles, C. 2017, in prep

Peek, J. E. G., Heiles, C., Douglas, K. A., Lee, M.-Y., Grcevich, J., Stanimirović, S., Putman, M. E., Korpela, E. J., Gibson, S. J., Begum, A., Saul, D., Robishaw, T., & Krčo, M. 2011a, The Astrophysical Journal Supplement Series, 194, 20

Peek, J. E. G., Heiles, C., Peek, K. M. G., Meyer, D. M., & Lauroesch, J. T. 2011b, The Astrophysical Journal, 735, 129

Penzias, A. A. & Wilson, R. W. 1965, The Astrophysical Journal, 142, 419

Peretto, N., André, P., Konyves, V., Schneider, N., Arzoumanian, D., Palmeirim, P., Didelon, P., Attard, M., Bernard, J. P., Di Francesco, J., Elia, D., Hennemann, M., Hill, T., Kirk, J., Men'shchikov, A., Motte, F., Nguyen Luong, Q., Roussel, H., Sousbie, T., Testi, L., Ward-Thompson, D., White, G. J., & Zavagno, A. 2012, Astronomy and Astrophysics, 541, A63

Pessah, M. E. 2010, The Astrophysical Journal, 716, 1012

Pessah, M. E. & Goodman, J. 2009, The Astrophysical Journal, 698, L72

Plaszczynski, S., Montier, L., Levrier, F., & Tristram, M. 2013, Monthly Notices of the Royal Astronomical Society, 439, 4048

Pringle, J. E. 1981, Annual Review of Astronomy and Astrophysics, 19, 137

Quinn, J. L. 2012, Astronomy and Astrophysics, 538, A65

Rand, R. J. & Kulkarni, S. R. 1989, The Astrophysical Journal, 343, 760

Rand, R. J. & Lyne, A. G. 1994, Monthly Notices of the Royal Astronomical Society, 268, 497

Rayleigh, L. 1917, in Proceedings of the Royal Society of London. Series A, 148–154

Recktenwald, A., Lücke, M., & Müller, H. W. 1993, Physical Review E, 48, 4444

Regev, O. & Umurhan, O. M. 2008, Astronomy and Astrophysics, 481, 21

Reichborn-Kjennerud, B., Aboobaker, A. M., Ade, P., Aubin, F., Baccigalupi, C., Bao, C., Borrill, J., Cantalupo, C., Chapman, D., Didier, J., Dobbs, M., Grain, J., Grainger, W., Hanany, S., Hillbrand, S., Hubmayr, J., Jaffe, A., Johnson, B., Jones, T., Kisner, T., Klein, J., Korotkov, A., Leach, S., Lee, A., Levinson, L., Limon, M., MacDermid, K., Matsumura, T., Meng, X., Miller, A., Milligan, M., Pascale, E., Polsgrove, D., Ponthieu, N., Raach, K., Sagiv, I., Smecher, G., Stivoli, F., Stompor, R., Tran, H., Tristram, M., Tucker, G. S., Vinokurov, Y., Yadav, A., Zaldarriaga, M., & Zilic, K. 2010, in Proceedings of the SPIE, Columbia University, New York, NY, 77411C

Rembiasz, T., Obergaulinger, M., Cerdá-Durán, P., Müller, E., & Aloy, M. A. 2016, Monthly Notices of the Royal Astronomical Society, 456, 3782

Riegel, K. W. & Crutcher, R. M. 1972, Astronomy and Astrophysics, 18, 55

Robitaille, J. F., Joncas, G., & Khalil, A. 2010, Monthly Notices of the Royal Astronomical Society, 405, 638

Rüdiger, G. & Hollerbach, R. 2007, Physical Review E, 76, 068301

Saul, D. R., Peek, J. E. G., Grcevich, J., Putman, M. E., Douglas, K. A., Korpela, E. J., Stanimirovic, S., Heiles, C., Gibson, S. J., Lee, M., Begum, A., Brown, A. R. H., Burkhart, B., Hamden, E. T., Pingel, N. M., & Tonnesen, S. 2012, The Astrophysical Journal, 758, 44

Schartman, E., Ji, H., & Burin, M. J. 2009, Review of Scientific Instruments, 80, 024501

Schnittman, J. D., Krolik, J. H., & Noble, S. C. 2013, The Astrophysical Journal, 769, 156

Seljak, U. 1997, The Astrophysical Journal, 482, 6

Seljak, U. & Zaldarriaga, M. 1997, Physical Review Letters, 78, 2054

Sfeir, D. M., Lallement, R., Crifo, F., & Welsh, B. Y. 1999, Astronomy and Astrophysics, 346, 785

Shakura, N. I. & Sunyaev, R. A. 1973, Astronomy and Astrophysics, 24, 337

Simard-Normandin, M. & Kronberg, P. P. 1980, The Astrophysical Journal, 242, 74

Sisan, D. R., Mujica, N., Tillotson, W. A., Huang, Y.-M., Dorland, W., Hassam, A. B., Antonsen, T. M., & Lathrop, D. P. 2004, Physical Review Letters, 93, 114502

Soler, J. D., Hennebelle, P., Martin, P. G., Miville-Deschênes, M. A., Netterfield, C. B., & Fissel, L. M. 2013, The Astrophysical Journal, 774, 128

Sousbie, T. 2011, Monthly Notices of the Royal Astronomical Society, 414, 350

Starck, J. L., Donoho, D. L., & Candès, E. J. 2003, Astronomy and Astrophysics, 398, 785

Stefani, F., Gerbeth, G., Gundrum, T., Hollerbach, R., Priede, J., Rüdiger, G., & Szklarski, J. 2009, Physical Review E, 80, 066303

Stefani, F., Gundrum, T., Gerbeth, G., Rüdiger, G., Schultz, M., Szklarski, J., & Hollerbach, R. 2006, Physical Review Letters, 97, 184502

Stil, J. M., Taylor, A. R., & Sunstrum, C. 2011, The Astrophysical Journal, 726, 4

Sun, X. H., Reich, W., Waelkens, A., & Enßlin, T. A. 2008, Astronomy and Astrophysics, 477, 573

Suzuki, T. K. & Inutsuka, S. 2014, The Astrophysical Journal, 784, 121

Terry, P. W., Baver, D. A., & Gupta, S. 2006, Physics of Plasmas, 13, 022307

Umurhan, O., Menou, K., & Regev, O. 2007a, Physical Review Letters, 98, 034501

Umurhan, O., Regev, O., & Menou, K. 2007b, Physical Review E, 76, 036310

Vallée, J. P. 2005, The Astrophysical Journal, 619, 297

Van Eck, C. L., Brown, J. C., Stil, J. M., Rae, K., Mao, S. A., Gaensler, B. M., Shukurov, A., Taylor, A. R., Haverkorn, M., Kronberg, P. P., & McClure-Griffiths, N. M. 2011, The Astrophysical Journal, 728, 97

van Engelen, A., Bhattacharya, S., Sehgal, N., Holder, G. P., Zahn, O., & Nagai, D. 2014, The Astrophysical Journal, 786, 13

Vasil, G. M. 2015, Proceedings of the Royal Society A: Mathematical, Physical and Engineering Sciences, 471, 20140699

Vazquez-Semadeni, E. 2012 (Springer), 401–444

Velikhov, E. P. 1959, Soviet Physics JETP, 36, 995

Vergely, J. L., Valette, B., Lallement, R., & Raimond, S. 2010, Astronomy and Astrophysics, 518, A31

Verheijen, M., Oosterloo, T., & Heald, G. 2009, Proceedings of Science

Verschuur, G. L. 1968, Physical Review Letters, 21, 775

Vidal, M., Leahy, J. P., & Dickinson, C. 2014, Monthly Notices of the Royal Astronomical Society, 461, 698

Vishniac, E. T. 2009, The Astrophysical Journal, 696, 1021

Weaver, H. 1979, Symposium-International Astronomical Union

Welsh, B. Y. & Shelton, R. L. 2009, Astrophysics and Space Science, 323, 1

Wheeler, J. C., Kagan, D., & Chatzopoulos, E. 2015, The Astrophysical Journal, 799, 85

Willis, A. P. & Barenghi, C. F. 2002, Journal of Fluid Mechanics, 463, 361

Wolfire, M. G., McKee, C. F., & Hollenbach, D. 2003, The Astrophysical Journal, 587, 278

Woltjer, L. 1967, Radio Astronomy and the Galactic System, 31, 479

Zaldarriaga, M. 2001, Physical Review D, 64, 103001

Zaldarriaga, M. & Seljak, U. 1998, Physical Review D, 58, 023003

—. 1999, Physical Review D, 59, 123507

Zweibel, E. G. 2005, in Fluid Dynamics and Dynamos in Astrophysics and Geophysics, ed. A. M. Soward, C. A. Jones, D. W. Hughes, & N. O. Weiss, 115